

Biomechanics of Spinal Metastases

Ondrej Holub

Submitted in accordance with the requirements for the degree of
Doctor of Philosophy

The University of Leeds
School of Mechanical Engineering

April, 2014

The candidate confirms that the work submitted is his/her own, except where work which has formed part of jointly-authored publications has been included. The contribution of the candidate and the other authors to this work has been explicitly indicated below. The candidate confirms that appropriate credit has been given within the thesis where reference has been made to the work of others. Jointed-authored publication currently under review includes low-modulus cement testing in section 5.2 which was undertaken in collaboration with the University of Uppsala, in particular with visiting researcher Alejandro Landa Lopez under the framework of the project SpineGo and supervised by Dr. Cecilia Persson. The candidate confirms that work conducted in collaboration with co-authors of this study is distinguished and acknowledged later in the text.

This copy has been supplied on the understanding that it is copyright material and that no quotation from the thesis may be published without proper acknowledgement.

The right of Ondrej Holub to be identified as Author of this work has been asserted by him in accordance with the Copyright, Designs and Patents Act 1988.

Acknowledgements

This work was conducted in the framework of the Marie-Curie ITN framework. Project was funded through the European Community, Grant Agreement n° PITN-GA-2009-238690-SPINEFX.

It is my pleasure to gratefully thank all the people that made this thesis possible and who have supported me in my research in the past few years.

First of all, I would like to express my gratitude to my PhD. supervisor Prof. Richard M. Hall for putting together this wonderful European project I was proud to be part of. I would also like to thank him for giving me the opportunity to join the University of Leeds as a Marie Curie Research Fellow and for his support during my research and while I was writing my thesis. I would like to thank Prof. Nik Kapur, my second supervisor, for his full support when conducting the theoretical part of this work as well as for his fruitful comments when writing up the results. In fact, I would like to thank both of my supervisors for being great people not only in science but also in real life.

I would like to acknowledge also all the colleagues whose contributions have been essential in different ways for the accomplishment of the sub-studies that compose this thesis. It was a pleasure to join a group of highly skilled researchers with whom we also had good times back in Leeds. First, I would like to thank the members of the PVP group around Richard. Particularly I would like to acknowledge Daniel Skrzypiec who brought priceless experimental skills to the lab, collaborated on the experimental part of this thesis and contributed with fruitful discussion throughout the work. In particular, Daniel was the main researcher in the MM augmentation study taking the lead in the initial fracturing of MM samples used in this study. I would also like to thank Adam Liddle and Vishal Borse who were the core of the PVP group when I started and introduced me to the experimental facilities and scanner. Vish also assisted with the injection procedure for the PMMA study. Thanks also go to Antony Bou Francis for his energetic attitude towards every task encountered while keeping good company as we were on most occasions the last leaving any social events we participated in

around the world. Further thanks go to Nicola Brandolini for both professional collaboration and friendship, assisting me in the CaP augmentation study and conducting all his experiments with a high level of proficiency and willingness to share his theoretical knowledge. In fact, I would like to acknowledge all colleagues from the Institute of Medical and Biomedical Engineering, University of Leeds, for everyday help particularly in the laboratory. Thanks go to many of them who were simply around sharing their particular knowledge in their field, such as Nagitha Wijayathunga, Nic Roberts, Sami Tarsuslugil, Tony Herbert and many others.

It wouldn't be a proper acknowledgement without mentioning all the lads from office 346: we had some good times, hey? In particular I would like to acknowledge Mehran Moazen for good scientific discussions.

My further acknowledgement goes to colleagues of the SpineFX project all around Europe, the other Marie-Curie Fellows for being such a great network of young, dynamic and bright researchers with great potential in cutting edge science. Three years for conducting our studies was quite a short time to fully deploy the potential of the network in terms of collaborations, but with many Fellows I managed to stay in touch for scientific discussions throughout and outside of the project.

With regards to the work on biodegradable materials I would like to acknowledge that the augmentation material has been developed by the Network partner BONESUPPORT AB. with researcher in charge Eva Lidén and Industrial Fellow colleague Argyrios Kasiotas who contributed to this work in providing the filling material and training me in using it.

I am also glad to acknowledge Alejandro Lopez and Cecilia Persson for collaboration on PMMA cement testing. While Cecilia contributed in research discussion and supervision before and during the study design, Alejandro contributed with his cement and in conducting the main body of the re-fracture experiment with training provided. Regarding the work I conducted in Vienna I would like to acknowledge Enrico Dall'Ara, one of the most experienced young researchers I have ever met who was always willing to share his point of view without undervaluing views of others. I would also like to thank Prof. Philippe Zysset for his targeted comments when preparing and conducting the micro-indentation study and to Uwe Wolfram for providing his data for comparison as well as for fruitful scientific discussions.

I would also like to take this opportunity to thank my parents Mirka and Ruda, particularly for supporting me in my studies and in fact for being a good example of well-educated people which persuaded me to start my studies in the first place.

And the most important acknowledgement, which goes to my life partner and my lovely daughter, I wish to express my thanks in my mother tongue: Rézi, tohle byla nejzajímavější epizoda našeho života. Sama víš nejlíp, že tahle práce je velkou měrou taky tvou prací. Jsem pyšný, co vše jsme dokázali a moc ti děkuju za podporu a hlavně ti děkuju za to nejcennější v našem životě: za Rebečku. Rebečko, tobě moc děkuju, za to jak jsi byla skvělá, když jsem pracoval na téhle práci, za tvé sílu dodávající úsměvy, za motivaci, za tvou chuť do života, ale hlavně za to, jak skvěle se k nám s maminkou chováš. Jsi super parťák do života a na čas v Leedsu tak nikdy nezapomenu.

Abstract

The lack of suitable models for prediction of the vertebral body (VB) failure load for a variety of pathologies hampers the development of indications for surgical and pharmaceutical interventions and the assessment of novel treatments. Similar models would also be of benefit in a laboratory environment in which predictions of failure load could aid experimental design when using cadaveric tissue. Finite element modelling shows great potential but the expertise required to effectively deploy this technology in a clinical environment precludes its routine use at the present time. Its deployment within the laboratory environment is also time consuming. An alternative approach may be the use of composite beam theory structural analysis that takes into account both vertebral geometry and the bone mineral density (BMD) distribution and they are utilised to predict the loads at which vertebrae will fail.

As a part of this work, vertebrae suffering from three distinct pathologies (osteoporosis, multiple myeloma (MM) and metastases) were tested in a wedge compression loading protocol (WCF) as a determinant for vertebroplasty treatment. MM bone was first tested for changes at the bone tissue level by means of depth-sensing micro-indentation testing. In the second part more than one hundred VBs were subjected to a destructive *in-vitro* WCF experiment, while CT images were used for *in-silico* structural and morphological assessment. In the last part, two vertebroplasty cements, calcium phosphate and PMMA, were tested.

At the tissue level MM bone shows rather moderate changes which are of such small magnitude that alone would not be sufficient to change the overall vertebral strength. Relatively good predictions of VB strength were obtained when using image-based fracture prediction suggesting that bone distribution and pathological alterations to its structure make a significant contribution to overall VB strength. The results of VB reinforcement using either of the cements show increased strength while stiffness was restored only when PMMA cement was injected in lower porosity samples.

Table of Contents

Chapter 1 Introduction	1
1.1 Clinical drivers – defining the problem.....	1
1.2 Aims and objectives of the study	4
Chapter 2 Literature Review	6
2.1 Anatomy	6
2.1.1 Spine.....	6
2.1.1.1 Biomechanics of the spine	7
2.1.2 Vertebra	8
2.1.2.1 Thoracic vertebrae	8
2.1.2.2 Lumbar vertebrae.....	9
2.1.3 Bone.....	9
2.1.3.1 Cortical bone	10
2.1.3.2 Trabecular bone	12
2.1.4 Morphology and mineral density of human vertebrae	13
2.2 Pathology	16
2.2.1 Osteoporosis	16
2.2.1.1 Definition, screening and occurrence of osteoporosis.....	17
2.2.1.2 Osteoporotic fractures and their systematic clinical impact.....	18
2.2.1.3 Treatment of osteoporosis.....	19
2.2.2 Metastases to bone	19
2.2.2.1 Metastasis: Definition and occurrence.....	19
2.2.2.2 Clinical and patient related impact due to metastatic infiltration – scoring systems.....	21
2.2.2.3 Treatment of secondary tumour to bone - state of the art.....	23
2.3 Vertebral fractures.....	24
2.3.1 Definition, occurrence and classification of vertebral fractures	24
2.3.2 Biomechanics of vertebral fractures	25

2.3.3 Treatment of vertebral compression fractures - state of the art.....	26
2.4 Vertebroplasty in VCF treatment	27
2.4.1 PVP in osteoporotic fractures.....	27
2.4.2 Vertebroplasty in metastatic bone	28
2.4.3 Complications and controversy surrounding vertebroplasty.....	29
2.4.3.1 Controversy of PVP.....	29
2.4.3.2 Complications.....	30
2.5 VCF cadaveric studies	30
2.5.1 Biomechanics in cadaveric studies	31
2.5.2 Biomechanical assessment in vertebroplasty.....	32
2.5.3 Types of augmentation cement	33
2.5.4 Prophylactic augmentation	33
2.6 Predictions of vertebral compression fractures	33
2.6.1 Clinical models to identify vertebrae prone to fracture and use of numerical models in clinical practice	33
2.6.2 Engineering principles in fracture prediction.....	34
2.7 Morphology and material properties of the bone	38
2.7.1 Material properties of human bone.....	38
2.7.2 Bone material models for fracture prediction.....	39
Chapter 3 Development of a fracture prediction tool.....	42
3.1 Development of an <i>in-silico</i> fracture prediction tool.....	43
3.1.1 Introduction to vertebral bone fracture prediction	43
3.1.1.1 Finite Element modelling in WCF	43
3.1.1.2 Fast and simplistic engineering principle models	44
3.1.2 Methods used in development of the fracture prediction tool	45
3.1.2.1 Composite theory approach	45
3.1.2.2 Implementation of the composite beam theory into a comprehensive computational package	47
3.1.2.3 Vertebral body image segmentation (masking)	49
3.1.2.4 Analytical verification and surrogate model validation.....	53
3.1.2.5 Fracture prediction tool validation using historical data.....	57
3.1.2.5.1 Collected historical samples used for validation	57

3.1.2.5.2 Historical data - Scanning procedure	57
3.1.2.5.3 Historical data - Wedge compression fracture	58
3.1.2.5.4 Predicting historical data - beam theory and BMD-based method	58
3.1.3 Results in predicting historical data	61
3.1.3.1 Historical data – Collected osteoporotic samples	61
3.1.3.2 Historical data - Collected metastatic samples	63
3.1.3.3 Historical data - Collected multiple myeloma samples	66
3.1.4 Initial validation using historical data - Discussion	68
3.1.4.1 BMD based prediction used on historical data	68
3.1.4.2 Image processing and density-to-modulus material model	69
3.1.4.3 Validation of the fracture prediction tool on historical samples	70
3.2 Commissioning of cadaveric Wedge Compression Fracture testing rig	71
3.2.1 Introduction to cadaveric testing of human samples	71
3.2.2 Wedge compression testing - Methods	73
3.2.2.1 Cadaveric sample selection and preparation	73
3.2.2.2 Tissue collection, dissection and storage	75
3.2.2.3 Cadaveric sample scanning	76
3.2.2.4 Single vertebra Wedge Compression Fracture rig	77
3.2.3 Fracturing of cadaver samples - Results	82
3.2.3.1 WCF in osteoporotic samples	82
3.2.3.2 WCF in multiple myeloma samples	84
3.2.3.3 WCF in metastatic specimens	84
3.2.4 Initial fracture of tested samples - Discussion	86
3.2.4.1 WCF testing protocol	86
3.2.4.2 Limitations of the sample population and treatment history of the donors	86
3.3 Fracture prediction tested on large sample population: three pathologies	87

3.3.1 <i>In-silico</i> vs. experiment strength comparison	87
3.3.1.1 Reducing fracture prediction range to a single slice	88
3.3.1.2 Density-to-modulus model calibration	89
3.3.2 Comparison between predicted and experimental data – Results for three pathologies.....	90
3.3.2.1 Predicted osteoporotic samples	90
3.3.2.1.1 Weakest slice selected from 80% of vertebral body height - OP	90
3.3.2.1.2 Single slice analysis tested on osteoporotic samples - OP	92
3.3.2.1.3 Material model calibration in osteoporotic population.....	93
3.3.2.2 Predicted multiple myeloma samples.....	93
3.3.2.2.1 Weakest slice selected from 80% of vertebral body height - MM	93
3.3.2.2.2 Single slice analysis - MM	95
3.3.2.2.3 Material model calibration - MM.....	95
3.3.2.3 Predicting fractures in metastatic specimens	96
3.3.2.3.1 Weakest slice selected from 80% of vertebral body height - mets	96
3.3.2.3.2 Single slice analysis - mets.....	98
3.3.2.3.3 Material model calibration – mets ...	98
3.3.3 Fracture prediction tool used in three distinct pathologies - Discussion	99
3.3.3.1 Single slice analysis	100
3.3.3.2 Retrospective density-to-modulus model fit.....	101
3.3.3.3 Structural assessment in predicting OP, MM and mets – comparison to sophisticated FEA models.....	103
3.3.3.4 Comparison of fracture prediction tool to other analytical models.....	104
3.3.3.5 Limitations of fracture prediction used in this study	105
3.4 Commissioning of the fracture prediction tool – Summary	105

Chapter 4 Determination of the mechanical properties of trabecular bone utilising microCT assessment and micro-indentation.....	107
4.1 Pathology specific morphology.....	107
4.1.1 Introduction to assessment of micro-properties of the bone	107
4.1.2 Methods used in morphology assessment	108
4.1.2.1 Sample population	108
4.1.2.2 Morphology image processing	108
4.1.2.3 Comparing the morphology to cadaveric testing ...	112
4.1.3 Morphology of human bone - Results.....	112
4.1.3.1 Morphology assessment	112
4.1.3.1.1 Morphology of osteoporotic bone..	112
4.1.3.1.2 Morphology of multiple myeloma bone	112
4.1.3.1.3 Morphology of metastatic bone.....	113
4.1.3.2 Morphology as a fracture prediction and comparison to composite beam theory fracture prediction tool.....	113
4.1.4 Morphology assessment in bone with cancer and OP - Discussion.....	116
4.2 Micro-indentation of multiple myeloma bone	118
4.2.1 Introduction to micro properties of multiple myeloma bone	118
4.2.2 Methods of bone micro-properties assessment.....	119
4.2.2.1 Multiple myeloma bone indentation - sample selection.....	119
4.2.2.2 Nearby lesion localisation.....	120
4.2.2.3 Sample preparation prior to indentation testing.....	121
4.2.2.4 Indentation procedure	124
4.2.2.5 Statistical analysis used in micro-indentation study	125
4.2.3 Micro-properties of multiple myeloma and comparison to non-affected population - Results.....	125
4.2.3.1 Indentation properties - comparison between MM groups	126
4.2.3.2 Indentation properties - comparison between MM and non-MM samples.....	127

4.2.3.3 Bone material properties in proximity of lesion.....	130
4.2.4 Underlying material properties of multiple myeloma bone - Discussion.....	132
4.3 Trabecular bone micro-properties assessment - Summary.....	134
Chapter 5 Investigation into the use of vertebroplasty for the augmentation of osteoporotic and metastatic lesions	136
5.1 CaP vertebroplasty: effect of filling ratio on biomechanics in a single vertebra study	136
5.1.1 Introduction to ceramic cement PVP	136
5.1.2 Methods used in CaP PVP	138
5.1.2.1 CaP study design	138
5.1.2.2 Sample population and group allocation prior to CaP augmentation	140
5.1.2.3 CaP PVP and repeated fracture testing	140
5.1.3 Volume optimisation in CaP vertebroplasty - Results.....	142
5.2 Low modulus PMMA vertebroplasty	148
5.2.1 Introduction to acrylic cement augmentation in OP and metastatic bone.....	148
5.2.2 Methods used in assessing low-modulus PMMA cement	149
5.2.2.1 PMMA PVP - Study design	149
5.2.2.2 Sample population and group allocation prior to augmentation	151
5.2.2.3 PMMA PVP and refracturing experiment.....	151
5.2.3 Augmentation results when using PMMA in augmenting OP and metastatic bone	152
5.2.4 Biomechanical effect due to varied PMMA cement stiffness- Discussion	154
5.3 Biomechanics of augmentation using CaP and PMMA cement - Summary.....	157
Chapter 6 Conclusion and Future perspective.....	159
6.1 Non-invasive predictors of fracture in patients with different pathologies.....	159
6.1.1 Summary of findings in structural assessment of metastatic and non-metastatic bone	159
6.1.2 Original contribution	160
6.1.3 Future perspective in structural assessment of metastatic bone.....	161
6.2 PVP use in treatment of vertebral compression fractures	163

6.2.1 Osteo-conductive cement augmentation.....	163
6.2.2 Low-modulus PMMA cement augmentation.....	163
6.2.3 Original contribution	164
6.2.4 Future perspective in CaP and PMMA augmentation	165
References.....	167
List of Abbreviations.....	185
Appendix A: Historical data assessment.....	187
Appendix B: Validation of vertebral body segmentation.....	189
Appendix C: Donors' medical records available for this study	192
Appendix D: Morphology assessment	196
Appendix D.1: Osteoporosis.....	196
Appendix D.2: Metastases	197
Appendix D.3: Multiple myeloma.....	197
Appendix E: Cadaveric testing: Strength/stiffness per level	198
Appendix E.1: Osteoporosis.....	198
Appendix E.2: Multiple myeloma	203
Appendix E.3: Metastases.....	204
Appendix F: Micro-indentation	205
Appendix F.1: Post-hoc statistical analysis	205
Appendix F.2: Humidity and temperature adjustment	206
Appendix F.3: Results – graphical form.....	207
Appendix G: Bi-axial eccentric loading.....	208
Appendix G.1: Introduction to asymmetric beam theory.....	208
Appendix G.2: Theoretical consideration for asymmetric beam profile	208
Appendix G.2.1: Bi-axial eccentric loading in asymmetric profile: definition.....	208
Appendix G.2.2: Moment notation.....	209
Appendix G.3: Application of asymmetric beam theory.....	210
Appendix G.4: Fracture prediction when accounting for bi-axial eccentric loading: Results	210
Appendix G.5: Conclusion when comparing uni and bi- axis eccentric loading with respect to fracture prediction.....	214
Appendix H: Image processing: vertebral body boundary estimation	215

List of Tables

Table 1 Incidence of metastases and bone reaction due to presence of cancer, ratio between osteoblastic/osteoclastic bone formation [3].....	20
Table 2 Classification of the metastatic infiltration (red arrow) to spine according to Tomita et al. [30].....	22
Table 3 Vertebral Compression Fracture (VCF) classification according to Genant et al. [76].....	25
Table 4 Comparison of assorted <i>in-silico</i> approaches used in vertebral body fracture prediction models	37
Table 5 Technical annotation of different densities and density-based morphological indices.....	40
Table 6: Analytical verification of the mathematical solution which was used in the fracture prediction tool. Results show very negligible difference even when manual definition of AP points has been conducted (when defined numerically with pixel precision, the results were identical)	55
Table 7 Cadaveric samples collected and used for wedge compression fracture testing.....	74
Table 8 List of all spines used for wedge compression fracture testing	75
Table 9 Cadaveric VB outer morphology measurement – sample with pre-existing vertebral body fracture.....	84
Table 10 Pearson’s Correlations (r) between the biomechanical experiment and the image-based analysis	114
Table 11 Pearson’s correlation coefficients (r) as the result of the multivariate regression analysis.....	115
Table 12 Base group sample allocation comprising twelve samples from six donors with diagnosed MM cancer compared to a non-affected population	122
Table 13 Number of indentations and samples for each of the base groups, together with non-MM group acquired by Wolfram et. al. [36]	122
Table 14 Indentation moduli, hardness and indentation energies for MM groups for axial and transverse indents (a significant difference (labelled (*)) was found only between axial and transverse directions).....	127

Table 15 Comparison between MM infiltrated samples and samples without MM infiltration (significant difference $p < 0.05$, labelled (*))	128
Table 16 Coefficient of determination (adjusted R^2) and its significance in the vicinity of the lesion	132
Table 17 Vertebral strength and stiffness enhancement after VB augmentation (mean difference pre- and post-augmentation), significance level of $p = 0.05$ shows that a statistical difference was found in vertebral strength pre- and post-augmentation fracture in the group filled with 10% of vertebral body volume ..	144
Table 18 Vertebral strength and stiffness improvement after VB augmentation (mean difference pre- and post-augmentation), significance level of $p = 0.05$ shows that a statistical difference was not found in change of stiffness before or after augmentation in OP samples, but differences were found in all other instances.....	154
Table 19 Comparison of the effect of the augmentation between the two tested cements showed a significant difference in cemented vertebrae in oncological samples, but failed to be significantly disparate for neoplastic pathology.....	154
Table 20 Historical data: Experimental, BMD and fracture prediction data of metastatic samples from a donor with bladder cancer.....	187
Table 21 Medical history details as acquired from GIFT banks.	195
Table 22 Morphology assessment: Osteoporosis (mean \pm stdev).....	196
Table 23 Morphology assessment: Metastases to spine (mean \pm stdev)	197
Table 24 Morphology assessment: multiple myeloma (mean \pm stdev)	197
Table 25 Post-hoc statistical analysis for multiple myeloma bone material properties.....	205
Table 26 Predicted and experimental values in <i>in-silico</i> assessment of vertebral strength in simulated metastatic infiltration and a real sample.....	211

List of Figures

- Figure 1** The aim of this work is to combine knowledge of mechanical properties of vertebral bone and experimental testing on both tissue and organ level on pathology specific samples for use in vertebroplasty. 5
- Figure 2** Figure depicting human spine with detail to lumbar and thoracic vertebrae. (A- Vertebral Body, B- Vertebral foramen, C- Transverse process, D- Lamina, E- Spinous process, F- Pedicle) 7
- Figure 3** Schematic figure of a bone structure at different scales – organ-, meso- and micro-scale (A- Osteon of cortical bone, B- Haversian canal, C- Volkmann’s canal, D- Vessels and nerves, E- Lamellae, F- Canaliculi, G- Osteon of trabecular bone, H- Osteoblasts, I- Osteoclast, J- Osteocytes) 10
- Figure 4** Microscopic image of cortical shell and trabecular bone interface depicting difference between cortical shell (left top) and notably more porous trabecular bone (right bottom). Cortical bone is characteristic of osteons forming around the Haversian canal where older osteons are overlaid by new ones. On the contrary trabecular bone is characterised by layers of bone where the central canal is not present. This is understood to be a reason for deterioration of bone emerging from outer layers towards the centre (such as thinned trabeculae in osteoporotic patients) 11
- Figure 5** Microscopic image of trabecular bone, single trabecula in detail: trabecular bone is a very porous structure where each trabecula is formed around its main axis composed of layers which form externally 13
- Figure 6** Morphometrical indices to qualitatively assess bone structure in-situ. Trabecular spacing (Tb.Sp), thickness (Tb.Th), number of trabeculae (Tb.N), connectivity density (Conn.D) or level of isotropy (MIL) 14
- Figure 7** Comparison of “healthy” high-mineral-density bone (left) and low-mineral-density osteoporotic bone (right). Lose of trabecular struts in OP bone is predominantly in horizontal direction [21] as indicated by red arrow. Structural integrity in osteoporotic bone while compromised has been well documented and is believed to be related to a simple loss of supporting material, however the cancer-bearing bone is yet to be thoroughly investigated 17

Figure 8: Engineering beam theory principles used in predicting vertebral strength during the wedge compressing fracture	46
Figure 9 The fracture prediction tool developed in this work comprises steps in which VB cross-sectional boundaries are obtained by a series of morphological operations, then each voxel within this mask is converted to an elastic modulus with which to create a series of modulus maps of the axial slices. Vertebral strength is taken as yield load of the weakest slice	48
Figure 10 Graphical User Interface (GUI) designed for purposes of the fracture prediction tool.....	49
Figure 11: Vertebral body boundary estimation: a microCT image is first taken and binarised according to a pre-set histogram threshold value, this is followed by a number of morphological operations such as filling the gaps and removing disjointed particles before the final mask is obtained (A). As shown in the GUI snapshot (B) this method can account even for more challenging low density human cadaver samples	51
Figure 12 Manual correction of the VB boundaries combined with area-based filtering algorithm. The area-based filtering algorithm identifies slices where the pixel count of the masked area suddenly changes with respect to the previous slice. If such a step change occurs, the border is replaced with the previous one until the slice where the border area falls back into a user-specified difference between calculated cross-sectional areas is reached.....	52
Figure 13 Manual correction of boundary outlines. In case of a “morphologically challenging” sample (e.g. very low trabecular bone density or metastasis), manual correction is required. Such a problem can occur due to a low density gradient between the bone and the background (A). In such cases manual correction (B) allows the user to correct the boundaries to include the whole vertebral body (C).....	53
Figure 14: Analytical verification of the fracture prediction script. A false image of a sample consisting of composite layers of varying stiffnesses was imported as a simulated CT image. Points defining the AP-axis were imported manually (green markers at the margin of the composite) and load axis was defined at 25% of the AP axis (green “o” marker).....	54

Figure 15 Validation study of the fracture prediction tool using surrogate plastic models representing different scenarios of metastatic infiltration. The blue arrow indicates metastatic infiltration in the human vertebral body modelled as a void in a simplified vertebral body. Models are listed from left to right according to their strength (anteriorly positioned vertebrae resulted in the highest strength compromise compared to healthy vertebrae on the right)	56
Figure 16: Example of microCT vertebral body assessment depicting severe metastatic infiltration. An axial slice obtained from microCT (above) shows a notable influence on the internal structure when mixed lesions are present. Beneath is a 3d representation of the infiltrated vertebra	60
Figure 17 Bland-Altman analysis of predicted and experimentally obtained fracture loads for collected osteoporotic samples. The difference between both datasets indicates modest limits of agreement lower than ± 1 kN	62
Figure 18 Plot of the predicted versus experimentally determined failure load. Beam-theory method (red “o” marker) shows good agreement and correlation in comparison to the formerly used product of BMD and cross-sectional area (blue “Δ” marker), with the example in the bottom right corner depicting a sample reaching 6.03kN strength most probably due to the presence of extra-vertebral body formations. In fact, all samples in the red-dashed area contained similar osteophytes	63
Figure 19 Example of a severely infiltrated sample containing multiple osteoclastic lesions together with extra-vertebral body formation in the anterior part of the vertebral body	65
Figure 20 Twelve samples infiltrated by bladder cancer were subjected to an experimental compression test following a microCT assessment. The initial fracture prediction (red) failed to correlate with experimental values; however the correlation improved after removing the extra-VB formation (blue) from assessment	66
Figure 21 Experimental and predicted values of vertebral strength based on beam theory prediction. Contrasting colours indicate different spines which highlights a possible peculiarity of Spine 2 MM which has been notably and consistently overestimated	67
Figure 22 Initial scan of sample “Spine 2 MM L5” and modulus map masking. (a.) Possible pre-existing (not cured) fracture resulting in a disconnected piece of bone. (b.) <i>In-silico</i> masking of the disconnected element (indicated by the red arrow) enabling an assessment of the contribution to the strength of the sample	68

Figure 23 Wedge compression fracture in-vivo and in-vitro simulated WCF. All fractured vertebrae found in spines had a characteristically deformed vertebral body towards the anterior side (example in A). This type of fracture (WCF) is typical for osteoporotic/metastatic bone 72

Figure 24: WCF type of fracture can be obtained experimentally where an intact bone is compressed eccentrically. This figure illustrates a sagittal slice of vertebra scanned in microCT image before and after inducing the fracture 73

Figure 25: Harvesting of vertebral samples. The figure depicts disarticulation of levels T10, T11, T12 (from left to right) with enlarged bridging osteophytes (“Spine 2 mets”)..... 76

Figure 26: The enhanced single vertebra compression rig, an illustration of a CAD model (A). The rig consists of a base fitted into the frame of the Instron testing machine and 3 precisely positioned LVDTs to capture the change in inclination of the top loading plate, compressed by the ball joint driven by the cross-head. The bottom figure (B) illustrates schematically the positioning of the sample. The sample is aligned in the recess using a Delrin fitting and dental plaster embedding. The top PMMA imprint allows loading of the sample without introducing tension on the posterior part of the vertebral body 79

Figure 27: Single vertebra mounting rig. The top illustration (A) represents a CAD model of the mounting rig designed to position and embed the sample prior to testing. Subsequent images represent positioning which allows aligning with the loading axis (B), embedding of the bottom endplate (C) and making an impression of the top endplate (D) 80

Figure 28 Testing rig mounted to uniaxial compression machine (Instron). Sample wrapped in a purified-water-soaked tissue is compressed between the top loading plate and the bottom part of the rig. While the bottom of the sample is partially embedded and the coupling between the cross-head and the loading plate is performed by a ball joint, the loading axis remains at the same position while the loading plate is allowed to tilt around this axis..... 81

Figure 29 A typical vertebral compression test data readout as a function of time (a.) later compiled in a form of load-displacement curve (b.). The curve is characterised by an initial ramp-up sequence reaching a load of 50N which is maintained for 5 minutes to simulate preloading conditions and allow the specimen to settle in the mould. When loaded at constant rate, the sample typically remains in the elastic region until yielding to the plastic region where fracture is followed by a short softening. The end-point of the experiment was at 25% strain followed by a 10 minute relaxation period at 50N (initial fracture, sample Spine BS 3–T10)..... 83

Figure 30 Spine 2 mets: Initial strength and stiffness for corresponding spinal level..... 85

Figure 31 A characteristic slice-by-slice fracture load prediction identifying the weakest slice where each step on the y-axis represents analysis of one axial CT slice. It should be noted that the weakest slice appears predominantly in the mid cranio-caudal section of the vertebral body which allows minimising of the range of analysis excluding bony endplates. The typical prediction curve is characterised by the low degree of variability of predicted strength within the vertebral body. Mid-slice analysis could then provide sufficient illustration of degree of vertebral strength compromise with minimal time and scanning effort..... 88

Figure 32 Structural assessment of the osteoporotic sample. On the left is a microCT image of the weakest slice identified by the fracture prediction tool. On the right is the corresponding modulus map..... 90

Figure 33 Fracture prediction - osteoporotic samples: Eight spines (fifty-four samples) were experimentally tested and compared to the predicted vertebral strength..... 91

Figure 34 Fracture prediction - osteoporotic samples: Bland-Altman plot indicating a large discrepancy due to outliers belonging to a single donor (SpineGo 4). Peculiarity of SpineGo 4 could not be assessed but was believed to come from presence of healing woven bone which appears high in mineral component but lacks the structural integrity of fully healed bone (typical for early stage of healing) 92

Figure 35 Structural assessment of a multiple myeloma sample. On the left is a microCT image of the weakest slice identified by the fracture prediction tool. On the right is the corresponding modulus map. The arrows indicate widespread multiple myeloma lytic lesions. Here the lesions filled with material with low mineral density result in a low modulus ($E=f(\rho)$) hence negligibly contributing to the wedge compression strength 94

Figure 36 Structural assessment of multiple myeloma bone with severe infiltration causing disintegration of the natural structure of the trabecular bone	94
Figure 37 Predicted strength compared to experimental data in multiple myeloma sample set	95
Figure 38 Structural assessment of a sample with osteolytic infiltration to the vertebral body. The lesion (indicated by a blue arrow on the left) replaces the natural trabecular bone with a highly vascularised but low density tissue which results in an almost negligible contribution to the strength (the red arrow on the corresponding modulus map with automatically detected VB boundaries). Despite the confirmed metastatic infiltration, only three samples exhibited a morphological alteration due to the presence of cancer	96
Figure 39 Fracture prediction of metastatic samples. This diagram presents <i>in-silico</i> predicted fracture loads compared to those derived from the cadaver testing.....	97
Figure 40 Structural assessment of a sample from a spine with metastatic infiltration but without presence of a lesion in the vertebra.....	97
Figure 41 Bland-Altman plot indicating relatively good agreement between predicted and experimental strength in an assessment of the metastatic samples.....	98
Figure 42: Protocol defining the VOI within the trabecular structure.	109
Figure 43: Single step flowchart of the Morphological assessment. (ISQ - microCT scanning file; GOBJ - microCT file defining ISQ specific volume of interest mask; SEG_CYL – 3d binarised image stack of representative trabecular bone region; BMD,BV/TV, Tb.Sp, Tb.Th, Tb.N and Conn.D represent morphological indices discussed in the text).....	110
Figure 44: Principle of iterative selection thresholding technique proposed by Ridler and Calvard [236] and adopted to microCT measurements performed in this study.....	111
Figure 45: Graphical User Interface (GUI) of a custom-compiled script used to view the ISQ scanning files, to estimate the BMD, BV/TV and optimal threshold within the desired VOI (based on GOBJ). Subfigure (A) shows an example of vertebra scanned in microCT100, a program which allows a slice by slice list, is able to adjust brightness and highlights segmented bone according to the estimated threshold detailed in subfigure (B).....	111

Figure 46: Vertebral body section cut along a plane perpendicular to the vertebral axis in the middle of the multiple myeloma bone without any visible lesion (A), moderately infiltrated sample (B) and sample severely affected by MBD (C)..... 120

Figure 47: Visualised distance transform algorithm to estimate the trabecular spacings and thicknesses which highlights morphological changes due to lytic infiltration to bone. Segmented image (A.), Tb.Sp (B.) to identify a cancer lesion (multiple myeloma cancer)..... 120

Figure 48 Micro-indentation sample preparation: Lesion has been identified based on segmented microCT images superimposed by lesion map highlighting bone separations >3.5mm. Reference grooves made prior to scanning were used as a reference guideline for latter cutting. Figure depicts an example of a single coupon containing a lesion cut with respect to the cutting grooves 121

Figure 49: MicroCT assessment followed by sample cutting according to a suggested cutting path. Bone is represented as segmented tissue (red) whereas fitted spheres of different colours according to their size represent the lesion (>3.5mm), thus predicting the lesion position (left). A cleaned and embedded sample with rough demarcation of the lesion borders is annotated with a permanent marker (right)..... 123

Figure 50 Micro-indentation: the border of the lesion has been quantified as the closest trabecula-intersecting indentation plane. In case of multiple occurrences, lesions have been labelled independently (as in the example), together with a record of the position of at least two reference markers for orientation and indent position/bone overlap 125

Figure 51 Micro-indentation of multiple myeloma bone: Indentation properties in form of whiskers plot. No significant difference was found between samples with different progression of multiple myeloma infiltration. Only marginal difference was found between myeloma-affected and unaffected population 129

Figure 52 Multiple myeloma bone sample. Indent positions with respect to the border of the lesion are superimposed over a picture of the indented bone. Each indent is represented as a blue star marker, whereas the border coordinates are represented by a solid blue line..... 130

Figure 53 Change of indentation moduli depending on the distance from a lesion 131

Figure 54: Alpha-TCP cement study flowchart. Three groups of different vertebral volume fill were separately tested and compared for difference in observed vertebral strength..... 139

Figure 55: α-TCP cement augmentation: Needle is inserted via pedicles (A) similarly to clinical application. When positioned to anterior middle region of VB, cannula is inserted to inject an appropriate volume of cement in order to create two symmetrically placed boluses (represented in the rendered bone/cement model depicted in B, red representing cement, yellow representing bone).....	141
Figure 56 A representative experimental read-out of augmented vertebra during the re-fracture experiment. Here raw testing data (in (A)) represent displacement data (dashed red) coupled by readout frequency with the load read-out data (green). The re-fracture experiment follows the same protocol as for the initial fracture (Figure 29). The augmented vertebra is represented by increased resilience where cement enhances the load-bearing capabilities of the vertebra (load displacement curve in B).....	143
Figure 57 Vertebral strength after augmentation was found to be significantly higher in 20 and 30% VB fill (significance level $p<0.05$ indicated by *)	144
Figure 58 Vertebral stiffness of augmented vertebrae where no difference was found in osteoporotic samples $p>0.05$, but the stiffness has decreased in both oncological groups ($p<0.05$) Short term biomechanical effect when using CaP PVP - Discussion.....	145
Figure 59: Study flowcharts for two scenarios, osteoporotic (a) and metastatic (b) vertebral augmentation studies comparing two cements: non-modified cement (G1) and one with enhanced formula (G2)	150
Figure 60 Vertebral strength after augmentation was found to be significantly higher in all tested groups ($p<0.05$).....	153
Figure 61 Vertebral stiffness of augmented vertebrae: no difference was found in osteoporotic samples, but it has decreased in both oncological groups	153
Figure 62 Initial fracture prediction assessment (without masking the CSA).....	188
Figure 63 Additional fracture prediction assessment (masking the Osteoblastic lesions)	188
Figure 64: The buoyancy principle has been used to measure the volume of a vertebral body. First (depicted in (A)) the experimental setup and the principle have been tested on a metal ball-bearing with known volume ($\Delta V<0.2\%$) and later used on porcine vertebral bone samples (in (B)). Compared to the traditional Archimedes principle, here the volume is not required to be measured in terms of displacement but can be calculated based on change of weight (with precision of $0.01g=0.01cm^3$).....	190

Figure 65: Validation of vertebral body image segmentation script. The numerical approach was validated by means of compared volumes obtained experimentally and using the microCT approach. Initial results (in the graph as blue diamond markers) have later highlighted a discrepancy in measurements and led to uncovering faulty calibration of the microCT by the manufacturer. Corrected data (depicted as red squares) were found to possess volumetric differences of -1.59% (-0.19cm³) (RMS 2.25% (0.34cm³)).....	191
Figure 66 Strength and stiffness data for osteoporotic study for each spine and vertebral level used in the study - Spine BS 1 ...	198
Figure 67 Strength and stiffness data for osteoporotic study for each spine and vertebral level used in the study - Spine BS 2... 	199
Figure 68 Strength and stiffness data for osteoporotic study for each spine and vertebral level used in the study - Spine 3 BS... 	199
Figure 69 Strength and stiffness data for osteoporotic study for each spine and vertebral level used in the study - SpineGo 1	200
Figure 70 Strength and stiffness data for osteoporotic study for each spine and vertebral level used in the study - SpineGo 2....	200
Figure 71 Strength and stiffness data for osteoporotic study for each spine and vertebral level used in the study – SpineGo 4 ...	201
Figure 72 Strength and stiffness data for osteoporotic study for each spine and vertebral level used in the study – SpineGo 5 ...	201
Figure 73 Strength and stiffness data for osteoporotic study for each spine and vertebral level used in the study – SpineGo 6 ...	202
Figure 74 Multiple myeloma samples: Initial strength and stiffness for corresponding donor and spine level	203
Figure 75 Spine 1 mets: Initial strength and stiffness for corresponding spinal level.....	204
Figure 76 Graphical interpretation of means (\pm stdev) of micro-indentation properties of multiple myeloma bone	207
Figure 77 stress profile due to eccentric loading considered as super-positioned stress induced by (i) compression loading (left) and (ii) bending moment (right)	209
Figure 78 Moment notation with respect to modulus weighted centroid (Green) in asymmetrical vertebrae where the cross-sectional profile has been altered due to presence of a lesion (pale blue).....	210
Figure 79 Predicted strength was highly associated with values experimentally obtained in both cases where only uni-axial (left) or bi-axial eccentricity (right) has been considered.....	212

- Figure 80** No notable difference in prediction error with respect to overall vertebral strength has been found between the two methods used (left: uni-axial eccentricity used in the main body of the thesis, right: extension to bi-axial eccentricity)..... 212
- Figure 81** Accounting for spatially varying point of the highest stress allowed to identify where is the vertebra likely to fail (yellow marker). Figure depicts four tested simulated lesions along a real metastatic sample, in all illustrating position of loading axis (green round marker) located on the mid-sagittal axis (red-dashed line), neutral axes (red-solid lines) intersecting the modulus weighted centroid (square green marker)..... 213
- Figure 82** Boundaries of the vertebral body have been estimated using a custom-compiled script. Here, ct-images have been treated on slice-by-slice basis while storing the original image along the binary mask. Binarisation comprised of replacing any negative density values with background (marrow) density, followed by tresholding with subsequent void filling subroutine..... 215

Preface

Spinal metastases are an increasingly challenging pathology faced by clinicians as patient survivorship improves. A number of these metastases are osteolytic in nature and the subsequent fracture is associated with significant morbidity. Improved methods of fracture risk and prediction are urgently required to aid clinical planning and assessment of the treatment outcomes.

Vertebral compression fractures are currently being treated conservatively by a combination of bed rest, braces, pain killers and pharmacologic therapy [1]. Minimally invasive treatment such as percutaneous vertebroplasty (PVP) shows promising results in terms of pain management with considerably lower risk than open surgery. Although PVP has been shown to be safe, its biomechanical character is still not well understood which may lead to a cascade of alterations in load distribution amongst adjacent levels. Moreover, due to heterogeneous changes in bone structure such those caused by cancer infiltration, the percutaneous vertebroplasty may be different from the one prescribed for osteoporosis. For instance, a vertebral body with a lesion-creating cavity may need to be treated differently than homogeneously deteriorated osteoporotic vertebrae. Further, the fact that lesions themselves are more readily identifiable using modern imaging techniques and that it may be possible to identify vertebrae in the spine at risk of failure brings to the fore the possibility of prophylactic treatments.

There are two essential everyday questions posed in clinical environments for treatment of cancer patients: “what to use” and “when to use it”. *In-silico* modelling provides a possible way to provide answers if used in appropriate way. Also, models to assess bone quality prior to the collapse of the vertebral body would be beneficial both in a laboratory and clinical environments.

For both pre-clinical and clinical applications, there is a strong need for an effective experimental design to deploy treatment optimisation studies. This design comprises an appropriate and tested laboratory methodology as

well as a tool to predict the structural properties of every sample prior to testing. Such methods could also be deployed in laboratories providing better approaches to experimental design. Previous investigations have shown potential for the use of image-derived bone mineral density distribution assessment as a deployment of Finite Element modelling but this procedure would be time-consuming. Previous research has indicated a strong link between bone structure as the disease progresses and the fracture [2, 3]. Nonetheless, very little is known about the material laws of a bone infiltrated by cancer. In order to help computational models predict failures more reliably, an investigation of the affected tissue is required.

This thesis aims to challenge the lack of basic understanding of structure-strength relationship in the biomechanics of spinal metastases. Throughout the thesis, its aim and objectives follow the introductory section and are followed by a literature review to gather known information from the most recent relevant scientific sources. The literature review is followed by three chapters to encompass the objectives of this work, each comprising Introduction, Methods, and Results sections followed by a Discussion. The last chapter of the thesis presents the conclusion reached by this work while proposing a future perspective.

Chapter 1 Introduction

1.1 Clinical drivers – defining the problem

Vertebral fractures are a significant cause of debilitating back pain, particularly in females suffering from brittle-bone disease or osteoporosis. One in three women will be affected by osteoporosis and there is a lifetime risk that 50% of women and 20% of men will sustain a vertebral fracture by the age of 50 [4]. Based on demographic changes, the expenditure dedicated to osteoporosis treatments is expected to rise from 30 billion € per year in the EU at present to almost 77 billion € per year in 2050 [5].

Whilst osteoporotic vertebral compression fractures (VCFs) have been widely studied both clinically and biomechanically, the fractures arising from metastatic infiltration in the spine are relatively poorly understood. Significant issues arise from weakening of the bone due to metastatic invasion of the vertebral bone causing it to become weak and prone to fracture under loads such as those experienced in everyday activities.

The incidence of vertebral fractures in cancer patients increases as the treatment of primary cancers improves due to on-going exposure to the progression of the disease. Unlike the vertebral fracture observed in osteoporosis, metastatic VCFs are particularly problematic as they have a high incidence of spinal cord compression (25% of cases), causing paralysis and loss of bowel and/or bladder function, as well as the associated pain [6]. Such late stage secondary events are often associated with terminal illness in which life expectancy is reduced to perhaps no more than 12 months [7]. Thus clinicians and patients have to consider issues concerning quality of life as the disease may become debilitating when VCFs occur [8, 9].

Current conservative treatment of vertebral compression fractures uses a combination of bed rest, braces, pain killers and pharmacologic therapy [1]. In osteoporotic patients the therapy primarily consists of drugs promoting bone growth such as bisphosphonates, vitamins and mineral nutrients [10]. However, in cancer patients for whom palliative care is a key issue, pain relief is paramount in seeking to provide adequate quality of life for the remainder of the patient's lifetime. Whilst use of bone-enhancing drugs may be beneficial in the medium term, interventions which improve quality of life in the short term are paramount, comprising in the first instance a

prescription of analgesics to provide the desired pain relief. An alternative intervention may be required where this treatment is unsatisfactory. Major surgery, in which recuperation would impact severely on the patient's remaining quality of life, is often contraindicated because of both patient fragility and poor bone quality arising from the metastatic infiltration itself. Minimally invasive approaches which have shown benefit are vertebroplasty and kyphoplasty, as they have demonstrated sufficient stabilisation and pain relief coupled with little post-procedure pain and/or rehabilitation particularly in the osteoporotic cohort [11, 12]. The technique of injecting bone cement through a hollow needle without need of open surgery seems to provide the desired structural reinforcement with significant and, most importantly, immediate pain relief within 24 hours after the surgical intervention. The same techniques are currently being utilised on a small scale for the treatment of patients with metastatic disease cohort [11-14].

Recent studies on the effectiveness of vertebroplasty in the osteoporotic cohort [15, 16] initially introduced a controversy to the technique but later studies [17], in which more relevant control groups were utilised, have shown improvements in the patient outcomes compared to conservative cohorts. Treatment of osteoporotic fractures brings typically excellent results with most patients describing the loss of pain as complete or near complete within two days with further gradual improvement in the first 6 months [18]. Initial results reported for vertebroplasty in cancer sufferers shows similar levels of satisfactory outcomes when compared to osteoporotic patients [8, 19], although the requirements of each patient group are not the same and the goals of utilising the technique may not be comparable. The rate of postoperative complications such as leakage of the cement and/or adjacent accelerated vertebral fracture may be different in patients treated for metastatic fractures due to differences in the systemic and local effects of the disease on the bone structure. Osteoporotic degeneration appears as a fairly uniform bone loss, although there is an increase in the inter-vertebral variability of porosity with age reflecting a reduction in homogeneity [20-22]. This is in contrast to vertebral bone loss in metastatic disease in which focal lesions are the cause of the structural deterioration of the VB. These differences may affect the rates at which complications and treatment interventions may occur.

Key-hole surgery in cancer patients brings the promise of pain management with considerably lower risk than open surgery but it has yet to be optimised for cement augmentation in which the goals of surgery may be

different from that prescribed for osteoporosis. For instance, a VB with a lesion that breaches the cortical wall and hence increases the risk of cement leakage may have to be treated differently than osteoporotic vertebrae. Further, the fact that lesions themselves are more readily identifiable using modern imaging techniques and that it may be possible to identify vertebrae in the spine at risk of failure brings to the fore the possibility of prophylactic treatments. The challenge here is to identify those vertebrae most at risk, such that unnecessary procedures are avoided.

In developing the augmentation procedures in terms of both the cement and the delivery process, preclinical studies have an important role to play. A number of biomechanical studies have already addressed a number of issues arising from use of augmentation utilising both experimental investigations [3, 23] and computational modelling, principally using the finite element method [24-26]. The volume [27-29] and type of cement [30] as well as the method of delivering the cement [28, 31, 32] have been common subjects of investigation within osteoporotic models. Here, the use of cadaveric material for the *in-vitro* assessment of this procedure has been a key element of these investigations both directly and in the validation of computational models. However, little work has been undertaken on metastatic bone disease and this has hampered the development of both (1) the augmentation techniques for these pathologies and, importantly, (2) models with which to predict fracture in a prophylactic setting and their use as a measure of outcome.

Biomechanical *in-vitro* assessment of these structurally compromised specimens is an important method for gaining an understanding of the mechanics of structural behaviour under load. Finite element modelling has demonstrated great potential but is dependent on a detailed knowledge about the properties of bone at a tissue level as well as a solid validation methodology in order to be able to demonstrate its full potential. Hence a well-established experimental methodology is needed to support a development of the computational model and its validation. Secondly, despite numerous studies on human bone mechanical properties at a tissue level [33-37], very little is known about material laws of bone infiltrated by cancer. In order to help computational models predicting failures more reliably an investigation of affected tissue is required.

Currently, biomechanical investigations of vertebroplasty for use in cancer patients are few in number and are limited to preliminary studies [38,

39]. However the usage of cadaveric tissues arising from these diseases within *in-vitro* experiments is technically very difficult and arises from:

- i. The limited availability of these tissues
- ii. The heterogeneric nature of the infiltration.

Therefore an effective experimental design is crucial for such studies. This design comprises an appropriate and tested laboratory methodology as well as a tool to predict structural properties of every sample prior to testing. This tool is essential especially when investigating prophylactic treatment. Previous investigations have showed potential of the use of image-derived bone mineral density distribution assessment as the deployment of FE-modelling would be time consuming.

From a clinical point of view the essential questions arising from challenging metastatic vertebral fracture treatment for treatment of cancer patients are “what to use” and “when to use them”. Models underpinning the basic science of fracture and the most important parameters that may help to restore the compromised vertebral strength would significantly benefit the clinical environment. Also, models to assess bone quality prior to the collapse of the vertebral body would benefit from both a laboratory and clinical environment.

In the following sections the anatomy and biomechanics of the spine that are pertinent to the problem outlined above are described together with their modification following the onset of a diseased state where the focus is on the fracture of the infiltrated vertebrae. Previous models, both cadaveric and computational, for understanding and predicting fracture are discussed in addition to the use of micro-indentation on elucidating the properties of bone at a tissue level derived from these tissues. Finally, vertebroplasty, the technique for overcoming both pain and the structural instability arising from these fractures, will be discussed. In light of these discussions the aim and objectives of the project will be defined in the following section.

1.2 Aims and objectives of the study

The overall aim of this project is to investigate the biomechanical imprint of bone deterioration due to the presence of structure-changing pathologies, explore possible structural biomarkers of weakened vertebrae and investigate minimally invasive treatment modalities in such bone where the disease weakens the bone and ultimately leads to vertebral fracture.

The goals follow the principle stated by WHO: “*add life to years, not just years to life*” and focus on treatments which aid pain-free mobility and increase the quality of life for people with bone disease, cancer patients in particular. Following the findings from the literature review, the research project focuses on three interrelated areas for which there is limited knowledge and understanding (Figure 1). Objectives have been postulated as follows:

- i. The development of a model of fracture prediction that can be utilised within the scope of data produced through CT imaging which will be validated against *in-vitro* experimental data of vertebrae containing osteoporotic and metastatic lesions.
- ii. To perform an assessment of the structural and mechanical properties of trabecular bone utilising microCT assessment and micro-indentation.
- iii. To investigate the use of vertebroplasty in the augmentation of osteoporotic and metastatic lesions.

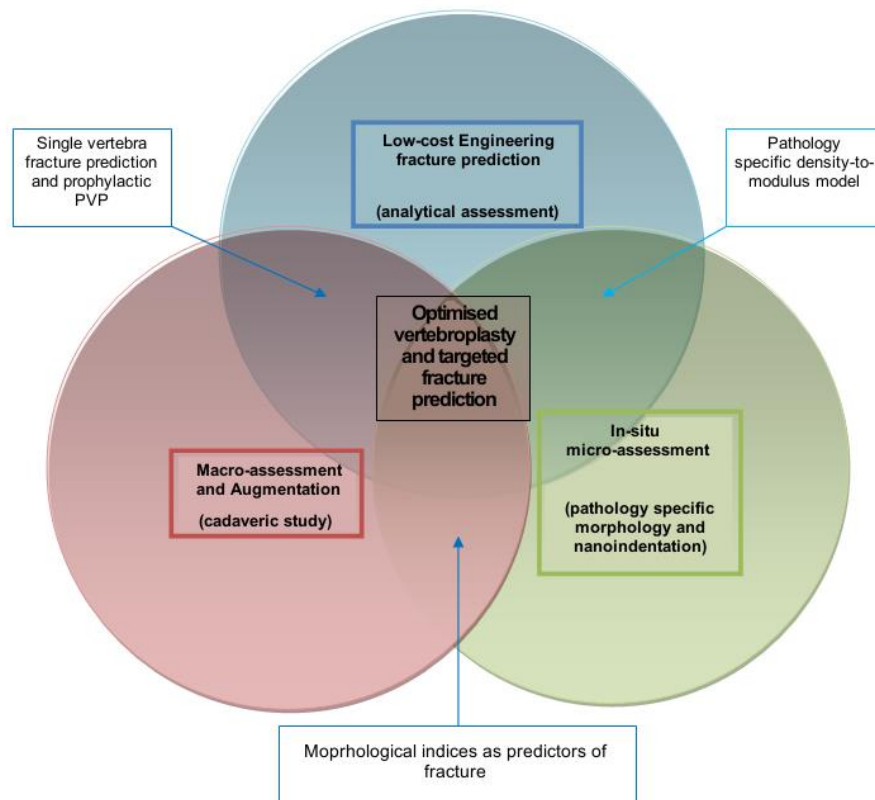


Figure 1 The aim of this work is to combine knowledge of mechanical properties of vertebral bone and experimental testing on both tissue and organ level on pathology specific samples for use in vertebroplasty.

Chapter 2

Literature Review

2.1 Anatomy

2.1.1 Spine

The spine is a multi-segmental complex mechanical structure which forms part of the musculoskeletal unit of the trunk together with the rib-cage and the pelvis. Its functions are to [40]:

- i. Protect the spinal cord
- ii. Provide stability to the upper torso whilst allowing the transfer of load
- iii. Aid motion of the upper torso
- iv. Aid motion of the upper and lower limbs.

The human spine constitutes of 24 non-fused pre-sacral vertebrae. They are, as shown in Figure 2, divided into seven cervical, twelve thoracic and five lumbar vertebrae together with nine vertebrae fused within the sacrum and coccyx. Each single vertebra is separated from the adjacent ones by an intervertebral disc anteriorly and two facet joints posteriorly. These joints allow movement between vertebrae and, hence, of the upper body, and the discs in particular aid the transfer of load from one vertebra to the next downwards to the pelvis [41]. These joints also provide stability particularly towards the end of the range of motion and/or where motion may be considered detrimental to the surrounding organs or vessels.

Whilst vertebral pairs in the cervical spine demonstrate the largest range of motion for many, if not all, the degrees of freedom, the thoracic spine on the other hand is connected to the 24 ribs and has significantly decreased mobility [42]. The lumbar spine consists of visually larger vertebrae capable of bearing greater loads and moments as well as increased mobility compared to the thoracic spine but significantly less mobility than the cervical spine.

Laterally, a non-pathological spine has four main curvatures, two kyphotic ones on the thoracic and sacral regions and two lordotic curvatures in the lumbar and cervical regions. In the coronal plane no such curves are

noted beyond those as further curvature is generally minor and clinically insignificant.

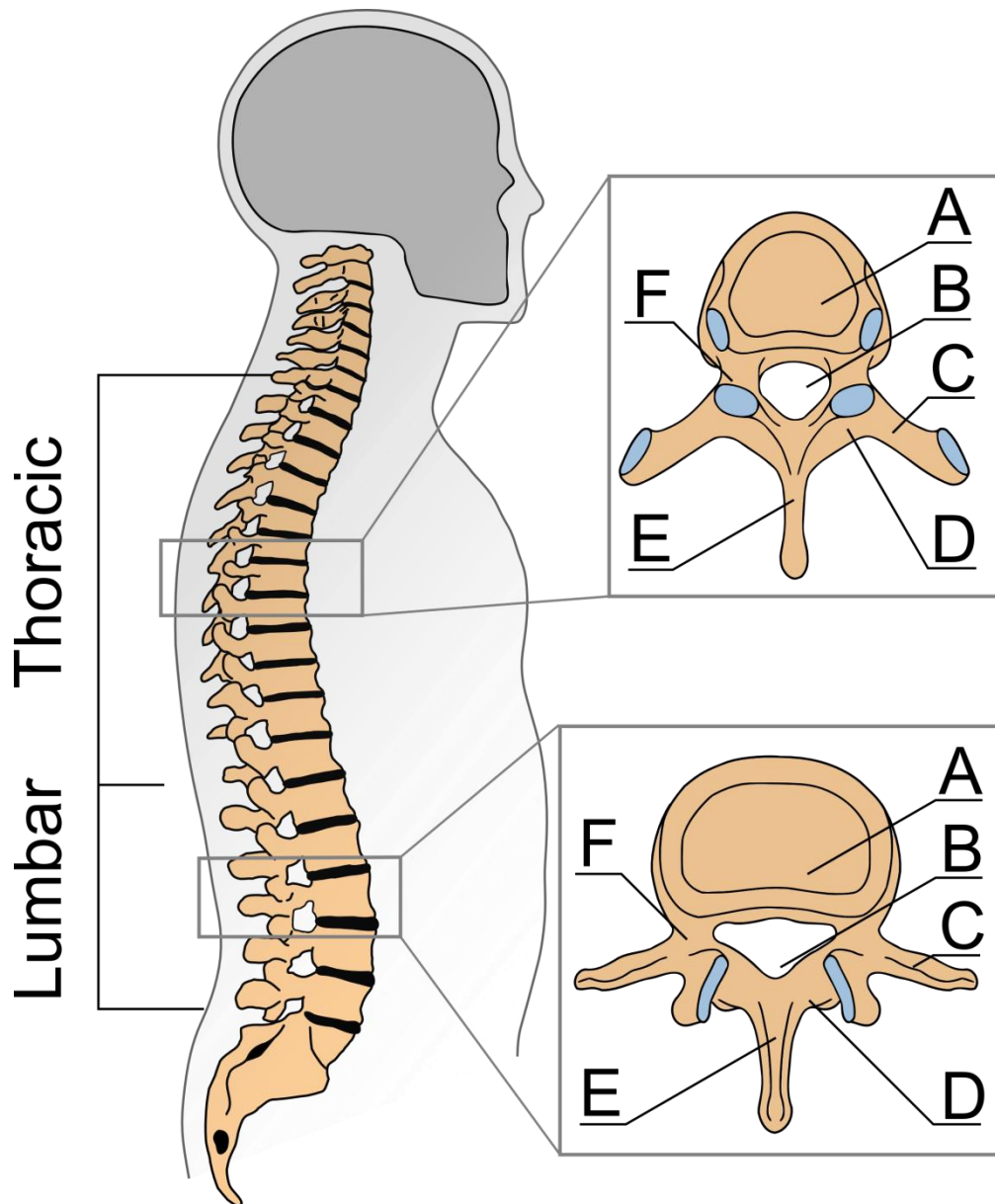


Figure 2 Figure depicting human spine with detail to lumbar and thoracic vertebrae. (A- Vertebral Body, B- Vertebral foramen, C- Transverse process, D- Lamina, E- Spinous process, F- Pedicle)

2.1.1.1 Biomechanics of the spine

The primary function of the spine is to protect the vulnerable spinal cord whilst allowing both movement and stability at any given position including the upright position [43]. The spinal cord is protected by the bony structures of posterior vertebral elements, including the pedicles and lamina, and anteriorly by the vertebral bodies. Between vertebrae the nerve roots emanate from the cord through the intervertebral foramen. Any reduction in this space through trauma, vertebral fracture and/or degenerative disc

disease leads to nerve compression and related pain and/or loss of function [44]. From a biomechanical point of view, the spine has to sustain large loads as the centre of gravity is shifted from its main longitudinal axis leading to forces that are significantly greater than would arise from the weight of the upper torso alone [42]. Exercise performed during daily life strongly influences loads which vertebrae have to transmit. According to *in-vivo* measurement the lumbar disc pressure measured during bed rest is one quarter of that measured when standing upright [45, 46], suggesting that a simple task can significantly increase compressive loads in the spine which has to be considered when designing a treatment tool for patients who are expected to be discharged from medical care.

2.1.2 Vertebra

Vertebrae are the relatively large bony units from which the spine is comprised. A typical vertebra consists of an anteriorly placed vertebral body and posterior elements - the vertebral arch enclosing the vertebral foramen and processes. The vertebral body is a kidney-shaped structure comprising an inner trabecular bone and outer vertebral shell which allows it to transmit the majority of the compressive load within the spine [43]. The size of the vertebral body varies with level, the largest cross-sectional area being in the lumbo-sacral region. The size of the vertebral body is determined by the load bearing demands of the upper body above the index vertebra [42]. As noted above, the neural arch protects the spinal cord which resides in the spinal canal whereas the spinous and transverse processes, which are attached to the arch, anchor muscles and ligaments of the spinal musculo-ligamentous complex.

The vertebral body has a thin vertebral shell and an internal structure containing cancellous bone which harbours a significant quantity of bone marrow. In keeping with these large amounts of bone marrow the vertebral body is well vascularised and this may be a reason why the spine is the third most common site for metastatic disease after the liver and lungs. The posterior elements consist mostly of cortical bone and are much less vascularised. As this work focuses strictly on fractures in the thoraco-lumbar region only those two regions will be discussed in the following sections.

2.1.2.1 Thoracic vertebrae

Between the cervical and lumbar spine, there are 12 thoracic vertebrae which are attached to the rib-cage. The T1 vertebra, the closest to the cranium, is the smallest and the size of the vertebrae gradually increases

down the spine in the caudal direction. The rib-cage is attached by a series of articular facet joints (*costal facets*) and in combination with the associated ligamentous structures restricts range of movement; furthermore its larger moment of area, arising from the rib-cage which is shifted away from the axis of rotation, also contributes to the enhanced stiffness of this region. In combination both factors provide increased stability to the whole thoracic structure to protect the vital organs inside the rib-cage.

2.1.2.2 Lumbar vertebrae

The lower non-fused five vertebrae between the thoracic spine and sacral region form the lumbar spine. As loads here are significantly larger than those found in the thoracic and cervical regions, these vertebrae are correspondingly bigger. The different morphology of facet joints depicts a different biomechanical environment with larger ranges of motion in certain degrees of freedom but more limited ranges in others e.g. in the axial rotation and the translational forward motion.

2.1.3 Bone

Bone is a solid living organ. Being constantly modelled and remodelled, the bones, to some extent, reflect the needs of the body's biomechanical environment. Hard bone tissue forms two microscopically distinct types of bone: the cortical (compact) and trabecular (spongy) bone which can be differentiated according to their relative density [47]. Micro-composition of the bone is depicted in Figure 3. The cortical bone forms the hard dense exterior shell around the sponge-like trabecular bone, where spaces between the trabeculae are filled with bone marrow and interwoven by a vascular system [48]. The remodelling aids bone adaption in response to external loads but with age and various pathologies the ability to sustain this process is reduced and the equilibrium between absorption and replacement of bone decreases along with the quality of the bone structure.

Apart from mechanical support, bones have several other functions such as synthetic (blood production) or metabolic (mineral storage, fat storage, acid base balance, storing heavy metals and helping to maintain balance in the mineral and hormone levels of the blood). However this study will focus only on the mechanical functions of the bone.

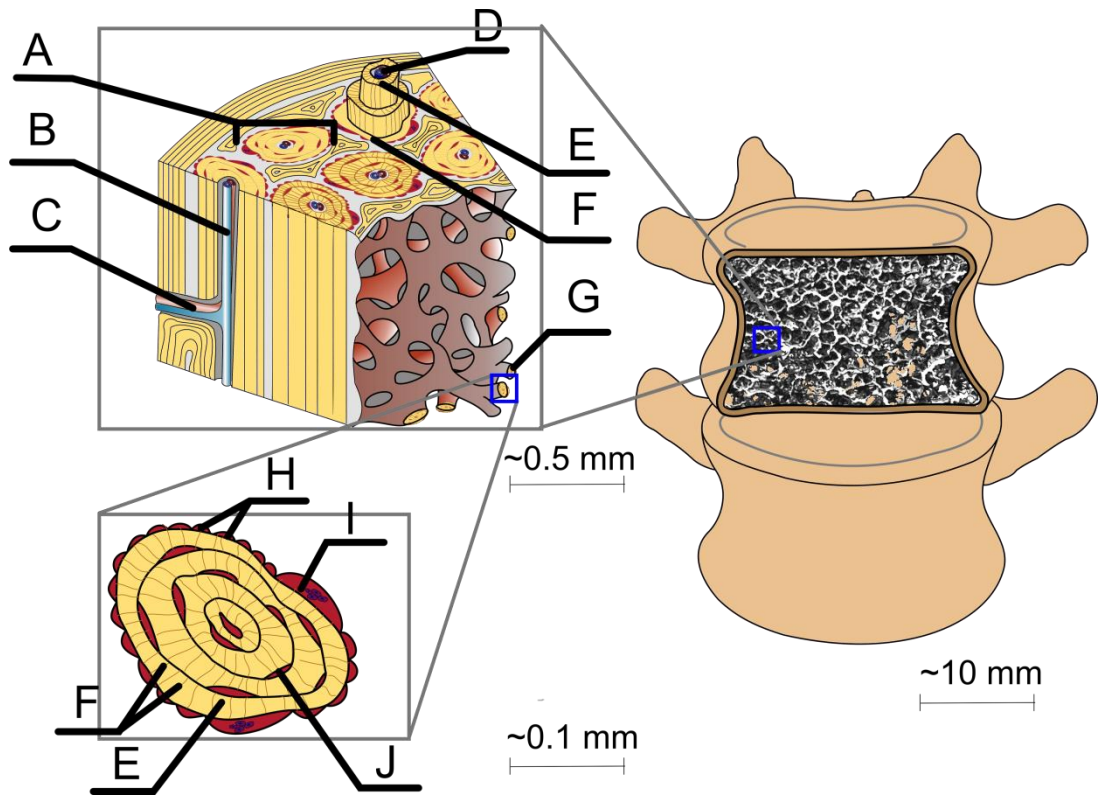


Figure 3 Schematic figure of a bone structure at different scales – organ-, meso- and micro-scale (A- Osteon of cortical bone, B- Haversian canal, C- Volkmann’s canal, D- Vessels and nerves, E- Lamellae, F- Canaliculi, G- Osteon of trabecular bone, H- Osteoblasts, I- Osteoclast, J- Osteocytes)

2.1.3.1 Cortical bone

The shell surrounding the internal part of the bone and forming its outer shape is composed of thin but dense cortical (*compact*) bone. Regarding composition, the cortical bone consists of secondary osteons embedded in interstitial tissue made of primary and older secondary osteons (Figure 4). An osteon - the fundamental functional unit - is a concentrically layered structure where each layer (lamella) is 1-5 μm thick [49]. Between some lamellae, osteocytes reside within lacunae (10-50 μm), and the centrally placed canals are called Haversian canals [49]. As published, the density and size of the lacunae in human vertebra are similar in both cortical and trabecular bone (CS-area 55 μm^2 in average, density 156/ mm^2). Counts of osteocyte lacunae correspond to the remodelling activity and have been shown to be higher in osteoporotic patients [50].

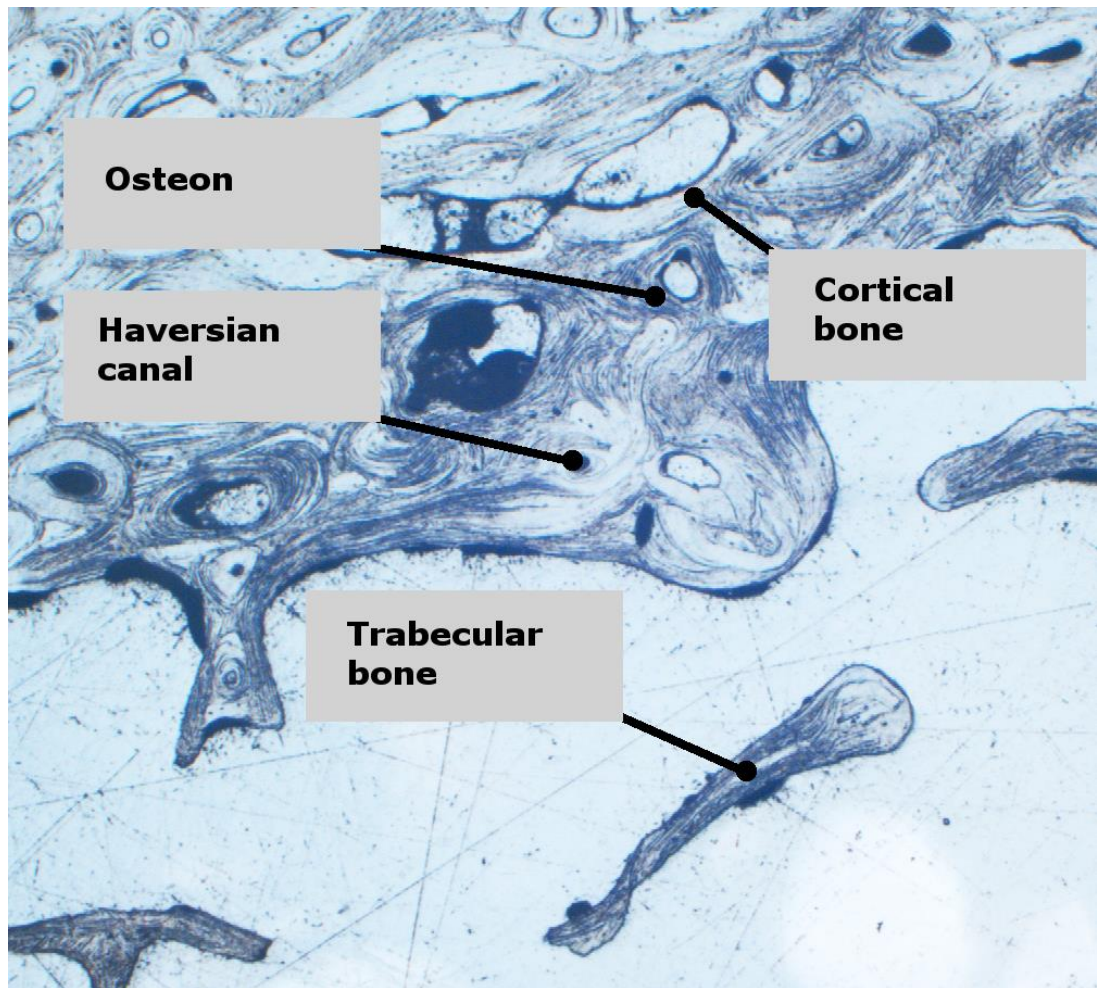


Figure 4 Microscopic image of cortical shell and trabecular bone interface depicting difference between cortical shell (left top) and notably more porous trabecular bone (right bottom). Cortical bone is characteristic of osteons forming around the Haversian canal where older osteons are overlaid by new ones. On the contrary trabecular bone is characterised by layers of bone where the central canal is not present. This is understood to be a reason for deterioration of bone emerging from outer layers towards the centre (such as thinned trabeculae in osteoporotic patients)

Modelling (addition or removal of bone to alter shape) and remodelling (removal and replacement of bone in a systematic fashion within bone multicellular units) are both extremely important parts of the bone life cycle which allow responses to changes in mechanical environment or bone micro-damage. The turnover in cortical bone is significantly lower than in the trabecular one (3% turnover rate of cortical bone compared to 26% in trabecular bone [49]). The cortical bone is remodelled from the bone surface through tunnelling resorption by osteoclasts. This cavity is then filled by osteoblasts forming a new bone in a lamellar pattern. Every new osteon is

enclosed and separated from an old bone by a cement line (0.5-1 μ m). Mineralisation of a new bone is gradual and by the time of formation its mineral density is around 70%. In less than six months, the mineral density of the newly formed bone increases to 90 to 95% [49]. Studies using indentation techniques and ultrasonic experiments on mechanical properties of bone at a tissue level have confirmed that trabecular bone is almost 20% softer than the cortical material [34, 37, 51, 52], which may arise from the greater mineralisation and reduced number of lacunae in cortical bone.

2.1.3.2 Trabecular bone

The porous sponge-like structure within the cortical bone is referred to as trabecular bone. Similarly to cortical bone, healthy trabecular bone remodels to create a well-organized structure which provides an enhanced strength-to-weight ratio with space available for other components such as bone marrow [53]. The trabeculae are remodelled in a very short timescale compared to cortical bone, adapting quickly to changes in a mechanical environment.

The trabecular bone has a very high porosity and comprises approximately 20% of the total bone mass. A typical trabecular thickness varies between ten and several hundred μ m [49]. Usually trabecular bone does not contain whole osteons (Figure 5), but rather portions of bone where remodelling has occurred in the form of pits rather than tunnels. Exceptionally a whole osteon can be seen if the thickness is higher than approximately 350 μ m [49]. This exception aside, trabeculae are either cylindrical (rod-like) or plate-like structures which have concentric layers (lamellae) around their principal axis without a central canal.

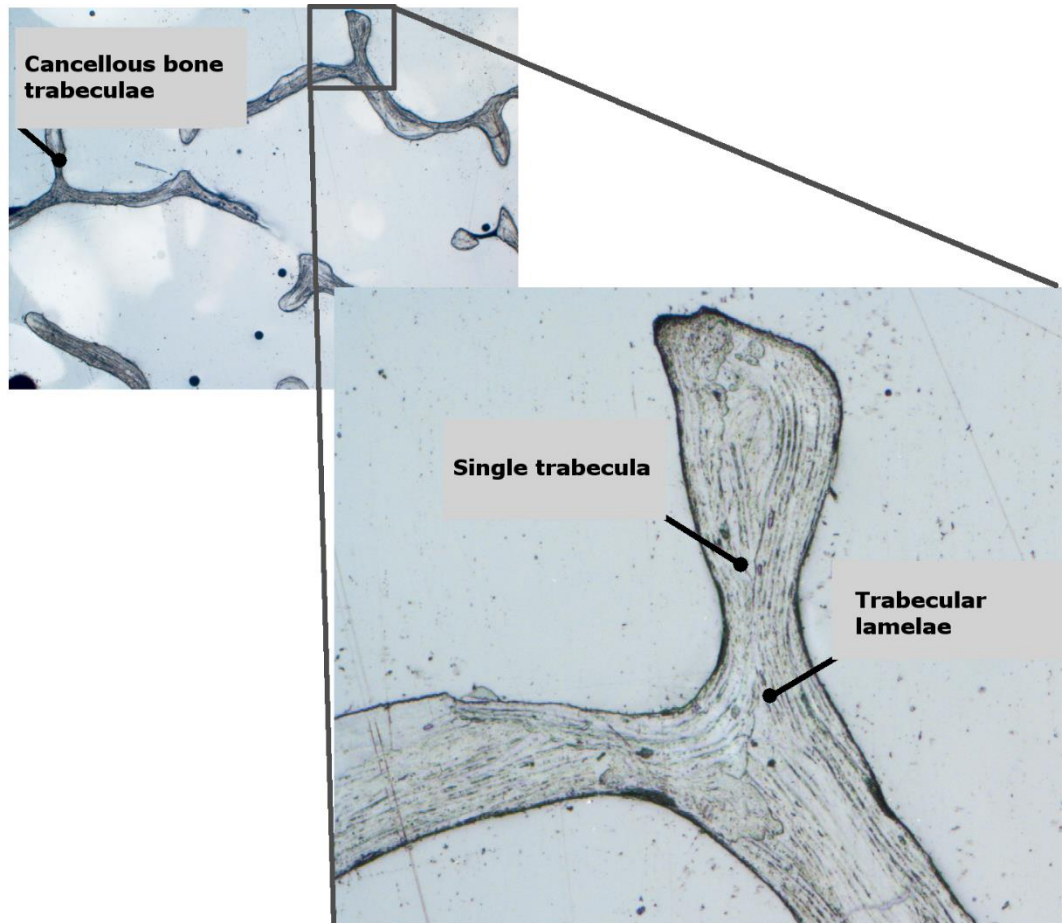


Figure 5 Microscopic image of trabecular bone, single trabecula in detail: trabecular bone is a very porous structure where each trabecula is formed around its main axis composed of layers which form externally

2.1.4 Morphology and mineral density of human vertebrae

While the external shape of the bone is mainly driven by its kinematic purpose and it can be modified in response to external loads, the cancellous bone is more readily modified due to a higher rate of bone turnover. This can be seen in the pattern of the trabecular bone accommodating the principal directions of stress [53].

Histological, and later microCT, assessment of bone has uncovered the trabecular micro-structure which is formed from rod-like structures and/or plate-like structures. The main structural property indices that are commonly used in the description of bone (Figure 6) are denoted by:

- i. Trabecular spacing (Tb.Sp)
- ii. Thickness (Tb.Th)
- iii. Number of trabeculae (Tb.N)

- iv. Volume fraction (BV/TV)
- v. Connectivity (Conn.D)
- vi. Level of isotropy (Mean intercept of length (MIL)).

All these variables are modified by the gradual morphological changes that occur during ageing. Particularly, a decrease in volume fraction and connectivity of the trabeculae and a corresponding increase in spacing are observed as a person's bone becomes osteopenic and then osteoporotic [54]. In addition, comparative studies have shown a gradual corresponding change from plate-like to a predominantly rod-like structure with increasing age [54]. These changes make trabecula more inclined to bend and buckle which leads to lower structural stiffness and strength.

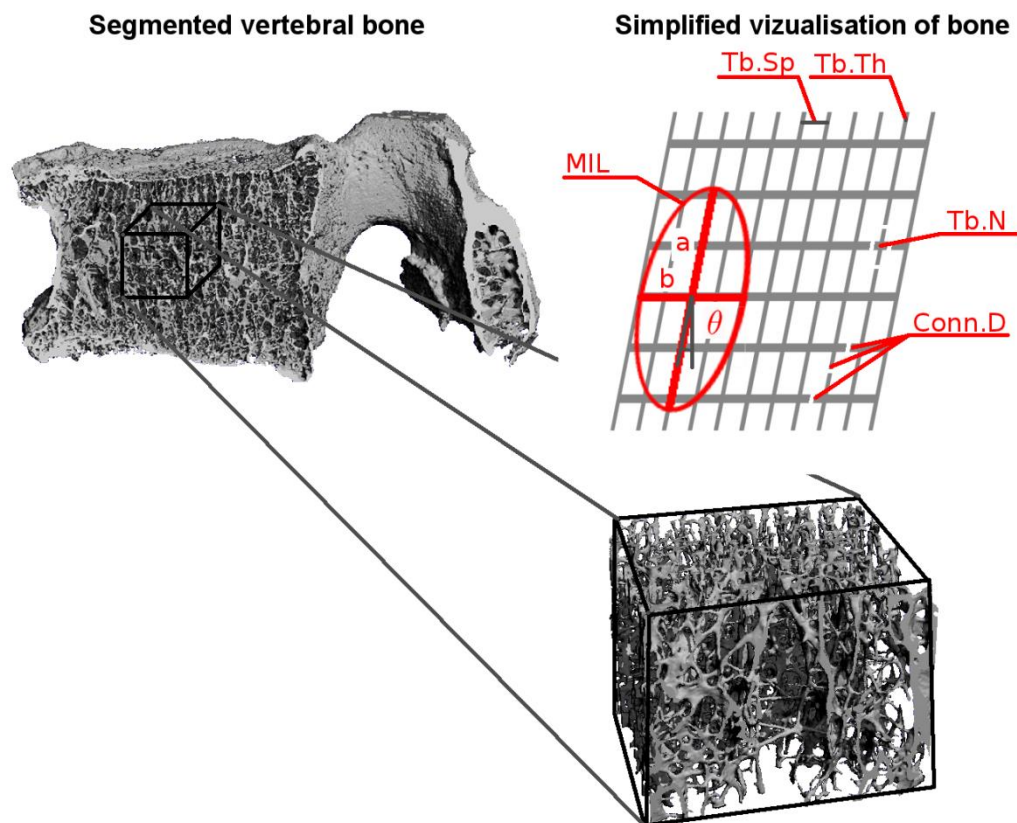


Figure 6 Morphometrical indices to qualitatively assess bone structure in-situ. Trabecular spacing (Tb.Sp), thickness (Tb.Th), number of trabeculae (Tb.N), connectivity density (Conn.D) or level of isotropy (MIL)

Increasing spatial resolution of modern 3D imaging tools allows assessing the bone *in-situ* and non-invasively. Segmenting these images can provide morphometrical indices for qualitative assessment. Bone volume fraction has been shown to be a better predictor of compressive strength of cored trabecular bone when compared to BMD [22, 55]. Investigations of

trabecular thickness, number and separation have their roots in histological sections [56] but later, in the case of 3D imaging tools, a direct measurement method had to be adopted [57]. In theory, the algorithm uses the fitting of spheres to or between segmented bone structure using a distance transform, which is used to determine the three-dimensional distance between each structure. These modern algorithms can minimise the effects of partial volumes using a mid-axis transformation method to identify trabecular elements. Studies have shown that a single trabecula has a thickness (Tb.Th) in the order of 100-200 μm leaving the trabecular spacing (Tb.Sp) one order higher depending on the anatomical location of the bone.

The connectivity of bone is defined as the number of struts which have to be separated to isolate two nodes of a bone [57]. While the connectivity is hard to express as a specific volume, a connectivity density (Conn.D) as a value normalised to the volume of interest is widely used. Average connectivity density for human bone varies between 2-5 mm^{-3} [54, 58] and strongly decreases with age by approximately 15% per decade [54]. However cadaveric studies done by Kabel et al. [59] showed that Conn.D provides very limited information on material properties of the bone structure.

The remodelling of bone according to Wolff's law causes anisotropy in the bone's structure, particularly of the trabeculae [53]. One way of defining anisotropy is through some alignment of the principal axis to the reference frame. The most commonly used method is the Mean Intercept of Length (MIL). The principle of this method is based on a count of intersections between a linear grid and a segmented material as a function of the grid's orientation. The MIL is then the ratio between the total line length and number of intersections. Visually, the results can be expressed as an ellipse where the major axis (a) corresponds to the principal axis of the bone, the minor axis (b) to its perpendicular axis, and the angle from the reference frame axis to the principal fabric direction is denoted θ [60] as depicted in Figure 6. Even though the trabecular bone cannot be described as an isotropic material, recent indentation studies show that the main difference is only between the principal trabecular axis and its perpendicular axis, yet the difference in helical winding around the main axis remains the same, thus one can assume the trabecular bone is transverse isotropic [36, 61]. The MIL defining the magnitude of transverse isotropy is then in the order of 1.5 towards the principal axis [61].

An assessment of trabecular bone quality can be obtained using bone densitometry although the increasing sophistication of other tools is reducing its dominance as a clinical tool. In current state-of-art radiography a localised bone reduction of an area larger than 1cm^2 with a bone loss greater than 50% is required for any reasonable surety in identifying significant changes in BMD. Further, the technique is reported to give false-negative screenings resulting in up to 34% of undetected vertebral fractures [62] and up to 40% of undetected metastatic lesions [63]. The use of Dual-energy X-ray Absorptiometry (DXA) provides a quantitative means of assessing BMD but lacks the resolution to discern non-uniformly distributed changes within bone or geometrical aspects that impact on the bone's ability to sustain a load. Whilst biomechanical studies have shown that bone mineral content is a good single predictor of trabecular strength, the recent consensus is that BMD alone contributes no more than 50% of the vertebral strength [55]. It was widely recognised that predictive power can be increased by linking assessments of BMD with geometric measurements. Initially, these led to investigations of utilising the product of BMD and endplate area [3, 64], or BMD and minimal cross-section area [65, 66]. This method shows reasonably good predictions when compared to *in-vitro* experiments but requires volumetric CT measurements.

Several studies suggest that not only BMD but many other bone properties have a significant impact on the quality of the bone [2, 55, 58, 64, 67-70]. These include the architecture of the structure itself, the degree of mineralisation, micro-structure damage and accumulation including micro-cracks within the struts. However, each of these would rely on techniques that are unlikely to be assessable *in-vivo* within the foreseeable future. The tools that have the greatest potential for use *in-vivo* are those that demonstrate high spatial resolution such as micro computed tomography (microCT) which has demonstrated its potential in *ex-vivo* studies or the corresponding, peripheral *in-vivo* studies which utilise high-resolution quantitative computed tomography (HR-pqCT).

2.2 Pathology

2.2.1 Osteoporosis

Osteoporosis is one of the most widespread diseases in the world affecting bone tissue in the elderly. Early osteoporosis is asymptomatic and results in the reduction of bone mineral density (BMD) which leads to increased bone fractures. These fractures are thus called osteoporotic

fractures and their treatment imposes an increasing economic burden on the health system.

2.2.1.1 Definition, screening and occurrence of osteoporosis

Osteoporosis is characterised by the thinning of trabecular elements due to bone mass loss (Figure 7). This is related to an imbalanced resorption of bone without appropriate bone adaptation. Thinned trabeculae result in increased bone fragility which weakens generally strong bone architecture and subsequently leads to osteoporotic fractures when the natural load exceeds the bone strength. The most common sites of these fractures are hip, spine, forearm and humerus [71]. The incidence and mortality of vertebral compression fractures (VCF) is not well documented [72] as it is believed that only from one fifth to one third of all VCFs are actually symptomatic and recognised [73, 74] which accounted for a rough estimate of 1.4 million VCF worldwide in the year 2000 [71].

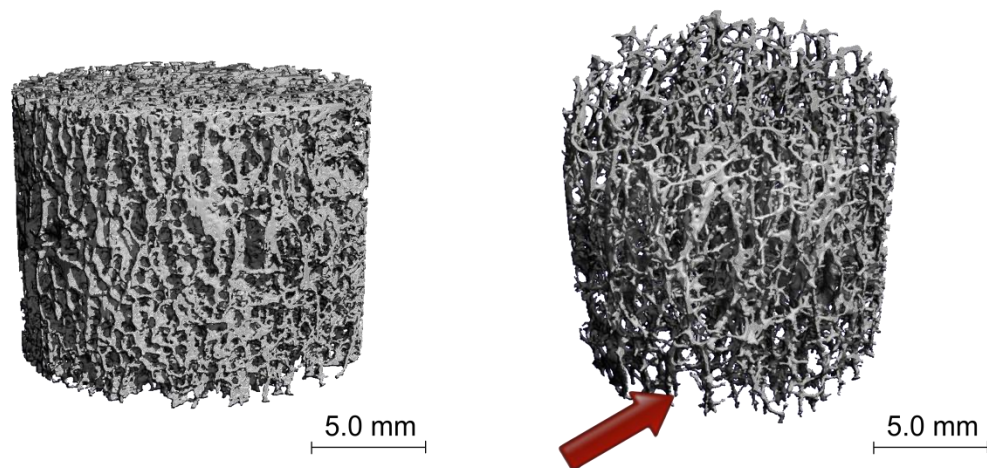


Figure 7 Comparison of “healthy” high-mineral-density bone (left) and low-mineral-density osteoporotic bone (right). Lose of trabecular struts in OP bone is predominantly in horizontal direction [21] as indicated by red arrow. Structural integrity in osteoporotic bone while compromised has been well documented and is believed to be related to a simple loss of supporting material, however the cancer-bearing bone is yet to be thoroughly investigated

Clinically the most important goal is to prevent osteoporosis and bone fractures, which emphasises the importance of appropriate screening. According to guidelines provided by WHO (The World Health Organization), osteoporosis is defined as the probability of fracture due to bone quality

compared to averaged values obtained from a population. The probability of fracture and hence the progress of osteoporosis is measured according to a T- and Z-score, where the T-score is a count of standard deviations below an average young person at the peak of bone mineral quality while Z-score compares the number of standard deviations to an average person of the same age. The average density measurements are based on large studies conducted worldwide. WHO defines four groups: Normal group (T score<1), Osteopenia (1<T score<2.5), Osteoporosis (T score >2.5) and severe osteoporosis (when bone contains non-traumatic fractures). Even though this method of bone quality estimation is widely spread, WHO currently provides data only for Caucasian US North American females. Several studies show a variation between different groups, thus a good comparison is essential to use the T-score bone quality assessment.

The average bone mineral density (BMD), which is currently the most widely used predictor of bone quality, is measured either using ultrasound with limited usability in the most commonly affected areas such as hip and spine or using absorptiometric techniques such as Dual Energy X-ray Absorptiometry (DXA) or computed tomography (CT). DXA is the most commonly used tool in osteoporosis screening as it provides a cheap, fast and robust quantitative measure for clinicians to estimate the potential risk of fracture at low radiation dosage (approximately 10 μ S for spine) [20]. However DXA measurements reflect BMD alone, which is only one of many contributions to vertebral strength [70] and is insensitive to geometrical changes which can lead to up to 70% of fractures remaining undetected when only BMD is being assessed [76]. Furthermore, conventional standalone DXA shows a significant insensitivity in the screening of a wider population [77] and in fact can lead to significant misdiagnosis in cancer patients [78] where up to 75% of cancer patients are wrongly diagnosed as non-osteoporotic.

Clinical computer tomography (qCT) shows great potential to provide more accurate diagnoses of osteoporosis and fracture risk estimations (discussed in the section: 2.6), however its higher radiation dosage (30-100 μ S for the spine [20]) is a significant factor to be considered before replacing DXA in osteoporosis screening.

2.2.1.2 Osteoporotic fractures and their systematic clinical impact

In symptomatic osteoporosis the clinical goals are the prevention of the gradual loss of bone quality and treatment of fractures if they occur. The spine is one of the most common sites of osteoporotic fractures and 2.35

million new VCFs were estimated to have arisen in 2010 in the EU [72], the number of which is expected to rise by about 16% by 2020 across most western countries [79-81]. Postmenopausal women are more likely to develop osteoporosis (increased incidence by 60%), however the age-standardised mortality and health consequences appear to be higher in men [4, 82].

Osteoporotic fractures represent a long-life debilitating event which can lead to further disability and early mortality, hence efficient prevention of the fractures is the stated aim of many biomechanical and clinical studies.

2.2.1.3 Treatment of osteoporosis

Treatment of osteoporosis is based on medication to sustain or increase the bone mass and hence, restore its natural strength. Maintaining a good lifestyle and changing to a healthier one may be recommended. As the patient becomes older, medical treatment to induce and/or maintain bone quality may be prescribed such as the use of bisphosphonates.

2.2.2 Metastases to bone

Metastases are so-called secondary tumours as they are related to another neoplastic disease located elsewhere. They are usually asymptomatic until the structure of the surrounding bone is affected, which may lead to functional changes and fracture. Changes in bony structure are very rarely accompanied by adequate structural adaptation and an elevated risk of failure of the bone is often noted [83].

2.2.2.1 Metastasis: Definition and occurrence

The growth of secondary tumours is a malignant process involving cancerous cells spreading from their original site [84]. The exact incidence is unknown due to difficulties in screening but it is believed to comprise about 300,000 cases annually in the USA [19, 85].

Due to a high vascularisation of the trabecular bone there is a higher chance for the cancer cell to infiltrate the vertebral body. Incidence increases with age with the highest peak at 50 years but is very rare in children [86]. The most common primary tumours to metastasise to bone are breast, prostate, lung and thyroid [87]. Spinal metastases occur in more than 30% of all cases where the patient died from neoplastic disease, and in almost 80% of patients with breast or prostate cancer [9, 85, 88, 89]. The spine is affected in more than 50% of patients suffering from prostate, breast or lung

cancer. In general, the spine is the 3rd most common site of bone metastases.

Bone metastases can result in three types according to an increased (osteoblastic) or decreased (osteoclastic) growth of the native tissue or a mixture of these two (Table 1). Bone as a living organ is closely related to the remodelling process by exhibiting activity where osteoclasts resorb the bone tissue and osteoblasts form new tissue at the same site. However, the presence of the cancer tissue creates a hostile environment resulting in the uncontrolled behaviour of tissue remodelling. The initial management of the tumour has not yet been clearly described, but it is believed that the change in the bone tissue is related to a hormonal reaction unbalancing the remodelling process in the vicinity of the lesion [84]. This results in most cases in osteolytic lesions (~70% of incidences of bone metastases). Purely osteoblastic lesions are rather rare (~10%) and mostly develop in breast and prostate cancer patients [86] but however dense this new tissue is the vertebral strength is unlikely to be increased.

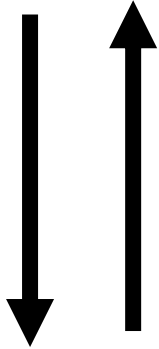
Cancer type	Incidence of Bone Metastases	Nature of Bone Metastases
Myeloma	70-95%	Osteolysis (forming lesions osteolytic in nature)  Osteosclerotic (forming lesions osteoblastic in nature)
Renal	20-25%	
Melanoma	14-45%	
Bladder	40%	
Thyroid	60%	
Lung	30-40%	
Breast	65-75%	
Prostate	65-75%	

Table 1 Incidence of metastases and bone reaction due to presence of cancer, ratio between osteoblastic/osteoclastic bone formation [3]

Multiple myeloma (MM) is a rare type of cancer accounting for about 1% of newly diagnosed cancer cases with a very low full recovery rate. The survival time is five years in about 15-20% of cases and less than one year

when MM bone lesions are present and untreated [9]. The average age of patients with diagnosed MM is 50 years and 2/3 of affected patients are men [90-92]. Myeloma is a malignant cancer of plasma cells resulting in widespread osteolytic bone deterioration where bone is replaced by a dark red gelatinous cancer tissue [93, 94] and the prognosis in developing metastases is between 95-100% [9]. Osteolytic effects are caused by an osteoclastic/blastic imbalance in the remodelling process where osteoclasts are stimulated by cytokines released by plasma cells and resorption becomes dominant in the remodelling process. Despite the ubiquitous nature of the disease, the osteolytic reaction tends to be confined resulting in localised lesions [95]. The structural changes in myeloma patients are in general not accompanied by osteosclerotic bone growth but in most cases are associated with a generalised osteoporosis. Healing of the bone can be observed only in patients who are in complete remission from the disease [96]. MM lesions are characterised as irregular in shape and lacking a periosteal re-healing effect on the interface between lesion and surrounding bone, which results in a reduction of bone structural properties [95].

2.2.2.2 Clinical and patient related impact due to metastatic infiltration – scoring systems

Structural weakening of the vertebral body can have catastrophic consequences on patients' quality of life. Excluding osteoporosis, the most common cause of pathological fractures of a bone is a metastatic disease. Up to two-thirds of patients where metastases are already formed will experience debilitating skeletal related events (SREs) and related disability and severe bone pain [8]. As the occurrence of fractures is higher in patients with metastases in general [6] and the risk of fracture is even elevated in patients with MM cancer [83], a reliable scoring system and fracture prediction tool to assess weakened structure is needed.

Apart from differentiation based on the nature of bone metastases, more complex classifications use information based on the compartmental state of the vertebra, whether the cortical wall was breached and the general performance of the patient (depicted in Table 2). These scoring systems indicate recommended surgical treatments and predicted survival periods specific to the patient. The scoring system proposed by Tomita [30] is based on three prognostic factors:

- i. grade of malignancy (slow growth, 1 point; moderate growth, 2 points; rapid growth, 4 points)

- ii. visceral [internal organs] metastases (no metastasis, 0 points; treatable, 2 points: untreatable, 4 points)
- iii. bone metastases (solitary or isolated, 1 point; multiple, 2 points).

Summation of the score points indicates the life period prognosis (2-3 points indicates 18-84 months, whereas 6-7 points decreases the prognosis to 5-33 months [30]); this demonstrates that for example only a single occurrence of multiple metastases decreases the lifetime prognosis by half. Surgical recommendation for score groups 2-3 is marginal excision, and for groups with 4 to 5 points, intra-lesional or marginal excision is recommended. Immediate spinal stabilisation is recommended for patients with a prognostic score of 6 to 7 points for short term palliation, whereas patients with a higher prognosis score are generally not recommended for surgical intervention [30].

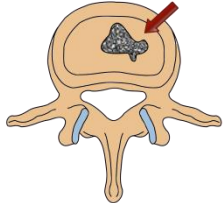
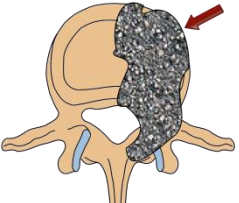
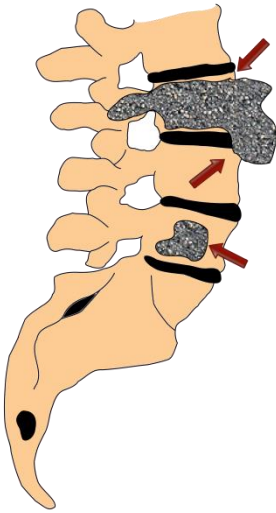
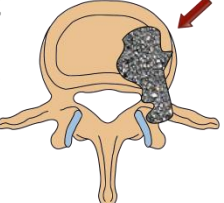
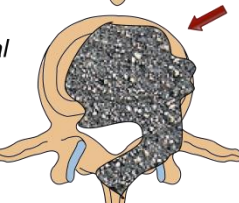
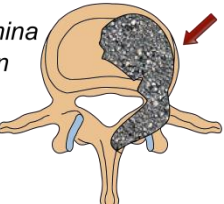
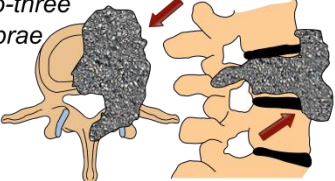
Intra-Compartmental	Extra-Compartmental	Multiple level infiltration
<p>Type 1 <i>vertebral body</i></p> 	<p>Type 4 <i>epidural extension</i></p> 	<p>Type 7</p> 
<p>Type 2 <i>pedicle extension</i></p> 	<p>Type 5 <i>paravertebral extension</i></p> 	
<p>Type 3 <i>body-lamina extension</i></p> 	<p>Type 6 <i>two-to-three vertebrae</i></p> 	

Table 2 Classification of the metastatic infiltration (red arrow) to spine according to Tomita et al. [30]

An even more complex scoring system by Takahashi et al. [97, 98] was adopted and generally accepted as the current gold standard for both medical and scientific purposes when scoring the patient's survivability. Takahashi's classification combines the previous system with the general

performance of the patient, the location, origin and character of the metastases, whether the cortical wall has been breached, and most importantly how accessible and removable the lesions are. The aim of this system is to quantify and classify a survival prognosis and suggest a treatment procedure for the patient.

2.2.2.3 Treatment of secondary tumour to bone - state of the art

Once the metastasis is present the disease is very rarely treatable to complete remission and the focus is often palliative. Apart from the radio-therapeutic and radio-pharmaceutic palliation for localised metastatic bone pain, there is no class of approved drugs for prevention or delay of bone metastases and to achieve a complete remission of the metastasis two possible options remain: removing the metastases surgically or preventing SREs by restoring the natural strength of the bone. Currently the cancer-related bone complications are reduced through the use of a class of drug called bisphosphonates [8, 10, 99]. Subsequent pain management is however necessary for the patient with the help of controlled analgesic treatment, psychosocial therapy, functional therapy (physiomedical rehabilitation or physiotherapy), nerve blockage or epidural therapy. However bisphosphonates are not always recommended as a drug as they may induce growth of neoplastic tissue [100] and appear to be successful only in mid-term treatment [101].

Surgical intervention is a solution to be considered when bone pain is no longer manageable, to restore stability or to perform decompression of the nerves or the spinal cord [102]. The optimal treatment solution is often case-specific and dependent on the neurosurgeon's experience and abilities. A general approach is hardly to be recommended due to the non-uniform nature of the disease. However in younger patients, the tendency to remove the tumour completely remains even with a higher risk of complication. This can be achieved with *en-bloc* resection which prevents any possible spread of cancerous cells from the tumour site. Stabilisation metalwork tools require strong bone to anchor the screws and often cannot be used independently of other tools in older patients where the disease is combined with osteoporosis with increased bone fragility. In general open surgery is not recommended if it is not absolutely necessary due to the potentially chronically poor health condition of the patient and an increased risk of surgical complications [6, 12, 86, 103, 104].

Percutaneous vertebroplasty (PVP) [3, 12-14] and Kyphoplasty (PKP) [11, 12] appear to be alternative options in older patients where

complete remission of the cancer is unlikely. Vertebroplasty in metastatic patients uses synthetic acrylate (PMMA) which results in an ideal curing time and additionally its thermo-reaction while curing takes place, next to the stabilisation of the fracture, is also often believed to be an additional source of good pain relief results. Secondly, the injection of the cement provides a tool which non-destructively moves the cancer tumour from the structurally weakened site very often without corrupting the integrity of the lesion [12]. A further option is to combine the removal of the secondary tumour with subsequent augmentation. Biomechanical studies showed lower injection pressure is needed after removal with decreased complications due to extravasation in laser assisted removal-ablation [105] as well as in radiofrequency assisted removal – coblation [38, 104]. Despite its simplicity and efficiency, vertebroplasty in SREs related to cancer are still only possible with significant resultant complications [13] which are in most cases related to leakage [106, 107].

All of this, however, produces relatively poor results and leads to a significant burden being placed on medical care expenditure. It has been estimated that the palliative treatment of bone metastases exceeded almost \$12.6 billion in the US in 2005, which comprised 17% of the total direct medical expenses for oncology [108]. One of the reasons is that up to 75% are misdiagnosed in fracture risk predictions based on BMD [78]. Hence an improvement in preventing and providing sufficient treatment SREs in patients suffering from the metastatic infiltration to bone would bring a great benefit on a large scale.

2.3 Vertebral fractures

2.3.1 Definition, occurrence and classification of vertebral fractures

The vertebral compression fracture progresses through loads exceeding the strength of the vertebra. Such a fracture occurs when the bone structure is either weakened by the demineralisation process (general bone loss-lowered BMD) or the presence of a secondary tumour (localised structural changes). The natural strength of the vertebrae is disrupted when the bone is replaced by tissue which comes with neoplastic pathology and replaces the natural bone. Even though very little is known about the mechanical properties of metastases, all types of metastases show a significant decrease in strength. Osteoblastic lesions which are defined by the

production of a form of compact bone do not appear to increase the strength of the bone [95].

Vertebral fractures are classified according to their gross morphological shape change from a radiography examination. The classification comprises the severity of collapse and the anterior/posterior location of the compressed bone and has a defined height reduction of 20% or more [109]. Classification of fractures can be found in Table 3 however more than two thirds are asymptomatic and are never detected [74].

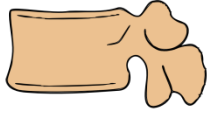
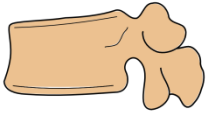


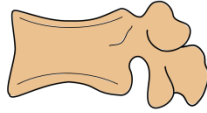
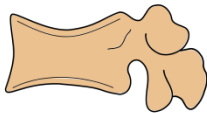

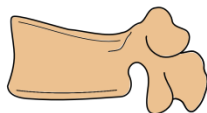
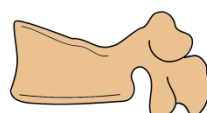

Normal/ uncertain		Fractured		
		Mild	Moderate	Severe
	Anterior			
	Middle			
	Posterior			

Table 3 Vertebral Compression Fracture (VCF) classification according to Genant et al. [76]

2.3.2 Biomechanics of vertebral fractures

Vertebral fractures occur when loading exceeds vertebral strength. A typical fracture is a wedge fracture where the anterior wall fails to support the load and collapses. The overloading of vertebrae occurs due to either exceeding normal physiological conditions or when the bone structural properties are weakened due to pathological changes such as generalised osteoporosis or cancer infiltration.

Due to marginal variation in mineral composition of the naturally occurring bone [49], the bone structural properties together with bone mineral density are believed to be by far the most contributing factor to vertebral strength [20, 22, 54, 59, 64, 68-70, 110-112]. Osteoporosis appears to have no or very limited effect on the mechanical properties of the

bone at the tissue level [21, 36]. This implies that the alteration arises from the reduction in bone mass. However it is still debated whether this also applies for metastatic tissue [67, 68]. At organ level this type of fracture can be reproduced *ex-vivo* with a combination of compression and bending testing.

2.3.3 Treatment of vertebral compression fractures - state of the art

Treatment of VCF arising from both spinal metastases and osteoporosis was traditionally recommended to comprise bed rest, immobilisation and/or use of analgesics for pain management. However with increasing life expectancy, treatments with an emphasis on an improved quality of life for severe osteoporosis or cancer suffering patients have become less important and are increasingly supplemented with minimally invasive treatment techniques.

The aim of VCF treatment mirrors the need to protect the patient from pain. The secondary aim is to restore stability of movement whilst protecting the spinal cord. Principally, management can be classified by three major possible solutions: conservative treatment, immediate decompression or the stabilisation of the spine. Classic pedicle screws or spinal fusion show good results in younger patients, however according to Gebhard [113], in patients with generalised and severe osteoporosis, use of cement-augmented screws is recommended as the weakened structure can no longer support the inserts and becomes susceptible to loosening of the screws.

In general, open surgery is not recommended in patients with cancer as their general condition and lowered immunity increases mortality. On that account palliative treatment accompanied by a combination of spinal function restoration with minimally invasive surgery would be a great advantage. Vertebroplasty (PVP) is increasingly used as such a technique. During this key-hole surgery technique a small amount of polyacrilate or mineral based cement is injected through an inserted needle directly into the vertebral body under fluoroscopic guidance.

2.4 Vertebroplasty in VCF treatment

2.4.1 PVP in osteoporotic fractures

Indication for treatment of vertebral fractures comes from a detailed examination of the patient including identification of localised tenderness or severe back pain (localised or in some cases intractable), confirmed by a radiographic and/or MRI examination. After careful examination the patient is prepared for the operation lying face down either under a full or local anaesthesia. Trocar (a cannula with inserted hollow needle) is pierced through the skin at such an angle so as to be pointing to the anterior part of the affected vertebral body through pedicles. When the trocar is introduced through a pedicle under fluoroscopy guidance, the hollow needle is retracted and vertebral body is filled through the cannula with slow retraction to introduce a sufficient volume of cement without extravasation. Once the vertebral body is sufficiently filled, the needle is retracted leaving only small signs of the intervention.

Introducing the cement through both pedicles (bi-pedicularly) compared to a single pedicle approach results in higher strength [32], preventing collapsing of the vertebra to non-augmented side [31, 32], however as stated by Tohmeh et al. [32] even the uni-pedicular approach provides sufficient restoration of both strength and stiffness. Injected trans-pedicularly, vertebral stiffness is higher compared to the extra-pedicular approach [114] whereas no difference was found in restoration of strength. Although biomechanically the aim of the procedure is to prevent further the collapse of the vertebra by the injection of a sizable quantity of cement, it has been observed that even small quantities of the injected agent may be sufficient for pain relief in the near- and medium-term.

Clinically between 1-6mL (~10-30%) [115] is being injected or the endpoint of injection is limited to avoiding possible extravasation [116], supported by cadaveric studies suggesting that even small cement volumes can restore the vertebral strength depending on vertebral size [28, 29, 117]. A study by Molloy [27] suggested 30% vertebral body fill to restore the stiffness which is in agreement with a recent clinical study by Nieuwenhuijse et al. [118] where 24% vertebral body fill was proven the most beneficial in terms of pain relief. Higher volumes are questionable due to an increased risk of extravasation [106, 116, 119] without any effect on biomechanical enhancement as stiffness and strength were found to be only weakly correlated with the volume fill [28, 117, 120].

As the PMMA cement sets in less than thirty minutes the patient can be discharged home after a short period of post-operative nursing care when the anaesthetic has worn off, usually the same day with rapid pain reduction reported within a few days of intervention [121, 122]. For CaP cements the length of recuperation may be longer due to the slower setting of this cement.

The exact mechanism of the pain relief is still not adequately reported but is believed to be attributed to exothermic reaction ($>70^{\circ}\text{C}$) during curing of the PMMA, the toxic effect of the monomer on tumour cells and/or prevention of micro-fractures in the bone [123]. Both the thermoreaction and the toxic effect however only partially explain the pain relief, while non-thermoreactive, non-toxic calcium phosphate (CaP) cements have also been reported to provide satisfactory pain relief [124, 125]. More generally, it is believed that the pain relief comes from the stabilisation mechanics where the fractured bone (and micro-fractures) are supported and constrained against any micro-motion.

2.4.2 Vertebroplasty in metastatic bone

Conservative non-operative treatment in cancer patients with bone metastases includes drug and hormone treatment as well as extensive chemo and/or radiotherapy [126]. However, these modalities usually have a slow effect on pain relief (the radiotherapy has a delayed effect of 2 weeks to effective pain relief and 12-20 weeks for maximal benefit of pain reduction [127]). Open surgery management is often contraindicated by poor life prognosis where several guidelines do not recommend operating under an estimated life expectancy of three months [104]. Even though comorbidity in treatment of spinal metastases is generally accepted, the use of a minimally invasive pain reduction tool such as PVP [128] might be advisable to improve quality of life in late stages of the disease. As spinal metastases most frequently involve the anterior elements [129], vertebroplasty shows very promising results in osteoporotic patients and currently the use of the technique is expanding to cover treatment of spinal VCF due to neoplastic infiltration. Neoplastic tumours can either be removed using specialised approaches [105, 130] or carefully displaced by injecting cement in proximity of the lesion, which may however increase the injection pressure compared to PVP in osteoporotic bone alone and lead to uncontrolled extravasation [106].

Studies here listed showed the impressive potential of PVP in providing fast and efficient pain reduction treatment with a much lower complication

rate when compared to open surgery [104]. However more long-term follow-ups and randomised controlled trials need to be conducted.

2.4.3 Complications and controversy surrounding vertebroplasty

As a relatively young technique (first used by Galibert et al. [131]), aspects of the PVP approach are still evolving and the need for randomised controlled trials (RCTs) have been sought to ascertain the most effective use of this technique. This section though focuses on the possible complications and controversies that have arisen from subsequent RCTs.

2.4.3.1 Controversy of PVP

Studies by Buchbinder et al. and Kallmes et al. [15, 16] questioned the beneficial effect in a sham study comparing PVP and placebo and reported no difference between the groups. Buchbinder et al. compared, in a multicentre single-blinded, randomised trial, thirty-five patients given PVP and thirty-six patients with a sham injection. No benefit was observed amongst either group at a 6-month follow-up. Kallmes in a similar study compared 68 to 63 patients provided with PVP and sham treatment, respectively. Similarly no beneficial effect was found during the follow-up. Even though both studies were very well conducted their results raised questions, and yet were at odds with clinical experience from different medical centres elsewhere. Both studies were criticised to have imposed a number of limitations e.g. exclusion criteria (>50% of patients in Kallmes group, >70% of patients in Buchbinder's), suboptimal treatment (injected cement fills <10% VB) and misdiagnosis (MRI not used to confirm acute fractures). Further, the sham group was not an approach that could be utilised in clinical practice and hence did not allow the surgeon any alternative therapy.

Contrary to studies by Buchbinder et al. and Kallmes et al. [15, 16] numerous clinical studies report significant and rapid pain relief in patients with osteoporotic (e.g. [17, 18, 89, 115, 118, 123, 132-135]) and/or neoplastic disease (e.g. [13, 107, 128, 136])

However, inconsistency in the beneficial effect shows that more studies are required to underpin all aspects of vertebroplasty in its clinical use. Biomechanical studies are needed to determine the effect of parameters such as volume fill and/or the use of prophylactic augmentation, as well to develop and tailor the vertebroplasty materials to provide pathology-targeted treatments.

2.4.3.2 Complications

Vertebroplasty currently has three main indications for use in treatment of vertebral fractures. These comprise of fractures due to 1) high impact load, 2) osteoporotic bone loss and 3) presence of spinal metastases. Each indication has, however, a substantial risk of complications. In general, the most significant potential complication is damage to neural tissue in proximity of the vertebra. PVP in metastatic spine is related with increased rate of complications [13] the majority of which are due to leakage [106].

The material used can also contribute to an increased occurrence of complications. Using PMMA cement can lead to catastrophic effects of thermal [137] and mechanical damage [107] to the spinal cord, and is believed to be the cause of increased occurrence of fractures in levels adjacent to those augmented [119, 122]. The true reason for the adjacent fractures is however still unknown as they may also arise from a related change in spinal shape after the fracture occurs as well as from the natural progression of the osteoporosis.

Alternative biodegradable bone cements however lack biomechanical support with which to augment the weakened structure [138] and are currently recommended for fractures of little instability or where stabilisation is provided by instrumentation, say, as in a burst fracture. However, CaP cements are of great interest due to their predicted long term outcomes with bone remodelling [124].

The biomechanically related complications arise, in part, from the lack of basic science in PVP and several key factors remain to be solved [139]. These comprise investigating the importance of cement distribution [28, 120], biocompatibility/biodegradability [30] of the material used and tailoring its mechanical properties [23, 25, 128]. More clinically-focused questions include the timing of treatment [3, 140] and long-term outcomes, especially those due to the occurrence of an adjacent fracture [122, 141, 142].

2.5 VCF cadaveric studies

The biomechanics of osteoporotic vertebral fractures at the organ level has been widely studied both clinically and biomechanically [21, 22, 50, 52, 66, 143], however fractures arising from metastatic infiltration in the spine are relatively poorly understood [83, 95, 144, 145]. This section focuses on the most essential aspects of designing a study investigating the

biomechanics of wedge compression fractures in bone with metastatic infiltration.

2.5.1 Biomechanics in cadaveric studies

Vertebral fracture occurs when the loading exceeds vertebral strength due to either a much higher than normal impact loading in physiological conditions [39] or compromised bone quality [1, 75, 87, 146]. Loading occurs in the form of compression, rotation, shear or distraction forces or a combination of these and can be simulated *in-vitro* by introducing specific boundary conditions applied to the specimen. Here, as the scope of the study is to investigate the wedge compression fracture (WCF), the aim is to replicate fractures falling into the category of anterior severe fractures according to Genant et al. [109] as categorised in Table 3.

Conditions with which to induce a wedge fracture on a single vertebra have been proposed by a number of authors. The generally accepted conditions are those in which the specimen is subjected to combined compression and anterior bending by means of eccentric loading. In studies by Tschirhart et al. [39], Whealan et al. [2] or Windhagen et al. [147], the authors used a set of hydraulic actuators to simulate such conditions, whereas other authors [3, 29, 38, 65, 66, 144] proposed using a ball joint to simulate similar conditions at lower cost where fixed single axis loading is desired.

In all the works mentioned, the preloading cycle (e.g. [64, 66] is followed by compression of the specimen to failure [39] or to a predefined reduction of the vertebral height [3, 64]. This is usually driven either by subjected load [64, 146] or displacement of the cross-head through which the load is applied [3, 65, 66] with subsequent unloading.

Typically the load-displacement curve from such loading consists of a non-linear toe-region, followed by a linear elastic region until the specimen begins to yield reaching the first peak (zero-slope) fracture load. This is typically followed by post-fracture softening which can be explained by broken trabeculae of the cancellous bone sliding along each other, with a subsequent secondary increase in resilience due to pore-closure and densification of the compressed structure. There are however several techniques for ascertaining the stiffness: by using a linear fit within the most linear region [3, 29, 65], by qualitatively estimating where the slope appears to be at maximum, or as a combination of both where the slope is taken from the linear fit of a region with highest slope. Although a discussion around

appropriate techniques still persists, it seems that the most reproducible and robust is the one based on using a strain window [148, 149]. Such technique is discussed in more detail by Buckley [150], who states that despite the use of the linear fit within a manually selected region being generally accepted, using a 1% strain window approach provides better repeatability and a more user-independent tool to estimate the stiffness.

The composition of testing specimens – i.e. number of levels tested - is still being debated from using single vertebra [3, 26, 29, 65, 66, 95, 144], two functional spinal units (FSU) [64] or multi-segment spinal specimens [2, 39, 147]. The single vertebra studies show good consistency in simulating the wedge fractures, whereas a multi-segment study provides a more realistic loading scheme. In the latter, the adjacent intervertebral disks distribute the load more in a manner that is more akin to an *in-vivo* situation. However in this case the control of loading is limited.

Compared to multi-level segments, a single vertebra embedded into PMMA guarantees control of the distribution of the load along the endplate. A recent finite element study by Maquer et al. [151] showed a good correlation between fracture loads determined when VBs were loaded through the vertebral disks and when embedded in PMMA. However, the study pointed out a distinct difference in damage concentration compared to loading a multi-segment.

A special type of the single vertebra study with boundaries that are even more accurately defined is when both the cortical endplates are fully removed in order to create two perfectly parallel surfaces [152]. This was later improved to give an accurate description of the boundary states by using three differential transformers (LVDTs) attached to the top loading plate [66]. Such information was later used in developing more accurate FE models with the data providing validation [153].

2.5.2 Biomechanical assessment in vertebroplasty

The beneficial effect of PVP has been widely presented in clinical studies where pain is substantially reduced usually within days of the procedure and key studies thereof were presented earlier in the work. This keyhole surgical operation is a cheap and efficient way to reduce pain in patients treated for vertebral fractures caused by the presence of osteoporosis and collapsing vertebrae when cancer metastases are present within the spine. However, very little is known about biomechanical aspects of the treatment.

2.5.3 Types of augmentation cement

The decision of which cement to administer to a patient is fraught with difficulty and currently often relies on surgeon preference, including selection from the numerous new formulations that are put forward by commercial companies.

Ceramic cements show satisfying long term results as they remodel and are replaced by the surrounding bone, but are often more difficult to handle and have specific uses limited to stable fractures due to their lower strength which hence cannot provide the initial supportive effect within days after the operation. Hence these CaP cements benefit younger patients with good bone quality but would be contraindicated for patients with neoplastic disease due to concerns regarding the support of metastatic growth.

The second type of cement, alternative to the ceramic one, is a much stronger acrylic material which is however almost five times stronger than natural bone and forms a stiff pillar compromising an unnatural distribution of loads with the index and adjacent vertebrae. Hence, a lower-modulus cement may help in reducing adjacent vertebral fracture. Nonetheless these polymeric cements treat the condition, but sit unaltered in the bone and remain as a foreign body.

2.5.4 Prophylactic augmentation

Prophylactic augmentation is a way to reinforce the weakened structure before the fracture occurs and saves the patient from experiencing debilitating fractures. This intervention has so far provided good biomechanical results as it can maintain vertebral stiffness while supporting the vertebra to reach higher failure loads (e.g. [3, 154]), but it needs thorough investigation as most studies lack multi-segment testing which would truly reflect the biomechanics of adjacent levels. Moreover, the general tendency in clinical practice is not to use this approach as the state-of-art prediction approaches lack a robust method in defining the weakened vertebrae.

2.6 Predictions of vertebral compression fractures

2.6.1 Clinical models to identify vertebrae prone to fracture and use of numerical models in clinical practice

Despite increasingly successful treatment modalities such as vertebroplasty, a significant number of patients with osteoporosis or

metastatic infiltrations are not treated [155]. One of the main contributing factors to missing the opportunity for treatment lies in the failure to identify the risk factors for fracture.

Assessing weakened vertebra or progression of osteoporosis is challenging and in clinical application it is currently based on empirical modelling such as using DXA based t/z-scores [5], a FRAX prediction tool [156], Fracture Risk Index (FRI) [157] or Trabecular Bone Score (TBS) [158]. All of the models compare the single subject to a large population of epidemiologic statistical models. However, these models do not provide patient-specific pathological assessment such as determination of fracture risk in metastatic patients or in general in patients with variance in distribution of bone tissue, for example those with large deformities or osteophytes.

2.6.2 Engineering principles in fracture prediction

As published in 2003 by Bouxsein et al. summarising one decade of intensive collaboration of the biomechanical community on vertebral morphology-strength assessment: “Despite these new insights, important issues remained unresolved” [70], furthermore the same author describes a necessity to link clinical models with engineering principals to characterise a bone’s ability to resist fracture.

Here, one of the first models was proposed [64], a simple engineering principle taken from a strength assessment gained when subjecting structure to compressive loading. The author used the product of the volumetric BMD (representing characteristic of the material) and the endplate area. Later the model was altered to match engineering structural principles of the weakest slice and the product of BMD and minimal cross-section area was used [148]. Both methods, using the endplate or minimal cross-sectional area, showed good correlation when predicting the vertebral strength ($\sim R^2=0.6$ for endplate area [64] and $\sim R^2=0.7$ for minCSA [66]). Despite a high correlation between predicted and tested vertebral strength, from an engineering point of view, this approach is successful only when subjected to pure compression with a lack of flexural moment. It is due to this missing component of accounting for bending forces that they fail to predict anterior compression fractures where eccentric forces are implied. Moreover, despite its relatively good results in correlation to *in-vitro* experiment strength values, the method also fails to assess the vertebral weakness qualitatively.

The Finite Element (FEA) approach has in the last decade been shown to be a useful tool in assessing the behaviour of the bone when subjected to extensive load (e.g. [26, 28, 65, 66, 151, 159]). Such models are effective tools in underpinning the basic science and have worked well in helping to design an appropriate experimental setup prior to cadaver testing. FE models have also shown potential in accurate prediction of fractures [66], even in samples such as those with metastatic infiltration [160, 161].

A summary of the different approaches used for predicting biomechanics of vertebral bone in Table 4 indicates a widespread range of success. Here, beside a more conventional indicator of correlation (coefficient of determination (R^2)), published data were also reanalysed to provide the mean difference and limits of agreements (± 1.96 standard deviation) as a measure of the statistical metric of agreement between measured and predicted datasets as proposed by Bland-Altman [162]. Each dataset was obtained from published predicted-measured plots using plot digitising software [163].

Comparison shows that more sophisticated methods have relatively good prediction power (between 0.78 and 0.96) but similarly to other methods often do not agree with experimental data also with respect to the 1-1 line. This is in the majority of cases due to a limited number of samples counterbalanced by repeating optimisation of the sample-specific model.

Even though the FE approach shows promise once the model is properly calibrated, it faces challenges such as the fact that it often requires (i) well defined boundary conditions; (ii) complex geometry which comes with demanding high computational requirements; and (iii) demanding resources in terms of high resolution input images. Even though high resolution images for voxel based models (e.g. [112, 164]) can be obtained *ex-vivo* using techniques such as XtremeCT (side of an isotropic voxel down to 0.082mm) or microCT (down to 0.004mm), *in-vivo* modelling is limited to homogenised FE models [65, 165] from qCT images (2-0.5mm depending on allowed radiation exposure). Moreover, due to the challenging computational complexity the computational models often have their number of elements reduced in order to minimise the computation time required [166]. This however results in an influential partial voxel effect where for illustration a single trabecula (thickness ~ 0.1 mm) can fit the voxel in cross-section ten times and the cortical shell (thickness ~ 0.3 mm) almost three times. Despite these challenges the FE approach shows promising results even in post-yield characteristics [153] with accurate input data and boundary conditions.

Authors	No. of samples (donors)	Demographics	Age of donors	<i>In-silico</i> to experiment strength prediction				
				<i>In-silico</i> approach	R ²	Mean [kN]	LoA [kN]	Boundary conditions
Dall'ara et al. [167]	N=37(10)	OP	44-82	analytical: <i>minCSA*BMD</i>	0.70	N/A [†]	±1.81	EPs, PEs Removed
Crawford et al. [65]	N=13(13)	OP	37-87	analytical: <i>minCSA*BMD</i>	0.65	N/A [†]	±2.64	EPs Fixed, PEs Removed
Zainali et al. [168]	N=9(3)	OP	42 [‡]	analytical: <i>axial rigidity (σuBV/TVmin)</i>	0.85	-0.85	±0.68	EPs Fixed, PEs Removed
Buckley et al. [148]	N=27(30)	OP	80-97	analytical: <i>axial rigidity (EAmin)</i>	0.80	N/A [†]	±1.28	EPs Fixed, PEs Removed
Windhagen et al. [147]	N=30(30)	mixed*	48-99	analytical: <i>axial rigidity (EAmin)</i>	0.85	N/A [†]	±1.18	3 levels segment
Whelean et al. [2]	N=18(34)	mixed*	37-102	analytical: <i>beam theory</i>	0.69	-0.43	±1.24	3 levels segment
Crawford et al. [65]	N=13(13)	OP	37-87	linear elastic FE: <i>voxel-based</i>	0.85	-1.3	±1.86	EPs Fixed, PEs Removed
Dall'ara et al. [167]	N=37(10)	OP	44-82	non-linear FE: <i>homogenised</i>	0.78	1.28	±2.10	EPs, PEs Removed
Pahr et al. [169]	N=37(10)	OP	44-82	non-linear FE: <i>homogenised calibrated</i>	0.92	0.1	±0.96	EPs, PEs Removed
Zainali et al. [168]	N=9(3)	OP	42 [‡]	linear elastic FE: <i>voxel-based</i>	0.82	-0.04	±0.84	EPs Fixed, PE Removed
Zainali et al. [168]	N=9(3)	OP	42 [‡]	linear elastic-linearly plastic FE: <i>voxel-based</i>	0.92	0.86	±0.53	EPs Fixed, PE Removed
Buckley et al. [170]	N=75(44)	OP	54-97	linear el.-perf. plastic FE: <i>voxel-based FE</i>	0.80	-0.38	±1.32	EPs Fixed, PE Removed

... table continued on following page...

Authors	No. of samples (donors)	Demographics	Age of donors	<i>In-silico</i> to experiment strength prediction				
				<i>In-silico</i> approach	<i>In-silico</i> approach	<i>In-silico</i> approach	<i>In-silico</i> approach	<i>In-silico</i> approach
Imai et al. [171]	N=12(4)	mixed**	31-83	linear el.-perf. plastic FE: <i>homogenised</i>	0.90	-0.05	±0.57	EPs Fixed, PE Removed
Imai et al. [171]	N=12(4)	mixed**	31-83	linear elastic-linearly plastic FE: <i>homogenised</i>	0.96	0.25	±0.51	EPs Fixed, PE Removed
Chevalier et al. [172]	N=12(4)	OP	47-83	fabric non-linear FE: <i>voxel-based</i>	0.76	1.94	±2.03	EPs Fixed, PE Removed
Chevalier et al. [172]	N=12(4)	OP	47-83	fabric non-linear: <i>homogenised</i>	0.89	1.75	±1.55	EPs Fixed, PE Removed

Legend: "Mean" - mean of difference between experiment and predicted strength, "LoA" – limits of agreement; Demographics: "OP" - healthy or osteoporotic, "mixed**" - simulated lesions, "mixed***" –author's note gives a list of deaths including one from bladder cancer (not distinguished in statistics); Age of donors: "42[±]" average donor age (range not listed); Mean: "N/A[†]" data pooled from retrospective linear fit; Boundary conditions: "EP fixed" - both endplates were embedded in parallel PMMA end-caps, "PE removed" - posterior elements were cut/trimmed at vertebral body, "Bot EP fixed" - bottom endplate embedded in PMMA whilst PMMA "impression" positioned on top endplate, "NU intact" - neural arch was kept intact whilst processes were trimmed

Table 4 Comparison of assorted *in-silico* approaches used in vertebral body fracture prediction models

A compromise to the complex FE modelling method is the use of engineering principles known as composite beam theory which is then applied to the bone structure. Such an approach was for example used by Snyder et al. [145] and on whole vertebral bodies by Nazarian et al. [68] where cored metastatic samples were subjected to stepwise loading. Here, the density information obtained from the tomographic examination is converted to a modulus map and the weakest slice is identified as a slice with minimal strength. Compared to the complex FE modelling, the limitation of this approach is that apart from identifying the weakest slice it lacks a qualitative aspect of evaluation. However, the method has been shown to be superior in providing better correlation to experimental strength than BMD standalone or BMD X minCSA. The full potential of this technique still needs to be explored including within the clinical setting.

2.7 Morphology and material properties of the bone

2.7.1 Material properties of human bone

Bone as a hierarchical material can be investigated on different levels of its composite structure. Pooled from literature [55, 173-175], the trabecular bone has hierarchical mechanical properties at the following levels:

- i. *Macroscale*: "At the whole organ" (in order of cm, stiffness $\sim 1.5\text{kN/mm}$)
- ii. *Mesoscale*: At the trabecular bone (in order of mm, Young's modulus(E)= $\sim 0.5\text{ GPa}$)
- iii. *Microscale*: Bone structural unit (single trabecula) (order or 100s μm , $E=\sim 15\text{GPa}$)
- iv. *Sub-microscale*: Single lamella level (2-7 μm , $E=\sim 30\text{GPa}$)
- v. *Nanoscale*: Mineralised collagen fibrils and Hydroxyapatite crystals (order of 100s nm, $E\sim 1\text{GPa}$ and 100sGPa respectively)

Only limited work has been done to assess the material properties at the nano-scale, the undertaking of which remains technologically challenging. Experimental challenges were however bypassed using the computational approach of multiscale modelling [177-179].

At the sub-microscale, the single lamella can again be investigated by computational modelling as a composite of a matrix embedded network of preferentially oriented fibrils reinforced by apatite crystals [175, 176, 180, 181] or by means of diamond tip indentation tests adopted to such a small scale (nano-indentation) [174, 182].

Stepping up to mesoscale, the single trabecula can be measured by means of micro-indentation; here the hardness and stiffness can be derived from indenting the bone tissue with a tip substantially larger than the trabecular lamellae. Results show that both the hardness and stiffness were independent of age, gender or progress of osteoporosis [36, 183, 184] and this was confirmed even at the lamellar level [185, 186]. Even though the bone tends to act as an anisotropic material, studies by Wolfram et al., Rho et al. [36, 51] describe it as transversally isotropic with a ratio of longitudinal/axial anisotropy ranging only from 1.1 to 1.3 (at its largest in cranio-caudal bone orientation direction).

To this point there is only one study in the literature where metastatic bone has been assessed. Here, Nazarian et al. [68] reported that both the hardness and stiffness measured by means of nano-indentation are half of

the values when compared to osteoporotic and healthy patients. However, the reported values of the elastic tissue modulus of healthy bone (0.47 GPa) are almost two orders of magnitude lower than the ones reported in the literature (~10-20 GPa depending on the sample conditions and anatomical sites e.g. [184, 187]) This indicates possible problems in their experimental procedures or a large effect of damage on the bone indentation properties [35] which is typical for bone subjected to yield. This is also later contradicted in the same publication when cored samples from the same donors were subjected to compression at mesoscale (results comparable with those published elsewhere [30, 188, 189]) and it was concluded that metastatic trabecular bone biopsies showed similar mechanical properties (elastic modulus and yield strength) compared to osteoporotic bone once bone density was accounted for [68].

2.7.2 Bone material models for fracture prediction

Bone mechanical behaviour modelling and fracture prediction are for obvious reasons strongly dependent on the specified material properties (e.g. [190]). The bone material model determines the properties of the element and if not set correctly will result in a poor agreement between the simulation and the modelled physical situation. By using modern imaging tools such as CT, the aspect of variance in porosity can be accounted for; nevertheless the bone material model derived from density-based imaging tools has still not been adequately investigated.

This section discusses experimentally obtained material models with a focus on using the models from CT-data and the mathematical relation between the modulus of elasticity (E) and measured tissue density (ρ). Through a series of experiments Kayak et al. [191] reported that hydrated tissue mass correlates to the mass of bone tissue when burned to an ash and similarly to its density, measured by means of tomography assessment with high correlations between all steps reported ($\rho_{\text{dry}} \rightarrow \rho_{\text{ash}}$ $r=0.996$ and $\rho_{\text{wet}} \rightarrow \rho_{\text{ash}}$ $r=0.99$, $\rho_{\text{ash}} \rightarrow \rho_{\text{ct}}$ $r=0.98$). Although the correlation in the reported study was not presented alongside indications of the agreement, the study strongly indicates that the non-mineral component of the bone remains consistent and therefore the density-based imaging tools, even though predicting only the mineral component of the bone, can be used to predict material properties of tissue *in-situ*. To clearly summarise, the definitions of the densities used in literature and within this study are defined in Table 5.

Nomenclature	Abbreviation	Units	Details
Apparent density	ρ_{app}	$\frac{g}{cm^3}$	$\frac{\text{hydrated tissue mass}}{\text{unit volume}}$, as derived from experimental measurement
Apparent dry density	ρ_{dry}	$\frac{g}{cm^3}$	$\frac{\text{dry tissue mass}}{\text{unit volume}}$, as derived from experimental measurement
Ash density	ρ_{ash}	$\frac{g}{cm^3}$	$\frac{\text{ash content}}{\text{unit volume}}$, as derived from experimental measurement
CT density	ρ_{ct}	HU	derived from attenuation coefficient (mineral component only), calibrated against phantom with known density
Bone mineral density	BMD(vBMD) or ρ_{BMD}	$\frac{mgHA}{cm^3}$	$\frac{\text{mineral content}}{\text{unit volume}}$, units based on calibration phantom used
radiographic BMD	BMD(aBMD)	$\frac{g}{cm^2}$	$\frac{\text{projected mineral content}}{\text{area}}$
Bone volume fraction	BV/TV	1	$\frac{\text{segmented bone volume}}{\text{unit volume}}$, strongly dependent on BMD-to-BV/TV conversion or segmentation method used
Porosity	-	1	$1 - BV/TV$

Table 5 Technical annotation of different densities and density-based morphological indices

In order to postulate a relationship between the density and stiffness of the bone, experimental testing needs to be performed. This approach for assessing the material properties usually comprises platen testing [111, 188, 191-198], 3 point bending [199, 200] and the use of end-caps [196, 201, 202]. In the platen test, samples are compressed between two plates and the stiffness is derived from the load-deformation curve recorded by the load cell. The end-cap method tries to avoid detrimental consequences (artefacts) due to structural and frictional end-effects at the interface between the sample and platen by casting the bone's end into a PMMA disk [196]. The three-point bending test is predominantly used for long bones but was used also by Snyder et al. to investigate stiffness of the cortical bone [200].

Supported by the authors listed above the mathematical relation between density and modulus can be expressed thusly as a power law (eq. (1.1)):

$$E = a + b\rho^c \quad (1.1)$$

From the literature, for human trabecular bone “a” generally does not notably differ from 0, “b” varies from 0 to a few 10s, and the density powered by “c” varies from 0 to ~3 (an average of 1.76 for pooled literature data).

The predominant nomenclature has not been agreed on within the literature, and the nature of the density used in publication models varies from ρ_{app} [149, 165, 194, 195, 197, 199, 200, 202-205], ρ_{dry} [188, 193], ρ_{ash} [191, 192, 198], ρ_{BMD} [201] to BV/TV [33, 111], with each presenting a notably different material model. Any comparison of different models should be hence undertaken with appropriate normalisation. For example a publication by Helgason et al. [189] provided a comparison of models for human bone using known conversions between densities to normalise the input variable all to ρ_{app} and normalise strain rates [206]. Such a normalisation however still showed a notable discrepancy between the results from different publications even for the same anatomical site and type of bone.

The same authors conclude that although normalised, the dataset “cannot be assumed equally valid and cannot be pooled together statistically, to derive an average elasticity–density relationship”. They propose a retrospective numerical material model tuning using a training set to extrapolate a representative material model for a specific model.

Chapter 3

Development of a fracture prediction tool

The first objective of this thesis was to develop a fracture prediction tool for laboratory use which would allow improved assessment of vertebrae for use in designing experimental studies and potentially as a prophylactic augmentation tool where the weakened vertebra is targeted before the fracture occurs. This chapter hence focuses on developing such a tool while presenting verification and validation studies using cadaver samples representing structurally compromised vertebrae. The sections of this chapter comprise three distinct subchapters:

- i. Section 3.1 introduces the theoretical approach required to underpin the image processing based fracture prediction followed by detailed development steps of the composite beam theory fracture prediction tool. Moreover this section comprises initial validation using historical data.
- ii. Section 3.2 introduces the experimental protocol for testing a single vertebra used for structural assessment. This section also provides a full list of samples used for the purpose of this study, highlights methods of cadaveric testing and scanning and includes the initial fracture assessment of pathological samples diagnosed as osteoporotic (OP) and multiple myeloma cancer bone (MM) as well as samples from spines infiltrated with metastases (mets).
- iii. In the final section of this chapter (section 3.3) the proposed fracture prediction tool is deployed in order to predict the strength of weakened vertebrae in comparison to an actual experiment. Furthermore, the fracture prediction tool is tested to observe whether the time required for assessment is reduced, followed by a calibration of the material-law used.

Each chapter comprises of an Introduction subsection, putting literature findings to appropriate context followed by the methods used, the results of the study and a discussion thereof. The entire chapter is then briefly summarised in the last section.

3.1 Development of an *in-silico* fracture prediction tool

3.1.1 Introduction to vertebral bone fracture prediction

Based on engineering principles, the structural properties and related fracture behaviour of a bone are attributes of a geometrical pattern combined with material quality. The geometrical disposition reflects the state of a bone which is prone to failure due to unnatural morphological changes [207] and is often undervalued by studies which present this only in the examination of healthy or heterogeneously affected tissue such as osteoporotic tissue. The quality of underlying material properties results from the biochemical equilibrium in the microenvironment of the bone [49] and is represented by the spatial stiffness and yield potential. When combined, these attributes represent the structural rigidity of the organ and also, if being analysed quantitatively, contain information about whether bone is prone to fracture.

Although the collagen component of a bone composite cannot be assessed using computed tomography (CT) a high correlation between the apparent and mineral density has been reported in literature [198]. Human bone tissue mineral composition appears in tomography images as a attenuation magnitude approximately equivalent to 1.5 gHA/cm^3 [49]. Here, every prismatic reconstructed image unit (voxel) represents a ratio of mineral components within a particular volume which can vary from negative values (due to calibration where air appears at approximately -0.1 gHA/cm^3) to the total maximum density of the bone. Hence, if the scanning resolution allows and the voxel is situated entirely inside the bone, a coarsening of the resolution will result in a variation between those two values, the so-called partial volume effect. This is important to understand in order to distinguish between prediction models based on a segmented (BV/TV) image and density based modelling. To some extent, the partial volume effect can be used as a measure of the porosity of the trabecular bone on a sub-voxel scale. This approach avoids a common issue in which the bone is segmented in an insufficient resolution but with an appropriate material model to represent a conversion between the partial content of the bone and the related modulus of elasticity.

3.1.1.1 Finite Element modelling in WCF

Mainly due to the recent availability of high performance computers, several studies also investigated the use of a finite element approach for assessing the material properties of the bone. Such an approach shows

substantial potential, particularly due to the convincing physical background of the method. This assures robustness and allows for the possibility of extending the same principles to different loading conditions. Also, compared to more simplistic analytic theories it can help to underline damage or fracture localisation and can be also deployed to investigate post-yield behaviour of the fractured bone [153]. However, there are many limitations to using this sophisticated approach such as well-defined boundary and loading conditions or computational time and costs [166]. As an example, one study [172] documented the time dependency of 72 simulations of surface-based models and 12 simulations of voxel model as long as 60 days of cumulated processing time.

3.1.1.2 Fast and simplistic engineering principle models

This section compares data drawn from literature to find a relatively fast, yet reliable, straightforward method which could be used as a fracture prediction tool.

Brinckmann et al. [64] proposed a prediction based on the product of the endplate area and BMD, giving agreement between the experimental and predicted strengths of $R^2=0.66$ which was later improved by a more meaningful model representing the mechanic of solids in which the endplate area was replaced by a minimal cross-sectional area of the sample. Using this model, various authors [65, 167] observed correlations ranging between $R^2=0.65$ and $R^2=0.70$. When accounting for varying densities regardless of distribution, different studies [147, 168, 170] obtained even more reliable predictions ranging from $R^2=0.8$ to $R^2=0.85$. All three authors, despite using different notations, employed the axial rigidity of the weakest slice as the measure of the organ's strength when subjected to compression. Similar to the model investigated in this study, Whealan et al. [2] have further shown that by adding a parameter accounting for flexural rigidity and incorporating both the variations in density together with spatial distribution, the prediction correlates much closer with experimental data when the sample is also subjected to combined loading. Here, according to physical principles, the authors used the engineering composite theory combining axial and flexural rigidities using a slender beam approximation, which resulted in a more robust structural assessment which is applicable to different test sets and loading conditions compared to pure compression models.

Here, the composite beam theory has already been proven [65] to be competitive to computationally demanding finite element (FE) modelling where the requirement for high precision scanning as a precursor to FE

modelling still hampers clinical usability. This engineering beam theory has also been suggested to be superior to those methods based on BMD of the bone used in clinical practice [2]. However, this methodology has never been robustly validated against a wider range of neoplastic pathologies. This section aims to encompass a solid theoretical background for the proposed fracture prediction tool. It describes the development of the tool and presents subsequent verification and validation on historical data. Later this method will be used in a cadaveric study comprising three morphologically distinct pathologies.

3.1.2 Methods used in development of the fracture prediction tool

3.1.2.1 Composite theory approach

The theoretical approach for determining strength comes from a coarse simplification based on the assumption that the whole spinal structure is a single unit. Based on the Euler-Bernoulli beam equation, the stresses in such a construct can be analytically assessed to determine its strength. A long thin unit under combined loading such as compression and bending can be simplified to a single slender beam. Then the stress is linearly distributed from the neutral axis to the most distant point on the beam's surface. In the region of linear stress-strain curve, where the simplified Hooke's law is still valid, the stress (σ) is proportional to the product of strain (ϵ) and elastic modulus (E):

$$\sigma = \epsilon E \quad (1.2)$$

In the case of combined compression and bending, the strain (ϵ) at a particular distance from the bending (neutral) axis becomes:

$$\epsilon = \frac{F_z}{EA} \pm \frac{M_y c}{EI_y} \pm \frac{M_x d}{EI_x} \quad (1.3)$$

Here F_z corresponds to the compression loading whereas EA and EI represent the axial and bending rigidity and M_y is a measure of loading corresponding to moment loading. The maximal strain occurs at the most distant point from the neutral axis. Here, the theoretical assumption determines that the point of the highest strain will be positioned directly on the axis of symmetry which intersects with the load axis. This results in the assumption that “ c ” represents the distance between the point of highest strain and the neutral axis, whereas “ d ” is to be substantially lower allowing the contribution of the moment M_x to be disregarded (more on bi-axial eccentric loading and asymmetric beam theory can be found in Appendix G: Bi-axial eccentric loading)

Hence for a known strain at which the fracture starts to propagate (component ϵ) and at a given geometrical distribution (components “c”, “A” and “ I_y ”) with known material properties (E), a maximum load at this strain can be established. Furthermore, a strong relation between the measured mineral density and its material properties suggests that the spatial elastic modulus ($E_{(x,y)}$) at every element of the tissue can be related to density from tomography images following a power law material model (eq. (1.4)):

$$E_{(x,y)} = a + b\rho_{(x,y)}^c \quad (1.4)$$

Subsequently, the bending stiffness component can be assessed according to equation (1.5):

$$EI_y = \sum_{i=1}^A E_{(x,y)} x_i^2 da - EAx_{E_{centr}}^2 \quad (1.5)$$

Here the second term translates as the second moment of area weighted by the spatial elastic modulus from the spatial coordinate system axis into the neutral axis. As the neutral axis is assumed to be identical to the modulus weighted centroid, its position is defined by:

$$y_{E_{centr}} = \frac{\sum E_{(x,y)} y_i da}{EA} \quad (1.6)$$

$$x_{E_{centr}} = \frac{\sum E_{(x,y)} x_i da}{EA} \quad (1.7)$$

Together, this represents an analytical approach which can be adapted to any structure where material properties and geometrical distributions under certain loads are known (Figure 8).

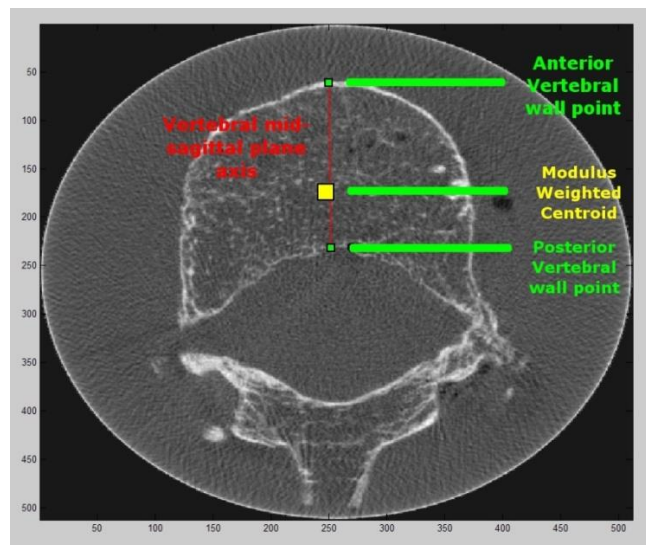


Figure 8: Engineering beam theory principles used in predicting vertebral strength during the wedge compressing fracture

3.1.2.2 Implementation of the composite beam theory into a comprehensive computational package

Structural analysis used in this approach combines CT images with minimal user interference estimates of the vertebral body strength. Firstly data taken from scans is loaded and converted into bone density. Secondly the vertebral body is masked from the surrounding areas. Finally a structural assessment, where the estimated bending and axial stiffnesses are combined using the beam theory, is used to estimate the minimal load required to induce fracture to the sample under given conditions. The detailed flowchart presented in Figure 9 illustrates blocks of operations delivered, from acquiring the CT images to reporting the predicted vertebral body strength.

A number of theoretical assumptions have been implemented as described in the previous section. Each axial image is considered as a cross-sectional cut of a slender beam with a modulus map defined directly by its local density distribution. In summary, the approach combines the bone strain (ϵ), axial rigidity (EA), bending rigidity (EI), geometrical distances between the neutral axis and load axis (a) and the most distant anterior point (c) and the body mask described in detail in section 3.1.2.3. The loading axis position and mid-sagittal plane orientation are derived from the experimental setup once defined by the user.

The bone strain (ϵ) corresponding to the fracture was set to 1% according to Keaveny et al. [195]. EA is estimated as a sum of all the density-based elastic moduli over the cross-section of the vertebral body, whereas EI is based on the moment of inertia which is obtained from a relationship of the voxel's normal distance to the axis perpendicular to a mid-sagittal plane intersecting the modulus weighted centroid squared.

To minimise an error due to misalignment, the script was adapted to any possible position of the image and hence the neutral axis does not have to align to the image matrix and is defined according to the anatomical plane of the measured specimen in general. The predicted fracture force is equivalent to the uniaxial force needed to induce the fracture at the same loading point as in the experimental setup. Here, the weakest slice is identified by analysing axial slices one by one, giving the estimated load, hence the one with the lowest F_z is the predicted fracture load of the sample.

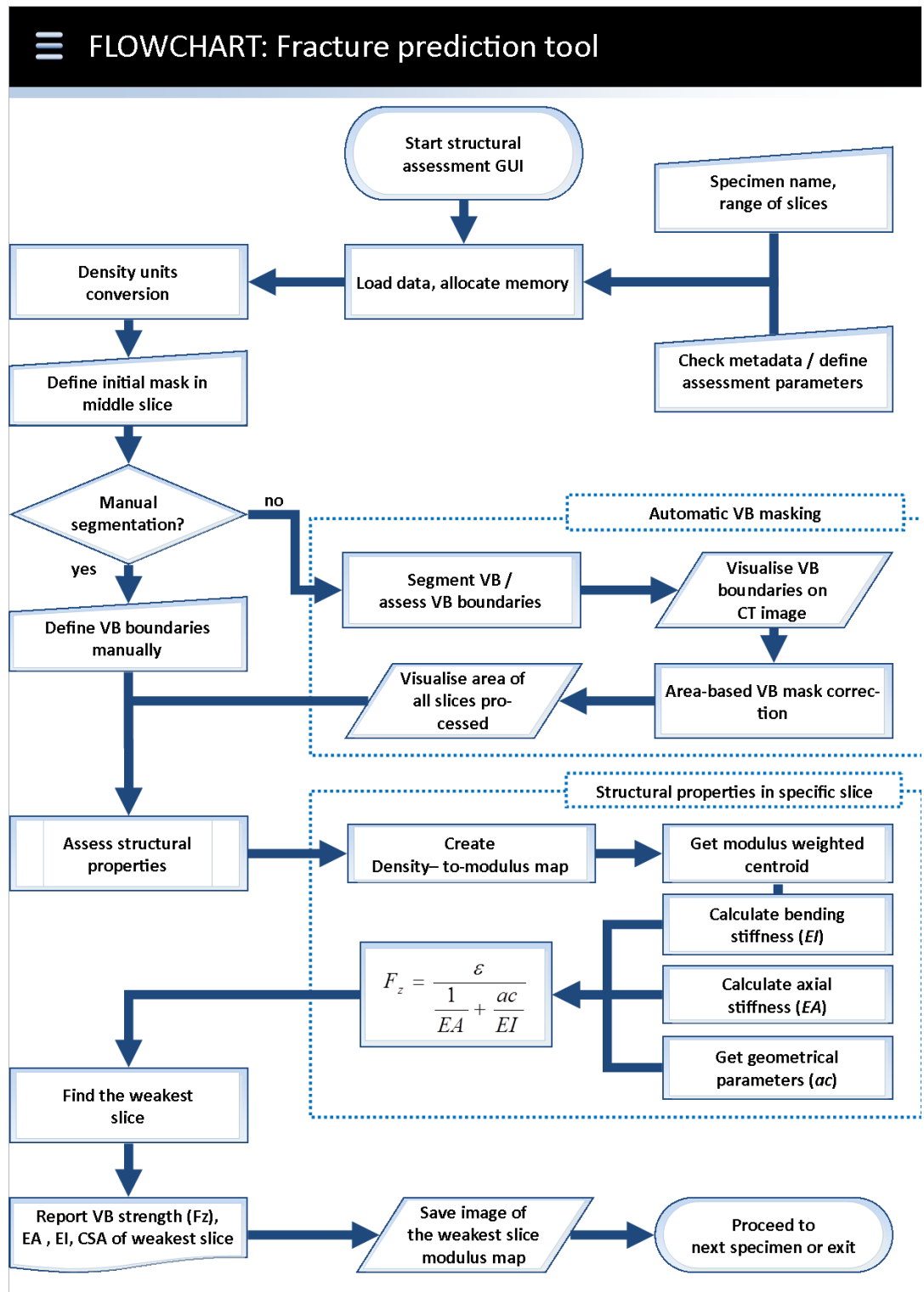


Figure 9 The fracture prediction tool developed in this work comprises steps in which VB cross-sectional boundaries are obtained by a series of morphological operations, then each voxel within this mask is converted to an elastic modulus with which to create a series of modulus maps of the axial slices. Vertebral strength is taken as yield load of the weakest slice

The output of the tool is presented as the predicted fracture load, bending rigidity and axial rigidity and represents the area of the weakest cross-sectional slice. A Graphical User Interface (GUI) has also been developed (depicted in Figure 10). The output results are saved to a separate file together with a modulus map of the weakest slice highlighting the position of the modulus weighted centroid, the load axis and the most anterior and posterior points of each particular slice.

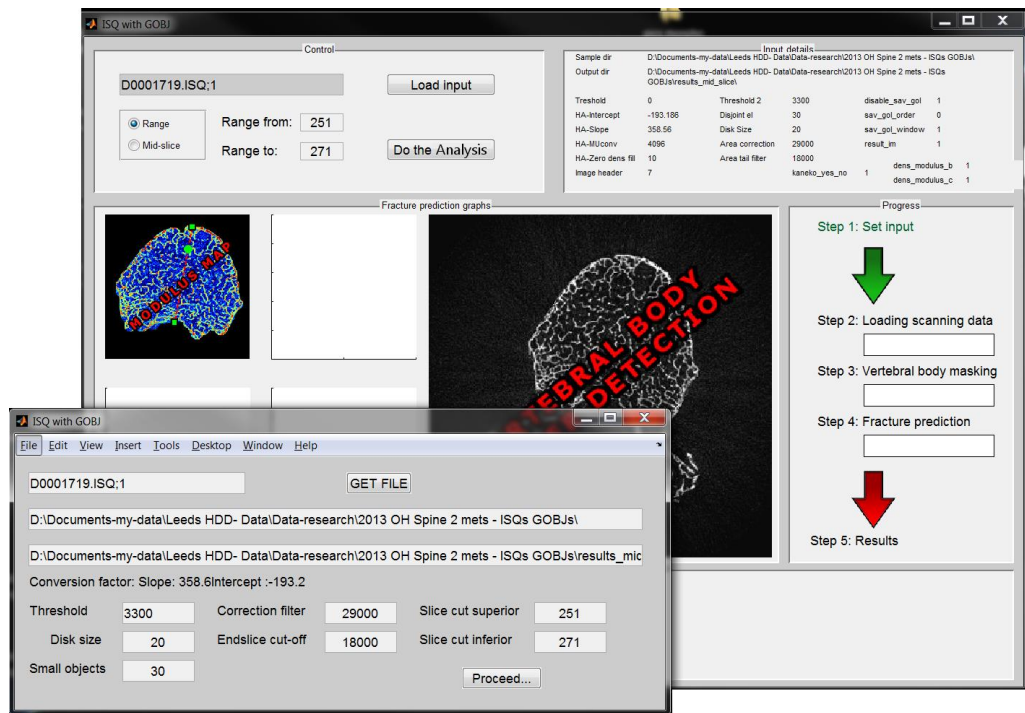


Figure 10 Graphical User Interface (GUI) designed for purposes of the fracture prediction tool

3.1.2.3 Vertebral body image segmentation (masking)

A series of binary image processing morphological operations has shown to provide a good compromise in terms of defining sufficiently accurate border detection (volume estimation) in a sufficiently short time, even when using a standard desktop PC. This approach was hence adopted in order to allow the tool to detect the vertebral body to minimise the length of calculations and to establish the most distant point in the vertebral cross-section. This approach was tested on different pathologies to assess its versatility and was validated experimentally against volume estimation. The following section details the particular background of such an approach.

A CT image can be represented as a three-dimensional array of attenuation coefficients expressed in grey-scale values. The spatial unit of the image-voxel (a three-dimensional pixel) comprises isotropic single value

information of a specific dimension depending on the scanning parameters and the resolution. Volumetric measurements are derived from the known voxel volume. Secondly, using the simple isometric voxel edge size, the distances and area measurements can be similarly derived.

To define the VB mask (i.e. to define a cross-sectional area slice-by-slice) and to automatically identify the most distant point of the vertebra, a semiautomatic subroutine was compiled in a computational environment using MATLAB [208]. The cross-section of a VB was established using two distinct sub-programs with additional subroutines. In the first program, the image in every slice was binarised based on a histogram cut and then filtered to remove disconnected elements with sequential flood fill morphological operations such as extrusion and dilation. All variables here listed are first predefined by the user according to the scanning resolution used and the quality of the bone, where for resolution of $70.8\mu\text{m}$ voxel edge size typical values may vary from $400\text{-}700\text{mgHA/cm}^3$ and 10-50 voxels for flood fill operations and increasing with increased resolution (due to lower partial volume effect). This step was repeated until the surrounding noise was removed providing clear and smooth boundaries of the vertebral body, as seen in the example in Figure 11 which shows the development and validation of the approach using porcine samples. Consecutively, this was repeated for every slice from the top to the bottom vertebrae with minimal intervention from the user.

However, as the tool is dependent on the difference between the degree of density inside the bone and the background, the automatic boundary estimation can be hampered for samples with a very low bone density or large lesions. The degree of rectitude is automatically assessed by comparing an area in the current slice to the area of the previous slice and if the criterion falls out of the tolerance area specified by the user, the border line is replaced by the one from the previous slice. This approach was shown to be sufficiently expedient and useful in non-uniform pathological samples and especially in samples with a high degree of lytic infiltration. In some cases the boundaries needed to be corrected manually. The manual correction (Figure 13) combined with the previously described self-correcting routine (Figure 12) have been proved to be suitable in all cases where the automatic tool failed to provide the boundaries independently. This subroutine significantly minimises pre-processing time with minimal effect on the final modulus map differences and needed to be deployed only on the more morphologically altered vertebrae.

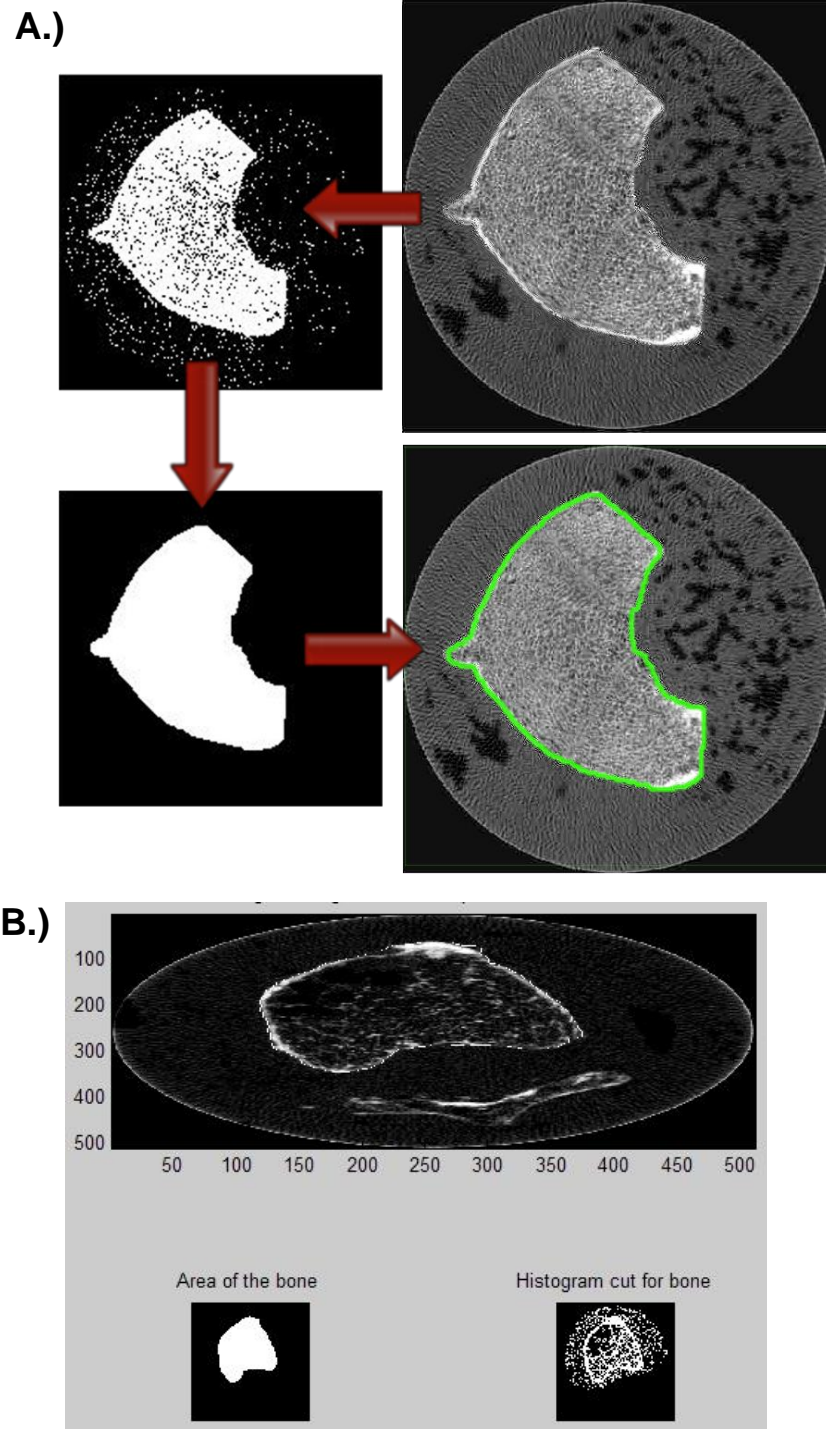


Figure 11: Vertebral body boundary estimation: a microCT image is first taken and binarised according to a pre-set histogram threshold value, this is followed by a number of morphological operations such as filling the gaps and removing disjointed particles before the final mask is obtained (A). As shown in the GUI snapshot (B) this method can account even for more challenging low density human cadaver samples

When the fracture prediction tool is used, the defined boundaries are displayed for every slice indicating the proposed edge as a thin white line superimposed on the original image (such as depicted in Figure 11 and Figure 13 (C)). The user can then determine if the boundaries have been estimated correctly, apply the self-correction subroutine, change the parameters for both subroutines and either re-run the analysis or perform a manual correction. However, it was found that the manual correction was needed only for analysis of the historical data where samples had been scanned in air without removing the air-bubbles. Since then, the self-correction subroutine was shown to be a sufficient tool for capturing incorrectly proposed boundaries.

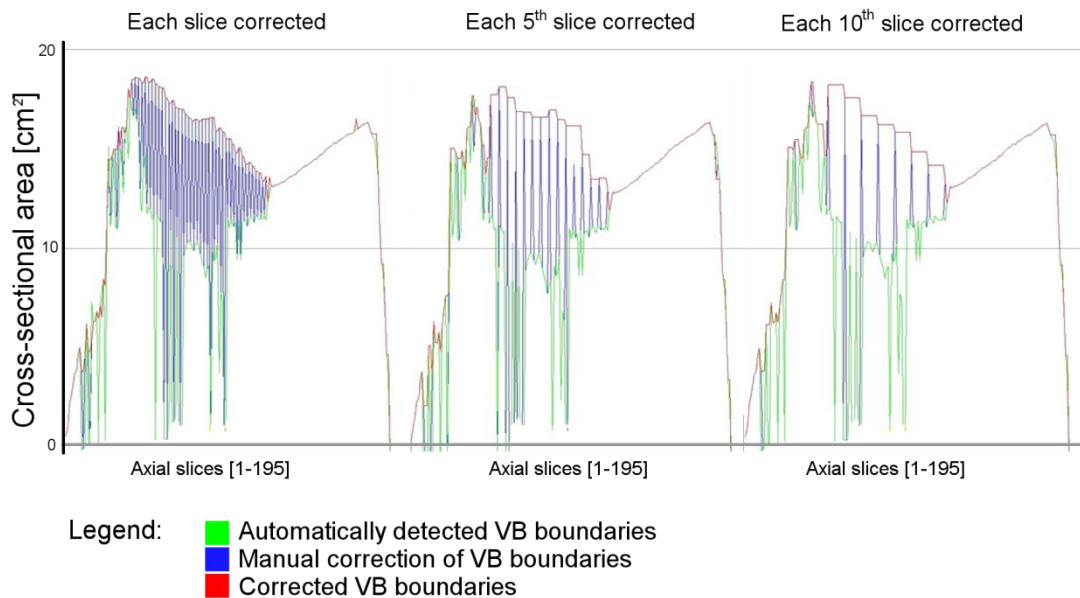


Figure 12 Manual correction of the VB boundaries combined with area-based filtering algorithm. The area-based filtering algorithm identifies slices where the pixel count of the masked area suddenly changes with respect to the previous slice. If such a step change occurs, the border is replaced with the previous one until the slice where the border area falls back into a user-specified difference between calculated cross-sectional areas is reached

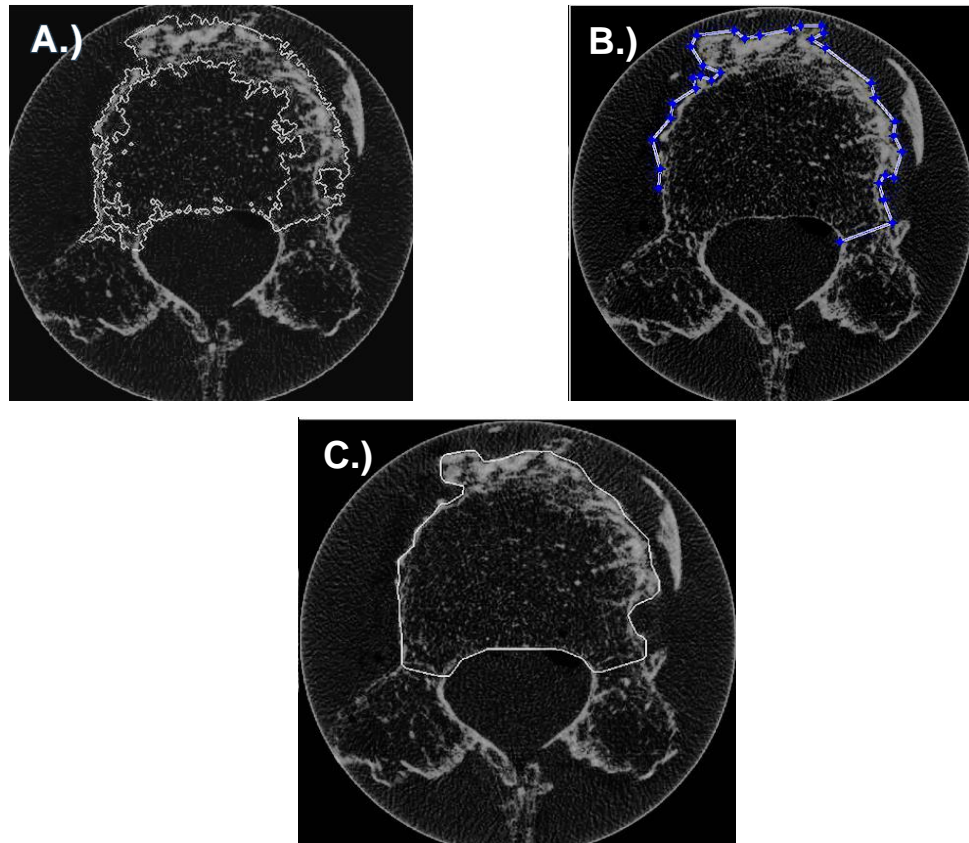


Figure 13 Manual correction of boundary outlines. In case of a “morphologically challenging” sample (e.g. very low trabecular bone density or metastasis), manual correction is required. Such a problem can occur due to a low density gradient between the bone and the background (A). In such cases manual correction (B) allows the user to correct the boundaries to include the whole vertebral body (C)

3.1.2.4 Analytical verification and surrogate model validation

In order to verify the tool, a comparison to a simplified scenario was conducted. Verification consisted of comparing estimated strength, axial and bending stiffnesses. *In-silico* and analytical values were compared firstly on samples of a simple homogeneous shape and later against a simple shape consisting of a non-homogeneous sample of up to six different material stiffnesses (Figure 14).

The results of the comparison are reported in Table 6 and show only a small difference found in EI_y and F_z . This was attributed to an error introduced by a user-based definition of the most anterior and most posterior points. This was further verified by setting the points as precise coordinates, which resulted in diminished difference between both values. The results presented here match the output values from the script, hence the script can be considered to be verified.

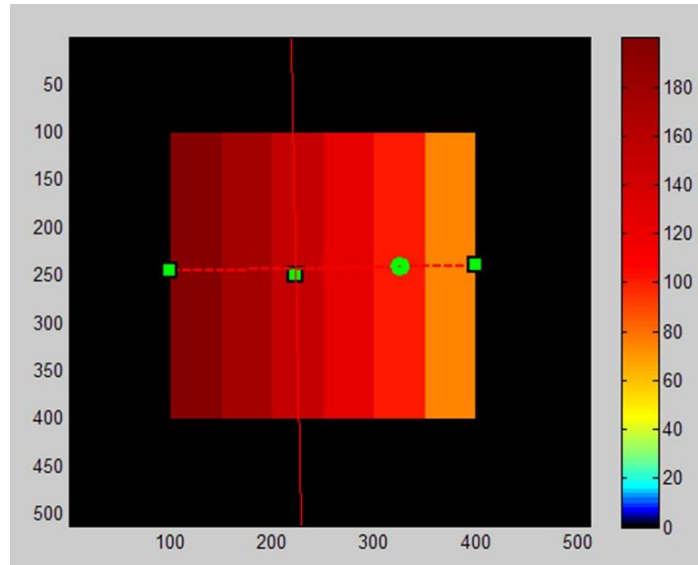


Figure 14: Analytical verification of the fracture prediction script. A false image of a sample consisting of composite layers of varying stiffnesses was imported as a simulated CT image. Points defining the AP-axis were imported manually (green markers at the margin of the composite) and load axis was defined at 25% of the AP axis (green “o” marker)

The script has been further validated using a set of surrogate models manufactured to represent infiltrated metastatic vertebra in which the strength was compromised due to location of the lesion (Figure 15). Tested plastic models were manufactured using two different prototyping methods, Stereo-lithography (SLA) and Selective Laser Sintering (SLS) prototyping methods in which the position of lytic infiltration has been altered according to a range of lesion locations. The gross vertebral body measures were taken from literature [209] and as further depicted in Figure 15 the lesion was represented as an empty void located anteriorly, antero-laterally and postero-laterally. The last model represented a non-infiltrated vertebral body without any lesion.

As a result, the predicted values strongly correlated with the experimental data (also depicted in Figure 15) for the whole range of experimentally obtained strength values (from 1.6 to 18.4kN). The strain at yield had to be adjusted to that prescribed for the Nylon 12 material ($\epsilon=22\%$) according to technical specification. However, no uniaxial tests to establish this value independently were carried out. For adjusted strain the mean difference was found to be -2.92kN with limits of agreement of ± 2.39 kN. Despite the lack of accurately measured material properties, this study showed two important findings: (1) despite the notable offset of the predicted

values, most probably due to incorrect yield strain for the particular polymeric material, it has been shown that the *in-silico* tool accounts for macroscopic imprint due to the presence of metastases with a strong correlation and (2) in agreement with other authors [210, 211], the position at which the lesion occurs leads to a significant effect in terms of the strength, which is implied by a strong correlation between predicted and experimental strength distributed from strongest (no lesion) to weakest (anteriorly-located lesion).

The experimental part of the work has been carried out by 3rd year project student, Eveline Sleiman [212]. The results have been implemented into the script and reanalysed by the author of this work. Here the experimental model has been compared to the *in-silico* approach in which the weakest slice, fracture load [kN], axial rigidity [kNm²] and bending rigidity [kN] were estimated.

	<i>In-silico</i>	<i>Paper calculated</i>
<i>EA</i> [kN]	2.7106 x10⁵	2.7106 x10⁵
<i>EI_y</i> [kNm²]	2.2430 x10²	2.2534 x10²
<i>F_z</i> [kN]	7.4963 x10²	7.5139 x10²

Table 6: Analytical verification of the mathematical solution which was used in the fracture prediction tool. Results show very negligible difference even when manual definition of AP points has been conducted (when defined numerically with pixel precision, the results were identical)

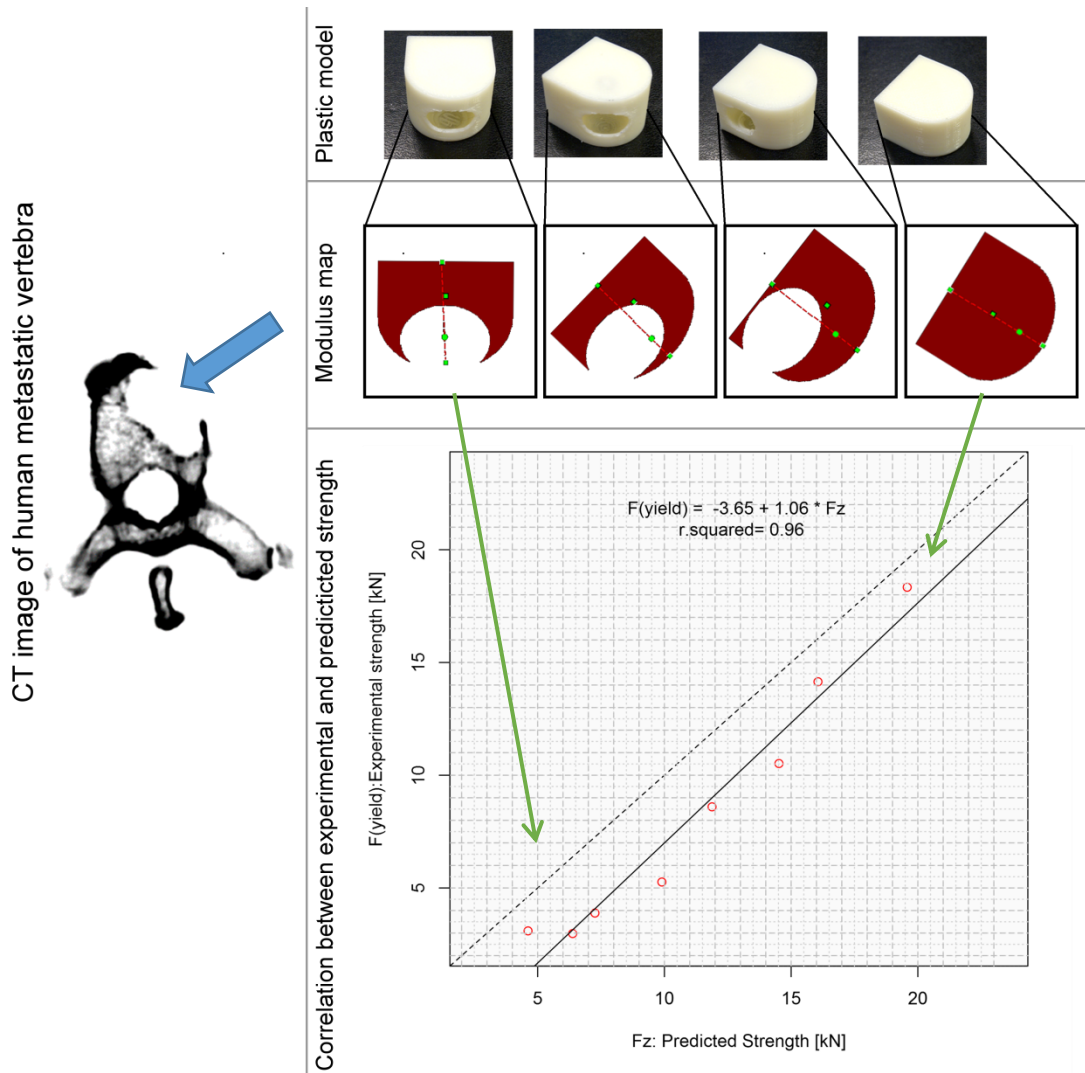


Figure 15 Validation study of the fracture prediction tool using surrogate plastic models representing different scenarios of metastatic infiltration. The blue arrow indicates metastatic infiltration in the human vertebral body modelled as a void in a simplified vertebral body. Models are listed from left to right according to their strength (anteriorly positioned vertebrae resulted in the highest strength compromise compared to healthy vertebrae on the right)

Here, finding (2) suggests that the anterior lesions have the greatest effect on vertebral strength in all investigated scenarios whereas posterior lesions have minimal or no effect on vertebral strength compromised for the investigated loading condition. These results are in accordance with the occurrence of vertebral collapse observed *in-vivo* [211]. Here both findings suggest that accounting for bending rigidity in the beam theory principle has a strong potential in vertebrae with an osteolytic reaction.

3.1.2.5 Fracture prediction tool validation using historical data

Initially, the developed fracture prediction tool was tested on samples of subjects with varying BMD distribution. This was done in order to verify the usability of the approach on oncological samples. This subsection describes data collection and retrospective use of the tool on historical data.

Fracture data and microCT images were pooled from previous studies where single vertebrae were experimentally tested to induce fracture. The collection criteria were defined thusly:

- i. A single vertebra compression wedge fracture conducted on human samples
- ii. Use of the same scanning protocol
- iii. Use of the same compression testing procedure with comparable output in terms of strength estimation

More specifically, samples were collected from studies in which all specimens underwent testing based on a single vertebra model used by Oakland, Furtado et al. [3, 38]. In this protocol, samples were disarticulated and freed of soft tissue through sequential trimming of the processes but preserving the integrity of the spinal canal by keeping the neural arch intact. All samples underwent initial microCT scanning and were subsequently fractured.

3.1.2.5.1 Collected historical samples used for validation

Pooled samples consisted of three morphologically distinct pathologies: osteoporosis, bladder cancer and multiple myeloma cancer. All specimens used for this retrospective assessment were rendered anonymous and checked for eligibility for use in this study in terms of the ethical considerations (ethical approvals 09/H1306/1, 10/H1306/60 and 10/H1306/83).

The final dataset consisted specifically of forty-one osteoporotic samples (OP) from a total of eleven spines, twelve samples from one spine from a donor diagnosed with bladder cancer with metastases to spine (mets) and finally of forty-four samples from three spines diagnosed with multiple myeloma (MM).

3.1.2.5.2 Historical data - Scanning procedure

All collected samples underwent scanning in microCT (uCT80, Scanco Medical AG, Bassersdorf, CH). The osteoporotic and bladder cancer samples underwent the assessment at a resolution of $148 \times 148 \times 148 \mu\text{m}^3$

voxel size and scanned in air, whereas the multiple myeloma samples were scanned with a final voxel size of $70.8 \times 70.8 \times 70.8 \mu\text{m}^3$ and scanned while submerged in water without applying vacuum prior to the scan. Furthermore, in all three cases the scanning parameters remained unaltered: 250 projections were used (70kV, 114mA, and 300ms) and reconstruction took place with the use of an in-built $200\text{mgHA}/\text{cm}^3$ beam hardening correction provided by the manufacturer (Scanco Medical AG, Bassersdorf, CH). All images were then converted to ρ_{BMD} using Hydroxyapatite phantom.

3.1.2.5.3 Historical data - Wedge compression fracture

The first and second datasets (OP, mets) were fractured in a custom-built testing rig and subjected to compression in a single axis compression machine (AGS-10kNG, Shimadzu Corp.). The third dataset (MM) was tested using the enhanced rig developed as a part of this work as per testing protocol described in subsection: 3.2.2.4: "Single vertebra Wedge Compression Fracture rig". In all cases the vertebral strength was taken from the first peak on the load-displacement curve (zero-slope).

3.1.2.5.4 Predicting historical data - beam theory and BMD-based method

All collected microCT images were assessed using the beam theory fracture prediction tool discussed previously. Where necessary, given the complex nature of the deterioration, a manual correction of the detected boundary was undertaken, in which case every fifth slice was corrected.

For the purpose of developing the model, multiple material laws suggested in relevant studies [200, 204, 213] have been initially tested for comparison with the model proposed by Kaneko et al. [198, 214], obtained based on metastatic and osteoporotic cored samples. The initial test was performed on a smaller number of samples (training dataset) and extended to the full population once the model with the closest agreement had been chosen.

In addition, the metastatic samples were reanalysed afterwards excluding the extra-vertebral body formations from the fracture prediction modulus map. Figure 16 depicts one of the samples containing such formations, comparing the morphological imprint of the lytic and blastic tumours. To exclude these formations, a similar tool to the one used to manually define vertebral body outlines was used to define the body without the external lesions.

The theoretical background of this assessment is that the structure is firmly attached to the vertebral body, hence is assumed to contribute to vertebral strength. According to engineering principles the osteo-sclerotic nature of the structure and its anterior position suggest that the structure will be expected to support the loads. This assumption is supported by the fact that, if the yield of the healthy and osteo-sclerotic tissue remains the same, than the bending stiffness - a significant contributor to the strength of the vertebra (subsection "Composite theory approach", eq. (1.3)) - is in fact a product of Young's modulus (density dependent variable) and distance from the neutral axis squared (eq. (1.5)). However, in tools such as those using standalone BMD without accounting for density distribution, this sclerotised tissue would not be considered, hence the strength predictions would be hampered.

Moreover, excluding (masking) of the mineralised tissue from the modulus map will decrease both the axial and bending stiffness in the fracture prediction equation. The comparison before and after the masking of the tissue from the prediction with sequential comparison to the experimentally obtained value can be then used to investigate whether the tissue is more likely to be mechanically supporting the vertebra and hence enhancing the vertebral strength.

The results of predicted strength prior to and after alteration of the masks were compared to those obtained experimentally and will be discussed in the results subsection.

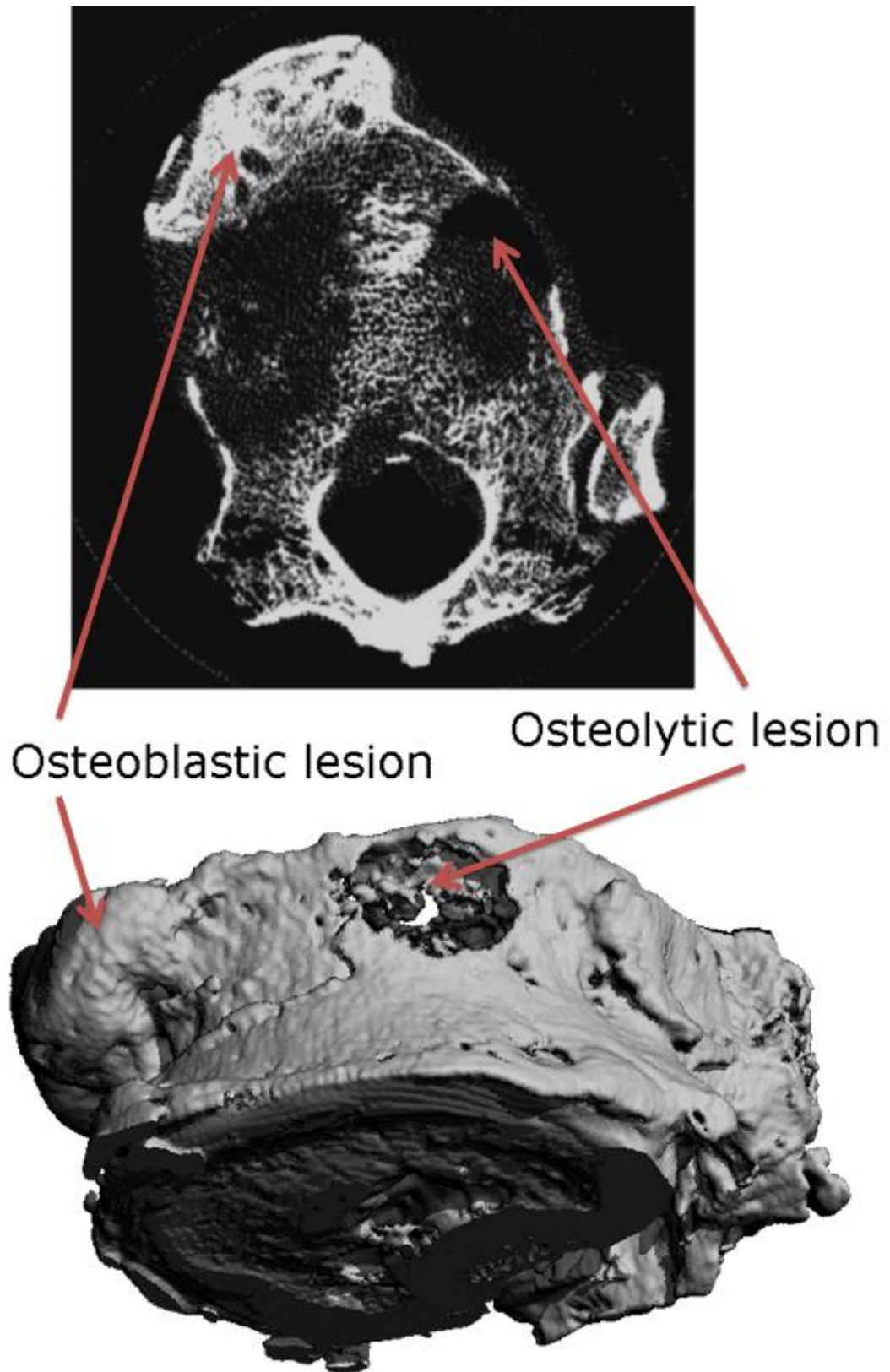


Figure 16: Example of microCT vertebral body assessment depicting severe metastatic infiltration. An axial slice obtained from microCT (above) shows a notable influence on the internal structure when mixed lesions are present. Beneath is a 3d representation of the infiltrated vertebra

3.1.3 Results in predicting historical data

3.1.3.1 Historical data – Collected osteoporotic samples

In total forty-one scans and experimental data of osteoporotic samples matching the criteria were collected for this retrospective analysis. Data from microCT scans were used to estimate fracture load based on a product of BMD and cross-sectional area and using a beam theory approach. The results of both methods were then compared to experimental compression test output. A typical output of the fracture prediction tool is shown in Figure 31, where the first slices clearly overestimate the strength due to the presence of the cortical wall. However, as the analysis takes into account only the weakest slice, an overemphasis on the strength of the bony endplates is irrelevant.

The dataset also consisted of 6 samples which showed unexpected strength (exceeding 3.9kN and up to 6.4kN). These samples were each treated in the same way in order not to bias the fracture prediction tool validation study.

With regards to the structural analysis compared to experimental data, the mean difference was -0.25kN, the limit of agreement was ± 0.91 kN (depicted in Figure 17) and the coefficient of determination R^2 was 0.93 ($p < 0.001$). In terms of accuracy, the mean difference was found to be sufficiently close to zero. The reason for discrepancy in the stronger samples originates in the nature of the location of high density bone, where the weight of each voxel of every pixel contributing to flexural rigidity is a product of density and distance from the bending axis squared. Sensitivity to any impairments of the density-to-modulus relationship or misalignment with bending rigidity is then overwhelmed by these osteophytes.

The results of the analysis based on the product of BMD and cross-sectional area proposed by Brinckmann [64] with the same apparatus show the adjusted linear interpolation coefficients ($a=0.32$ and $b=0.00308$; conducted by a former researcher from the University of Leeds using the same methodology and apparatuses [95]) to be significantly poorer in terms of both agreement and association (mean diff -0.7kN; limits of agreement ± 2.78 kN; coefficient of determination R^2 of 0.16 ($p=0.011$)). The comparison of both methods in Figure 18 displays data from which a number of observations can be made.

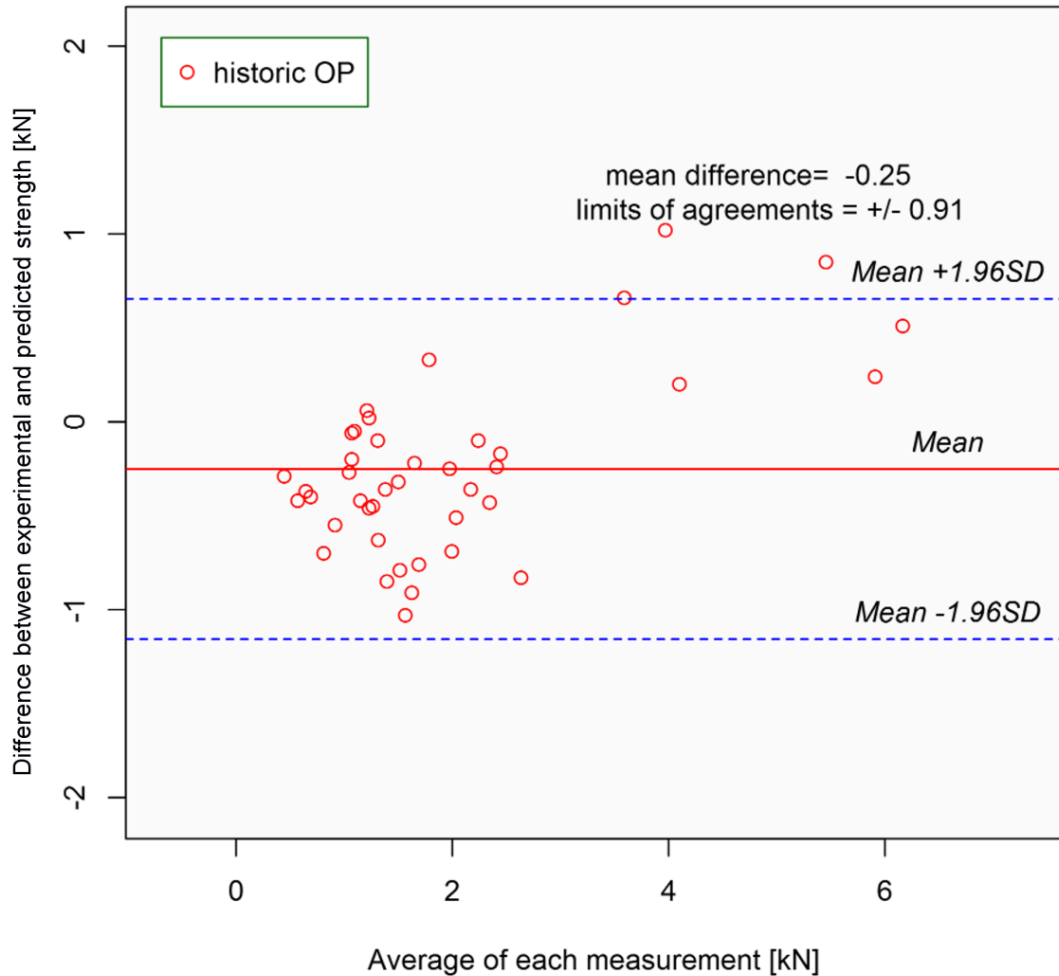


Figure 17 Bland-Altman analysis of predicted and experimentally obtained fracture loads for collected osteoporotic samples. The difference between both datasets indicates modest limits of agreement lower than $\pm 1\text{kN}$

Firstly, despite the high correlation in the structural analysis, the model tends to overestimate the failure load for small loads; nevertheless this is reversed for larger ones. The analysis based on Brickmann/Oakland's prediction [64, 95] tends to overestimate the failure loads for all samples except those where osteophytes are present.

In an attempt to discern the reasons for the discrepancy between the two models, the presence of osteophytes was investigated. First, three samples with clearly enlarged osteophytes (strength exceeding 5kN) were excluded, which altered coefficients of determination from $R^2=0.93$ to $R^2=0.83$ for the beam theory based method and from $R^2=0.16$ to $R^2=0.27$ for the BMD based method. Bland-Altman's mean difference and limits of agreement were found to be -0.31 ± 0.81 kN and -1.02 ± 1.7 kN for the beam theory and the BMD based method respectively.

Excluding additional stronger vertebrae (smaller osteophytes) altered the correlation, mean difference and limits of agreement to $R^2=0.75$; -0.39 and ± 0.6 kN for the beam theory and $R^2=0.4$; -1.2 and ± 1.14 for the BMD based method. It is interesting to note that despite the reduction in R^2 , the limits of agreement became narrower, which highlights that the use of R^2 alone is an inappropriate measure of accuracy and/or precision.

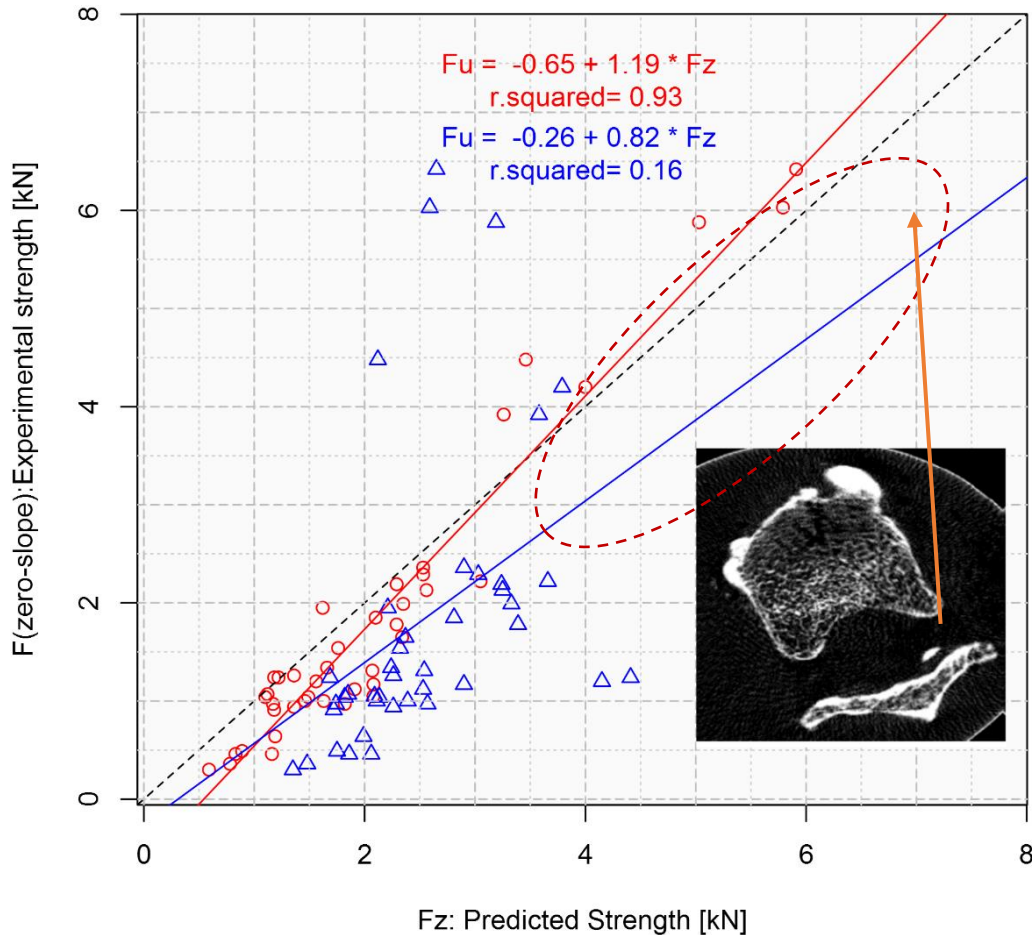


Figure 18 Plot of the predicted versus experimentally determined failure load. Beam-theory method (red “o” marker) shows good agreement and correlation in comparison to the formerly used product of BMD and cross-sectional area (blue “Δ” marker), with the example in the bottom right corner depicting a sample reaching 6.03kN strength most probably due to the presence of extra-vertebral body formations. In fact, all samples in the red-dashed area contained similar osteophytes

3.1.3.2 Historical data - Collected metastatic samples

This section introduces a retrospective assessment of twelve samples from one donor with diagnosed bladder cancer. A study in which the set of

samples was used [95] identified a notable compromise in the strength of the vertebral body, however has not adequately underpinned a relation between this and the internal structure prior to the testing and the experimental data.

The qualitative assessment of microCT images confirmed the presence of mixed lesions of severely infiltrated metastases, the majority of which appeared as an osteolytic cavity. In many cases the bone was malformed by the presence of enlarged extra-vertebral body formations such as those depicted in Figure 19. In four out of twelve specimens, notably enlarged lesions were present, in all cases in an anterior part of the vertebral body. In four other cases the osteoblastic reaction was smaller, but again present in the anterior part. In fact, the spine was affected by metastatic infiltration at all spinal levels (vertebrae) but three.

Quantitatively, the bone quality in terms of the Bone Mineral Density ranged from 78.1 to 136.1 (an average of 98.6 ± 18.1) mgHA/cm³. The vertebral body strength was unexpectedly high considering the eccentric loading and the bone quality and in terms of the zero-slope yield ranged from 1.4 to 4.2 kN (an average of 2.2 ± 0.8 kN) where the stiffness was assessed ranging from 1.0 to 2.9 kN/mm (an average of 1.9 ± 0.6 kN). The BMD as a standalone predictor failed to correlate with the fracture load ($R^2=0.09$, $p=0.349$). In addition, although the product of BMD and minCSA increased the prediction power, it still remained far below the correlation level ($R^2=0.16$, $p=0.197$).

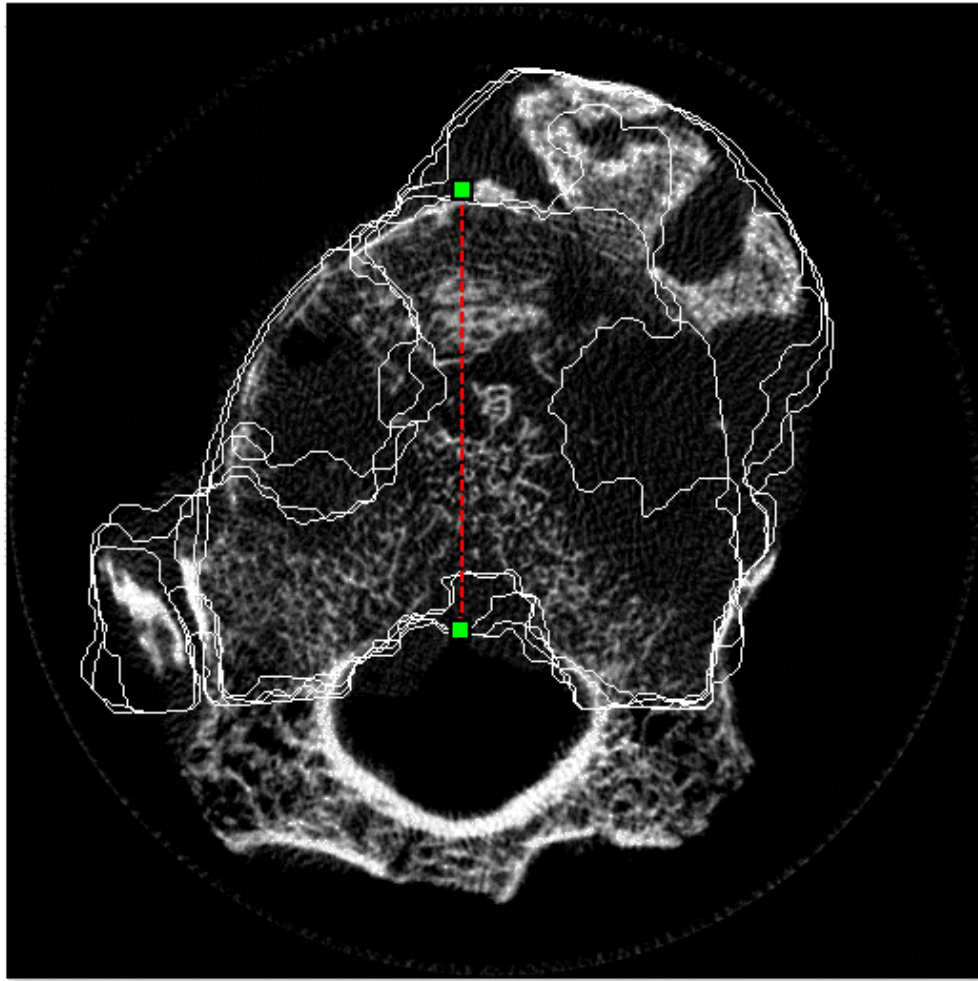


Figure 19 Example of a severely infiltrated sample containing multiple osteoclastic lesions together with extra-vertebral body formation in the anterior part of the vertebral body

Initial fracture predictions using the beam theory on average not only strongly overestimated the experimental data but also failed to correlate with the actual values. Assessment using the Bland-Altman method estimated the mean difference at -1.2kN with the limits of agreement at ± 2.7 kN, together with $R^2=0.18$ ($p=0.167$). This peculiar overestimation was in fact consistently present in specimens with a significantly enlarged extra-vertebral body formation. This was however not unexpected due to the relatively good results obtained for osteophyte formations discussed in the previous section.

A further analysis was undertaken to exclude the extra-vertebral lesions from the modulus maps which resulted in an improvement in the results. As depicted in Figure 20 the coefficient of determination improved from $R^2=0.18$ to $R^2=0.64$ ($p=0.02$), together with statistical results narrowing the limits of agreements to ± 0.96 and resulting in a smaller mean difference of -0.41 kN.

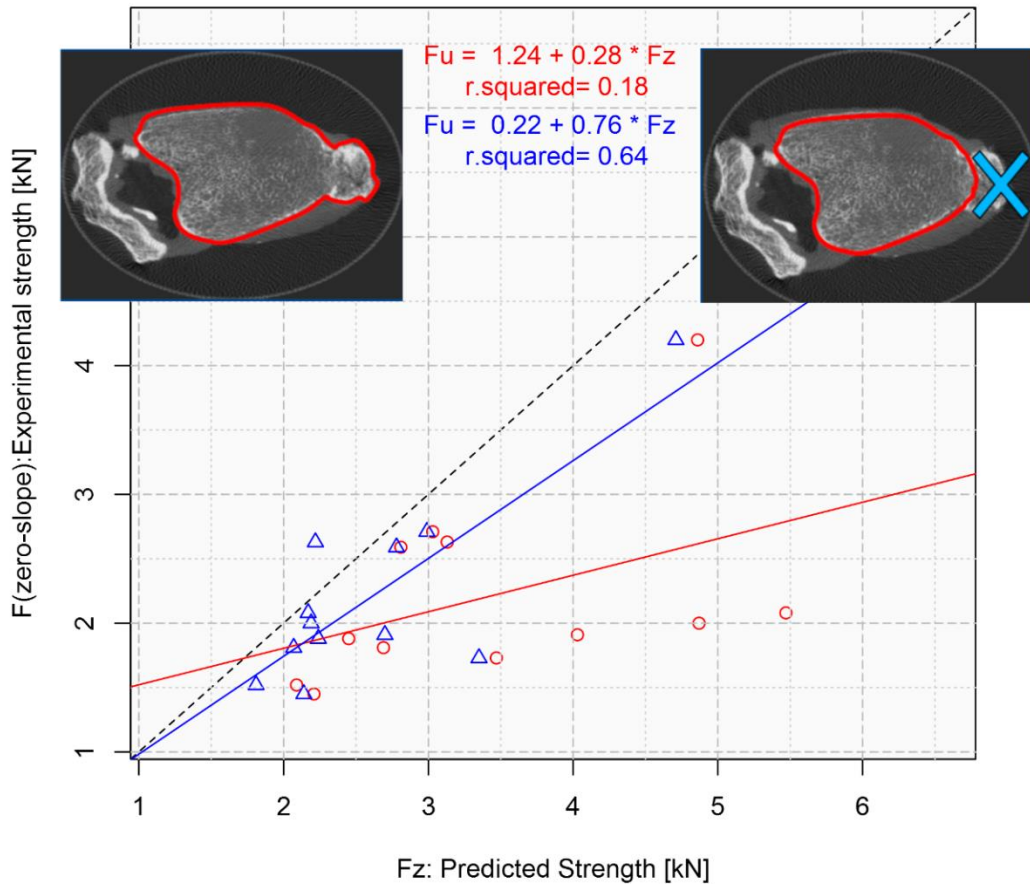


Figure 20 Twelve samples infiltrated by bladder cancer were subjected to an experimental compression test following a microCT assessment. The initial fracture prediction (red) failed to correlate with experimental values; however the correlation improved after removing the extra-VB formation (blue) from assessment

3.1.3.3 Historical data - Collected multiple myeloma samples

Analysis of the microCT assessment provided a quantitative measure of the bone quality BMD which ranged from 63.1 to 252.6 mgHA/cm³ (an average of 127.0 ± 54.7 mgHA/cm³).

When fractured, the zero-slope yield ranged from 0.3 to 7.1 kN (an average of 2.5 ± 2.1 kN), coupled with corresponding stiffness from 0.4 to 7.3 kN/mm (an average of 2.6 ± 1.9 kN). As a standalone predictor, both the BMD (R²=0.07, p=0.088) and the product of BMD and minCSA failed to show any correlation to the experimental data. As a matter of fact the minCSA together with the BMD even lowered the coefficient of determination down to R²=0.03 (p=0.277).

As depicted in Figure 21 the fracture prediction based on the beam theory shows a significant discrepancy between the spines and fails to

predict fracture with a sufficiently high correlation. In fact, the coefficient of determination for all samples altogether was $R^2 = 0.6$ ($p < 0.001$) with Bland-Altman's mean difference and limits of agreement of -1.05 and ± 2.61 kN respectively.

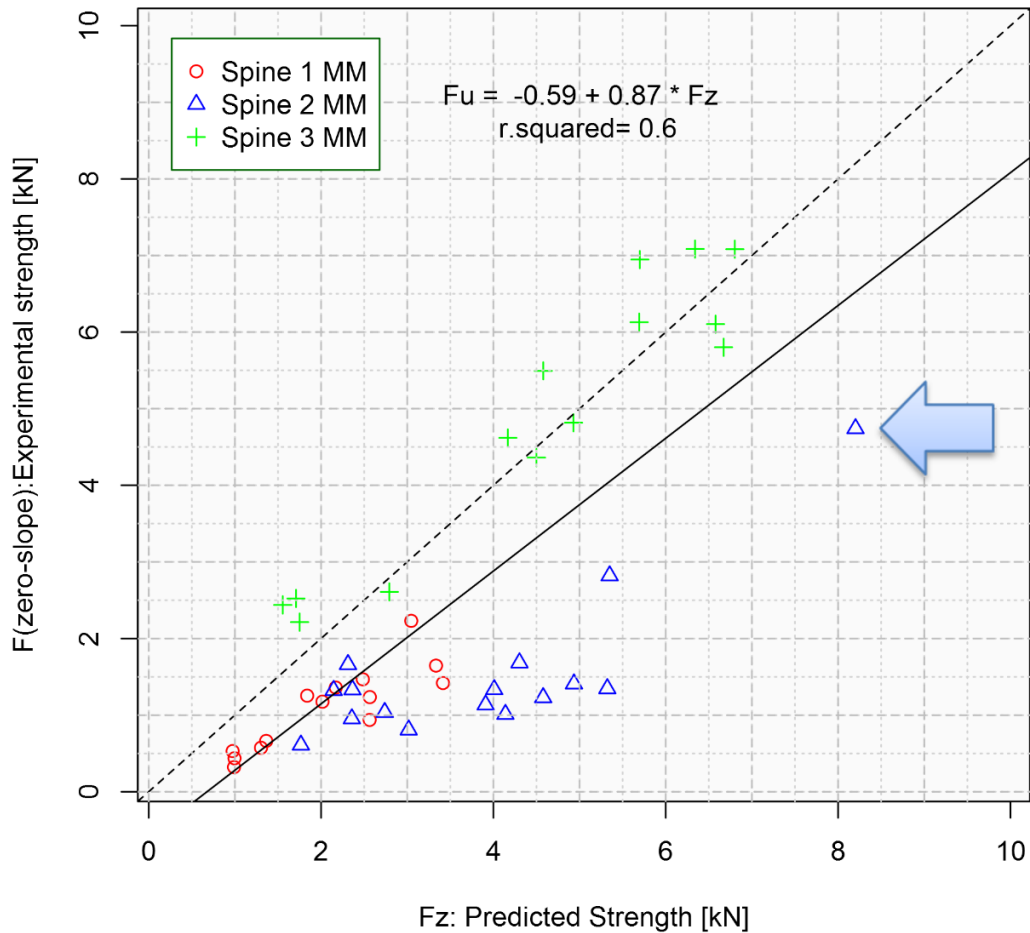


Figure 21 Experimental and predicted values of vertebral strength based on beam theory prediction. Contrasting colours indicate different spines which highlights a possible peculiarity of Spine 2 MM which has been notably and consistently overestimated

Detailed qualitative assessments of all images uncovered morphological changes in the bone structure of one outlying sample which was notably similar to the pre-existing fracture. This particular sample (Spine MM 2 - L5, indicated by the blue arrow in Figure 21) showed almost double the predicted strength at the “weakest slice” (the site at which the fracture was predicted) when comparing to experimental data (Figure 22 (a)).

Following manual exclusion of the fractured part of the vertebral body depicted in Figure 22, fracture load decreased by 20% to 6.3 kN moving

towards the experimental data and the linear regression line of the whole dataset (increase of R^2 to 0.62, mean diff -1.01, lim. of agreements ± 2.52), which underpins the necessity to carefully check samples for possible pre-existing fractures.

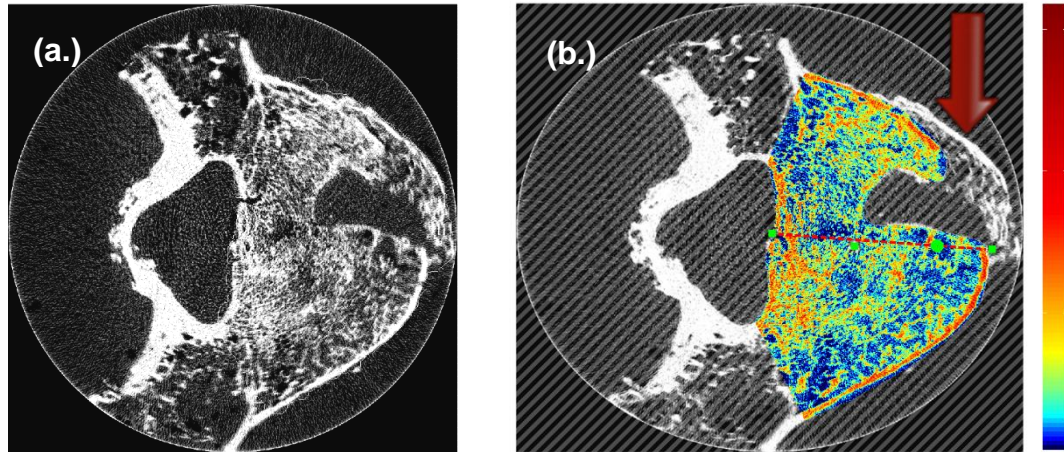


Figure 22 Initial scan of sample “Spine 2 MM L5” and modulus map masking. (a.) Possible pre-existing (not cured) fracture resulting in a disconnected piece of bone. (b.) *In-silico* masking of the disconnected element (indicated by the red arrow) enabling an assessment of the contribution to the strength of the sample

3.1.4 Initial validation using historical data - Discussion

3.1.4.1 BMD based prediction used on historical data

In agreement with data presented by other authors [170, 215], the preliminary data presented in this work indicated that using simplistic principles of the mechanics of solids such as those proposed by Brinckmann et al. [64] is not sufficient for any investigated loading scenario which introduces large bending moments. The prediction of vertebral strength based on a sample of averaged trabecular bone mineral and endplate area represents, from an engineering viewpoint, a model that is more adequate for an accurate assessment of the compression strength because it does not account for flexural stiffness. Unlike similar data reported while exhibiting a minimal cross-sectional area [65, 167], data presented here did not correlate with experimental data, which can again be explained by the fact that the experimental setup substantially contributed to bending. Moreover, since bone quality declines preferentially in the central region of the bone [216], the fact that the relative thickening of the cortical bone was not accounted for in this simplistic model hampers predictions in subjects with (1) higher bone

mass [217-219], (2) osteophytes as presented in this study, and (3) in non-uniformly distributed bone deterioration such as oncological patients.

3.1.4.2 Image processing and density-to-modulus material model

The structural assessment tool proposed in this work consisted of a series of steps which have been previously discussed. Prior to the strength assessment, each slice was masked to determine the boundaries of the vertebral body. Here, a series of documented morphological operations which processed the binary image have shown to provide a good compromise in terms of boundary detection which is sufficiently accurate in a sufficiently short time in terms of volume estimation, even when using a standard desktop PC (detailed flowchart can be found in Appendix H: Image processing: vertebral body boundary estimation).

Compared to other possible solutions using masking such as edge detection, gradient based masking or shape recognition [220-222], the approach used in this work has been found to be computationally straightforward with a relatively low time dependency. In fact, the time required in order to provide an estimation of the vertebral body boundary used in this work has been optimised and reduced to less than 2 minutes per sample, and additionally validated for accuracy and precision in a buoyancy experiment. Nonetheless, as presented here, the user here needs to rely purely on a GUI providing a slice by slice assessment to show whether the cross-section of the vertebral body has been estimated correctly or whether the secondary filtering based on a step-change in the cross-sectional area is accurate. Furthermore, this work has presented a manual correction which has been demonstrated to be particularly useful in morphologically deformed samples where the lesion has breached the cortical wall. Despite provision of this alternative, the use of a GUI and secondary filtering seemed to be sufficient for the majority of the close to two hundred samples presented in this study.

Throughout this work it has been hypothesised that the bone quality remains unambiguous throughout the organ and hence the density-to-modulus material model does not need to be adjusted. As presented by Wolfram et al. [36], who experimentally investigated osteoporotic bone by means of micro-indentation, the micro-properties of the bone correlate weakly in respect of their position within the vertebra as well as between different vertebral levels. The unambiguousness of cancer bone however remains unknown and will be verified later in Chapter 4 independently of the development of this fracture prediction tool.

3.1.4.3 Validation of the fracture prediction tool on historical samples

The model presented in this study was used throughout the initial testing and structural assessment of human vertebrae with three different pathologies sampled from other investigators (not published). Here, the assessment of the complete dataset has shown that the strength of the vertebral body can be predicted with a relatively high correlation and sufficiently narrow limits of agreement. A structural compromise (strength) was predicted in axial slices obtained from a tomography assessment. Similarly to previous investigators [2] it has been hypothesised that fracture would occur when the bone yields under compression by more than 1%, as has been measured by Keaveny et al. [195] and that this would occur at the structurally weakest slice, determined by the stress distribution exhibited under the effects of the Euler–Bernoulli beam theory. To the author's knowledge, this is the first work to adopt the use of a composite engineering principle on isolated vertebrae with a wide variety of experimental datasets and exhibiting different types of cancer.

For osteoporotic samples the image-derived prediction was able to account for as high a variation as 93% in results in which predicted strength was the independent variable, which is in a range comparable to sophisticated FE models [168, 169]. The prediction in metastatic samples was initially hampered by the presence of both osteolytic and osteoblastic lesions which has been overcome by removing the osteoblastic lesions from the modulus maps. These improved results have shown that the developed tool can account for 64% of the variability of fractures in samples with severe metastatic infiltration due to bladder cancer. Despite the need to predict the wide range of possible causes of failure, the model has proved to demonstrate a good precision in terms of the limits of agreement which have been maintained for both pathologies under $\pm 1\text{kN}$, which is in range of many sophisticated models (see Table 4, literature review section 2.6.2). The range of R^2 is understandable given the range of experimental strength and is below presented elsewhere. The state of deterioration however hampers the possibility of comparing the results as such samples have, to the author's knowledge, never been predicted for fracture using FE or any other engineering model.

An assessment of historical samples from patients with diagnosed multiple myeloma cancer proved to be far less successful compared to an assessment of osteoporotic samples. Here, the dataset which consisted of three spines showed that the strength of the regression of the predicted

forces contributed to a moderate 62% in the variability of the results, and despite strong inter-patient variability the data remained within the limits agreement of $\pm 2.5\text{kN}$ which is lower than most of the compared models (Table 4 in literature review section 2.6.2), but in the same range as the very sophisticated FE model [172] and the minCSAxBMD model proposed by Crawford et al. [65]. An over-predicted spine denoted as Spine 2 MM did not in fact show any peculiar morphology and its increased BMD, appearing as a notable thickening of the trabeculae, could not be considered sufficient reason to exclude the spine from analysis. Here only one sample could be justified to be reanalysed with caution and manually improved for accounted boundaries due to the discovery of a pre-existing fracture. The possibility to thoroughly investigate the nature of the discrepancy was hindered due to the retrospective nature of the dataset and the fact that they had been scanned with a lower number of projections.

In terms of accuracy, the predicted strength in all three pathologies was found to be in relatively good agreement with experimental testing. In particular, the osteoporotic and metastatic datasets were found to have been predicted with mean differences of -0.25 and -0.45kN respectively. The most notable difference in mean has been found in the multiple myeloma dataset, again due to the presence of Spine 2 MM.

Based on these initial results three assumptions have been made: (1) the material model proposed by Kaneko was adopted and thereafter used in all three studies with a sufficiently good outcome in terms of prediction, suggesting that it can be also used further; (2) the use of microCT assessment of 0.148mm edge voxel size and lower produced sufficiently accurate predictions when accounting for both geometry and the BMD; and (3) the dataset should not contain samples with pre-existing fractures.

3.2 Commissioning of cadaveric Wedge Compression Fracture testing rig

3.2.1 Introduction to cadaveric testing of human samples

This section describes an *in-vitro* approach to induce a vertebral fracture similar to fractures found *in-vivo* (illustrated in Figure 24 (A)). Wedge compression fractures are categorised as anteriorly collapsed vertebral bodies [109] and are characterised by a decreased vertebral height in the anterior region of the vertebral body. Using imaging tools such as CT, X-ray or DXA, the fracture is also visible as a densified region of bone where

trabeculae have compacted, locally increasing the volume fraction (Figure 23).

To reproduce the fracture, the vertebral body needs to be compressed by applying an eccentric axial load (Figure 24). This can be achieved using a single axis compression device with a ball-joint loading plate compressing, eccentrically, one of the endplates at a constant low speed displacement (quasi-static testing).



Figure 23 Wedge compression fracture in-vivo and in-vitro simulated WCF. All fractured vertebrae found in spines had a characteristically deformed vertebral body towards the anterior side (example in A). This type of fracture (WCF) is typical for osteoporotic/metastatic bone

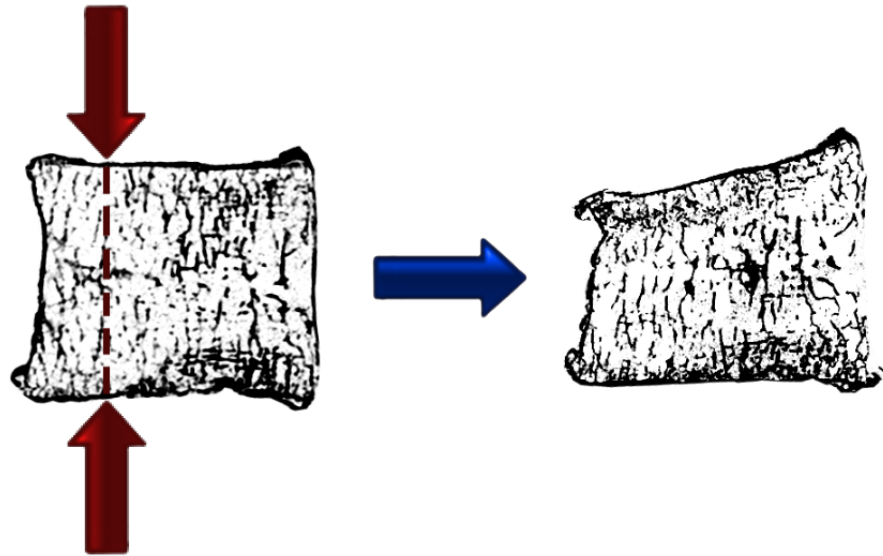


Figure 24: WCF type of fracture can be obtained experimentally where an intact bone is compressed eccentrically. This figure illustrates a sagittal slice of vertebra scanned in microCT image before and after inducing the fracture

3.2.2 Wedge compression testing - Methods

3.2.2.1 Cadaveric sample selection and preparation

Samples used in this study comprise of three distinct pathologies. The first comprised samples without any signs of neoplastic pathology (considered by the GIFT bank as osteoporotic), the second comprised those diagnosed with multiple myeloma cancer and the last came from patients with cancer with a high probability of osteolytic infiltration to the spine. In total, one hundred and ten samples were used in this study, all of which were acquired from a non-transplant tissue bank (GIFT, Leeds General Infirmary, UK and Science Care®, AZ, USA) following ethics committee approval (NRES, UK). More specifically, thirty-two samples from three osteoporotic spines were collected for PVP-CaP study (Ethical approval: 10/H1306/83), and twenty-five samples from five osteoporotic spines and twenty-four metastatic samples were collected for PMMA study (Ethical approval: 11/YH/0002). An additional ten samples from metastatic spines were harvested and used for morphology and fracture prediction assessment (Ethical approval: 10/H1306/83); and finally, nineteen samples from four spines with diagnosed multiple myeloma cancer were collected and used for morphology and fracture prediction assessment (Ethical approval: 10/H1306/60). The two metastatic spines were collected from

donors with (j) metastatic inflammatory carcinoma (breast cancer) and (ii) metastatic lung cancer. In total four single vertebrae samples needed to be excluded, more specifically one due to loss of measurement data during the experiment, two due to pre-existing fractures sustained after harvesting and one due to technical difficulties experienced during the re-fracture experiment. To clarify, a list of all studies and number of specimens used is included in Table 7 while Table 8 presents the list of all used spines together with their properties.

Study	Pathology	Number of spines	Number of samples collected	Number of samples excluded	Number of samples used in fracture prediction	Number of samples used in PVP
PVP-CaP	OP	3	32	3	29	29
PVP-PMMA	OP	5	25	1	25	24
	mets	2	34	0	34	24
Fracture prediction	MM	4	19	0	19	0

Table 7 Cadaveric samples collected and used for wedge compression fracture testing

	Spine gift bank name	Levels used	Age	Gender	Weight	Height
SpineBS 1	Gift 29/11	T7, T8, T9, T10, T11, L1, L2, L3, L4	88	F	54 kg	170 cm
SpineBS 2	Gift 13/11	T8, T9, T10, T11, T12, L1, L2, L3, L4, L5	82	F	51 kg	160 cm
SpineBS 3	Gift 32/11	T6, T7, T10, T11, T12, L1, L2, L3, L4, L5	72	F	51 kg	168 cm
SpineGo 1	S091157	T7, T8, T9, T10, T11, T12	66	F	36 kg	157 cm
SpineGo 2	C100098	T7, T8, T9, T10, T11	93	F	68 kg	168 cm
SpineGo 4	S091223	T7, T8, T9, T10, T11	102	F	61 kg	168 cm
SpineGo 5	GIFT 20/11	T7, T8, T9, T10, T11	74	F	108 kg	170 cm
SpineGo 6	GIFT 23/12	T7, T8, T9, T10, T11	77	F	38 kg	171 cm
Spine 1 mets	C121608	T1, T2, T3, T4, T5, T6, T7, T8, T9, 10, T11, T12, L1, L2, L3, L4, L5	41	F	73 kg	170 cm
Spine 2 mets	C121562	T1, T2, T3, T4, T5, T6, T7, T8, T9, 10, T11, T12, L1, L2, L3, L4, L5	85	M	43 kg	168 cm
Spine 4 MM	C101540	T5, T7, T8, T9, T10, L2, L5	68	M	68 kg	170 cm
Spine 5 MM	S101357	T8, T10, L2, L5	82	M	77 kg	178 cm
Spine 6 MM	S110132	T5, T7, T8, T9, T10, L2, L5	90	M	67 kg	170 cm
Spine 7 MM	S110807	L5	60	M	113 kg	175 cm

Table 8 List of all spines used for wedge compression fracture testing

3.2.2.2 Tissue collection, dissection and storage

Work done by Panjabi et al. [223] showed little or no influence of freezing on the change in quality of the cadaver tissue, hence all samples were kept frozen before dissection, after dissection and during every longer period between treatments. Human cadaver samples were either collected from the local GIFT bank, frozen and stored at -80°C or in the case of an

overseas donor tissue bank (ScienceCare, USA), samples were collected from a sealed parcel covered in dried ice. For long term storage, the samples were kept deep frozen at -80°C , while for imminent use the samples were placed in a freezer at -20°C and later defrosted overnight for either dissection or testing. For storage, every sample was fully wrapped in a purified water-soaked paper tissue to retain moisture and was sealed in a labelled plastic bag before being returned to the freezer. Samples were harvested from thawed spines where every sample was carefully disarticulated (Figure 25) using standard dissection and operation tools. The samples were then initially measured with Vernier callipers (part no. 50590, Draper, UK) and prepared for scanning.

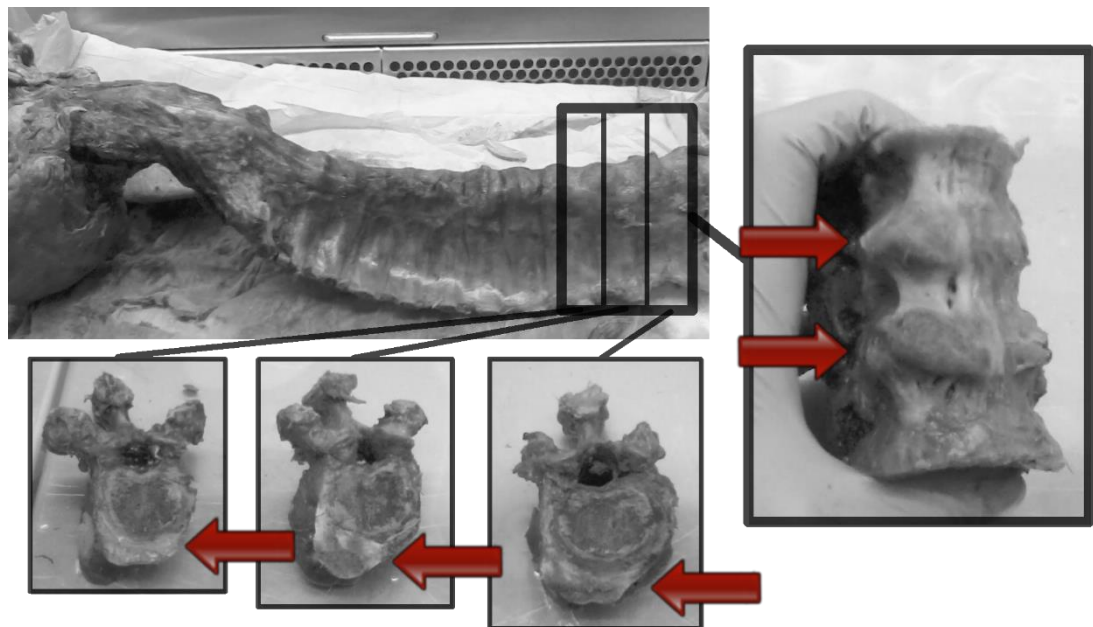


Figure 25: Harvesting of vertebral samples. The figure depicts disarticulation of levels T10, T11, T12 (from left to right) with enlarged bridging osteophytes (“Spine 2 mets”)

3.2.2.3 Cadaveric sample scanning

Prior to scanning every sample was separately placed in an appropriate scanning container fully submerged in purified water under vacuum for 5 minutes to remove any possible air-bubbles trapped in the bone marrow (CCL-31 vacuum pump [Javac, UK]). Using the vacuum pump prior to scanning and increasing the scanning resolution compared to previous studies was necessary in order to increase the spatial information obtained from the scanner especially for the morphology assessment and also as it was found that air bubbles trapped in the vertebral body strongly hamper accurate BMD measurements. Where necessary, the facets were

removed to allow the sample to remain anatomically horizontal during the scanning, but the neural arch remained intact.

All samples in this section underwent scanning in the most up-to-date microCT apparatus (microCT100, Scanco Medical AG, Bassersdorf, CH) at medium resolution of $70.8 \times 70.8 \times 70.8 \mu\text{m}^3$ voxel size with 500 projections (at 70kV, 114mA, and 300ms), with subsequent $1200 \text{mgHA}/\text{cm}^3$ beam hardening correction provided by the manufacturer (Scanco Medical AG, Bassersdorf, CH). All images were then converted to ρ_{BMD} using Hydroxyapatite phantom ranging from -200 to $800 \text{mgHA}/\text{cm}^3$.

3.2.2.4 Single vertebra Wedge Compression Fracture rig

The wedge compression testing rig was designed to produce fractures similar to the methods of previous investigators [3, 28, 29, 38, 66]. In addition displacement transducers were added based on the SpineFX collaborating partner TUVienna [66]. The rig was designed to fit the Instron uniaxial compression testing machine (model 3366, Instron, MA, USA), which was firmly attached to the frame to allow the maintenance of a fixed loading axis during testing. This design enabled more accurate positioning and a repeatable and stable mounting protocol. Further, the design allowed a quantitative measure of the boundary conditions through the attachment of three linear variable differential transformers (LVDT). According to Dall'Ara et al. [66] the more accurately known boundary conditions are of a great value when combining experimental data with numerical approaches such as FEA. Nevertheless in this study, the LVDTs were used only to verify whether the inclinations of the sample remained within the safe limits for the duration of the testing procedure.

The enhanced rig comprises of a base mounted to the testing machine, three LVDTs (ACT1000A, RDP Electronics Ltd, UK), a recess where the sample is positioned and a steel loading plate compressed by a ball-joint attached to the cross-head of the machine (depicted in Figure 26 (A)). The axial load was measured using a 10kN load-cell (Part no. 2530-443, Instron, MA, USA) fitted between the ball-joint and the cross-head of the compression machine.

The loading scenario combined an axial compression with bending by introducing an eccentric loading. Therefore, the bottom of the vertebra was firmly embedded whereas the top endplate was covered by a PMMA impression to compress the sample without inducing tension on the back of the vertebral body (depicted in Figure 26 (B)).

After the sample preparation described previously each specimen was prepared for testing by partial embedding to increase the reproducibility of the experimental setup. In order to position and embed the sample a custom-built rig was designed (Figure 27 (A)). This rig allows the positioning of the loading axis of the compression device with a point on the top endplate of the vertebral body representing 25% of the antero-posterior vertebral depth without the offset. Adjustable screws were used to restrain the sample in an aligned position (Figure 27 (B)) and it was later placed into a DELRIN ring and using a dental plaster (Suprastone, Kerr, CA, USA), embedded to the level of the plastic ring corresponding to submerging the samples 5mm into the plaster (Figure 27 (C)). When cured, the sample was turned and dipped into semi-cured PMMA (WHW Plastics, Hull, UK) to make a loose impression for the top contact (Figure 27 (D)).

The embedded sample was positioned into the compression rig (model 3366, Instron, MA, USA) and the crossbar with fitted pointer was lowered to verify the correct position of the loading. Later the pointer was replaced with a ball-joint and the vertebra was covered by the PMMA impression with the top loading plate placed over the top. In order to allow unrestricted movement of the two surfaces over each other, a thin layer of grease was inserted between the PMMA and the steel plate. Figure 28 illustrates the full experimental setup during the compression testing.

The testing machine was controlled using software provided by Instron [224]. The protocol consisted of preloading the sample by 50N for 5 minutes with subsequent compression at a 1mm per minute stroke to 75% of the average height of the original sample. When reaching the pre-set deformation, the sample was released at 1mm per minute stroke until reaching 50N again and held in that position for an additional 10 minutes before the test was finished. Once removed from the compression rig, the plaster base was removed with subsequent measurement of the VB dimensions taken before freezing.

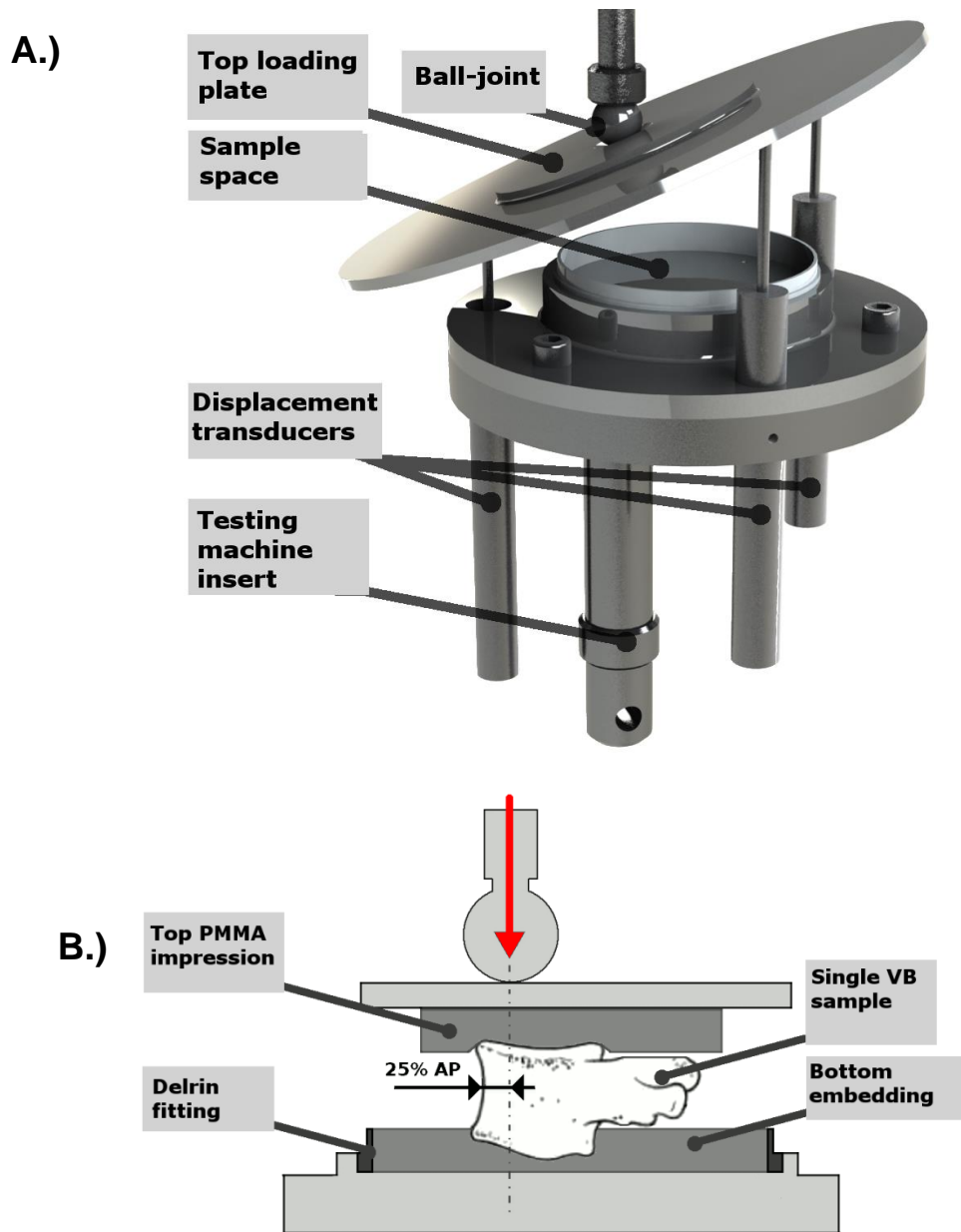


Figure 26: The enhanced single vertebra compression rig, an illustration of a CAD model (A). The rig consists of a base fitted into the frame of the Intron testing machine and 3 precisely positioned LVDTs to capture the change in inclination of the top loading plate, compressed by the ball joint driven by the cross-head. The bottom figure (B) illustrates schematically the positioning of the sample. The sample is aligned in the recess using a Delrin fitting and dental plaster embedding. The top PMMA imprint allows loading of the sample without introducing tension on the posterior part of the vertebral body

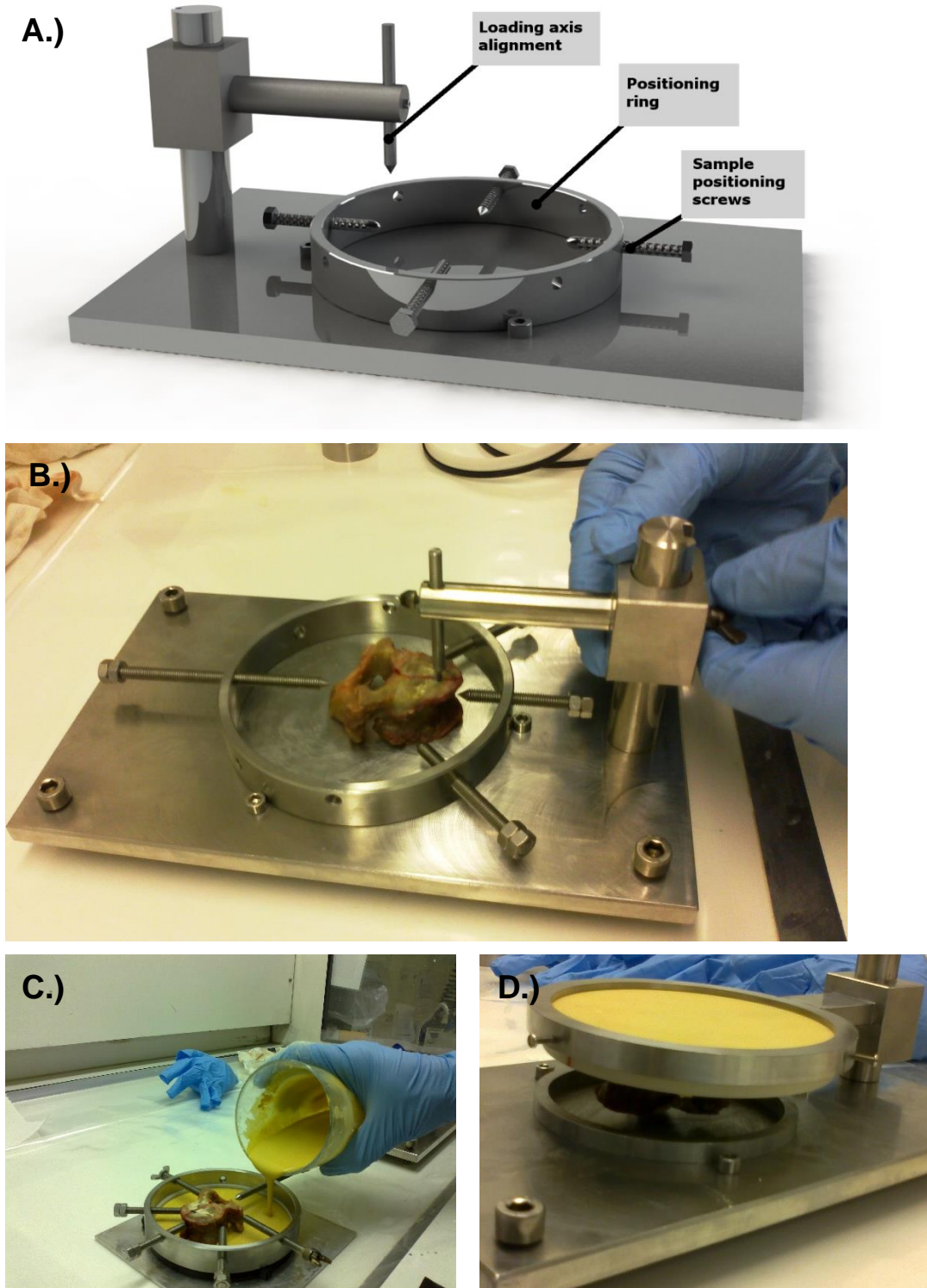


Figure 27: Single vertebra mounting rig. The top illustration (A) represents a CAD model of the mounting rig designed to position and embed the sample prior to testing. Subsequent images represent positioning which allows aligning with the loading axis (B), embedding of the bottom endplate (C) and making an impression of the top endplate (D)

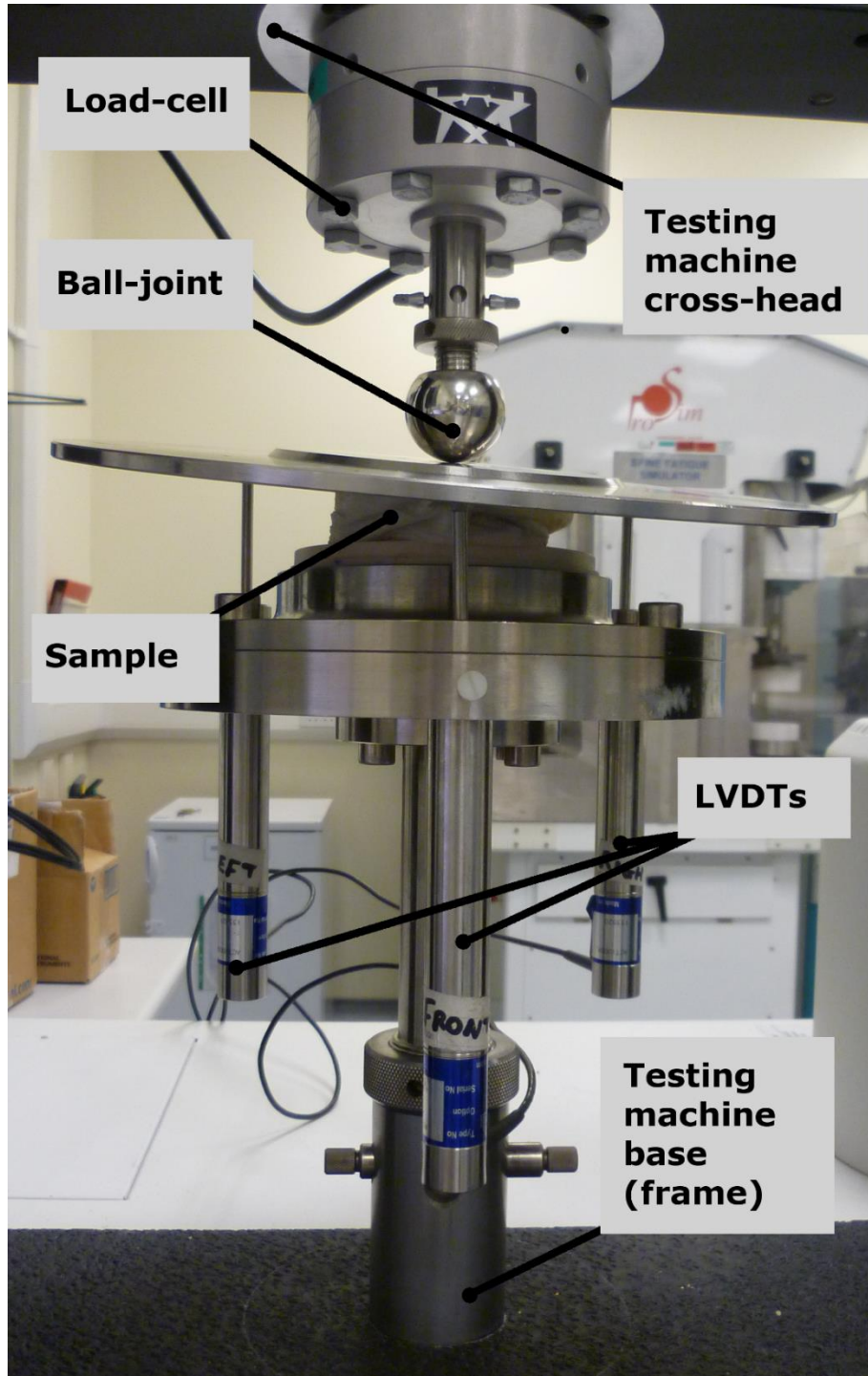


Figure 28 Testing rig mounted to uniaxial compression machine (Instron). Sample wrapped in a purified-water-soaked tissue is compressed between the top loading plate and the bottom part of the rig. While the bottom of the sample is partially embedded and the coupling between the cross-head and the loading plate is performed by a ball joint, the loading axis remains at the same position while the loading plate is allowed to tilt around this axis

Vertebral stiffness was defined as the maximum slope within the elastic region of the load-displacement curve from the experimental data post-processed in a custom-compiled MATLAB code [208]. The slope was defined using a 1% strain window approach based on the previously validated method proposed by Buckley et al. [148], whereas the vertebral strength was ascertained using a proof-load approach at 1% of the total strain.

3.2.3 Fracturing of cadaver samples - Results

Following the microCT assessment all samples from the previous section underwent experimental testing to induce WCF. This section aims to present the cadaveric experiment in detail for each of the three pathologies tested.

3.2.3.1 WCF in osteoporotic samples

The average specimen height was 22.9 (± 4.9), 25 (± 3.8), 23.5 (± 4.2), and 23.1 (± 3.7) mm at anterior, posterior, right and left margin of the endplate respectively, while the average width was measured as 39.1 (± 8.2), 34 (± 6.3) and 42.1 (± 8.6) mm at superior, middle and inferior levels respectively. The anterior-posterior length of the endplates was 31.5 (± 3.8) for superior and 32.1 (± 3.2) for inferior. Lastly the offset (overhang) was on average 3.1 (± 1.7) mm.

A typical single vertebra wedge compression fracture experiment lasted 1 hour for embedding followed by an imminent compression experiment lasting on average 20 minutes during which the specimen was kept moistened by paper soaked in purified water resulting in a typical experimental output as depicted in Figure 29.

To induce the wedge fracture by compressing each vertebra by 25% of its average height, the specimens were compressed on average by 5.9 (± 1) mm. The average strength was measured as 1.35 (± 0.91) kN and ranged from 0.34 to 3.55 kN. The average stiffness was 2.2 (± 1.0) kN/mm and ranged from 0.7 to 5.3 kN/mm.

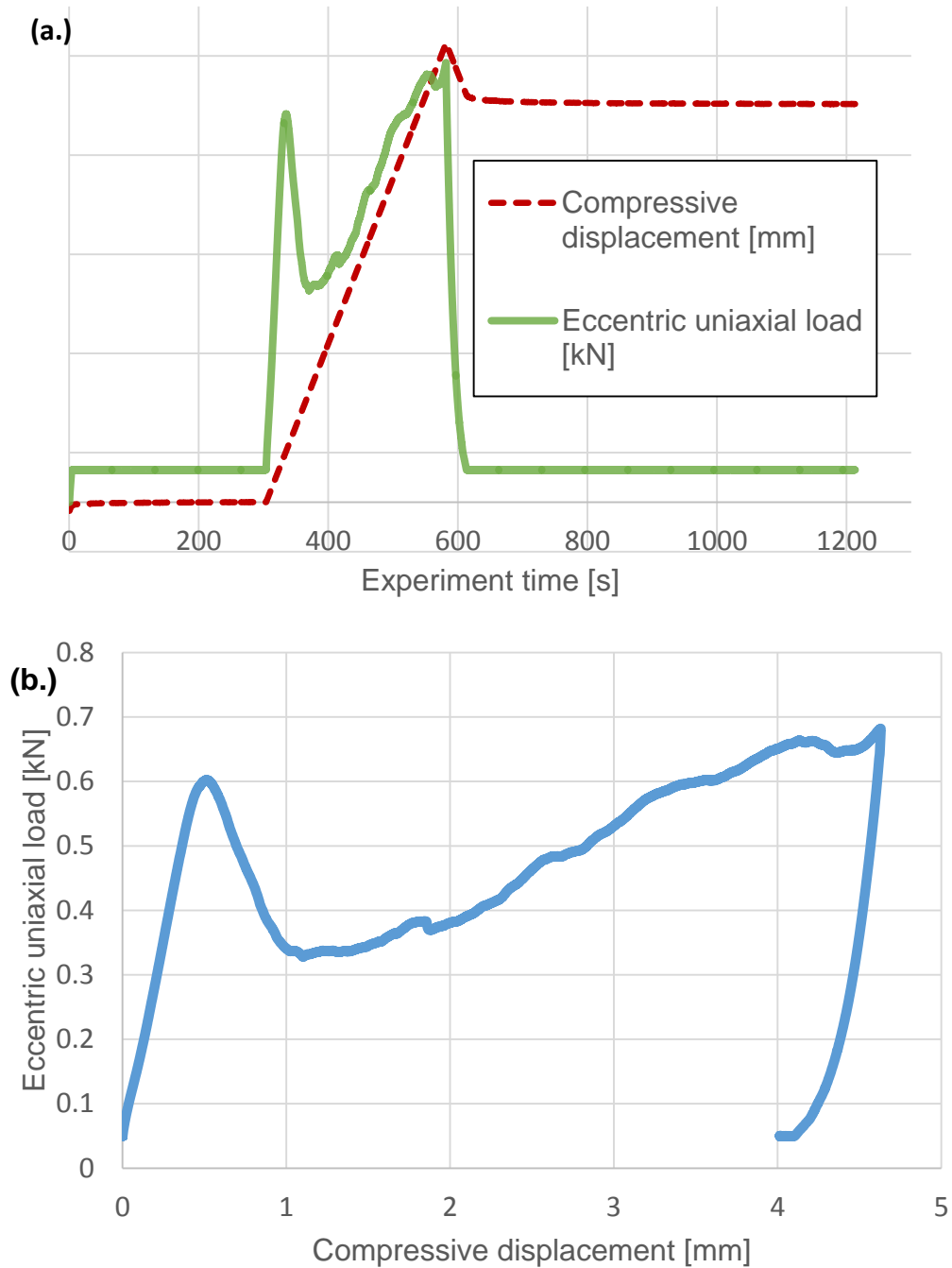


Figure 29 A typical vertebral compression test data readout as a function of time (a.) later compiled in a form of load-displacement curve (b.). The curve is characterised by an initial ramp-up sequence reaching a load of 50N which is maintained for 5 minutes to simulate preloading conditions and allow the specimen to settle in the mould. When loaded at constant rate, the sample typically remains in the elastic region until yielding to the plastic region where fracture is followed by a short softening. The end-point of the experiment was at 25% strain followed by a 10 minute relaxation period at 50N (initial fracture, sample Spine BS 3–T10)

As verified by post fracture measurement, the reduction of the height remained over 20% even after the relaxation period, which resulted in an increase of the angle between superior and inferior endplates from 3° to 11° (note that the anterior height was in most cases smaller compared to posterior height, which is typical for osteoporotic samples).

For samples SpineBS 3 - T09 and T08 the initial scan identified possible pre-existing fractures. Both specimens were hence dissected, cleaned and measured following the same protocol as for the other samples. As shown in Table 9, the anterior height of the fractured T09 was notably lower than other specimens from the same spine (namely specimens from levels T06, T07, T10, T11, T12, L1, L2, L3, L4 and L5), however the second sample with a possible pre-existing fracture (T08) had been fractured to such an extent that no vertebral body could be used for measurement as both endplates separated immediately after dissection.

	Height anterior	Height posterior	Height left	Height right	Width superior	Width middle	Width inferior	Ant-Pos superior
SpineBS 3 - T09	8	20	17	13	37	32	41	30
Spine BS 3 average T6-L5	22.7 (±4.3)	24.8 (±2.8)	22.8 (±2.9)	22.8 (±3.1)	42.9 (±10.2)	39.5 (±8.3)	46.8 (±9.3)	33.3 (±5.1)

Table 9 Cadaveric VB outer morphology measurement – sample with pre-existing vertebral body fracture

3.2.3.2 WCF in multiple myeloma samples

Eighteen samples from four spines with diagnosed multiple myeloma cancer were disarticulated and underwent compressive testing in the same conditions as the other pathologies. Here, the average strength was 2.73 (±1.17) kN, ranging from 1.31 to 5.47 kN. The average stiffness was 3.46 (±0.96) kN/mm and in range from 2.13 to 5.06 kN/mm.

3.2.3.3 WCF in metastatic specimens

Metastatic samples in this study consisted of 2 spines and were disarticulated into a total of thirty-four single vertebrae. The average specimen height was 22.8 (±5.2), 23.2 (±4.2), 22.3 (±4.3) and 22.8 (±4.5) mm in the anterior, posterior, right and left sides of the endplate respectively,

while average width was measured as 36.2 (± 10.0), 32.4 (± 7.4) and 38.5 (± 10.7) mm at superior, middle and inferior levels respectively. The anterior-posterior length of the endplates was 29.6 (± 7.6) mm for superior and 30.5 (± 7.5) mm for inferior. Lastly the offset (overhang) was on average 4.1 (± 2.8) mm.

To induce the wedge fracture by compressing each vertebra by 25% of its average height, the specimens were compressed by an average of 5.7 (± 1.1) mm. Following the strength and stiffness assessment, the average strength was measured as 2.86 (± 1.33) kN and ranged from 1.02 to 5.57 kN. The average stiffness was 3.57 (± 1.40) kN/mm and ranged from 1.24 to 6.60 kN/mm, as shown for the example of Spine mets 1 in Figure 30 describing strength and stiffness for each corresponding level (other tested spines in Appendix E: Cadaveric testing: Strength/stiffness per level).

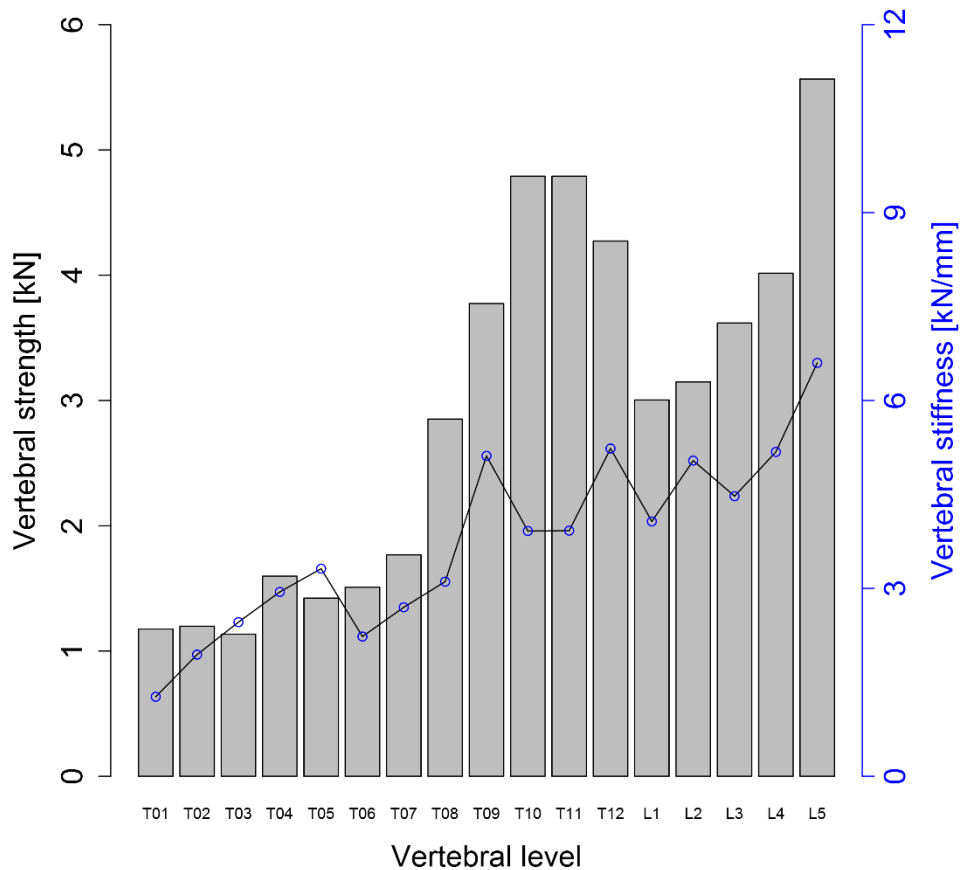


Figure 30 Spine 2 mets: Initial strength and stiffness for corresponding spinal level

3.2.4 Initial fracture of tested samples - Discussion

3.2.4.1 WCF testing protocol

The eccentric loading used in this work may also have introduced out-of-axis parasitic loads and moments which might have impaired the measured uniaxial load used to estimate the fracture load, although a uniaxial load cell is a reliable means of measuring load. For future experiments it is highly recommended to use a six-channel load cell which is to be attached from underneath the testing base to capture and quantify these loads.

Uniplanar motion which is expected during the wedge compression failure has been incorporated by a strongly eccentric anteriorly-located loading axis, ensuring that the axis of the minimum principal moment of inertia is closely aligned in the sagittal plane. In addition LVDTs were used to record any extensive tilting which did not occur in any of the 107 samples tested. Moreover, the anterior fracture was visually confirmed after completion of the test and the deflection of the endplate towards the anterior cortex was measured by the change of height of the anterior part of vertebral body by callipers. Contrary to the FE analysis, this is a necessary requirement for the beam theory principle as the most distant fibre is theoretically expected to be most subjected to yield. For example, as noted by Dall'Ara et al. [167] from their samples: only “*most of the vertebrae underwent an anterior wedge-shape fracture*” which could lead to a decrease in the prediction power of the beam theory, however it remains relatively easy to capture using the FE model presented in the study. This limitation can be avoided when considering bi-axial eccentric loading and asymmetric beam theory (discussed in Appendix G: Bi-axial eccentric loading)

3.2.4.2 Limitations of the sample population and treatment history of the donors

In the study presented here, the test population consisted of an osteoporotic group of relatively elderly patients (median 79.5 ± 12), where all eight spines were from female donors, contrary to the multiple myeloma test group where all four relatively elderly donors (median 75 ± 13) were male. In fact, the metastatic group consisted of only two donors, a relatively young female (aged 41) and an 85 year-old male. Although this is a relatively narrow demographic, osteoporosis predominantly affects women. Selecting a wider demographic in oncological pathologies is a challenge shared by

many other oncological studies [2, 67, 147, 198, 225] due to the limited availability of samples.

Concerning the level selection, the samples were harvested only from the thoraco-lumbar region due to clinical evidence proving that vertebral fractures typically occur between T6 and L3 [1, 226]. In fact, the samples discarded from this study due to the presence of pre-existing fractures (Spine BS 3: T8, T9) can confirm findings presented in a previous study [1] which reported that T8 and T9 are the most common levels on which fractures can develop. This study consisted of one hundred and seven vertebral bodies from which nearly 80% were between the range of T6 and T10, which is in fact more than in many other studies [167, 169, 170, 172].

The major limitation of the dataset population presented here is the limited information available about treatment history prior to the death of the donor. Each GIFT bank provided samples together with a tissue transfer agreement containing basic information such as primary cause of death and basic information of the most important treatment modalities used. The current standard of collecting the data however does not cover the requirement of recording all drugs administered prior to tissue collection, including drugs promoting bone growth such as bisphosphonates (list of available information for this study is provided in full in Appendix C: Donors' medical records available for this study). This limitation including a link to bisphosphonates will be later discussed in the micro-indentation study (section 4.2.4).

3.3 Fracture prediction tested on large sample population: three pathologies

3.3.1 *In-silico* vs. experiment strength comparison

This section presents the results of the composite beam theory fracture predictions and compares these *in-silico* predictions to the results of the cadaveric testing discussed in section 3.1.

The intention of this study was to investigate the vertebral strength in terms of the comparison between predicted and real experimental data. Although beam theory has already been used in previous studies, it has never been tested on a large data population comprising different pathologies. In this section the vertebral strength of each sample has been predicted in a reduced range of vertebral body height (80%) with a material model identical to one which is used in historical data assessment. MicroCT

scanned images (described in section: 3.2.2.3) were processed individually providing the predicted strength. This value was then compared to the experimental strength obtained per protocol described in 3.2.

3.3.1.1 Reducing fracture prediction range to a single slice

Although the principle of the beam theory is based on selecting the slice with a minimum predicted fracture load (weakest slice), the preliminary results discussed previously (section 3.1) have shown a notable pattern in the location of the weakest slice in a majority of cases (as shown in the illustrative Figure 31 in which different assessment ranges are defined). Structural weakening, which was observed as a fall in predicted strength, was appearing consistently in the middle section between cranial and caudal endplate. This in fact can be explained by the presence of increased bone density around posterior elements and closer to both endplates.

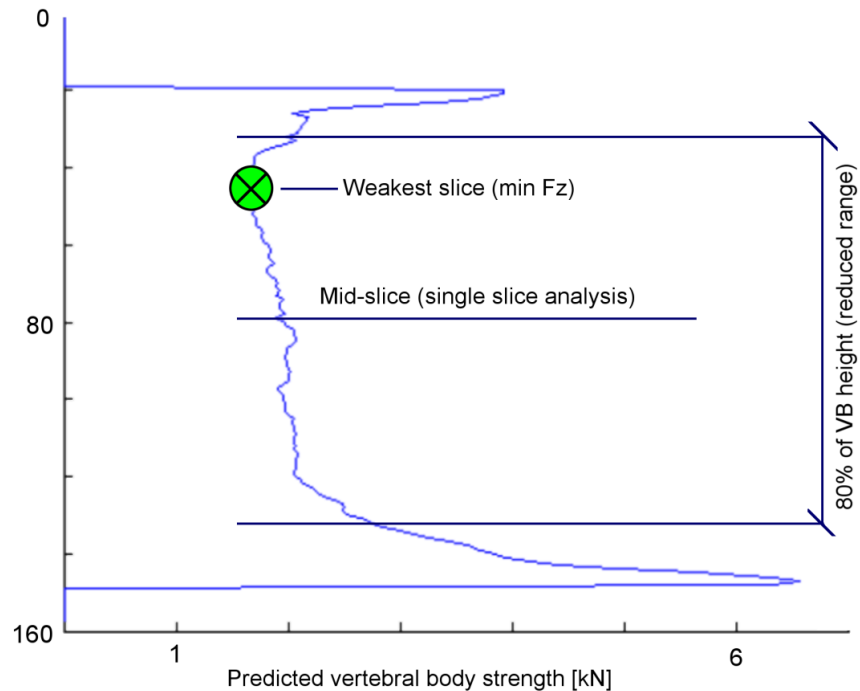


Figure 31 A characteristic slice-by-slice fracture load prediction identifying the weakest slice where each step on the y-axis represents analysis of one axial CT slice. It should be noted that the weakest slice appears predominantly in the mid cranio-caudal section of the vertebral body which allows minimising of the range of analysis excluding bony endplates. The typical prediction curve is characterised by the low degree of variability of predicted strength within the vertebral body. Mid-slice analysis could then provide sufficient illustration of degree of vertebral strength compromise with minimal time and scanning effort

This section aims to investigate the possibility whether one-slice analysis could predict vertebral strength with relative success under an assumption that deterioration of bone is heterogeneously distributed. Whether the degree of decreased prediction success falls in a reasonable range remains dependent upon a specific use, but could be highly beneficial in cases where exposure of the sample should be minimised from the whole vertebral body scan to a single slice. This preliminary investigation can be potentially useful in clinical application due to radiation safety requirements. Moreover, the mid-slice is relatively easy to identify with a relatively high repeatability in a very short time.

3.3.1.2 Density-to-modulus model calibration

The material model of the relationship between microCT derived density (ρ_{BMD} [mgHA/cm³]) and elasticity modulus (E [GPa]) is an important factor in the calculation of both the axial and the flexural rigidity and hence the predicted fracture load. Correlation has been proved in numerous publications and was thoroughly discussed in the literature review, however as noted for example in literature review by Helgalson et al. [189], finding an appropriate material model from literature data remains challenging as authors state: “The proposed relationships are substantially different one from the other”. The preliminary stage of this work was conducted on five different material models from literature [149, 198, 200, 204, 205, 213] comparing the difference in agreement to the respective dates of the literature. The best agreement for converting CT density to Young’s modulus was found by far to be the use of the model in the form described by Kaneko et al. [198] to eq. (1.8) and eq. (1.9). This model in fact seemed to be appropriate as the same author compared osteoporotic and metastatic tissue to find no significant difference between the two pathologies.

$$\rho_{ash} = 69.8 + 839 * \rho_{CT} \quad [\text{g/cm}^3] \quad (1.8)$$

$$E = 10.88 * \rho_{ash}^{1.61} \quad [\text{GPa}] \quad (1.9)$$

Nonetheless, this section aims to expose this model to a sensitivity study in order to calibrate the density-to-modulus in terms of agreement between predicted and experimentally obtained data. Such a procedure is a common tool to deploy and show full potential of a proposed model [169, 189, 227].

In summary, the density-to-modulus model (in form of eq. (1.4)) described in subsection: 3.1.2.1 was tested on the full sample population used in the main framework of this work while varying the linear coefficient

“b” and power-law coefficient “c” from 1-11 and 1-3, respectively. Over one thousand models have been tested in one-slice-analysis discussed later (in total over one hundred thousand single vertebra fracture predictions) and compared to the experimental data. Each dataset has been tested in respect of coefficient of determination, mean difference and limits of agreement. The proposed model was considered as the one which fits the criteria of exhibiting the lowest mean difference and limits of agreement with respect to “c” in a range not extensively varying between the three tested pathologies.

3.3.2 Comparison between predicted and experimental data – Results for three pathologies

3.3.2.1 Predicted osteoporotic samples

3.3.2.1.1 Weakest slice selected from 80% of vertebral body height - OP

For the *in-silico* analysis, no sample exhibited notable difficulties in automatically recognising vertebral body boundaries as is made clear by the example in Figure 32 depicting the initial scan of the weakest slice coupled with the modulus map. Despite a two-fold increase in resolution (74 μ m voxel edge size) compared to the historical osteoporotic dataset (148 μ m voxel edge size), all samples were processed in a relatively short time (~5 minutes per sample using a personal laptop computer).

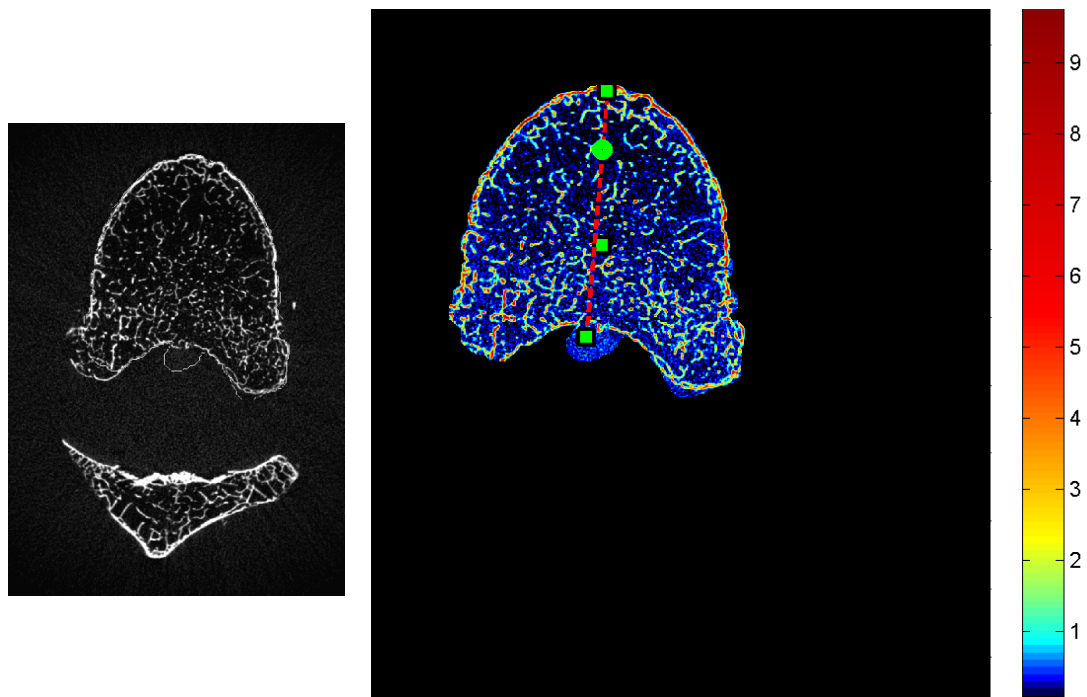


Figure 32 Structural assessment of the osteoporotic sample. On the left is a microCT image of the weakest slice identified by the fracture prediction tool. On the right is the corresponding modulus map

The predicted values were in the expected range between 1.24 to 8.85 kN (mean 3.28 ± 1.62 kN). With respect to experimental data as shown in Figure 33 and Figure 34, the mean difference between the predicted values and actual yield strength was -1.93 kN, with limits of agreement ± 2.02 kN and coefficient of determination $R^2=0.66$. Flexural and standalone compressional rigidity were found to only weakly correlate with the strength ($R^2=0.4$ and $R^2=0.38$ respectively). All evident outliers from Figure 33 and those confirmed from the Bland-Altman plot (Figure 34) consisted of samples from SpineGo 4.

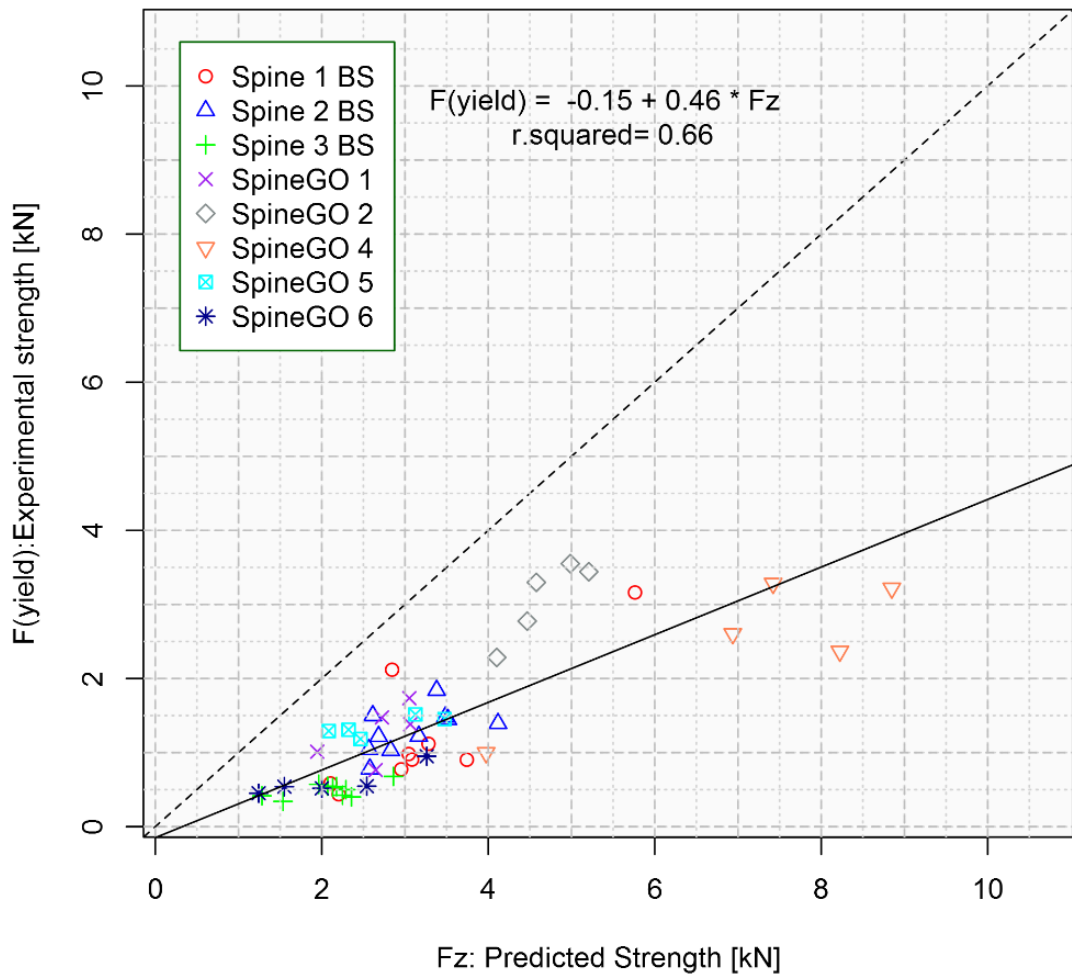


Figure 33 Fracture prediction - osteoporotic samples: Eight spines (fifty-four samples) were experimentally tested and compared to the predicted vertebral strength

Here, in an attempt to discern the causes of poor correlations, each spine and all coefficients of determination for Fz, EI and EA were examined separately. A statistical analysis of SpineGo 4 by itself showed a relatively high coefficient of determination ($R^2= 0.75$, $p= 0.057$), but with a substantial mean difference of -4.59 (limits of agreement ± 2.31 kN) compared to the

rest of the spines (on average -1.61 and ± 0.89 for mean difference and limits of agreement respectively).

By removing SpineGO 4 from the overall analysis, the R^2 increased to 0.75, and the mean difference improved to -1.66 together with decreasing the limits of agreement back to the expected ± 0.97 kN.

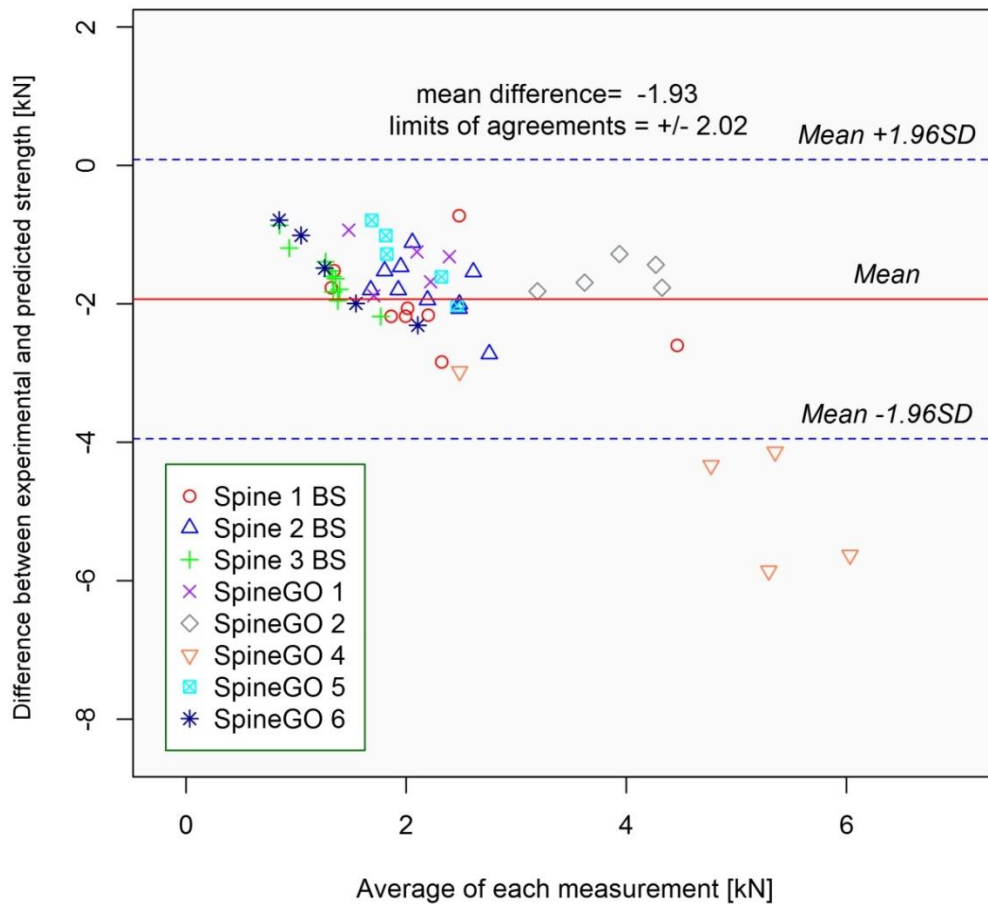


Figure 34 Fracture prediction - osteoporotic samples: Bland-Altman plot indicating a large discrepancy due to outliers belonging to a single donor (SpineGo 4). Peculiarity of SpineGo 4 could not be assessed but was believed to come from presence of healing woven bone which appears high in mineral component but lacks the structural integrity of fully healed bone (typical for early stage of healing)

3.3.2.1.2 Single slice analysis tested on osteoporotic samples - OP

In the second step, the range of slices used to determine the vertebral strength was reduced to a single slice in the middle section of the vertebra. The merit of this step was to reduce the time required as well as the need for computational power, which has resulted in less than 1 minute per sample

as only one set of two-dimensional image data was processed at one point. Compared to the “weakest slice” approach, the coefficient of determination was reduced by 12% ($R^2= 0.58$ ($p<0.001$)) with a moderate shift in mean difference by 25% remotely from a 1-1 agreement, along with widening the limits of agreement to ± 2.97 kN. This again was improved by removing SpineGo 4 from the assessment ($R^2=0.64$, mean difference: -2.07 , limits of agreement: ± 1.47).

3.3.2.1.3 Material model calibration in osteoporotic population

When the whole dataset has been reanalysed to identify the pathology specific material model the R^2 ranged between 0.59 and 0.67 and the mean difference between -4.7 and 1.1 kN while limits of agreement was limited to between ± 1.0 and ± 4.2 kN. The calibrated model has been selected as $b=3.5$, $c=1.25$ to meet agreement criteria with the same “c” coefficient. This resulted in $R^2=0.66$ with a mean difference of -0.14 kN and limits of agreement at ± 1.03 kN.

3.3.2.2 Predicted multiple myeloma samples

3.3.2.2.1 Weakest slice selected from 80% of vertebral body height - MM

A qualitative assessment of the microCT images uncovered a wide range of localised trabecular bone deterioration from smaller confined lesions (Figure 35) to a complex corrosion of the internal structure (Figure 36). Despite the compromised bone quality, the automatic vertebral body assessment was in most of the cases suitably efficient in estimating the outer boundaries which helped to process the images in a much shorter time (~ 7 minutes per sample).

Despite the compromised quality of the bone, the predicted values were notably higher in comparison to osteoporotic samples and ranged between 1.86 to 8.56 kN (mean= 4.57 ± 1.93 kN). With respect to the experimental data, the mean difference between the predicted values and actual yield strength was -1.84 , with limits of agreement ± 1.94 kN and coefficient of determination $R^2=0.83$. Flexural and standalone compressional rigidity were found to correlate with strength, with coefficients of determination $R^2=0.62$ and $R^2=0.73$ respectively. As depicted in Figure 37 the data were equally spread along the range without any obvious outliers however suggesting a systemic error in the agreement between predicted and experimental strength.

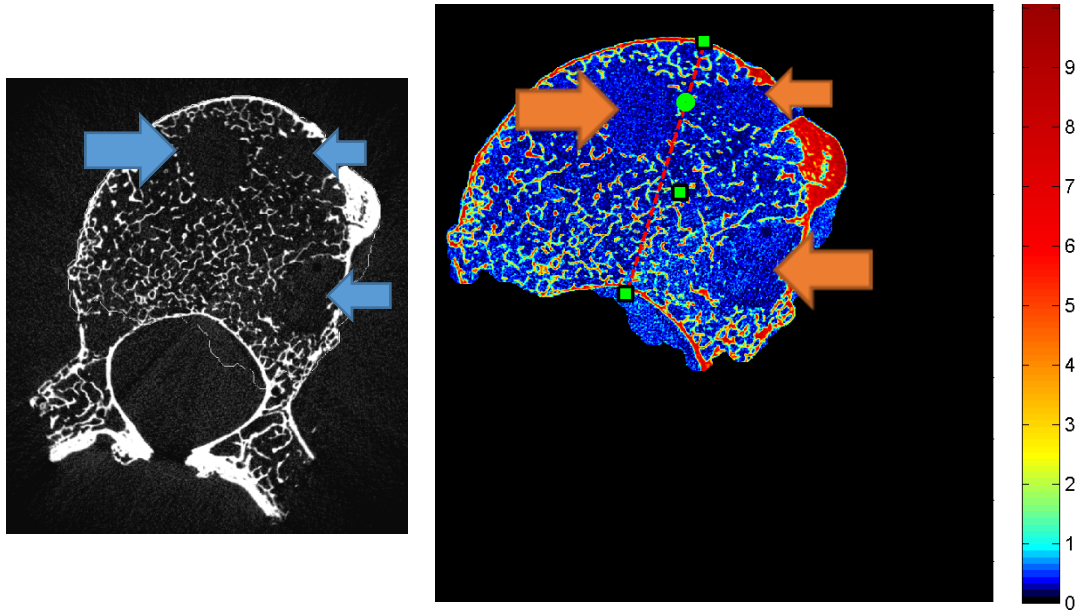


Figure 35 Structural assessment of a multiple myeloma sample. On the left is a microCT image of the weakest slice identified by the fracture prediction tool. On the right is the corresponding modulus map. The arrows indicate widespread multiple myeloma lytic lesions. Here the lesions filled with material with low mineral density result in a low modulus ($E=f(\rho)$) hence negligibly contributing to the wedge compression strength

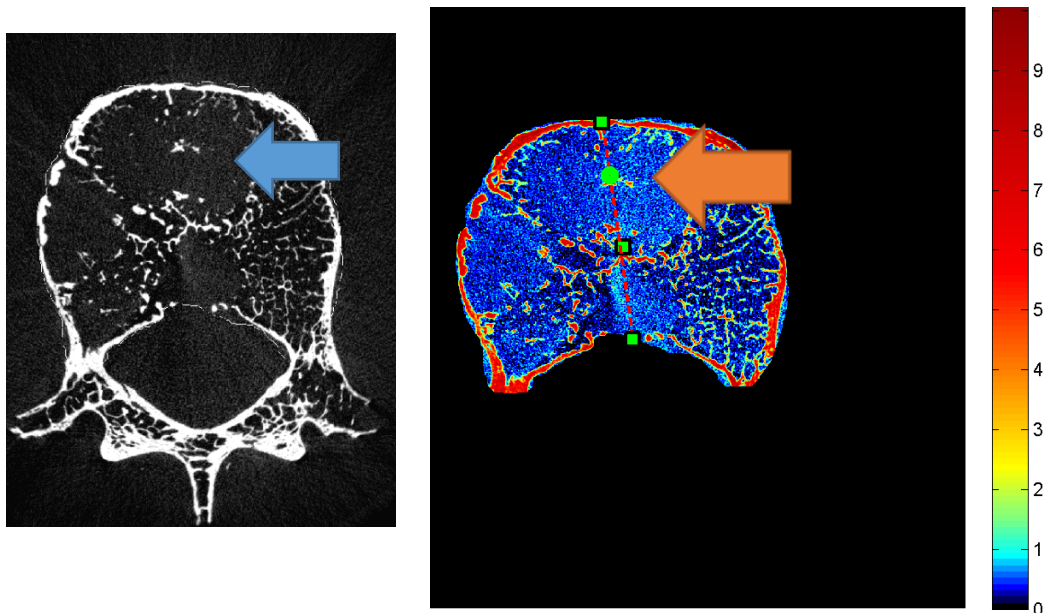


Figure 36 Structural assessment of multiple myeloma bone with severe infiltration causing disintegration of the natural structure of the trabecular bone

3.3.2.2.2 Single slice analysis - MM

Markedly, the reduction of the analysed range of slices to a single slice assessment did not impair the R^2 (single slice $R^2=0.82$), and despite altering the mean difference by 21% to -2.24 kN, it altered the limits of agreement only moderately to ± 2.18 kN.

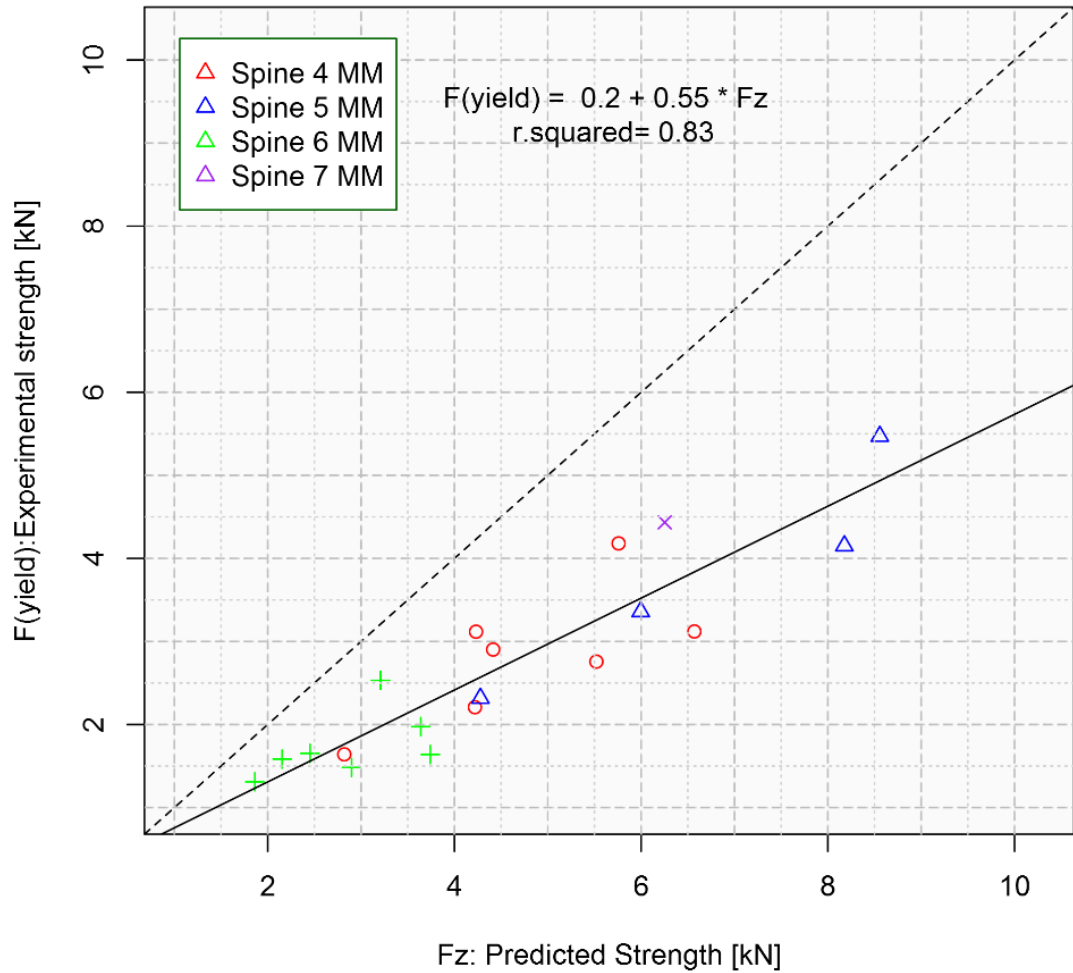


Figure 37 Predicted strength compared to experimental data in multiple myeloma sample set

3.3.2.2.3 Material model calibration - MM

This retrospective material model sensitivity study selected $b=2.5$, $c=1.25$ which resulted into $R^2=0.83$, with a mean difference of -0.09 kN and limits of agreement at ± 0.96 kN.

3.3.2.3 Predicting fractures in metastatic specimens

3.3.2.3.1 Weakest slice selected from 80% of vertebral body height - mets

In the last pathology dataset, 2 spines were assessed and their predicted strength was compared to the experimental data. The qualitative assessment uncovered a significant imprint in the bone tissue (Figure 36), however only 3 samples exhibited signs of notable infiltration, whereas the remaining tissue appeared to be unaffected by the presence of the disease in terms of lesion presence (Figure 40).

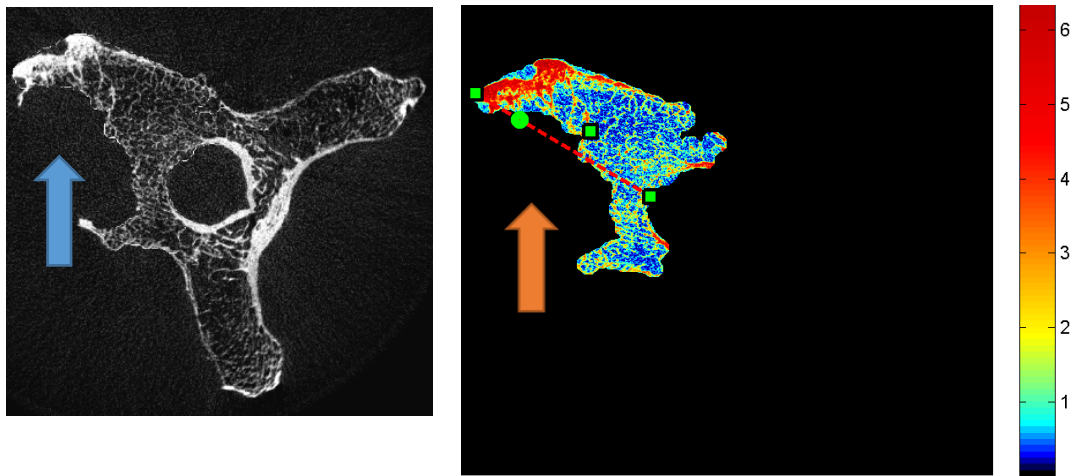


Figure 38 Structural assessment of a sample with osteolytic infiltration to the vertebral body. The lesion (indicated by a blue arrow on the left) replaces the natural trabecular bone with a highly vascularised but low density tissue which results in an almost negligible contribution to the strength (the red arrow on the corresponding modulus map with automatically detected VB boundaries). Despite the confirmed metastatic infiltration, only three samples exhibited a morphological alteration due to the presence of cancer

In respect to fracture prediction, the strength was estimated to range between 1.45 and 7.36 (mean= 3.54 ± 1.63 kN). A later comparison showed moderate correlation with the experimental data (coefficient of determination $R^2=0.77$, Figure 39), a low mean difference (-0.69 kN) and the narrowest limits of agreement (± 1.55) of all the three pathologies. Flexural and compressional rigidity alone were found to correlate with strength, with coefficients of determination $R^2=0.8$ and $R^2=0.75$ respectively.

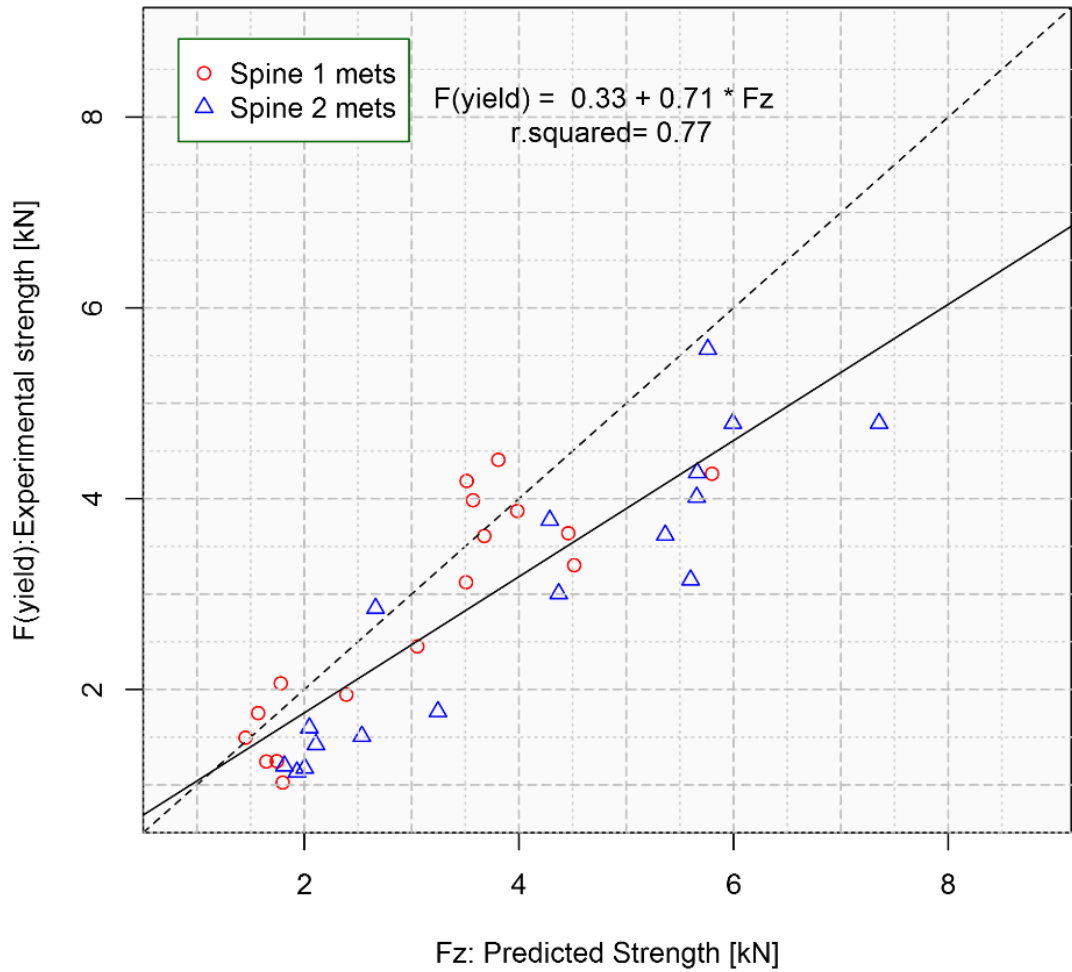


Figure 39 Fracture prediction of metastatic samples. This diagram presents *in-silico* predicted fracture loads compared to those derived from the cadaver testing

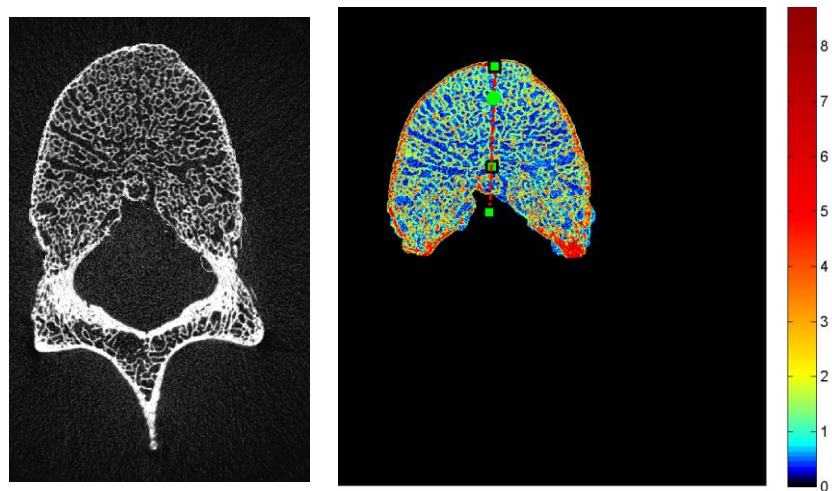


Figure 40 Structural assessment of a sample from a spine with metastatic infiltration but without presence of a lesion in the vertebra

3.3.2.3.2 Single slice analysis - mets

Similarly to the previous examples, the reduction of range of slices to one representative slice did not substantially reduce the prediction success, but instead impaired the correlation by 20% (single slice $R^2=0.62$), together with worsening the mean difference by 36% and limits of agreement by 38% to -0.94 and 2.14 respectively.

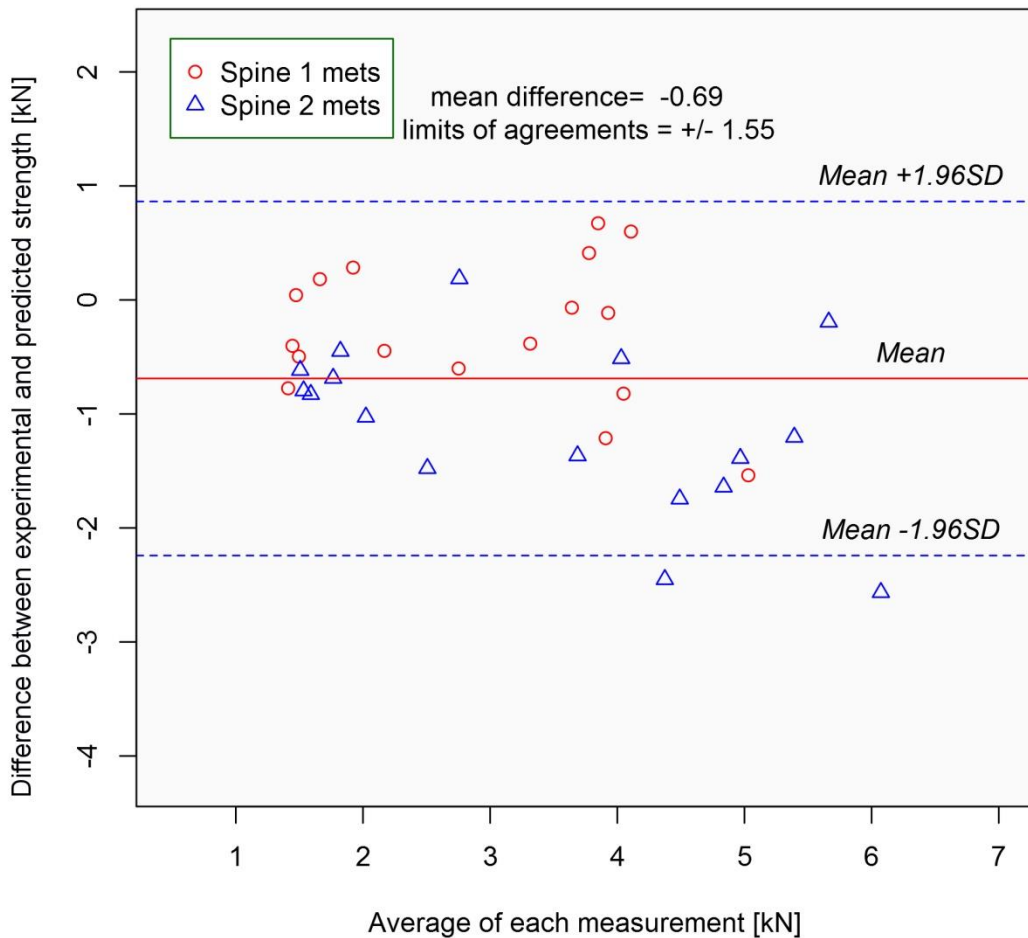


Figure 41 Bland-Altman plot indicating relatively good agreement between predicted and experimental strength in an assessment of the metastatic samples

3.3.2.3.3 Material model calibration – mets

For the last pathology material model tuning ranged in terms of the R^2 from 0.44 to 0.70, the mean difference ranged from -3.6 to 2.7kN while limits of agreement were limited to between 1.4 and 3.8kN. The calibrated model resulted in $b=6$, $c=1.25$, meeting the criteria of a fixed “c” coefficient. Results for this particular model were $R^2=0.67$, with a mean difference of 0.13 kN and limits of agreement at ± 1.52 kN.

3.3.3 Fracture prediction tool used in three distinct pathologies - Discussion

The structural analysis conducted in the second stage using samples from this study proved to demonstrate a relatively strong association between the predicted and experimental results, particularly in oncological pathologies where strengths have been predicted in both datasets with results varying by more than 77% without undertaking any additional corrections to the samples. The prediction of a particular osteoporotic dataset however appeared to be more challenging, resulting in a modest $R^2=0.66$. The possible reason for this discrepancy between the OP and other two datasets is that the OP dataset has clearly been affected by inter-spinal variability, in that by removing SpineGO 4 from the overall analysis, the R^2 increased to 0.75. The reason for the discrepancy could not be tested however is believed to be related to the presence of woven bone which despite its high mineral composition remains significantly weaker compared to mature lamellar bone. Woven bone is formed by fast activation of osteoblasts as a process of bone healing following a fracture. This is characterised by a lower degree of alignment of collagen fibres and the bone tends to be mechanically weak until replaced by lamellar bone [228]. In healthy tissue this would be a natural process of healing, which is however unlikely to happen in all tested samples in a single donor. An alternative explanation would be the presence of asymptomatic Paget's disease [229] which is characterised by enlarged bone structures with limited strength of the structure due to presence of woven bone. This however has not been confirmed in patient history details, unless it remained undiagnosed. As provided (listed in full in Appendix C: Donors' medical records available for this study), donor's history details state only mild scoliosis which is not likely to be linked to weakening of bone as observed here. Interestingly the morphology assessment of the particular spine (in "Appendix D.1: Osteoporosis") highlights increased bone mineral density together with notably high connectivity density (almost twofold the average of other spines). Neither trabecular spacing and thickness nor the number of trabeculae were found to be notably different.

Despite unexplained over-prediction in one spine, fracture prediction has shown a sufficient success rate when compared to experimental data.

3.3.3.1 Single slice analysis

In the subsequent step the hypothesis was that a single representative slice would reflect a weakening of the whole organ. Similar to the findings of previous investigators [147, 151], who also tested a reduced number of analysed slices, this has significantly reduced the time dependency of the complete analysis, in case of this study from one hundred slices to a single slice, progressing from a matter of minutes to seconds per sample. Such an approach is comparable to that presented by Windhagen et al. [147], where the representative slice was however selected intuitively and where a simulated lesion removed most of the original bone structure. Contrary to Windhagen's analysis, in this study the slice has always been selected from the central region between both endplates which is easy to identify from the anatomical reference scan (scout view). The correctness of this approach is of course only valid if the weakening is homogenous in nature, such as in OP and MM where the lesions do not seem to follow any particular pattern.

A notable impairment of correlations between the range of slices and one-slice analysis was however observed in the metastatic dataset. Here, the most affected sample was tested whether the size and position of the lesion with respect to mirror symmetry could hamper the use of the simplified beam theory. Asymmetric beam theory has been deployed resulting in marginal difference between the two methods. (more in Appendix G: Bi-axial eccentric loading). This hence suggests that the structural compromise has been located remotely from mid-slice along the cranio-caudal direction. Therefore either wider slice range assessment or combination with pre-screening lesion-detection should be considered once the vertebra is severely infiltrated.

Despite the issues in the metastatic dataset, the structural assessment showed promising results in terms of correlation; however the same results showed complications in terms of the agreement of the predicted and experimental strengths. Despite a relatively high correlation within all three pathologies, the model showed much lower precision and accuracy than was initially expected, based on the preliminary experiment. The discrepancy which was identified did in fact correlate with experimental strength leading to a notable over-estimation of the specimen's structural properties which was not observed in the assessment of historical data (section: 3.1.3). One possible explanation was a use of new scanning apparatus (microCT100 in this study compared to microCT80 in the previous

study). Unfortunately for this study, the transition from the use of microCT to assess the historical data and the use of microCT in the more recent study could not be accomplished using a proper scientific method due to a sudden breakdown of the previously employed machine. It is however believed that the inbuilt non-adjustable beam hardening (BH) correction algorithm could have contributed to this discrepancy. While the initial datasets were treated with a BH correction of $200\text{mgHA}/\text{cm}^3$, the more recent scans were treated with a BH correction six times higher for samples of similar size. A similar effect has been reported by Fajardo et al. [230] who identified not only the BH, but also the size and density distribution of the samples as notable contributors to the discrepancy in measurements. In fact, the mechanism of BH phenomena is in agreement with reported discrepancies, as it biases predicted densities in favour of the margins of the sample [230, 231]. Due to the fact that a moment of inertia accounts for the square of the distance from the neutral axis to each voxel, the difference in density with respect to the distance from the centre of each sample increases the weight of the spatially-dependent density-to-modulus bending rigidity. This in fact leads to an increase in the predicted strength of the sample as presented above.

Nonetheless, the two sets of sufficiently close correlations mentioned here suggest that the discrepancy between the scanners does not affect the correlation between data, and hence the relative comparison of strength is not impaired. This leads to the conclusion that the discrepancy, and hence the resulting accuracy and precision of the prediction, can be adjusted by choosing an appropriate material model.

3.3.3.2 Retrospective density-to-modulus model fit

Using a complete dataset calibration of the material model, which is a common approach for finite element methods used in previous studies [169], a notable improvement in the predictions of one slice analyses was demonstrated. Although the main criteria for the density-to-modulus power-law model were to adjust the results in terms of agreement with the experimental strength, the R^2 in the osteoporotic and metastatic samples improved by 14% and 8% respectively, together with maintaining a similarly superior R^2 in the multiple myeloma dataset. In terms of accuracy as defined by Bland and Altman [162], the models were calibrated so that even the lowest mean difference in the osteoporotic samples was found to be lower than 0.15kN. The largest scatter in terms of the limits of agreement has been observed to reach 1.52kN in the metastatic dataset.

The optimal material models were found to differ between datasets and although the power coefficient (“c”) could remain fixed between pathologies, the linear coefficient (“b”) required adjustment. Only a marginal difference between optimal models was found, which confirmed the findings from a recent micro-indentation study presented in this study. In the case of osteoporotic and multiple myeloma bone, the difference between the “b” coefficients of the tested power-law was found to be marginal, indicating only trivial differences in the properties of the micro-material. In contrast to these two datasets, the same linear coefficient of the material power-law for the metastatic bone has been found to be twofold that of the osteoporotic bone. This can be either explained as a result of the weakest slice contributing significantly more to raised levels of strength - hence the middle slice analysis could not account for structural changes in metastatic samples - or due to underlying differences at the tissue level.

Observed differences in the metastatic bone are rather surprising as this conflicts with studies by Kaneko et al. [198] and von Stechow [67], where both studies reported that the presence of metastases does not impair the estimation of the stiffness modulus gained from the density of the mineral component.

In fact, another study [225] disagrees with all of these findings, reporting that both lytic and blastic lesions are significantly less stiff than normal tissue. Hipp et al. [225] in their study also noted that although the apparent wet density of osteoblastic lesions in cancer specimens is greater than their ash density, they are less stiff than normal bone. The study thus concluded that fracture prediction tools based on a density-to-modulus model should be adjusted to take into account the effects of the metastases.

While all three contradicting studies [67, 198, 225] were conducted on cored trabecular samples, those conducted by Kaneko and Hipp were limited by the low number of samples available (three and two metastatic subjects in each of the studies respectively), while the study by von Stechow was conducted on ten subjects, without however distinguishing the primary cancer or the nature of the lesions. To the author’s knowledge, there is only one study which has been conducted where the cancer-affected (metastatic) bone was evaluated at the bone tissue level [68]. However, in that study authors reported values of an elastic tissue modulus of the healthy bone derived from nano-indentation (0.47 GPa) which were almost two orders of magnitude lower than the ones reported in the literature (~10-20 GPa) [36], indicating a possibly significant disparity in their experimental procedures or

a considerable detrimental effect of damage on the bone indentation properties [35]. Despite the systematic difference to values reported by other investigators, Nazarian et al. [68] reported the elastic modulus and hardness of the metastatic cancer bone as more than twofold lower than that of non-oncological tissue. Normal and osteoporotic indentations were not found to exhibit significant differences. Yet the actual potential variance between osteoclastic and osteoblastic lesions remains unclear as the researchers reported only primary cancer diagnoses and reported neither the presence of the lesion, nor the specific location of the indents.

Nonetheless, the inconsistencies between all the aforementioned studies, including this more recent one, raises concerns that the material properties of bone may be different with respect to the cancer type. Hence, to produce reliable data a calibration material model study should be conducted when testing different cancer samples.

3.3.3.3 Structural assessment in predicting OP, MM and mets – comparison to sophisticated FEA models

In contrast to the most recently developed finite element models used to provide an assessment of vertebral strength, the simplistic one-slice-analysis model has proved superior in terms of both accuracy and precision [65, 148, 167, 169-172]. In fact, only three studies [168, 169, 171] have been superior both in correlation and in agreement with measured data. Zeinali et al. [168] and Imai et al. [171] both tested models were modelled as linear elastic as well as improved linear elastic-linear plastic constitutive models, which were tested in homogenised and voxel-based models consisting of limits of agreement lower than 0.85kN, however both studies were limited in the number of samples tested which may have impaired the results which were obtained (N=9 and N=12 respectively). Pahr et al. [169] on the other hand, reused 37 samples earlier processed by Dall'Ara et al. [167] and reported that by calibration of the model on the same dataset, both accuracy and precision can be improved to an impressive mean difference of nearly zero, with ± 1 kN limits of agreement together with an impressive correlation of $R^2=0.92$. These in fact are quite comparable data in terms of agreement when comparing to the calibrated one-slice analysis, however R^2 is more difficult to compare as the range of experimentally obtained strengths was up to twofold larger in the finite element study mentioned (6.9kN in favour for FE [167] versus experimental ranges in this study: 3.2, 4.16 and 4.55 kN for OP, MM and mets respectively).

When considering the time dependency of the model used, literature very often lacks any indication of length of processing time which is however a significant factor in both the experimental and clinical environment. Although it is generally known that FEA is often limited by requirements consisting of preparation of the modelled sample prior to analysis, resulting in a lengthy modelling procedure and a reduced number of samples being able to proceed to testing. Considering the computational time alone, the models presented here could in theory be compared to coarsen homogenised models [167, 171] where the lower computational time and cost are counter-balanced by the lengthy effort required for the material mapping, segmentation and meshing, which all need to be adjusted separately for each sample. Even here, the one-slice-analysis is hardly comparable due to the fact that the time required performing an image-to-strength assessment, including data handling and preparation of the image, has been reduced to less than one minute. There is a strong potential in automatised fabric homogenisation which has been recently used to minimise the computational time required to approximately 30 minutes [169], but still requires well-defined boundary conditions and has been tested only in a pre-clinical environment.

3.3.3.4 Comparison of fracture prediction tool to other analytical models

In contrast to the work presented in this thesis, Whealan et al. [2] and Windhagen et al. [147] tested multiple segments, an analysis which probably represents the *in-vivo* state more accurately, but which hampers a methodological approach to understanding the load management within an isolated organ. In fact, the sample was tested in forward flexion, where the presence of intervertebral disc and posterior ligaments causes the load to be distributed more uniformly across both vertebral endplates towards compressional loading and is strongly dependent upon the pathological state of the soft tissue. Moreover, both studies have in reality covered predictions for particularly cancerous samples by pooling samples from donors without any oncological pathology and creating spherical cavities to simulate lesions. This however leads to an artificially distributed prediction across the range of experimental strengths and may have facilitated the acquisition of correlations of $R^2=0.69$ and $R^2=0.85$ respectively. The higher correlation in Windhagen's study can be explained by placing the simulated lesion always within the central region of the vertebral body, hence minimising the need for a flexural rigidity component.

3.3.3.5 Limitations of fracture prediction used in this study

The major limitation of this approach is that the outcome lacks any indication of fracture propagation or even of the relative position of the fracture. Although the slice-by-slice analysis can be used to predict the weakest slice, i.e. the site which is most prone to fracture, it lacks the ability to derive the relative stress distribution. Moreover, the linear elastic model which is the basis of the model proposed in this study cannot be used to quantify post-yield behaviour in any way. On the other hand, results suggested by Hong et al. [232] suggest that the model could easily be adjusted also for torsional loading, improving its versatility.

At last, it must be noted that the final results were calibrated using the entire dataset. Such simplification may offer a distorted interpretation of the performance of the developed model and lacks an engineering approach as data have not been delivered experimentally. Finally it is not guaranteed that this material model would work on different subsets.

Despite these limitations, the results are similar to those presented by Whealan [2], Windhagen [147] and many finite element approaches (e.g. [65, 167] and more). Even without adjusting the material model, it provides accurate information about the relative strength of the bone compared to other samples tested with the same model (Table 4, literature review section 2.6.2), which ensures a fast and robust benchmarking tool for use in a laboratory environment.

3.4 Commissioning of the fracture prediction tool – Summary

The fracture prediction tool adopted for purpose of this thesis and discussed in this chapter was initially tested using a dataset of osteoporotic, metastatic and multiple myeloma samples which matched testing and scanning criteria for the single vertebra study.

At first, the model was validated for use using historical data which showed promising results in terms of predicting the fracture based on the assessment of mineral component distribution using microCT images. In short, a relatively good agreement in terms of mean difference and limits of agreement was found (-0.25 ± 0.91 kN, -0.41 ± 0.96 kN and -1.01 ± 2.52 kN for OP, metastases and MM respectively), together with an indication of good correlations (up to $R^2=0.93$, 0.64 and 0.62 for OP, mets and MM respectively). This initial analysis underpinned two important findings: first, a strong necessity to identify any pre-existing fractures and also the existence

of possible differences in bone material properties; second, multiple myeloma bone predictions show large discrepancies in terms of both accuracy and precision, probably due to changes not only on a structural but also material level which should be further investigated.

Recent analysis of samples tested for the purpose of this thesis comprised altogether more than a hundred samples which have been collected, dissected and scanned before being subjected to an eccentric wedge compression fracture test. Here, samples were tested separately according to the nature of the bone disease (OP, MM and metastases). The results presented here underpin the overall stiffness and strength assessment used for the validation of the image-based fracture prediction tool in the following sections. OP bone was found to be both the weakest (1.35 ± 0.91 kN) and the least stiff (2.2 ± 1.0 kN/mm) from the investigated groups. From the other two tested pathologies, MM and metastases were found to be relatively comparable in terms of both the strength (2.73 ± 1.17 kN and 2.86 ± 1.33 kN respectively) and stiffness (3.46 ± 0.96 kN/mm and 3.57 ± 1.40 kN/mm respectively).

The results of the fracture prediction presented for each of the three pathologies were with relatively good correlation ($R^2=0.66$, 0.83 and 0.77 for OP, metastases and MM respectively) with however a wider range of agreement and considerable change in agreement compared to the initial study. The mean difference was found to be relatively poor when no samples were excluded from the study (-1.93 , -1.84 and 0.69 kN respectively) with relatively wide limits of agreement (± 2.02 , ± 1.94 and ± 1.55 kN respectively). Calibrated one-slice-analysis ranged in terms of multiplier of the material model from 3.5, 2.5 and 6 with limits of agreement ± 1.03 , ± 0.96 and 1.52 kN (for OP, MM and mets respectively). The mean difference for all three pathologies was <0.15 kN.

Chapter 4

Determination of the mechanical properties of trabecular bone utilising microCT assessment and micro-indentation

The second objective of this thesis was postulated regarding the limited understanding of underlying material properties of the cancerous bone. The necessity to underpin the alteration due to the presence of neoplastic pathology encompasses whether the deterioration of bone relates to changes at the meso- or micro-scale of trabecular tissue.

Section 4.1 focuses on the investigation of changes at the meso-scale level by means of image-derived assessment which was carried out by comparing morphology indices compared to the biomechanical metrics of each sample. The latter - the investigation at the micro-scale- was investigated in the following section 4.2 by means of micro-indentation assessing bone quality change in patients with diagnosed multiple myeloma cancer.

4.1 Pathology specific morphology

4.1.1 Introduction to assessment of micro-properties of the bone

The use of areal-BMD consistently fails to diagnose osteoporosis in the wider population (e.g. [62, 83, 226]). This could be explained by the fact that areal-BMD is based on accumulative planar X-rays and hence is dependent on the general size of the vertebra and mineral mass in the direction of the scan. Nevertheless, the size of the subject is not taken into account and hence can result in a systemic under-classification of osteoporosis. Despite its increasing general acceptance, the volumetric BMD used in this study is still considered more as a pre-clinical measure of bone quality due to the necessity of CT scanning and issues arising from relatively high radiation dosages, which increase with resolution together with the lack of proof, to be deployed purely as a measure of the weakening of the vertebral bone.

The objective of this study was to conduct a pre-clinical experiment that would provide a better understanding of the morphological nature of the tissue in combination with biomechanical testing that would assist in the development and optimisation of a treatment technique in pain management and techniques to prevent debilitating vertebral fractures. Volumetric BMD, as a mineral content per volume, provides measures which are corrected for

the volume of mass, however it lacks the large statistical data required to establish a precise threshold in clinical practice.

In this study the relative contributions of bone mass and trabecular microarchitecture to biomechanical metrics have been determined in a more complex loading scheme. The relationships between bone mass indices and trabecular morphometry on one hand and strength and stiffness on the other have been investigated. Pathologically unique samples have been examined by means of microCT assessment and later statistically compared to the complete organ wedge compression testing. This is in fact more clinically relevant [76, 233] than a similar assessment done on samples compressed axially [69, 234]. The consequences for the stiffness and strength of the organ have been presented earlier in this work in the fracture prediction tool development.

4.1.2 Methods used in morphology assessment

4.1.2.1 Sample population

Samples used for the morphological assessment study undertaken in this section comprised of the same samples used in the development of the fracture prediction tool, section 3.3. This more specifically comprised of fifty-four osteoporotic samples, thirty-four metastatic samples and nineteen samples from donors diagnosed with multiple myeloma. Details of the sample population together with basic donor information are listed in section 3.2.2.1. The same CT images as those used for beam theory-based predictions were treated in this analysis allowing a direct comparison with the previous data.

4.1.2.2 Morphology image processing

Scans were first carefully checked manually for scanning artefacts which would hamper the assessment and checked if all the slices have been reconstructed properly. The volume of interest (VOI) was chosen according to the SOP suggested by previous investigators [38]. In this protocol, trabecular BMD is evaluated safely within the inside volume of the bone as a specimen-specific cylinder with its cross-sectional base centred on the sagittal plane with a diameter of 60% of the antero-posterior vertebral body length and 80% of vertebral body height, defined by the first appearance of the cortical endplate on the axial slices (VOI depicted in Figure 42). The VOI (file extension GOBJ) was defined in the scanner evaluation program for later use within Image Processing Language [235].

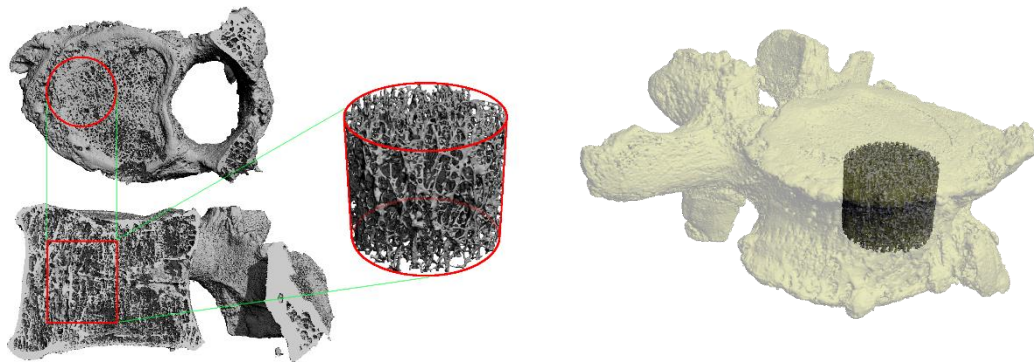


Figure 42: Protocol defining the VOI within the trabecular structure.

An overview of the steps taken to perform this basic morphometrical analysis is depicted in Figure 43. Prior to segmentation a measurement noise was partially suppressed within the VOI using a 3D Gaussian filter (filter width 1.2, filter support 2) followed by binarisation to differentiate between bone and the background. This method is often performed manually by selecting the threshold according to the researcher's best estimate. However, this technique, when tested on sensitivity to different microCT users, showed insufficient consistency between researchers. As an alternative method an iterative selection method proposed by Ridler et al. [236] was adopted. The method for selection of the threshold is based on an iteration to the weighted equilibrium of a density histogram as shown as "X" in Figure 44. To do so, the scanning density data (file extension ISQ) together with the volume of interest defined in the microCT scanner (file extension GOBJ) were simultaneously loaded and processed by a custom-build code [208] prior to derive the single threshold value (GUI depicted in Figure 45).

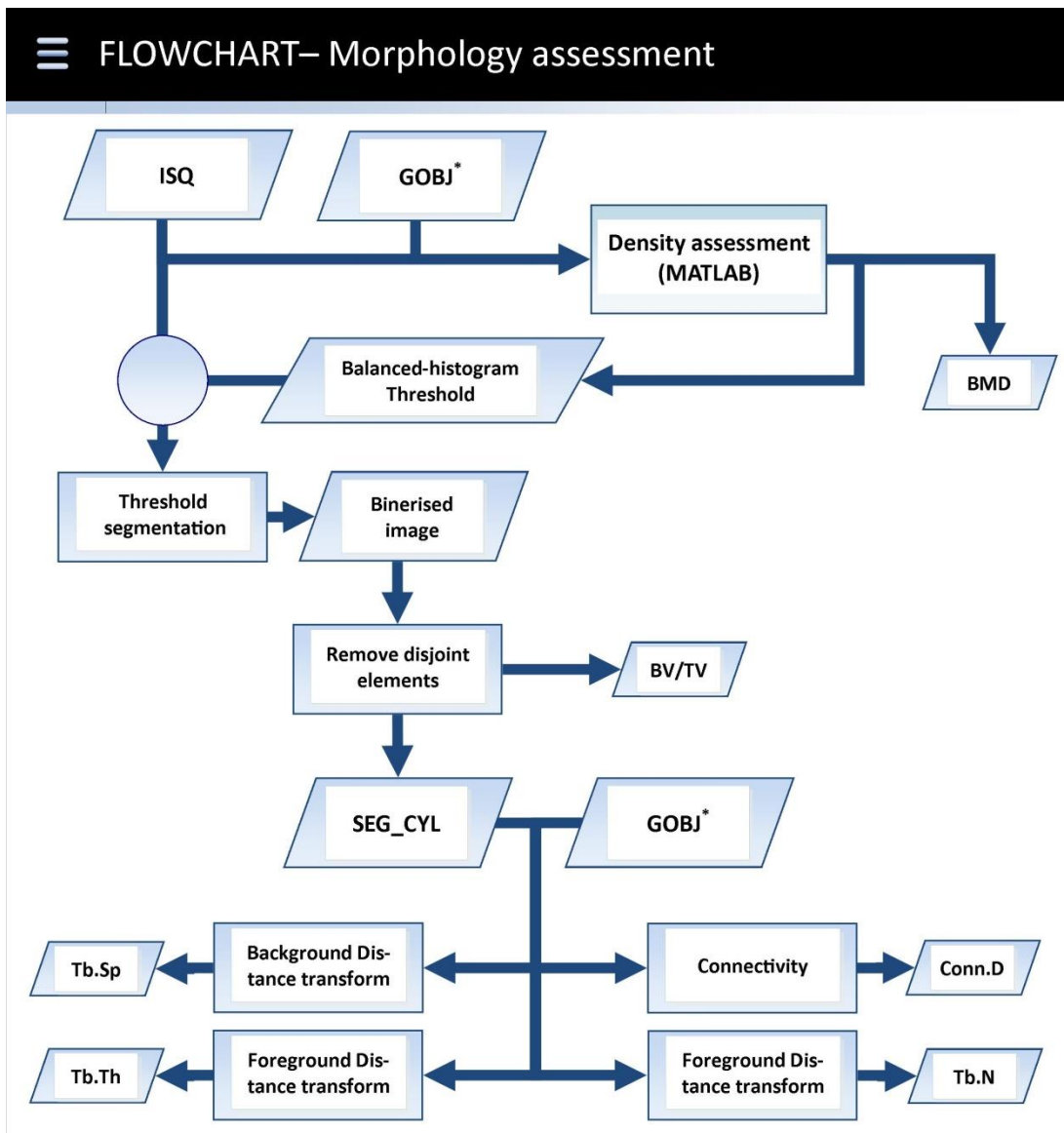


Figure 43: Single step flowchart of the Morphological assessment. (ISQ - microCT scanning file; GOBJ - microCT file defining ISQ specific volume of interest mask; SEG_CYL – 3d binarised image stack of representative trabecular bone region; BMD, BV/TV, Tb.Sp, Tb.Th, Tb.N and Conn.D represent morphological indices discussed in the text)

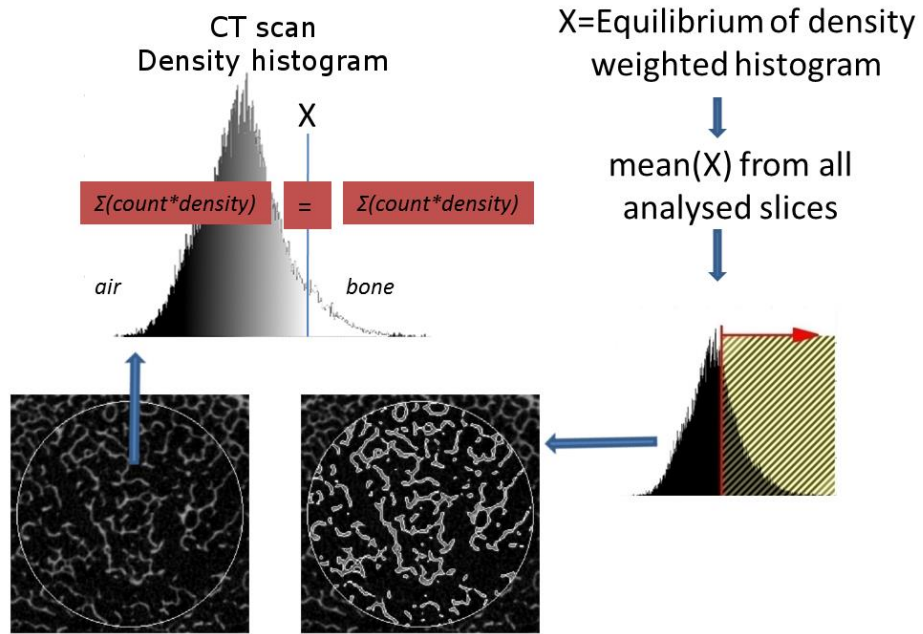


Figure 44: Principle of iterative selection thresholding technique proposed by Ridler and Calvard [236] and adopted to microCT measurements performed in this study

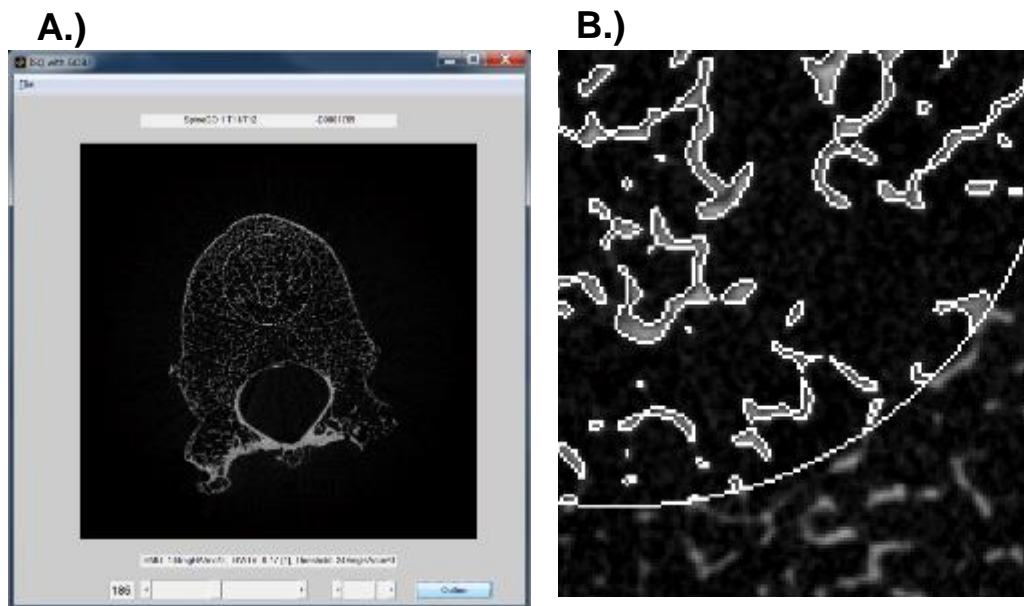


Figure 45: Graphical User Interface (GUI) of a custom-compiled script used to view the ISQ scanning files, to estimate the BMD, BV/TV and optimal threshold within the desired VOI (based on GOBJ). Subfigure (A) shows an example of vertebra scanned in microCT100, a program which allows a slice by slice list, is able to adjust brightness and highlights segmented bone according to the estimated threshold detailed in subfigure (B)

The binarised stack was later filtered using a ranking filtering approach which identifies and removes significantly minor disjointed elements. Subsequently, a morphological assessment was performed using a distance transform algorithm to deliver direct measurements of trabecular spacing (Tb.Sp), thickness (Th.Th) and number of trabeculae (Tb.N). Connectivity was performed using a ranking method whereas density was normalised to the size of the VOI. All these morphological indices were obtained using Image Processing Language [235].

4.1.2.3 Comparing the morphology to cadaveric testing

The trabecular microarchitecture indices were furthermore combined with measures obtained from the fracture prediction tool described previously in subsection 3.3: "Fracture prediction tested on large sample population: three pathologies" and compared to experimental data obtained from mechanical testing described in section 3.2: "Commissioning of cadaveric Wedge Compression Fracture testing".

Statistical analysis was performed using the computing environment R [237]. Morphological indices were compared to experimental data in terms of coefficient of determination (R^2) based on linear fit and multivariate regression between the selected variables.

4.1.3 Morphology of human bone - Results

4.1.3.1 Morphology assessment

4.1.3.1.1 Morphology of osteoporotic bone

With regards to the most commonly used bone quality indicators, the Bone Mineral Density (BMD) in this dataset was found to vary from 56.7 to 204.7 mgHA/cm³ (mean 124.6 ± 39.9 mgHA/cm³), whereas the bone volume fraction (BV/TV) varied from 0.1 to 0.23 (mean 0.17 ± 0.04). The trabecular structure indices Tb.Sp, Tb.Th, Tb.N and Conn.D varied from 0.9 to 2.07 mm (mean 1.31 ± 0.3), 0.26 to 0.42 mm (mean 0.3 ± 0.03), 0.97 to 2.07 per mm (mean 1.36 ± 0.28) and 0.29 to 1.62 per mm³ (mean 0.81 ± 0.4) respectively.

4.1.3.1.2 Morphology of multiple myeloma bone

An assessment of the multiple myeloma samples revealed that the Bone Mineral Density (BMD) varied from 100.4 to 194.3 mgHA/cm³ (mean 124.1 ± 28.3), whereas the bone volume fraction (BV/TV) varied from 0.1 to 0.22 (mean 0.15 ± 0.04). The trabecular structure indices Tb.Sp, Tb.Th, Tb.N and Conn.D varied from 0.95 to 3.84 mm (mean 1.68 ± 0.82), 0.27

to 0.53 mm (mean 0.32 ± 0.06), 1.05 to 3.76 per mm (mean 1.75 ± 0.8) and 0.22 to 1.13 per mm^3 (mean 0.67 ± 0.29) respectively.

4.1.3.1.3 Morphology of metastatic bone

Morphology alone in metastatic samples provided an assessment of Bone Mineral Density (BMD) varying from 109.3 to 239.9 mgHA/cm^3 (mean 152.3 ± 34.2), whereas the bone volume fraction (BV/TV) varied from 0.18 to 0.34 (mean 0.27 ± 0.05), The trabecular structure indices Tb.Sp, Tb.Th, Tb.N and Conn.D varied from 0.69 to 1.15 mm (mean 0.8 ± 0.11), 0.28 to 0.37 mm (mean 0.31 ± 0.02), 0.8 to 1.2 per mm (mean 0.9 ± 0.09) and 0.77 to 2.88 per mm^3 (mean 1.91 ± 0.68), respectively.

4.1.3.2 Morphology as a fracture prediction and comparison to composite beam theory fracture prediction tool

Generally speaking, fracture prediction using the beam theory has provided promising results when assessing the weakening of the vertebra. This section aims to establish the relative links between the vertebral biomechanical behaviour of the bone-mass coupled with an assessment of the trabecular micro-architecture in comparison to image-based beam theory fracture prediction.

Multivariate correlation was possible due to combining the previously presented morphological indices, beam theory fracture predictions and experimental data. Table 10 details results from a number of observations which have been made. Stand-alone morphology indices were found to weakly correlate with the experimental data, here only BMD and BV/TV were found to correlate with the vertebral strength but only with moderate success given their different pathologies. Tb.Sp and Tb.N were found to correlate weakly or not at all with strength and stiffness. The beam theory was found to strongly correlate with the biomechanical testing in both cases, using the representative range of images and also in the case where only one slice (Fz.OneSlice, El.OneSlice and EA.OneSlice) has been used.

Multivariate regression - part correlation							
Composite Beam Theory							
Dependent variable		Strength					
Independent variable		<i>Fz.range</i>	<i>El.range</i>	<i>EA.range</i>	<i>Fz.OneSlice</i>	<i>El.OneSlice</i>	<i>EA.OneSlice</i>
Pathology	Osteoporosis	0.81	0.61	0.63	0.76	0.7	0.67
	MM	0.91	0.79	0.86	0.91	0.88	0.86
	Metastases to spine	0.88	0.87	0.90	0.79	0.78	0.86
	All	0.77	0.63	0.69	0.68	0.64	0.64
Dependent variable		Stiffness					
Independent variable		<i>Fz.range</i>	<i>El.range</i>	<i>EA.range</i>	<i>Fz.OneSlice</i>	<i>El.OneSlice</i>	<i>EA.OneSlice</i>
Pathology	Osteoporosis	0.73	0.78	0.82	0.67	0.67	0.63
	MM	0.64	0.49	0.57	0.63	0.62	0.65
	Metastases to spine	0.73	0.78	0.82	0.66	0.67	0.74
	All	0.65	0.58	0.63	0.58	0.57	0.57
Morphology indices							
Dependent variable		Strength					
Independent variable		BMD	BV/TV	Tb.Sp	Tb.Th	Tb.N	Conn.D
Pathology	Osteoporosis	0.55	0.73	-0.68	-0.06	-0.68	0.81
	MM	0.79	0.30	0.16	0.53	0.15	0.02
	Metastases to spine	-0.23	0.21	0.04	0.62	0.09	-0.16
	All	0.36	0.51	-0.22	0.30	-0.20	0.38
Dependent variable		Stiffness					
Independent variable		BMD	BV/TV	Tb.Sp	Tb.Th	Tb.N	Conn.D
Pathology	Osteoporosis	-0.38	0.08	0.16	0.53	0.22	-0.25
	MM	0.44	0.05	0.37	0.50	0.36	-0.22
	Metastases to spine	-0.38	0.08	0.16	0.53	0.22	-0.25
	All	0.27	0.44	-0.17	0.26	-0.15	0.30

Table 10 Pearson’s Correlations (r) between the biomechanical experiment and the image-based analysis

When combined together, the correlation with biomechanical assessment significantly improved for all pathologies, in terms of both the strength and the stiffness (Table 11). This suggests that despite their weak correlation as standalone predictors, all parameters in some measure contribute to the organ’s mechanical resilience. However, statistically only trivial contributions to the correlation were found in the spacing index (Tb.Sp)

and number of trabeculae (Tb.N) for all three pathologies. By excluding the two indices from the multivariate regression, the correlation coefficient decreased only marginally (by 4.1, 1.2 and 0.9% for strength in OP, MM and mets respectively and by 2, 13.7 and 5.8% for stiffness in OP, MM and mets respectively).

Multivariate regression - final correlation			
Dependent variable	Strength		
Independent variable	Morphology indices combined	Morphology + Beam theory	
Pathology	Osteoporosis	0.84	0.90
	MM	0.88	0.98
	Metastases to spine	0.76	0.97
	All	0.66	0.92
Dependent variable	Stiffness		
Independent variable	Morphology indices combined	Morphology + Beam theory	
Pathology	Osteoporosis	0.74	0.80
	MM	0.81	0.96
	Metastases to spine	0.70	0.89
	All	0.61	0.83

Table 11 Pearson’s correlation coefficients (r) as the result of the multivariate regression analysis

The multivariate regression performed discerned that the best association between the whole organ’s mechanical properties and microCT images can be obtained by combining bone mass parameters (BMD,BV/TV) and microstructure properties (Tb.Th, and Conn.D), together with parameters concerning the modulus distribution (EA, EI and Fz). One must however consider that to achieve such a good correlation, at least 80% of the vertebral body had to undergo a detailed microCT assessment in comparison to an assessment with only one slice which was able to correlate with considerable success. Namely, compared to the complex

assessment of all contributors, the one slice assessment (Fz.OneSlice) showed correlations lower only by 25.2, 12.0 and 10.9 % in terms of strength prediction for OP, MM and mets respectively and 21.6, 32 and 17% in terms of stiffness prediction for OP, MM and mets respectively. Overall, one slice analysis correlated by 30.4% less in terms of strength of all samples, and by 31.1% less in terms of stiffness of all samples.

4.1.4 Morphology assessment in bone with cancer and OP - Discussion

The BMD values presented in this work are in agreement with literature in the case of osteoporotic bone [238], although the BMD of both oncological pathologies was expected to be much lower [95]. The reported values for single vertebra were however as low as $8\text{mgHA}/\text{cm}^3$, suggesting that the area in which authors measured the BMD was extremely deteriorated in terms of content of the calcified bone, in fact often suggesting that no bone remained at all. A notably increased BMD and BV/TV in metastatic bone was caused by the relatively good condition of the bone which had been harvested from the two patients and by a lack of osteolytic lesions. The assumption that the bone from these patients was relatively healthy is supported by other morphological indices reinforcing the quality of the structure of the bone. In fact, a superiority of connectivity and a decreased number of trabeculae and separation thereof both suggest a much higher quality of bone when compared to the other two investigated pathologies. The bone volume fraction (BV/TV) presented here is in agreement with several studies [239-241] although values in literature do vary from 0.08 to 0.39. Disagreement was found towards both ends of the range. Ladd et al. [242] and Follet et al. [243] reported bone fractures within the lowest limits of the range in contrast to Ouyang et al. [244] who reported values twofold higher than the values which have been presented in this work. The osteoporotic and multiple myeloma datasets are in agreement with observations of oncological tissue presented by Nazarian et al. [68] who failed to show a significant difference between the datasets belonging to their two pathologies. The trabecular morphometry indices have been found to lie within a similar range to those reported elsewhere [239, 243] but this has also been opposed by several other studies [240, 243, 244].

The large discrepancy which exists within the literature examined is explained by the lack of a “gold standard” for assessing bone structure using the CT. Examples in which this lack existed include the geometrical calibration, the range of the employed density calibration phantom, the

resolution [239], scanning parameters, beam hardening correction [231], the position of the vertebra with respect to the scanner [230] etc. In addition, one needs to pay attention when comparing *in-vivo* and cadaver samples due to the influence of the surrounding tissue on the resulting densities [34].

Although a biomechanical assessment with the objective of identifying key components in a structural assessment has been well documented for compression testing [69, 217, 234] (and includes references within a review article by Bouxsein et al. [70]), it had yet to be validated for wedge compression loading. This study has however presented a correlation with the bone strength in a limited number of cases and a very weak or no correlation with its stiffness.

This is in contrast to findings which have been presented for strictly compressional loading where bone mass such as BMD and BV/TV explains the largest measure of variation by far in both stiffness and strength [69]. For more complex loading it has been reported that BMD and BV/TV correlated only moderately with the bone strength for osteoporotic samples only, and only BMD correlated with strength in multiple myeloma samples. This indicates two possible explanations: 1) literature-based data agrees in the investigation of osteoporotic bone where data are not comparable to other pathologies; and 2) findings from compressional loading cannot be directly translated to loading with an excessive bending component. The first possible explanation was again confirmed by assessing the density of connectivity, which was believed by many authors to be a link explaining the remaining unknown variation of results when correlating bone mass with strength [59]. Despite high correlations for osteoporosis, this failed to be repeated in experiments performed with the other two pathologies.

In fact, the second possible explanation is similar to findings presented by Crawford et al. [245] who suggested that an additional metric to account for bending rigidity is needed. In their validated FE simulation, the authors proposed that even the multiplication of the axial stiffness (effectively a product of BMD and the cross-sectional area) by the square of the antero-posterior vertebral body depth gives a significantly higher correlation to the bone strength. Multivariate regression analysis presented in this study has shown that the number of trabeculae together with the trabecular spacing indices do not strongly improve correlation with vertebral strength, however this is believed to be due to the fact that they share the same derivation algorithm with trabecular thickness, hence are not independent. To account for the bending component, it has been further

investigated that a combination of beam theory and the morphological indices did account for a variation of results with correlation to strength ranging between 81% and 96%, and to stiffness ranging from a modest 64% up to 92%.

The results presented in this study suggest that although a morphology assessment can help to underpin the structural properties of vertebral bone, the benefits of using morphology as a precursor of fracture may be overwhelmed by the need for a large volume of images to be scanned with high accuracy. Moreover, the general understanding of the relationship between bone structure and biomechanical performance, and the ways in which they correlate, may be inflated by a comparison with simplistic uni-modal loading and the transition to a more complex scenario remains unaccounted for.

4.2 Micro-indentation of multiple myeloma bone

4.2.1 Introduction to micro properties of multiple myeloma bone

Multiple myeloma is a bone marrow cancer derived from aberrant plasma cells and is often associated with a myeloma bone disease. The lesions of myeloma bone disease are frequently widespread resulting from a tumour-induced osteoclast/osteoblast imbalance in the remodelling process where the bone resorption becomes dominant. Myeloma bone disease results in a deficiency of the load bearing capacity, resulting in significant morbidity and utilisation of healthcare resources. However, the nature of the weakening has not been adequately assessed. In particular, it remains unclear whether besides bone loss, the material properties of the neighbouring tissue also become degraded.

Previous studies have shown that age has little or no influence on the mechanical properties at the tissue level [36, 184], which remains an important encounter in supporting the theory that a reduction in bone stiffness in osteoporotic patients is primarily due to changes in BV/TV and not in the material properties of the bone per se. However, this has not been proven in cancer patients who are known to be affected by an increased risk of fractures occurring compared to an osteoporotic population [83]. A comparison to a non-affected population has clearly shown the structural changes in patients suffering from this neo-plastic disease [91, 92], however there exists only limited knowledge concerning whether the multiple myeloma affects the bone mechanical properties at the tissue level.

Due to a direct link between bone density and its stiffness moduli used in various fracture prediction tools, an investigation of the unambiguousness of underlying material properties of bone is also required to prevent misleading predictions. A comprehensive assessment of the mechanical properties of vertebrae at the tissue level affected by multiple myeloma, as yet unreported in literature, is needed to extend the usage of tools developed to predict vertebral strength, such as those employing finite element methods. Such a methodology needs as its input a number of reliable mechanical properties which might be different from the normal or osteoporotic aspects, such as elastic modulus at the tissue level. Moreover, the deterioration of the bone tissue in function of its distance to the lesion can be modelled, if necessary. Hence the aim of this study was to investigate the mechanical properties of bone tissue, measured by means of micro-indentation in patients with myeloma bone disease, and compare the findings with non-affected patients.

Therefore, the hypotheses for this study are listed as follows:

- i. Vertebral tissue indentation properties of MM bone are influenced by the presence of a lesion with progression of the lytic infiltration.
- ii. Vertebral tissue indentation properties of MM bone are different when compared to indentations in healthy bone tissue.

4.2.2 Methods of bone micro-properties assessment

4.2.2.1 Multiple myeloma bone indentation - sample selection

Spines with a diagnosis of MM were acquired from a non-transplant tissue bank (GIFT, Leeds General Infirmary, UK and Science Care®, AZ, USA) following ethics committee approval (Ethical approval: 10/H1306/60). Two vertebrae (L4 and T6) were extracted from the thoracolumbar spine of six subjects. Specimens were divided into two groups according to a microCT assessment of each vertebra (voxel size $70.8 \times 70.8 \times 70.8 \mu\text{m}^3$, microCT100 [Scanco Medical, Bassersdorf]): samples without any visible lesion (group MM.N, example depicted in Figure 46 (A)) and specimens with myeloma bone disease (MBD) infiltration to the bone (groups MM.L, two examples depicted in Figure 46 (B) and (C)). After removing posterior elements, the samples were partially embedded in PMMA to allow precise cutting. In addition reference grooves were made in the cortical shell.

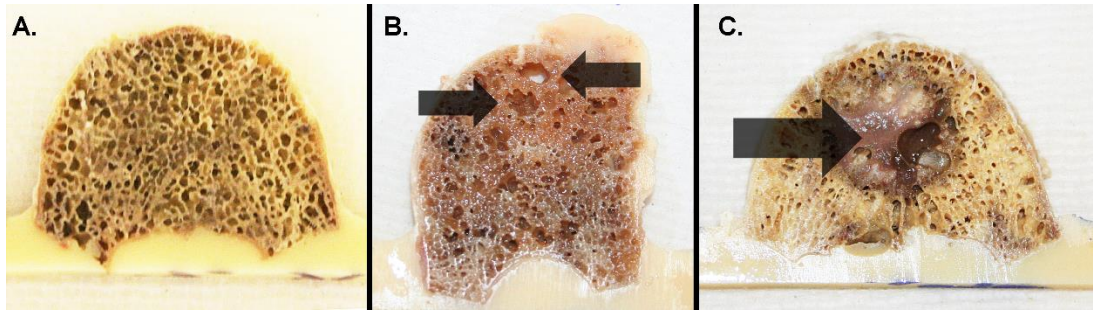


Figure 46: Vertebral body section cut along a plane perpendicular to the vertebral axis in the middle of the multiple myeloma bone without any visible lesion (A), moderately infiltrated sample (B) and sample severely affected by MBD (C)

4.2.2.2 Nearby lesion localisation

Repeated microCT scans with the same parameters provided quantitative information about the position and size of any lytic infiltration with respect to the reference grooves. To automatically locate the lesions, a distance transform algorithm was used [235]. This method is, as illustrated in Figure 47, based on fitting spheres of different sizes into the background of a segmented 3D image of the bone [57], where the segmentation threshold value was obtained using an iterative selection method [236] in a custom compiled image processing script [208].

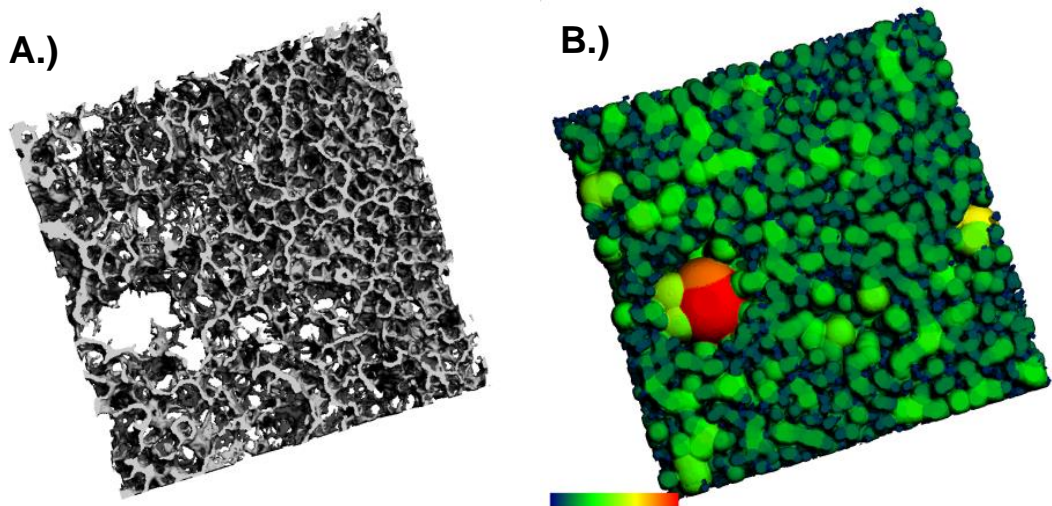


Figure 47: Visualised distance transform algorithm to estimate the trabecular spacings and thicknesses which highlights morphological changes due to lytic infiltration to bone. Segmented image (A.), Tb.Sp (B.) to identify a cancer lesion (multiple myeloma cancer)

4.2.2.3 Sample preparation prior to indentation testing

According to the position of the lesions, from each sample, two to three 5 mm thick slices were cut using a high precision diamond band saw [EXACT 310, Exakt Apparatebau, Norderstedt, Germany] perpendicular to the cranio-caudal axis. From each of these slices, one to four 15x15 mm samples were prepared. In particular, samples from groups infiltrated by cancer were cut through the lesion (MM.L) and are later depicted in Figure 48. Moreover, a control sample was extracted from each vertebra in a region without any visible cancer infiltration to the bone, according to the microCT images (MM.L.C). In one case there was not enough trabecular bone to take a control sample as most of the trabecular structure was affected by the lytic lesions. Samples from the group without any visible lesions (MM.NL) were taken from the middle region of the vertebral body. Therefore, samples were divided into three groups as reported in Table 12, whereas the number of samples tested is reported in Table 13.

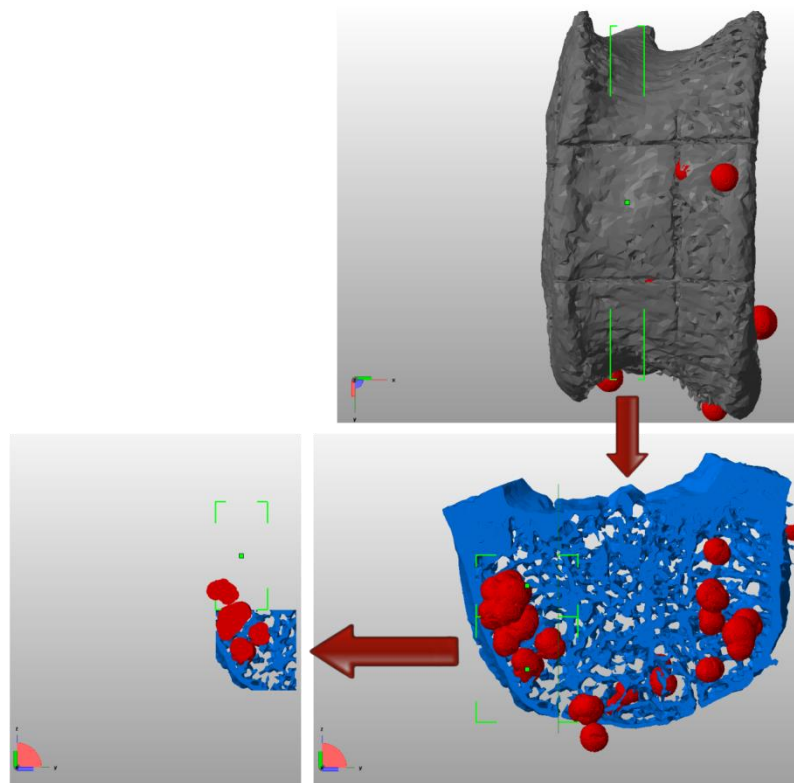


Figure 48 Micro-indentation sample preparation: Lesion has been identified based on segmented microCT images superimposed by lesion map highlighting bone separations $>3.5\text{mm}$. Reference grooves made prior to scanning were used as a reference guideline for latter cutting. Figure depicts an example of a single coupon containing a lesion cut with respect to the cutting grooves

Study groups		
Group name	Infiltration to the bone	Details
MM.L	Myeloma bone disease (MBD)	Four patients with lytic invasion to the vertebral bone, samples taken from proximity of the lesion
MM.L.C	MBD (Control)	Samples from the same vertebrae of MM.L group but taken from the non-affected site
MM.N	MM without visible lesions	Two patients with diagnosed MM cancer without visible lesions
Non-MM	No MM cancer	Samples from thirty-two donors without diagnosed MM cancer (data collected from [36])

Table 12 Base group sample allocation comprising twelve samples from six donors with diagnosed MM cancer compared to a non-affected population

	MM.L	MM.L.C	MM.N	non-MM
Transversally-cut trabeculae	1079	311	293	243
Axially-cut trabeculae	408	76	100	243
Number of samples	N=31	N=8	N=9	N=27
Number of vertebrae	8	7	4	27
Number of donors		4	2	27
Vertebral levels		2xT6, 2xL4	T6, L4	T1-L3
Age range, gender (Male/Female)		60(M), 70(F), 68(M), 82(M)	87(F), 90(M)	21-94 (Median 65)

Table 13 Number of indentations and samples for each of the base groups, together with non-MM group acquired by Wolfram et. al. [36]

To remove the bone marrow, each sample was submerged in soapy water for 12 hours at 37°C following 7 minutes in an ultrasonic bath at 40kHz (U1250 Ultrasonic bath [Ultrawave Ltd.]). Where necessary, the residual

bone marrow was removed using a dental pick water lavage (oralB, professional dental care [Brown]) submerged in a warm bath so as not to damage the trabeculae. In some cases the cancerous tissue had to be carefully removed manually. The procedure was repeated until the samples were cleaned and free of any soft tissue.

Afterwards, samples were left to dry for 6 hours at room temperature and then fully embedded in epoxy resin (EpoFix [Struers A/S, Ballerup, Denmark]) with a vacuum applied for 5 minutes to remove air bubbles (CCL-31 vacuum pump [Javac, UK]).

Embedded samples were glued to a microscopic glass and polished using Ethylene glycol as a lubricant. The final polished surface was achieved by using a range of progressively smoother silicon carbide papers (P500, P1000, P2400, P4000 [Struers A/S, Ballerup, Denmark]) and finished with 3 μm and 1 μm diamond grain suspension on polishing cloth. Between every polishing step, the residual grinding particles were cleaned from each sample with water following an ultrasound bath in distilled water for 7 minutes at 35 kHz. Summary of the sample preparation from lesion localisation to labelling the lesion prior to micro-indentation testing is illustrated in Figure 49.

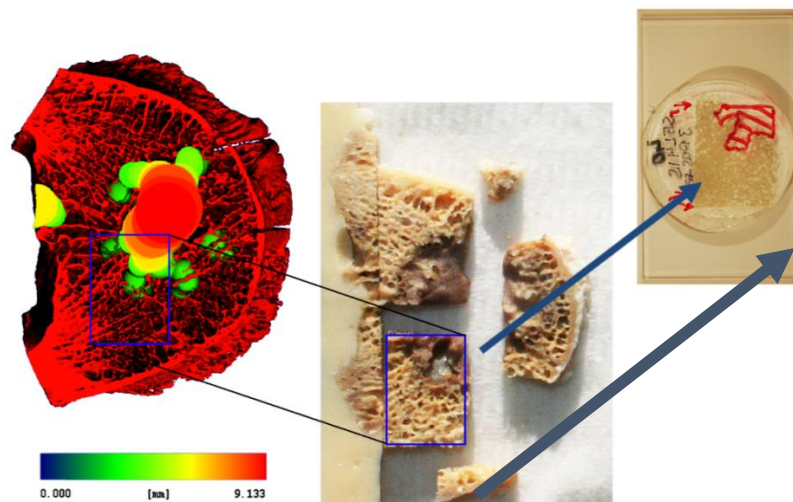


Figure 49: MicroCT assessment followed by sample cutting according to a suggested cutting path. Bone is represented as segmented tissue (red) whereas fitted spheres of different colours according to their size represent the lesion (>3.5mm), thus predicting the lesion position (left). A cleaned and embedded sample with rough demarcation of the lesion borders is annotated with a permanent marker (right)

The use of a validated experimental methodology [184, 246, 247] and the same apparatuses allowed comparison with previously published data [36]. In particular, comparisons were made between the present study and that study on indents performed along the cranio-caudal direction and located in the inner region of axial and transverse sections of trabeculae. In that study, 27 human vertebral samples were harvested from patients where medical history did not indicate any neoplastic disease.

4.2.2.4 Indentation procedure

Micro-indentation was performed during a secondment placement in the Vienna University of Technology, Institute of Lightweight Design and Structural Biomechanics. Indentations were performed under dry conditions by using a Berkovich diamond tip mounted on a CSM micro-indenter (NHT, CSM, Switzerland). Indents were load driven with a monotonic ramp at 120mN/min until reaching a set depth of 2.5 μ m following a hold time for 30s with sequential monotonic unloading again at 120mN/min. Indentation modulus (E_i) was computed according to the procedure suggested by Oliver and Pharr [248]. Indentation moduli (E_i), hardness (H), elastic energy (W_e) and plastic energy (W_p) were computed for each indentation. Ductility was estimated as a ratio of plastic indentation energy to total indentation energy ($W_p/(W_e+W_p)$).

Prior to the indentation, after mounting the sample to the base of the indenter, the borders of each lesion were recorded using an in-build optical microscope(as exemplified in Figure 50). Indents were placed in either axially- or transversally-sectioned trabeculae. Each indent was labelled as axial or transversal according to the nature of the cut. In both cases only the central region of the section was indented.

Every sample was indented with at least 40 indents. The load-displacement curve of each indent was carefully examined and, in case of observed indenter contact problems, the corresponding indent was excluded from the study. Temperature (τ) and humidity (κ) were constantly measured during the test ($\tau = 21.62 \pm 0.73^\circ\text{C}$, $\kappa = 50.33 \pm 4.9\%$). The indentation data representing a non-affected population, pooled from the previous study [36], were adjusted to the same reference temperature and humidity by performing a bi-linear least square fit. The affine adjustment function (eq.(1.11)) and the coefficients for each of the indentation variables (E_i , H , W_{el} and W_p (eq. (1.12), (1.13), (1.14) and (1.15)respectively)) are listed in Appendix F.2: Humidity and temperature adjustment.

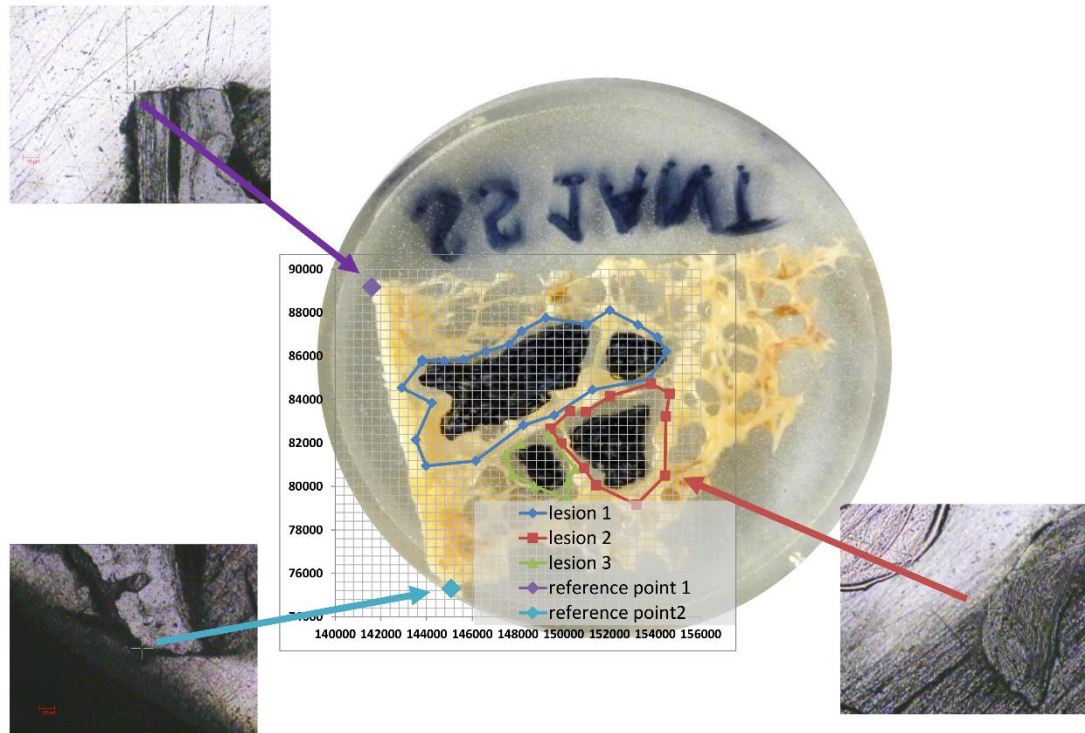


Figure 50 Micro-indentation: the border of the lesion has been quantified as the closest trabecula-intersecting indentation plane. In case of multiple occurrences, lesions have been labelled independently (as in the example), together with a record of the position of at least two reference markers for orientation and indent position/bone overlap

4.2.2.5 Statistical analysis used in micro-indentation study

Each hypothesis was statistically tested using repeated measures analysis which was performed using the computing environment R [237]. Datasets have been freed of the outliers below the 0.5th and above the 99.5th percentile, as such outliers are likely caused by the inconsistent slope of the load-displacement curve due to unforeseen micro-fracture, slippage of the sample or an accidentally indented underlying cavity. Variances were tested using ANOVA with a significance level of $p=0.05$ and groups were compared using Tukey's post-hoc method [249]. The difference between compared subgroups is presented as mean \pm standard deviation.

4.2.3 Micro-properties of multiple myeloma and comparison to non-affected population - Results

In total 2753 indents were used in the statistics, where 2267 indents from MM samples were pooled together with 486 indents of non-affected bone. A repeated measures analysis was performed on 149 samples (47

MM axial, 48 MM transverse, 27 non-MM axial and 27 non-MM transverse). The groups' normalities were checked using the Shapiro-Wilk test (for all groups $p \gg 0.05$). The average indentation modulus of the tested samples ranged between 10.2 and 18.4 GPa. The micro-hardness varied between 316.1 and 572.3 MPa. The elastic indentation energy varied between 7868 and 20147 pJ whereas the dissipated indentation energy was between 40853 and 71170 pJ.

4.2.3.1 Indentation properties - comparison between MM groups

Between groups MM.L (bone in proximity of a lesion), MM.L.C (taken distantly from a lesion) and MM.NL (without visible lesions) the indentation modulus (E_i) varied between 15.51 and 16.72 GPa in the axial and 13.9 and 14.16 GPa in the transversal direction. Indentation direction (axial/transverse) failed to show any significance in elastic energy (W_e , $p=0.78$) but was otherwise found to be significant for all other tested parameters ($E_i/H/W_p$, $p \gg 0.01$). Furthermore, no significant difference was found between all three multiple myeloma groups for axial or transverse direction (all $p \gg 0.5$, lowest significance level $p=0.13$ in E_i in axial direction). A detailed comparison of all tested indentation variables is listed in Table 14 and the Whisker plot in Figure 51 combines all groups together with comparison to non-affected population.

Base MM groups					
	Axial ^(*)				
	Indentation modulus Ei [GPa]	Hardness H [MPa]	Elastic energy We [μJ]	Plastic energy Wp [μJ]	Ductility measure [1]
	mean ± stdev	mean ± stdev	mean ± stdev	mean ± stdev	mean ± stdev
MM.L	15.51 ± 1.62	444.26 ± 45.06	14.51 ± 1.62	55.27 ± 4.38	0.79 ± 0.01
MM.L.C	16.72 ± 1.39	469.9 ± 29.41	14.92 ± 0.76	58.15 ± 5.26	0.79 ± 0.02
MM.NL	15.52 ± 0.93	446.55 ± 35.23	14.54 ± 1.27	55.94 ± 3.53	0.79 ± 0.01
	Transverse ^(*)				
	Indentation modulus Ei [GPa]	Hardness H [MPa]	Elastic energy We [μJ]	Plastic energy Wp [μJ]	Ductility measure [1]
	mean ± stdev	mean ± stdev	mean ± stdev	mean ± stdev	mean ± stdev
MM.L	13.93 ± 0.96	414.79 ± 33.87	14.38 ± 1.52	50.81 ± 3.18	0.78 ± 0.01
MM.L.C	14.16 ± 0.89	424.42 ± 38.68	14.70 ± 1.87	51.65 ± 2.76	0.78 ± 0.02
MM.NL	13.9 ± 0.98	420.64 ± 20.93	14.69 ± 0.76	51.76 ± 1.89	0.78 ± 0.01

Table 14 Indentation moduli, hardness and indentation energies for MM groups for axial and transverse indents (a significant difference (labelled (*)) was found only between axial and transverse directions)

4.2.3.2 Indentation properties - comparison between MM and non-MM samples

Given the lack of statistical differences, the multiple myeloma samples were combined into one group (groups prefixed MM) and compared to samples without a neoplastic pathology (non-MM group) taken from the study by Wolfram. The findings were dissimilar in axial and transverse direction (Table 15 (in graphical form in Appendix F.3: Results – graphical form)). In axial direction, the bone samples from the affected population did not seem to be significantly divergent in terms of stiffness (Ei, p=0.06), hardness (H, p=0.90) or plastic energy (Wp, p=0.43), but elastic energy (We) was found to be higher by 24.2% in MM bone (p<0.001), which is related to a 4% decrease in ductility (p<0.001).

Multiple myeloma bone and non-cancerous bone					
Axial					
	Indentation modulus E_i [GPa]	Hardness H [MPa]	Elastic energy W_e [μ J]	Plastic energy W_p [μ J]	Ductility measure [1]
	mean \pm stdev	mean \pm stdev	mean \pm stdev	mean \pm stdev	mean \pm stdev
Myeloma	15.69 \pm 1.52	448.52 \pm 41.66	14.58 \pm 1.44 ^(*)	55.83 \pm 4.39	0.79 \pm 0.01 ^(*)
non-MM	14.97 \pm 1.56	449.81 \pm 41.73	11.73 \pm 1.49 ^(*)	56.81 \pm 6.11	0.83 \pm 0.02 ^(*)
Transverse					
	Indentation modulus E_i [GPa]	Hardness H [MPa]	Elastic energy W_e [μ J]	Plastic energy W_p [μ J]	Ductility measure [1]
	mean \pm stdev	mean \pm stdev	mean \pm stdev	mean \pm stdev	mean \pm stdev
Myeloma	13.97 \pm 0.94 ^(*)	417.49 \pm 32.32 ^(*)	14.49 \pm 1.45 ^(*)	51.13 \pm 2.90 ^(*)	0.78 \pm 0.01 ^(*)
non-MM	11.87 \pm 0.93 ^(*)	373.68 \pm 30.5 ^(*)	10.96 \pm 1.41 ^(*)	47.19 \pm 4.37 ^(*)	0.81 \pm 0.01 ^(*)

Table 15 Comparison between MM infiltrated samples and samples without MM infiltration (significant difference $p < 0.05$, labelled (*))

In the transverse direction, all mechanical properties were found to differ ($p < 0.001$); in particular MM was found to be higher by 17.6%, 11.7%, 32.2% and 8% for E_i , H, W_e and W_p respectively. This resulted in an axial/transverse anisotropy stiffness ratio of 1.2 which is 10.9% lower than the non-affected population in this study. Moreover, the MM was found to be

less ductile by 4.4% in the axial and 4.1% in the transverse direction, where the ductility of the axial/transverse ratio was found to be the same among the affected and non-affected populations.

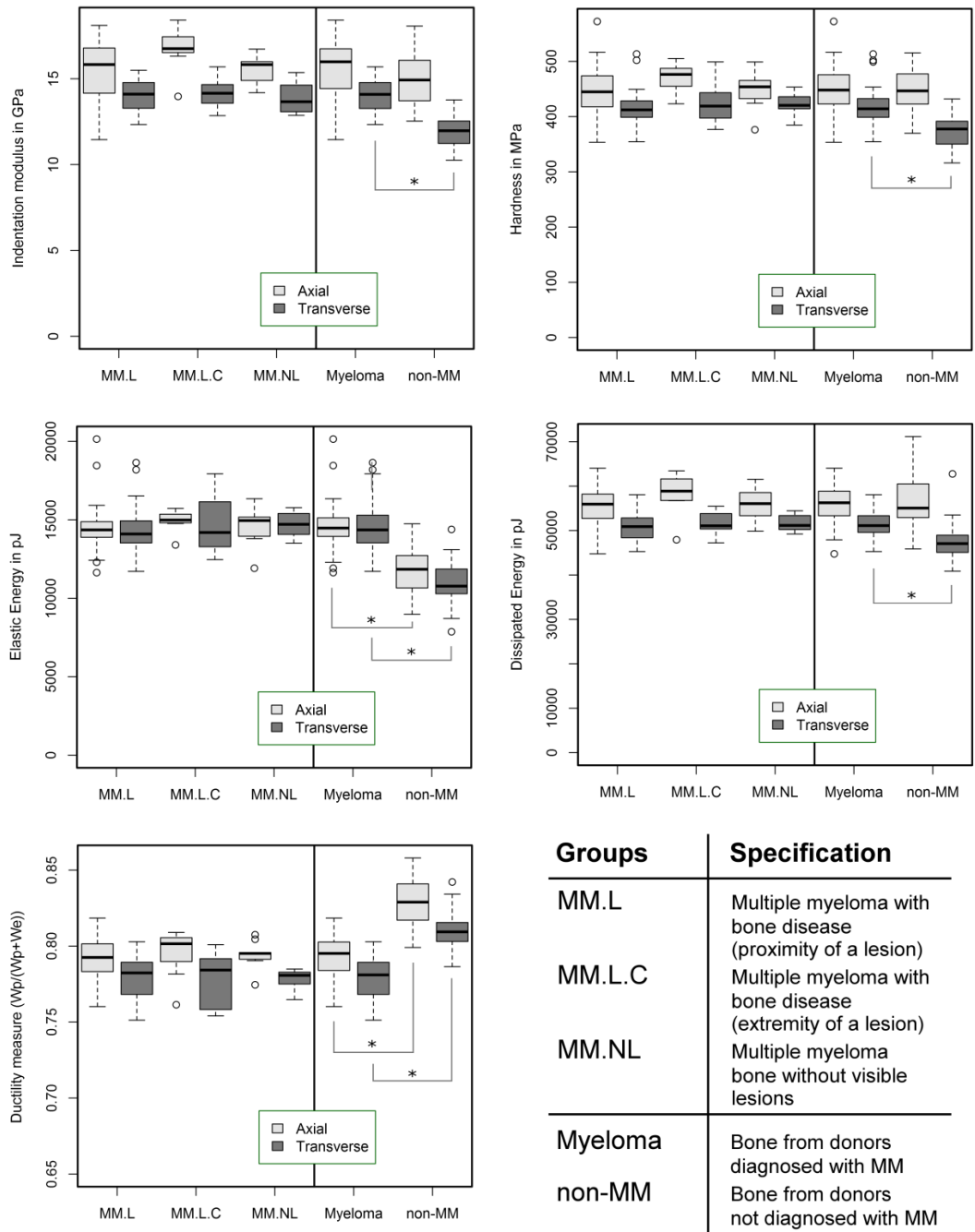


Figure 51 Micro-indentation of multiple myeloma bone: Indentation properties in form of whiskers plot. No significant difference was found between samples with different progression of multiple myeloma infiltration. Only marginal difference was found between myeloma-affected and unaffected population

4.2.3.3 Bone material properties in proximity of lesion

In order to investigate the influence of the distance from the closest lesion on the material properties a total of 1482 indentations were analysed. The indentation modulus was expressed as a function of the shortest distance between the point of indentation and the border of the lesion (Figure 52). In both cases - axial and transversal cuts – the results showed a small but significant trend in modulus change from the lesion towards the surrounding bone. Axially cut trabeculae showed a higher trend (adjusted $R^2=0.049$, $p<0.001$ in Figure 53 a.)). The transversally cut trabeculae showed a smaller, but still significant trend ($R^2=0.008$, $p=0.002$ in Figure 53 b)). In fact, only elastic energy failed to show any significant trend. In general the investigated correlations were found to be weak (Table 16).

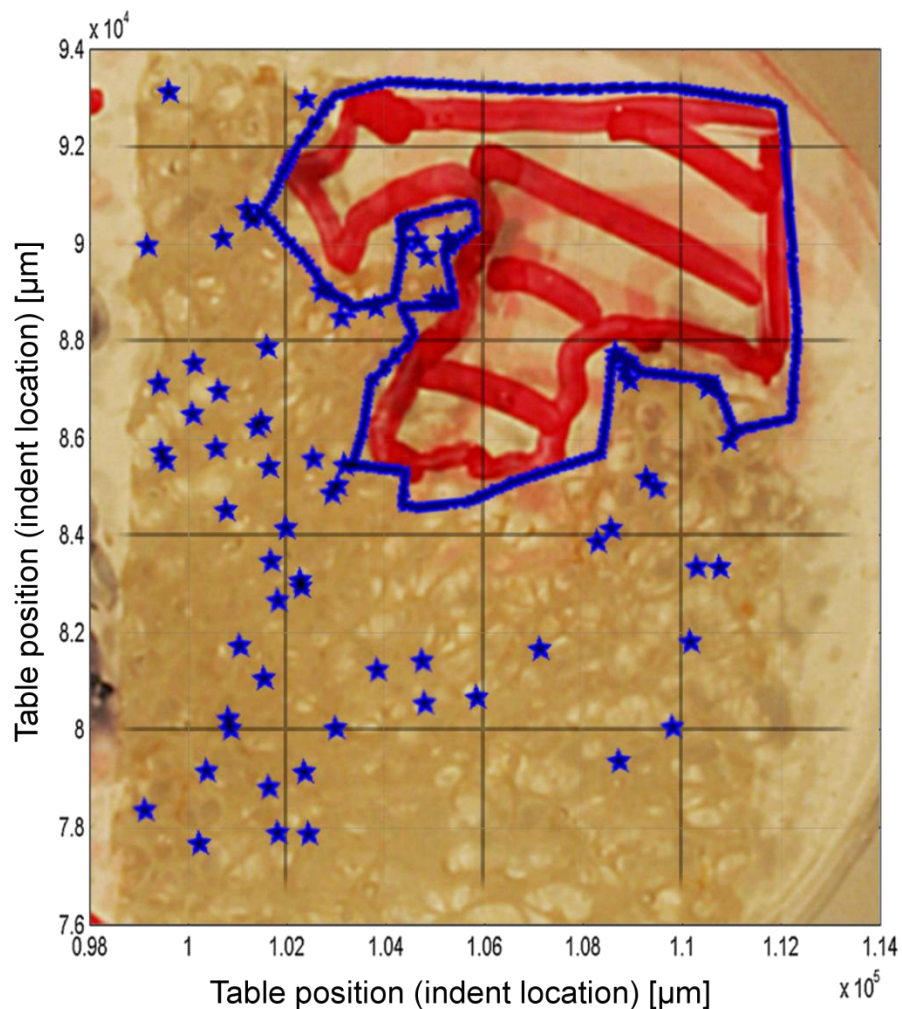
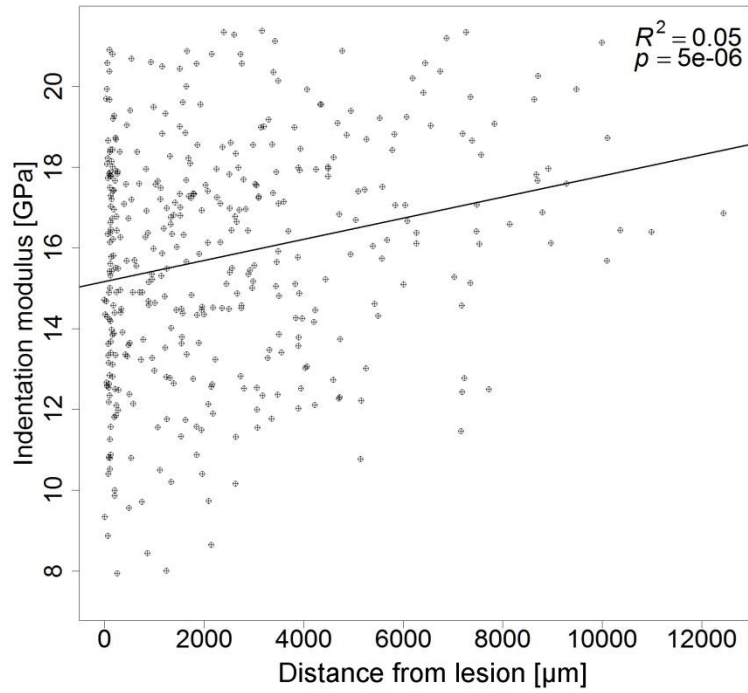
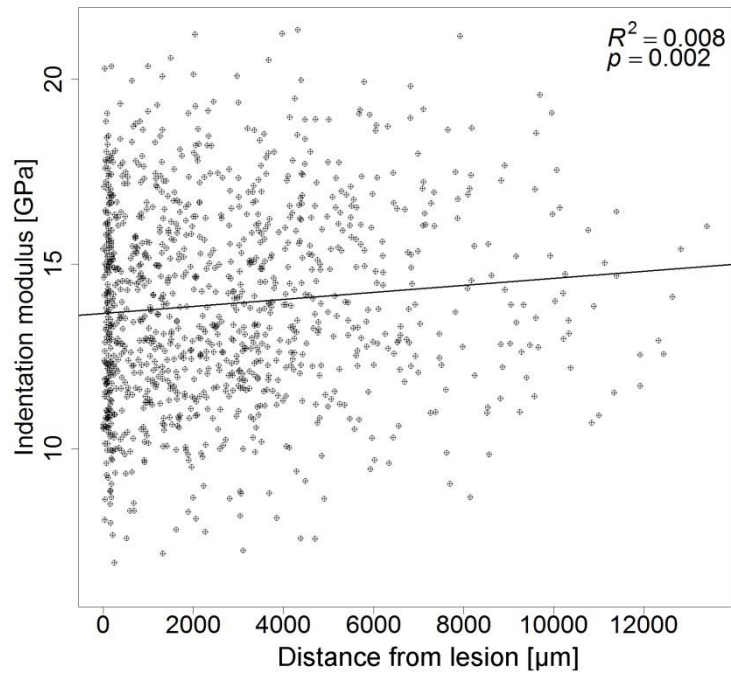


Figure 52 Multiple myeloma bone sample. Indent positions with respect to the border of the lesion are superimposed over a picture of the indented bone. Each indent is represented as a blue star marker, whereas the border coordinates are represented by a solid blue line



Axial indentation direction



Transverse indentation direction

Figure 53 Change of indentation moduli depending on the distance from a lesion

Indentation variable		Adjusted R ²	p-value
Axial	E _i	0.049	<i>p</i> <0.001
	H	0.015	<i>p</i> =0.008
	We	-0.002	<i>p</i> =0.584
	Wp	0.020	<i>p</i> =0.002
Transverse	E _i	0.008	<i>p</i> =0.002
	H	0.014	<i>p</i> <0.001
	We	0.005	<i>p</i> =0.013
	Wp	0.013	<i>p</i> <0.001

Table 16 Coefficient of determination (adjusted R²) and its significance in the vicinity of the lesion

4.2.4 Underlying material properties of multiple myeloma bone - Discussion

Firstly, bone samples from patients diagnosed with MM but without any metastatic infiltration were compared to bone samples from patients with developed myeloma bone disease (MBD). According to the results presented here, the material properties of the bone were not found to be significantly altered. Furthermore the results suggest only a subtle and insignificant increase in the stiffness of the bone at the extremities in cases where the sample was taken from a non-affected site.

When compared to a non-affected population, bone tissue from patients with diagnosed multiple myeloma cancer tended to be slightly but insignificantly stiffer in the axial direction. In the transverse direction, MM bone was shown to be ~17.6% stiffer and 11.4% harder, but was also found to be about 4% less ductile in both directions. The remainder of the tested indentation variables were found not to exhibit significant differences.

Furthermore, findings from the indentation of the bone tissue in the vicinity of the lesion showed only a very small decrease in stiffness in terms of the interaction between bone and lesion, despite its measured significance. This could indicate an increased remodelling of the bone at the periphery of the lytic defects that is associated with a reduced degree of

mineralisation and therefore indentation stiffness. This however contradicts the general understanding that MM inhibits the formation of new bone and that the time required for a lytic lesion to develop is faster than a complete remodelling cycle [250]. This rather small change in indentation variables towards the lesion is also in the same order of magnitude of the measurement error of the indentation technique hence should only be considered as fractional.

However, despite the indication that the bone generally tends to be stiffer in multiple myeloma cancer patients and considering that the increase in stiffness in the vicinity of a lesion is almost negligible, the relative change in mechanical properties at the tissue level remains consistent within the whole organ and is independent of how the disease propagates. A minor alteration in the material properties of bone tissue in multiple myeloma patients could be explained by increased mineralisation due to the frequent and prolonged use of bisphosphonates which reduces the natural bone turnover [251] and which then leads to increased bone mineralisation [252] and hence can result in an increase of the indentation properties [182]. Results in this study hence suggest that changes in multiple myeloma cancer bone, however insignificant, originate from a reduced turnover due to treatment methods rather than from the presence of the cancer directly.

The values presented in this study should be re-used with care when comparing them to actual physiological conditions as the study was performed under dried conditions. However, this study has aimed to detect differences in the mechanical properties of bone tissue through progressing pathology rather than to quantify accurate values under physiological conditions. Secondly, the study was limited due to the low number of patients available and the lack of detailed patient treatment histories, which could have added a significant variable to the material changes in patients' vertebral bone tissue. Lastly, for the following studies it is highly recommended to undertake additional compositional analyses such as mineralisation and collagen cross-linking assessments to help develop a better understanding of compositional changes occurring due to neoplastic pathology.

Following discussion in the fracture prediction section it remains unclear whether this behaviour observed in this study can be translated to any oncological pathologies.

To conclude, apart from very small changes in the vicinity of the lesion, it appears that the alterations of mechanical properties at the bone tissue level are rather ubiquitous in nature. Furthermore, it can be assumed that these small changes in material properties alone would not be sufficient to modify the overall vertebral strength. This leads to the hypothesis that the material law used in density image-based methods should remain unaltered in the case of multiple myeloma when compared to normal and osteoporotic bone.

4.3 Trabecular bone micro-properties assessment - Summary

Chapter 4 presented a comparative analysis of multiple contributors to biomechanical properties of weakened vertebral bone while focusing on the underlying micro-properties. The results presented here emphasise the benefit of using bone density distribution alongside bone deterioration measurements. Thereafter, results of the beam theory approach were compared to a morphological assessment and one-slice analysis. As has been noted, a full morphological analysis together with a composite assessment explains up to 84% of variations in strength for all samples (more specifically up to 81, 96 and 94% for OP, MM and mets respectively) and 69% of variations in stiffness (80, 96 and 79% for OP, MM and mets respectively). The single slice analysis was however proved to be a good indicator considering the dependency on time and exposure to scanning, with a reduction of only one-third in the coefficient of determination compared to multiple variable regression using beam theory and all morphology parameters.

The second section of this chapter presented the experimental testing of bone material properties by means of micro-indentation which was necessary to define more clearly the underlying properties of cancer bone. The aim of this section was to illustrate differences between multiple myeloma bone with and without lesions and to compare the material properties to a non-affected population.

As shown in this part of the thesis, no significant differences in indentation properties were found between bone taken from proximity to the lesion compared to bone taken more remotely ($p > 0.05$). Moreover, no differences were observed between bone taken from both of the MBD groups and bone taken from MM patients without the presence of lesions ($p > 0.05$). Compared to the non-affected population, the MM samples were non-significantly stiffer in the axial direction ($p = 0.06$) and by 18% stiffer

($p < 0.001$) in the transverse direction. Hardness was found to be higher in MM samples only in the transverse direction by 12% ($p < 0.001$).

The results presented here suggest that the weakening of the myelomic bone is predominantly due to structural changes which will be presented in the following sections. This however cannot be generalised to include all oncological samples due to notable differences in the metabolic management of different lesions depending on the identification of the primary cancer (such as indicated also by assessment of the bladder cancer samples in the preliminary study conducted in section 3.1.3.2: “Historical data - Collected metastatic samples”).

Chapter 5

Investigation into the use of vertebroplasty for the augmentation of osteoporotic and metastatic lesions

This last experimental section of the thesis focuses on optimising the vertebroplasty technique with subsections focusing on newly developed ceramic materials (section 5.1: CaP vertebroplasty: effect of filling ratio on biomechanics in a single vertebra study”) and a tailored PMMA bone filling material (section 5.2: “Low modulus PMMA vertebroplasty”). Each type of cement and details regarding their use have been discussed in the literature review (sections: 2.4 and 2.5). While CaP cement provides lower structural support, its main advantage comes from its biodegradable nature supporting newly formed bone, however the challenge lies in optimising the augmented volume of the cement with respect to altered biomechanical properties. Contrary to CaP, the PMMA cement provides fast and efficient short term support to the weakened vertebral bone but appears controversial due to an altered biomechanical imprint affecting the adjacent levels. This is believed to be due to its unnaturally high stiffness which will be investigated in the latter section of this chapter.

5.1 CaP vertebroplasty: effect of filling ratio on biomechanics in a single vertebra study

5.1.1 Introduction to ceramic cement PVP

Since introduction of the vertebroplasty in 1984 [131], the PMMA augmentation has become a relatively established technique for fracture treatment. There are however a number of reservations associated with using these acrylic cements in terms of intraoperative and long-term complications. The exothermic reaction during polymerisation exceeds the biological threshold of 40 degrees Celsius and can reach as high as 100°C [253-255], potentially damaging the surrounding tissue including the spinal cord and nerve roots [254-256]. This can be exacerbated due to the high injection pressure, often causing extravasation and/or pulmonary embolization [257]. Once delivered and integrated into the bone structure, acrylic cement irreversibly becomes a permanent foreign body due to the lack of osteo-conductivity and may interfere with natural bioactivity.

Considering the limitations of acrylic cements, recent attempts have aimed to develop a bone cement that would meet the biomechanical needs of stabilising the fracture [258] but which would eventually be reabsorbed and replaced by the natural bone [259]. In this matter the calcium phosphates have shown good potential in comparison to the PMMA, which is not osteo-conductive or resorbable. Turner et al. [260] compared PMMA with calcium phosphate cement in an *in-vivo* canine model and reported that in the framework of 6 months, bone augmented with CaP was found to be stronger than bone augmented with PMMA, which in fact became marginally weaker. Moreover, as reported in an animal study by Urrutia et al. [261], acrylic cements have been found to cause osteonecrosis in almost every second case tested. In contrast, a new bone formed around CaP cement was found to have developed as soon as two weeks after the operation [262] and was confirmed by Ikenaga et al. [263] and Knaack et al. [264], who reported the development of the same or even a superior quality of bone within as little as 12 weeks from its administration. This said, the biodegradable osteo-conductive materials provide a promising alternative to the current state-of-the-art standard PMMA cement particularly for younger patients who are not treated for malignant pathologies.

Nevertheless, the extent of any immediate biomechanical effect prior to the healing of the bone remains unknown. The restoration of the vertebral stability remains likely if both the strength and stiffness recover to the pre-fracture state of the bone [258], but avoids an excessive increase in stiffness which is typical for PMMA cements [265] and is one of the factors believed to increase stress in adjacent levels of the bone [266]. Although recent studies have provided important information on the biomechanical behaviour of the CaP after the augmentation, only limited information is available relating to the mechanical effects of the volume of injected cement. Whether CaP cements lack volume-strength and -stiffness correlation similar to that reported for PMMA [29] remains unknown.

The study presented here aims to quantify the material properties of a particular biodegradable material. Three groups augmented with different volume-to-fill ratios have been compared in a cadaveric destructive experiment. The samples collected were osteoporotic only and showed no sign of malignant pathologies, of which in total thirty samples were allocated to three groups according to their structural properties. To tackle the well-known difficulties in benchmarking the samples prior to testing, a newly proposed method of sample allocation has been conducted with the use of

non-invasive CT-based fracture prediction. Currently all studies face a problem in the selection of appropriate samples, using either BMD (e.g. [29, 267, 268]) or random selection (e.g. [265, 269]). Using the non-invasive fracture prediction method formerly described in this work allows for the choice of appropriate samples for testing, such as the collection of purely weaker samples prone to fracture. The benchmarking proposed here is based on Latin rectangle design [270]. The VBs were assigned to three groups, each of which contained the same number of specimens from each donor, allocated equally according to their predicted strength relative to the donor. When tested, the appropriateness of the distribution was confirmed against initial fracture data, with an equal distribution of actual vertebral strength and stiffness in each of the groups.

5.1.2 Methods used in CaP PVP

5.1.2.1 CaP study design

This study was designed in collaboration with SpineFX partner BONESUPPORT (BONESUPPORT AB, Lund, Sweden). In this study biocompatible alpha-tri-calcium cement developed by the company has been biomechanically tested. This study provides evaluation prior to the healing process with focus on optimisation of cement volume as described further and in the flowchart presented in Figure 54.

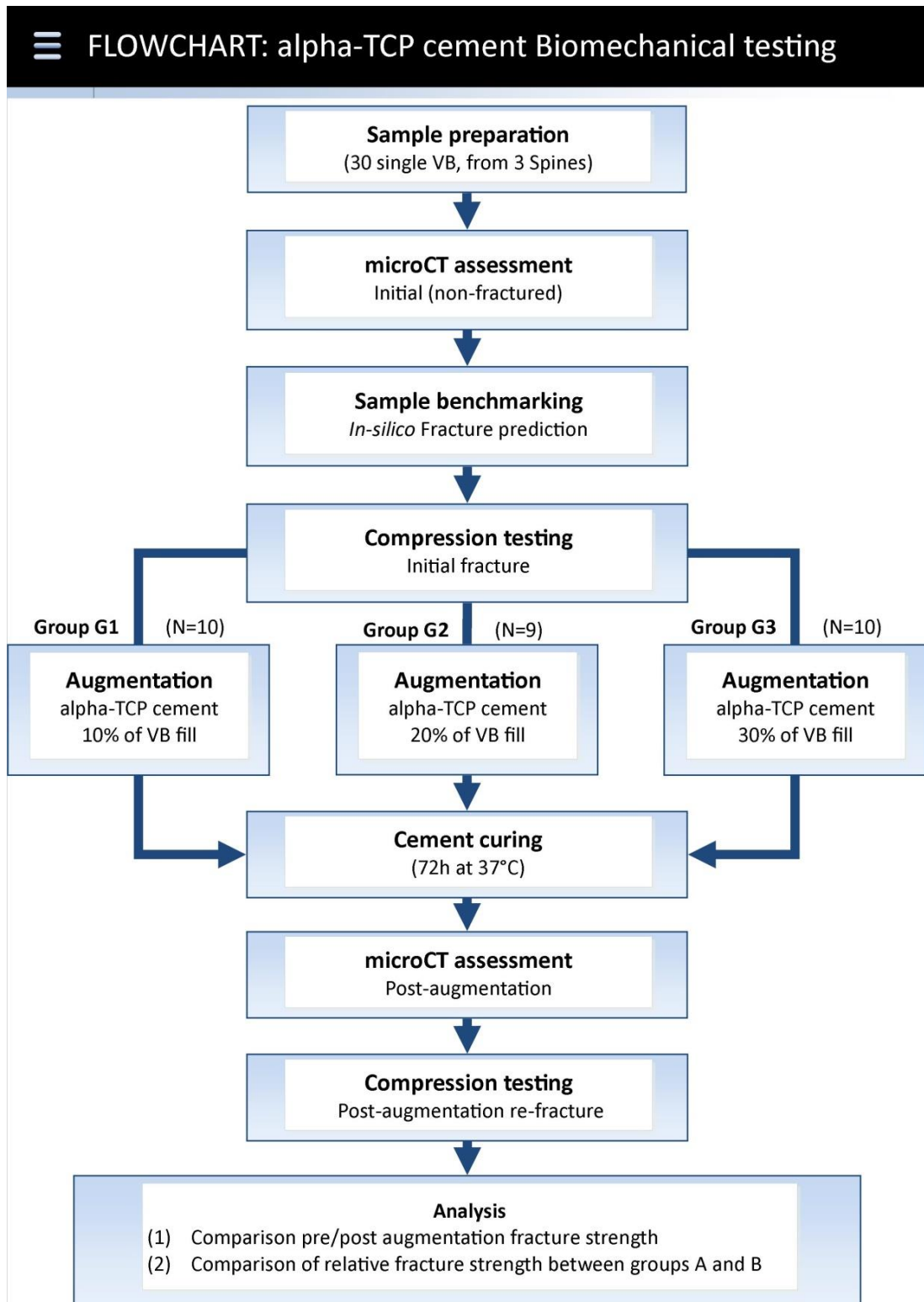


Figure 54: Alpha-TCP cement study flowchart. Three groups of different vertebral volume fill were separately tested and compared for difference in observed vertebral strength

5.1.2.2 Sample population and group allocation prior to CaP augmentation

This study comprised twenty nine thoraco-lumbar vertebral samples in total (3 spines denote as “SpineBS” in Table 8: subsection “Cadaveric sample selection and preparation”). The microCT assessment discussed in previous sections has in addition been used to estimate vertebral body volume using previously employed methods in order to remain consistent. For comparison the mean error between the semiautomatic method used a vertebral body boundary segmentation and this method was found below to be an accepted experimental error (mean error -1.21cm^3 (RMS=3.37), tested on 28 osteoporotic human vertebral bodies). This method was tested to estimate the vertebral volume calculated from the inferior, superior and middle vertebral body cross-sections and the vertebral height following equation (1.10), where V_{VB} denotes vertebral volume, and h_1 and h_2 denote the height between slices. CSA was estimated in three subsequent slices and averaged to minimise the measurement error.

$$V_{VB} = \frac{(CSA_{inferior} + CSA_{middle})}{2} * h_1 + \frac{(CSA_{superior} + CSA_{middle})}{2} * h_2 \quad (1.10)$$

Samples were benchmarked and allocated to three equal groups (A, B, C) entirely based on predicted vertebral strength (discussed in section 3.3), while the t-test statistical analysis on initial strength and stiffness was later used to verify equal distribution between tested groups. Every group represented a different volume of augmentation fill of 10, 20 and 30% of vertebral body fill for groups A, B and C respectively.

5.1.2.3 CaP PVP and repeated fracture testing

Prior to injection all specimens were submerged in Sodium Azide solution (0.03 wt% concentration) and kept in a temperature regulated oven (37°C) for 1 hour. Injection needles (gauge 11) were positioned towards the anterior wall of the vertebral body (Figure 55 (A)) and if needed were slightly retracted to allow the cement to smoothly fill the vertebral body. The cement was prepared following appropriate training provided by the collaborating company representative and immediately after mixing the cement was redistributed to 1mL syringes. Each fractured specimen was augmented bipedicularly until reaching the desired fill according to group allocation. When augmented the sample was again submerged in Sodium Azide solution (0.03 wt% concentration) and kept in a temperature regulated oven at 37°C for an additional 72 hours to simulate physiological conditions and allow adequate time for cement curing. The Sodium Azide solution was renewed

on the second day of curing. The importance of the curing lies in the ongoing conversion from α -TCP to calcium deficient hydroxyapatite (CDHA), which results in a strength enhancement. Here, both the time of curing as well as the temperature is important as both contribute to an enhancement of the quality of the crystallinity of the forming apatite.

After 72 hours samples were taken out of the oven, rinsed in soapy water followed by thorough rinsing in purified water, wrapped in moist tissue and left frozen at -20°C until scanning. The freezing of specimens prior to scanning permitted a prolongation of the handling time and the processing of all samples under considerably consistent protocols. Although curing at low temperatures is detrimental for CaP cements [259], it has been shown that freezing to temperatures of -80°C together with cement retarding additives are actually needed to prevent the beginning of the setting reaction [271]. Every sample underwent microCT scanning to verify correct placement of the injected cement. As depicted in Figure 55 (B), example samples were later processed in data visualisation software [272] for presentation purposes to illustrate the positioning of the cement bolus within the vertebral body.

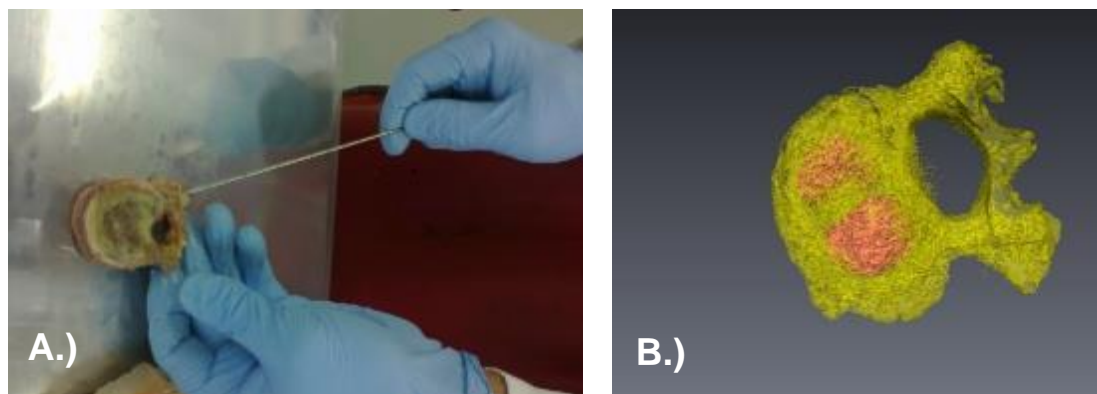


Figure 55: α -TCP cement augmentation: Needle is inserted via pedicles (A) similarly to clinical application. When positioned to anterior middle region of VB, cannula is inserted to inject an appropriate volume of cement in order to create two symmetrically placed boluses (represented in the rendered bone/cement model depicted in B, red representing cement, yellow representing bone)

Repeated mechanical testing was conducted as per protocol for wedge compression fracture following the thawing period overnight. The outcome of the mechanical testing was processed in a custom-build program (discussed in subsection “Single vertebra Wedge Compression Fracture rig”) to determine strength and stiffness during the testing.

Data were analysed in statistical computing language R [237]. The augmentation effects prior and after augmentation were tested using a paired t-test with significance level $p=0.05$.

5.1.3 Volume optimisation in CaP vertebroplasty - Results

The allocation of samples to groups has been statistically tested and it has been established that the vertebrae were distributed sufficiently without significant difference in mean strength and stiffness among the groups (ANOVA, student's t-test for strength G1 vs G2: $p>0.9$, G1 vs G3: $p>0.37$ and G2 vs G3: $p>0.31$, and for stiffness G1 vs G2: $p>0.91$, G1 vs G3: $p>0.52$ and G2 vs G3: $p>0.49$).

The group's annotated G1 (10% VB fill), G2 (20% VB fill) and G3 (30% VB fill) were injected according to the measured VB volumes which corresponded to 2.1 ± 0.7 , 4.3 ± 1.2 and 6.4 ± 2.0 mL of the cement respectively. Here, the gross measurement before and after the injection did not show any restoration of the vertebral height.

Later, all the samples underwent a re-fracture compression test resulting in a typical augmentation-amended load/displacement profile (Figure 56). Compared to the initial compression test of non-augmented vertebrae, the reinforced vertebrae showed a typical behaviour of continuous fracturing of trabecular bone which remained unaugmented. Later however, once the weaker bone is fractured, the stiffness of the cement becomes apparent, rapidly increasing the resilience. Such reinforced material results in a relatively linear load-displacement curve until fracture, which is typically followed by a drop in force. Under these circumstances the ratio between strength and stiffness becomes the most informative.

Comparing the samples pre- and post-augmentation has shown that the augmentation more than doubled the vertebral strength (Figure 57); only group 1 failed to reach the significance level of 0.05 (G1: $p=0.053$, G2: $p=0.023$ and G3: $p=0.007$). As shown in Figure 58 the stiffness was significantly lower than its initial value, specifically less than half of the initial stiffness in all three tested groups ($p=0.005$, $p=0.02$ and $p=0.004$ for G1, G2 and G3 respectively). Specifically, vertebral strength has increased compared to its initial values by 99.52%, 166.91% and 111.3% for groups G1, G2 and G3 respectively. The stiffness was restored by the augmentation only to 43.99%, 31.98% and 44.92% for groups G1, G2 and G3 respectively. Both the strength and stiffness improvements are listed in Table 17.

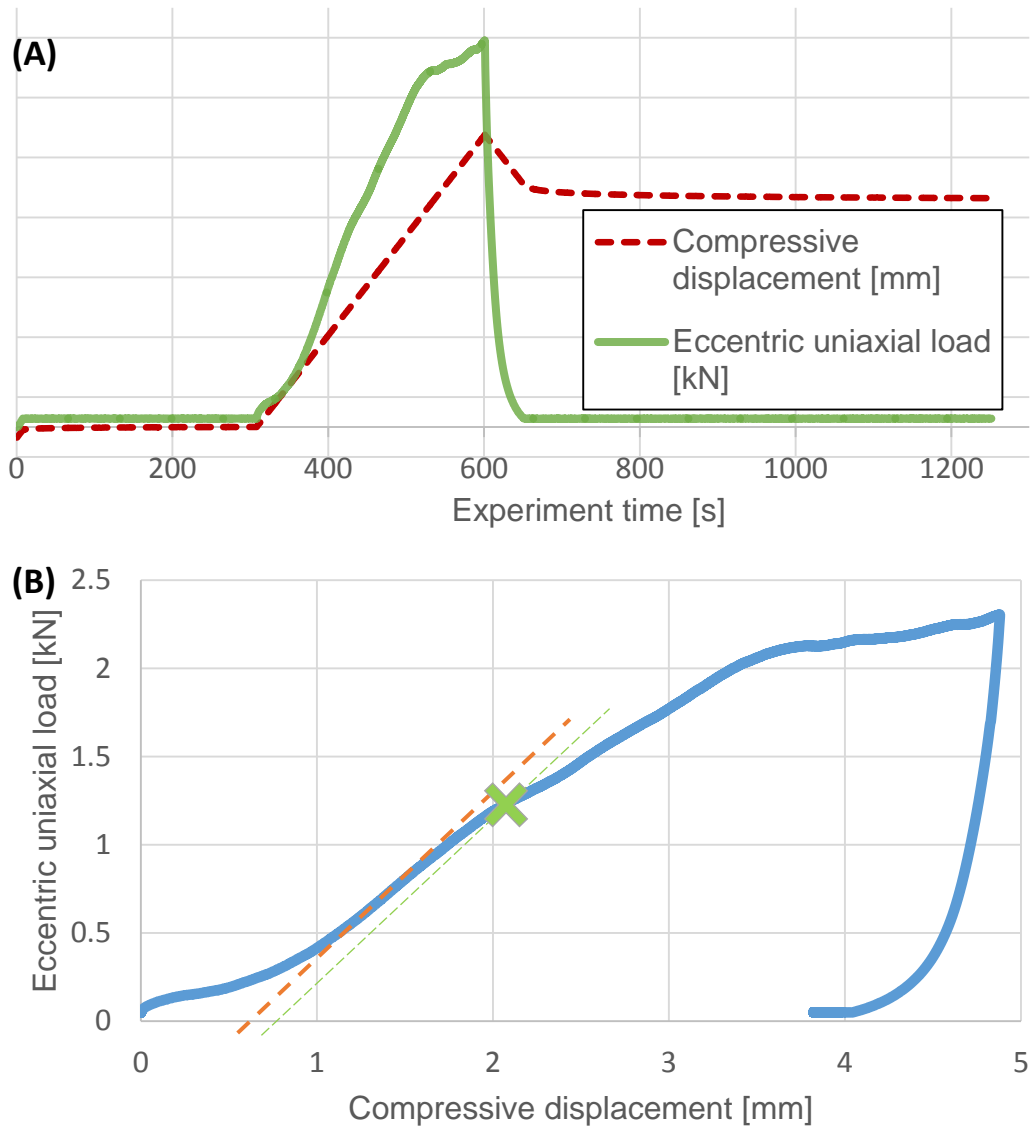


Figure 56 A representative experimental read-out of augmented vertebra during the re-fracture experiment. Here raw testing data (in (A)) represent displacement data (dashed red) coupled by readout frequency with the load read-out data (green). The re-fracture experiment follows the same protocol as for the initial fracture (Figure 29). The augmented vertebra is represented by increased resilience where cement enhances the load-bearing capabilities of the vertebra (load displacement curve in B)

Furthermore, there no influence was shown by the different filling ratios of 10%, 20% and 30% (denoted groups G1,G2 and G3 respectively) as both post augmentation strength and stiffness failed to show any difference ($p \gg 0.05$)

When compared with a statistical population of 29 samples, the CaP cement augmentation has been shown to increase the strength compared to the intact sample by 121% and restore the stiffness to 41% of the state before the fracture.

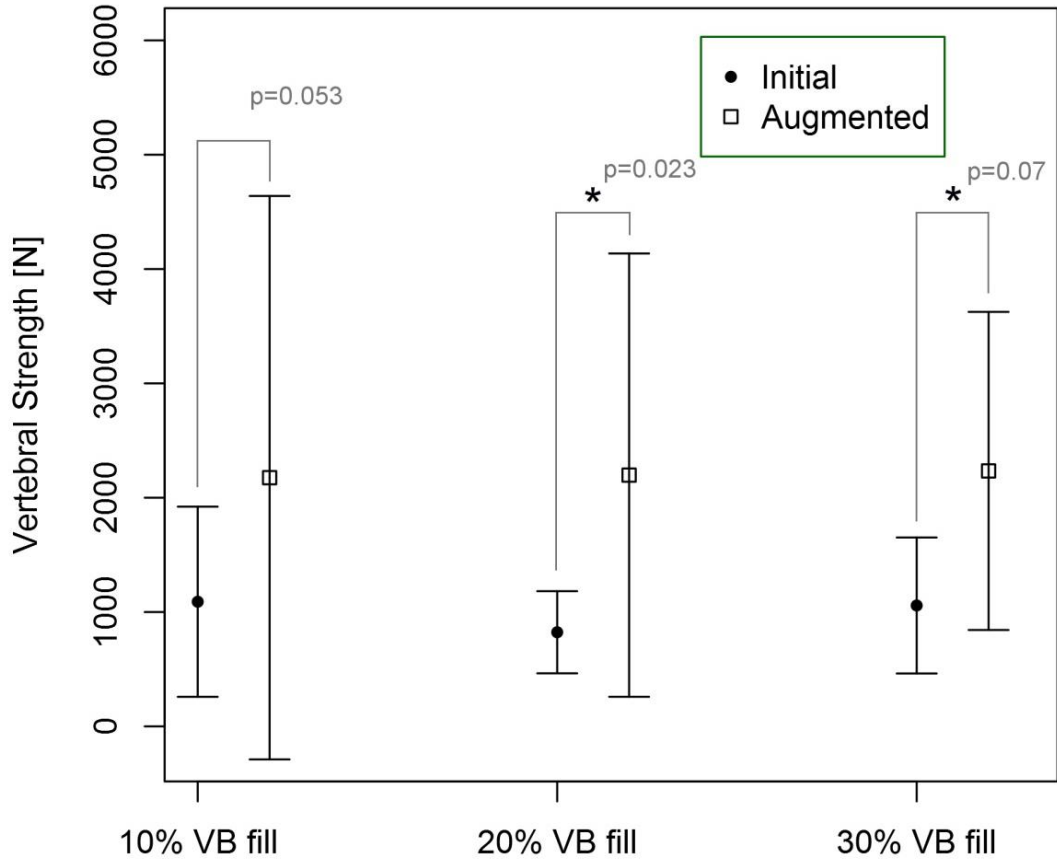


Figure 57 Vertebral strength after augmentation was found to be significantly higher in 20 and 30% VB fill (significance level $p < 0.05$ indicated by *)

	Strength (kN)	Stiffness (kN/mm)
VB fill of 10% (G1)	1.1($p=0.053$)	0.94($p=0.005$)
VB fill of 20% (G2)	1.4($p=0.023$)	0.58($p=0.021$)
VB fill of 30% (G3)	1.2($p=0.007$)	0.93($p=0.004$)

Table 17 Vertebral strength and stiffness enhancement after VB augmentation (mean difference pre- and post-augmentation), significance level of $p=0.05$ shows that a statistical difference was found in vertebral strength pre- and post-augmentation fracture in the group filled with 10% of vertebral body volume

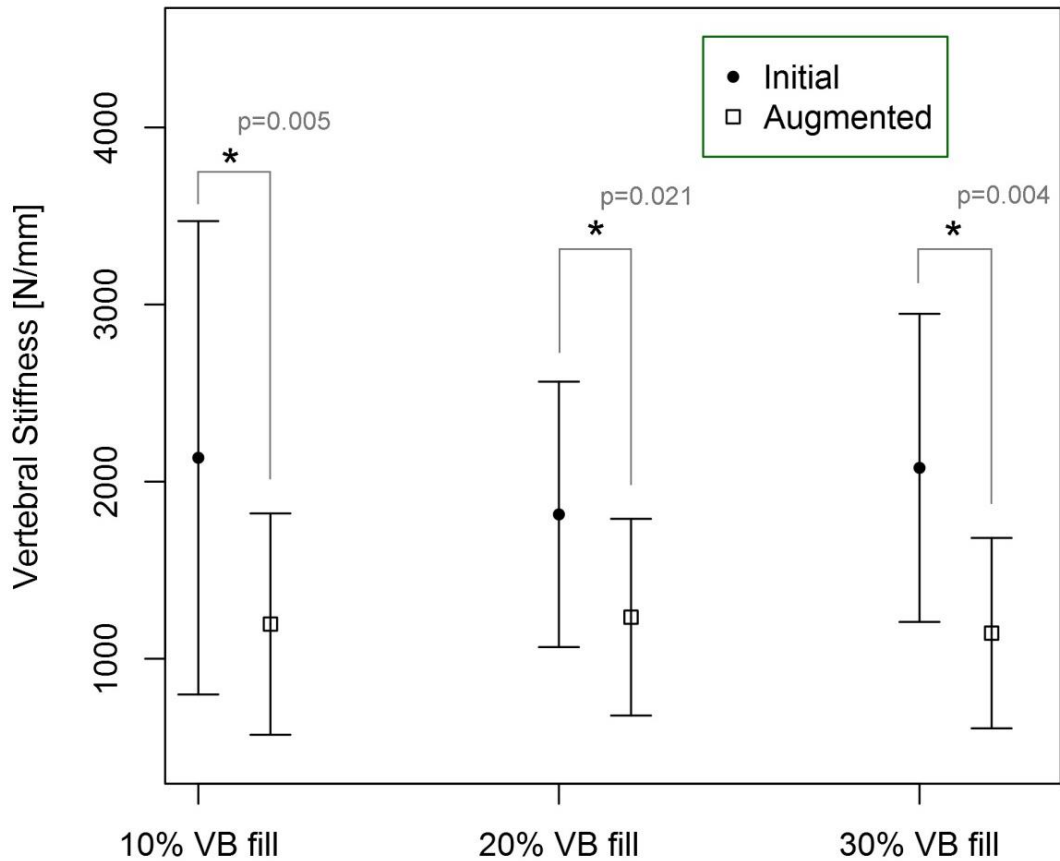


Figure 58 Vertebral stiffness of augmented vertebrae where no difference was found in osteoporotic samples $p>0.05$, but the stiffness has decreased in both oncological groups ($p<0.05$) Short term biomechanical effect when using CaP PVP - Discussion

In order to obtain a structural assessment of wedge compression fracture treatment, a clinical calcium phosphate vertebroplasty has been simulated under laboratory conditions. It consisted of the controlled administration of cement with a subsequent compression test. This study performed on human cadaver vertebrae evaluated the mechanical effect of newly developed calcium cement. Contrary to PMMA, the calcium phosphate cement is designed to support the natural growth and hence recovery of the fractured bone. Here, the introduced cement is primarily an agent to trigger the natural healing process [124], which should support the bone only up to point at which it is healed. The optimal amount of material which needs to be injected however remains unknown and the exact amount required may cause considerable issues during the surgical planning.

This study demonstrated that increasing the volume of the injected calcium phosphate cement from 10% to 30% of VB fill only showed a limited impact in terms of the vertebral biomechanical properties. Although the

volume fill has not statistically been found to be an impacting factor, the biomechanical properties of all tested samples have been found to significantly change following the vertebroplasty. In particular, the ceramic cement almost doubled the strength of the cadaveric vertebrae, while stiffness was almost halved when compared to pre-augmentation values. This indicates that while the strength has been fully restored to its initial value, the stiffness remained below its initial values.

Regarding the effects of different volumes of cement, this study concludes that even smaller volumes (~2mL, 10% of vertebral body volume) may be sufficient to stabilise the fracture, suggesting that the volume of introduced cement is not crucial in terms of biomechanical improvement. Although some degree of recovery of the stiffness is needed to prevent extensive micro-motion, it remains unknown whether a full restoration would in fact be beneficial for the healing process. The complexity of the healing process has long been studied by, among others, Claes et al. [273] who showed in an *in-vivo* ovine experiment that in fact, a substantial amount of micro-motion is required in order to trigger it. Whether human osteoporotic bone reacts in a similar pattern remains an open question and whether this then links to the use of low stiffness cements would need a thorough clinical investigation.

Nonetheless, these findings imply that volumes below 30% of VB fill are not a crucial factor in enhancing vertebral strength and stiffness. Hence, these results could be used if the volume of augmented cement needs to be adjusted instead according to the bioactive character of the cement to achieve the optimal conditions for healing of the bone without affecting the resultant mechanical properties of the augmented vertebra.

A similar trend to the results here has been shown by previous investigators [29, 30, 258, 267], i.e. that calcium phosphate cements have also been shown to restore or even increase the initial strength without restoring the initial stiffness, which was also presented for PMMA cements such as one used in clinical application with positive outcomes [274]

Conversely, Bai et al. [265] and Heini et al. [268] reported that both the strength and stiffness had been increased. In Bai's study, stiffness was restored to its initial values prior to the fracture (increasing from 0.08kN/mm to 0.1kN/mm), while Heini reported a greater than twofold increase in the initial stiffness after the augmentation (2kN/mm to 4.4kN/mm). A discrepancy in the measured stiffnesses is believed to occur due to different loading protocols. Here, Bai used the wedge compression fracture approach

although the pivot point was positioned posteriorly to laminas, contrary to Heini's pure compression where both endplates were firmly embedded and compressed to failure.

Moreover, the increased stiffness observed by Heini's contradictory study could be explained by a significantly higher augmentation ratio obtained when a fixed amount of cement has been augmented in vertebrae of different bone quality. Graphs from the author's paper also suggest a possible increase of strength above >40% fill but did not present data for stiffness, causing it to remain in doubt whether a similar effect would occur.

The study presented here is limited to an assessment of biomechanical behaviour in a relatively short time after the operation. The cadaver-based nature of the study hence limits any conclusions to the immediate behaviour of cement after three days of curing, and although temperature and humidity have been controlled, the cement has been left to cure without any natural preloading which could also potentially affect the setting and creeping of the material.

Clearly, a biomechanical evaluation during the later phases of the CaP/bone reabsorption needs to be conducted in order to confirm the findings from the pre-clinical animal studies [261, 263, 264].

Although some minor issues have been noticed due to the granulation effect of the mixture, only manual injection has been used which was considered to be much easier when compared to administration of a standard PMMA. The cases reported here were carefully examined with the intention of preventing the filter-pressing phenomena such as those reported by other investigators working with phosphate cements [275, 276], and in all cases was determined to be a typical clogging reaction of the calcium phosphate cement as reported by e.g. Montufar et al. [277]. A bias in the results due to filter-pressing phenomena has always been avoided by injecting the entire contents of the syringe and in case of observed granulation the batch was immediately discarded and the test repeated. Despite demonstrating only partial extravasation and no case of spinal canal extravasation, fluoroscopy guidance is strongly recommended due to the low viscosity of the cement.

The major limitation of this study proved to be the storage of samples which, although fully reported and monitored, needed to include freezing after the three day period of curing. The freezing of samples has however remained consistent within the study and allowed systematic logistical

handling without any unnecessary decay of the samples. Additionally, by freezing the cement the setting reaction is merely slowed down [259] and as Grover et al. [278] reported further, temperatures in excess of -80°C and over a month of storage would be required to significantly degrade the compression strength of the cement.

Yet it has been reported here that these fill volumes appear to have no effect on the restoration of stiffness before the commencement of the healing process. Although the resulting changes in strength and stiffness due to augmentation with the α -TCP cement presented here are similar to the conclusions obtained using a commercially available PMMA cement [258] which has been used clinically for many years, a clinical trial will need to be conducted to confirm this.

5.2 Low modulus PMMA vertebroplasty

5.2.1 Introduction to acrylic cement augmentation in OP and metastatic bone

Numerous studies have shown promising results in vertebral body fracture treatment using acrylic cements. Such treatment is recommended in many studies where conservative treatment is no longer effective. Despite large numbers of PVP operations worldwide, very little is known about the biomechanical contribution of the cement used.

One of the controversies of PVP comes from recent findings which show that administering this very hard cement (compressive strength ~ 0.1 GPa, elastic modulus ~ 2 -4 GPa [279, 280]) might be linked to an increased occurrence of fractures in adjacent levels [281, 282]. When cured, such material exhibits stiffness exceeding up to one order of magnitude with strength exceeding up to two orders of magnitude [279, 280] compared to the bone embedded within [189, 202].

Although the cause of adjacent vertebral fractures is not clear, the material properties of the cement used are considered to be one of the possible causes alongside other factors such as the endplate-to-endplate pillaring effect [122, 282], extravasation [266], the natural progress of the primary disease [283, 284] or a secondary effect of the disease treatment [285]. Another explanation however arises from a biomechanical viewpoint, such as dramatic changes in boundary conditions and the possible displacement of the primary loading vector due to the presence of the fracture.

Historically, acrylic cement has been used to stabilise fractures and reinforce vertebral bone in a very short time, however recent concerns report an increase in adjacent vertebral fractures, which questions the material properties of the used cements.

Computational modelling has suggested that the reduced strength can be explained by the “pillaring” effect of the cement bolus between both endplates [159, 266, 286, 287]. While clinical studies report, without any explanation, the increased occurrence of adjacent fractures (e.g. [122, 282, 288, 289]), they agree on the fact that PMMA acts as a foreign body inside the vertebra thus causing these problems, which now needs further investigation.

The studies mentioned above greatly succeeded in pinpointing the possible causes and basic science biomechanics of adjacent fractures, however they lack experimental confirmation and/or clinical evidence of suggested solutions. The studies mutually concluded that future investigation into the issue of reduced strength in adjacent levels should be conducted 1) using osteo-conductive (biodegradable) cement; 2) using low modulus cement. Where (1), in terms of pillaring effect investigations, requires long term follow-up studies exceeding cadaveric testing capabilities, the latter is presented here in a quasi-static biomechanical comparison of a standard off-the-shelf and low modulus PMMA cement.

5.2.2 Methods used in assessing low-modulus PMMA cement

5.2.2.1 PMMA PVP - Study design

This study was designed in collaboration with the University of Uppsala. The intention of this work was to investigate the mechanical properties of an enhanced cement formula which was tailored to address the increased occurrence of fractures due to the high stiffness of the injected cement in adjacent levels to those in which vertebroplasty is performed.

The enhanced cement which is from less stiff material was tested against the base PMMA commercially available cement and each cement was also tested in each of two pathologies to investigate use of the cement in (1) osteoporotic patients, (2) patients suffering from a cancer with metastatic infiltration. A schematic overall flowchart of the study is depicted in Figure 59.



Figure 59: Study flowcharts for two scenarios, osteoporotic (a) and metastatic (b) vertebral augmentation studies comparing two cements: non-modified cement (G1) and one with enhanced formula (G2)

5.2.2.2 Sample population and group allocation prior to augmentation

This study comprised twenty-four osteoporotic thoraco-lumbar samples (samples denoted as “SpineGO” in Table 8: subsection “Cadaveric sample selection and preparation”) together with twenty-four metastatic thoraco-lumbar samples (samples denoted as “Spine mets” in Table 8: subsection “Cadaveric sample selection and preparation”, levels T6-L5). Injection volumes were calculated based on the microCT assessment using equation (1.10). Initial fracture data together with fracture prediction data remain identical to those discussed in section 3.2: Commissioning of cadaveric Wedge Compression Fracture testing.

Based on the predicted strength each of the samples were benchmarked and allocated to one of two equal groups (G1 and G2). Here the group G1 represented base cement (non-modified Osteopal) whereas the group G2 represented modified cement (Osteopal 1.5%).

5.2.2.3 PMMA PVP and refracturing experiment

Prior to the injection all needles (gauge 11) were inserted under a fluoroscopic guidance by a trained surgeon (Vishal Borse). Needles were positioned through both pedicles facing the anterior part of the vertebral body. The insertion depth was recorded for later repositioning prior to the augmentation.

In addition all specimens were submerged in Sodium Azide solution (0.03 wt% concentration) and kept in a temperature regulated oven (37°C) for 1 hour. The injection needles (gauge 11) were re-inserted to their appropriate position and if needed were slightly retracted to allow the cement to smoothly fill the vertebral body. The cement was prepared by a skilled material scientist (Alejandro Lopez, University of Uppsala). The cement was mixed and distributed to 5mL syringes used for augmentation. Each fractured specimen was augmented bi-pedicularly until reaching a fill of 30% of its vertebral volume fill with cement according to the group allocation. Augmentation was performed without the fluoroscopy guidance due to (1) the requirement of mixing the cement in a ventilated fume cupboard, and (2) the preheating protocol required to minimise the time spent by each sample outside of a temperature-regulated environment. Then the augmented sample was again submerged in Sodium Azide solution (0.03 wt% concentration) and kept in a temperature regulated oven (37°C) for an additional 24 hours to simulate physiological conditions and allow adequate time for cement curing.

After a curing period of 24 hours, the samples were taken out of the oven, rinsed in soapy water followed by thorough rinsing in purified water, wrapped in moist tissue and left to freeze until scanning. Every sample underwent microCT scanning to verify correct placement of the injected cement (microCT100, [Scanco Medical AG, Bassersdorf, CH], voxel size $70.8 \times 70.8 \times 70.8 \mu\text{m}^3$, 500 projections).

Repeated mechanical testing was conducted as per protocol following the thawing period overnight. The recorded load-displacement outcome of the mechanical testing was processed in a custom-build program to determine strength and stiffness during the testing.

Data were analysed in statistical computing language R [237]. To compare the reinforcement effect between groups A and B, the groups were compared using a pair t-test with significance level $p=0.05$ [249].

5.2.3 Augmentation results when using PMMA in augmenting OP and metastatic bone

The allocation of samples used has been statistically tested and it has been proved to be equally distributed in terms of the strength and stiffness (for osteoporotic samples G1 vs G2: $p>0.4$ and $p>0.3$ for strength and stiffness respectively, for metastatic samples G1 vs. G2: $p>0.3$ and $p>0.3$ for strength and stiffness respectively).

Comparing the samples pre- and post-augmentation has shown that augmentation significantly increased vertebral strength for both pathologies (Figure 60), whereas stiffness (Figure 61) was restored in osteoporotic samples to initial values ($p>0.06$), however in oncological samples it was restored on average to 2.30 ± 0.97 kN/mm and 2.12 ± 0.35 kN/mm for cement 1 and cement 2 respectively.

Tested differences showed that in osteoporotic samples, cement 1 increased strength by 255.75% compared to an increase of 96.22% when cement 2 was used. In oncological samples the increase was similar for both cements (by 43.86% for cement 1 and 48.31% for cement 2). Whereas the stiffness was increased in osteoporotic samples by 17.35% in those instances where cement 1 was used, it decreased by 15.94% in the case of cement 2. In metastatic samples, it was found that stiffness was restored only to 45.33% and 48.26% of the pre-augmentation state for cements 1 and 2 respectively. Improvement values are listed in Table 18.

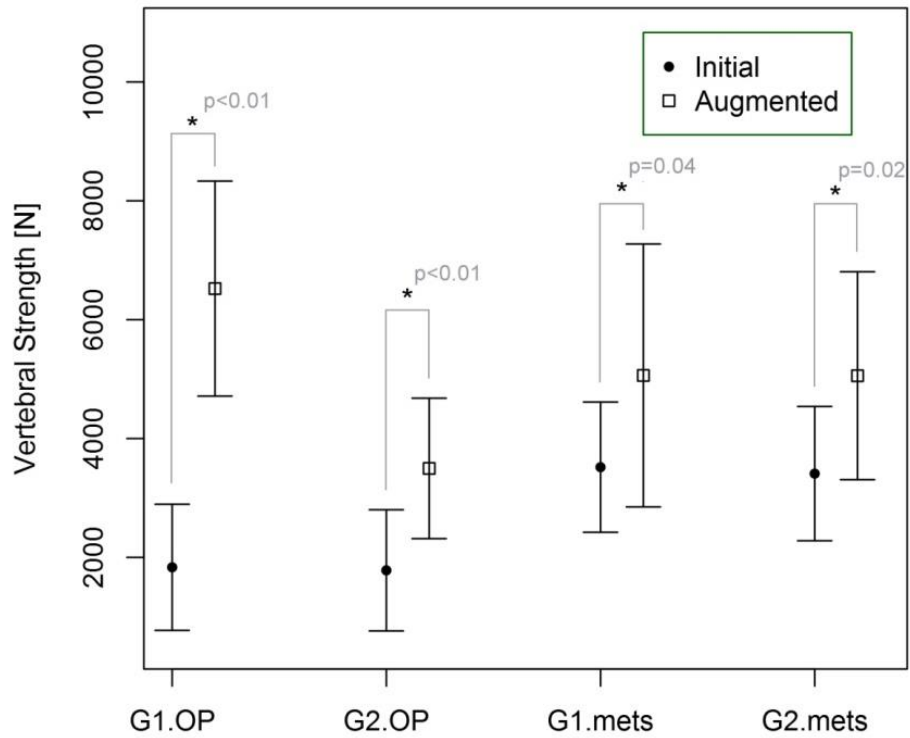


Figure 60 Vertebral strength after augmentation was found to be significantly higher in all tested groups ($p<0.05$)

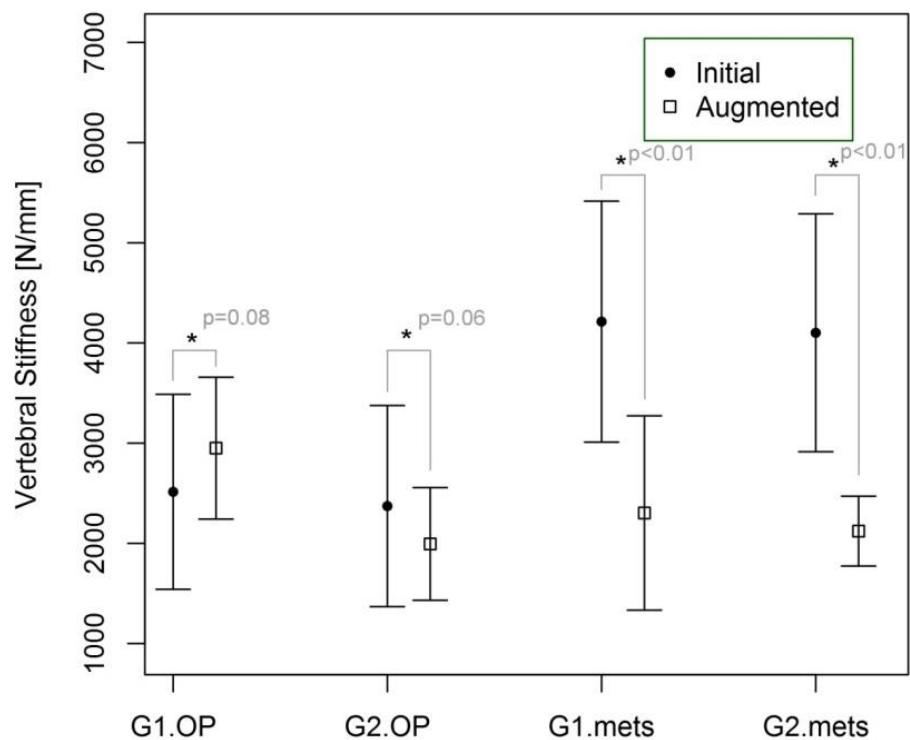


Figure 61 Vertebral stiffness of augmented vertebrae: no difference was found in osteoporotic samples, but it has decreased in both oncological groups

	Osteoporosis		Oncological samples	
	Strength (kN)	Stiffness (kN/mm)	Strength (kN)	Stiffness (kN/mm)
Cement 1 (G1)	4.69(p<0.01)	0.44(p=0.08)	1.54(p=0.04)	1.91(p<0.01)
Cement 2 (G2)	1.71(p<0.01)	0.38(p=0.06)	1.65(p=0.02)	1.98(p<0.01)

Table 18 Vertebral strength and stiffness improvement after VB augmentation (mean difference pre- and post-augmentation), significance level of p=0.05 shows that a statistical difference was not found in change of stiffness before or after augmentation in OP samples, but differences were found in all other instances

Moreover, the results in Table 19 show that cement 1 increased the strength of the osteoporotic sample by 3kN more than cement 2, but also caused an increase in stiffness by 1kN/mm compared to cement 2. This was not proved in metastatic samples where in fact any significant difference between cements 1 and 2 has not been found.

	Osteoporosis		Oncological samples	
	Strength (kN)	Stiffness (kN/mm)	Strength (kN)	Stiffness (kN/mm)
Cement 1 vs. Cement 2	3.03(p<0.01)	0.96(p<0.01)	0.004(p=0.48)	0.02(p=0.30)

Table 19 Comparison of the effect of the augmentation between the two tested cements showed a significant difference in cemented vertebrae in oncological samples, but failed to be significantly disparate for neoplastic pathology

5.2.4 Biomechanical effect due to varied PMMA cement stiffness- Discussion

One osteo-conductive material has been previously presented in this work. The aim of the study presented here was to investigate differences between the two acrylic (non-biodegradable) cements in two morphologically

different pathologies, where in fact in metastases only non-biodegradable material is recommended. Two cements of different compression stiffness derived from the same base product were thus investigated in a biomechanical cadaveric study, one of which is currently utilised clinically and the other of which is an off-the-shelf PMMA cement tailored to lower the stiffness. Secondly, while one of the investigated pathologies was found to be related to a loss of general bone quality, the other represented a rather dense tissue with regional bone loss in the area where the lesion was present. The metastatic sample in this study comprised samples with large confined osteolytic lesions, which were however present only in three out of twenty-four specimens. Moreover, due to their relative position within the vertebral body in addition to a thickened cortical bone in the anterior section, these lesions had a relatively low impact on the wedge compression strength of the organ per se. These factors combined eventually resulted in a relatively high strength and stiffness among the tested samples, even before the cement was administered.

Both groups thus substantially differed in their morphology. The first set of samples (metastases) was found to have inferior bone quality with regards to BMD ($148.7 \pm 35.6 \text{ mgHA/cm}^3$), trabecular thickness ($0.32 \pm 0.02 \text{ mm}$) and spacing ($0.81 \pm 0.12 \text{ mm}$) and was found to have substantially higher bone connectivity ($\text{Conn.D} = 1.82 \pm 0.7 \text{ mm}^{-3}$). However, the second set of samples demonstrated substantially lower bone quality in terms of lower BMD ($136.7 \pm 40.5 \text{ mgHA/cm}^3$) and marginally thinner trabeculae ($0.30 \pm 0.03 \text{ mm}$) together with significantly increased separation of the bone ($1.18 \pm 0.26 \text{ mm}$) and notably disconnected trabeculae ($\text{Conn.D} = 1.05 \pm 0.43 \text{ mm}^{-3}$).

To target the clinical relevance of using the low-modulus PMMA cement in non-prophylactic applications, a wedge compression fracture was induced to single vertebra samples followed by cement augmentation with a fixed relative volume fill. This was performed for two cements (low-modulus/non-modified) within two morphologically distinct groups of samples (OP/metastases). The results showed that both cements had substantially increased strength in both groups. While in osteoporotic samples the choice of cement showed a strong impact in terms of an increase in strength (the initial strength was increased more than threefold after augmentation with standard cement, and only twofold using the low modulus cement), in the oncological samples the choice of cement did not show a significant difference. Although no significant change was found between initial and re-

fracture stiffness, the OP samples augmented by the standard cement were almost 1kN stiffer compared to low-modulus cement. This was however not found in the oncological samples where both cements failed to restore the initial stiffness and strength, and the stiffness was not found to be different in any of the investigated cements.

Findings in the oncological samples are therefore in agreement with studies conducted by Boger et al. [23] and Kinzl et al. [24] who also reported on osteoporotic samples that standard and low-modulus PMMA cement restored both the strength and stiffness to their initial values before the fracture. On the other hand, it is rather interesting to note that the strength of the osteoporotic samples in this study was found to be more receptive to the augmentation material used. This is in agreement with a study conducted by Heini et al. [268] who also reported that cement augmentation is in fact more effective with bone demonstrating a higher degree of deterioration which is represented by lower BMD values. Moreover, a similar phenomenon was observed in experimental studies conducted on cored samples showing that the material properties of bone/cement structured material are much closer to the cement properties [24, 290, 291]. In fact, the augmented bone exhibits strong composite-like mechanical properties which are determined by the bonding of cement and bone, where in theory the bone, particularly in case of the vertical trabeculae, represents a more elastic structured material [292, 293] surrounded by a matrix of stiff and strong cement. Here, the material properties of low modulus cements such as the one used in this study and reported previously [291, 294] can be tailored in order to reinforce the damaged vertebra without radical changes in the stress profile transmitted to adjacent vertebrae [23].

Despite a relatively high number of samples used in this work, the study was limited by the availability of cancer donors. Moreover, the availability of oncological spines was complicated by the fact that the spines were acquired from overseas and despite a clinically confirmed metastatic infiltration to the vertebral bone, the severity of the morphological imprint was very low. Furthermore, the limited number of donors led to it becoming necessary to extend the harvesting of samples additionally to those from the lower lumbar region in order to retain the same dataset. Here, the wider selection of levels in the metastatic dataset might have influenced the overall results, however only if results could be examined together to obtain an overall comparison. This limitation has however been overcome by an only

relative comparison of pre- and post-augmentation mechanical properties and also by statistical evidence in equally distributed groups.

In conclusion, results presented in this study confirm that PMMA vertebroplasty can be used as a satisfactory biomechanical stabiliser of fractured vertebral bone. Both cements showed an increase in strength after reinforcement of the bone regardless of the cement used. Interestingly, a difference has been found in the type of cement used with relation to the morphological character of both groups. The metastatic group, here characterised by a higher bone volume fraction (BV/TV), was not as strongly influenced by the type of cement used resulting in less marked differences in both strength and stiffness. In contrast to this finding, the second group (OP), characterised by lower BV/TV, exhibited a more apparent influence of the use of cement. Considering similarities in bone/cement contribution observed in core samples previously discussed, this study also suggests a valuable correspondence at the organ level (whole VB). Moreover, the results suggest that tailored low-modulus cements can decrease the likelihood of an unnecessary increase in stiffness, which is believed to be a considerable factor in the increased occurrence of adjacent fractures.

5.3 Biomechanics of augmentation using CaP and PMMA cement - Summary

Two different cement types were biomechanically tested in two experimental studies. Both studies used the fracture prediction tool developed previously as a non-invasive precursor to benchmark specimens for effective group comparison ($p > 0.05$ between all groups in terms of strength and stiffness). Later both studies followed the same cadaveric testing protocol to investigate a biomechanical effect of (i) bio-degradable cement in the early stages following treatment and (ii) two acrylic cements of different stiffnesses.

First, cement based on a calcium phosphate formula has been tested in 29 osteoporotic samples divided into three groups with varying volumes of injected cement. The volume of injected cement (10, 20 and 30% of VB volume) has failed to show a significant influence on either improvement of strength ($p \gg 0.05$) or stiffness ($p \gg 0.05$). Overall, CaP cement has increased the strength by 121% whereas the stiffness was restored only to 41% of that prior to the fracture.

The second part of this section has provided results of testing acrylic cement (PMMA) with a tailored formula to reduce the baseline stiffness of the cement. This cement has been tested against off-the-shelf cement for a comparative study in osteoporotic and metastatic samples. All samples underwent fracturing followed by injection with 30% VB volume fill. Compared to the initial state, augmented vertebrae exhibited an increase in strength and decrease in stiffness regardless of the pathology and cement type used. In terms of biomechanical evaluation, non-modified cement (G1) has shown a substantial increase in strength but, accompanied by an increase in stiffness, was proved in samples with lower bone mass (OP samples). Tailored cement (G2) has shown an increase in strength in both cases but has not increased stiffness in either of the morphologically disparate groups.

Chapter 6

Conclusion and Future perspective

This section provides the conclusions reached by the work undertaken as a part of this thesis compared to works presented elsewhere. The chapter is segmented into two main bodies: “Non-invasive predictors of fracture in patients with different pathologies” and “PVP use in treatment of vertebral compression fractures” where each section highlights a summary of this work, the original contribution and a future perspective.

6.1 Non-invasive predictors of fracture in patients with different pathologies

6.1.1 Summary of findings in structural assessment of metastatic and non-metastatic bone

From the framework of validation and verification of image-based fracture prediction it has been concluded that the structural analyses based on composite beam theory show a relatively close association with vertebral compression strength in osteoporosis, multiple myeloma and metastatic bone. In fact, it was also shown that this “CT-to-strength” approach is comparatively fast and easy to use, and also provides an adequate vertebral strength benchmarking tool when performing experiments using wedge compression fracture models.

The first objective of this thesis was met as the developed model was tested on more than one hundred samples retrospectively by analysing tomographic images of historical data comparing the *in-silico* predictions with fracture data provided by previous investigators. Here, historical data comprised also a scarce amount of rare samples in which extra-vertebral lesions have developed prior to donation of the tissue. A numerical assessment of these samples concluded that this tissue may or may not contribute to the overall resilience of the whole organ depending on whether it suffered from osteoporotic osteophytes or osteoblastic lesions respectively.

For the latter part of the validation and for conduction of a cadaveric study, an enhanced fracture rig was developed on which more than one hundred samples of three pathologies were fractured. From this study relatively good predictions of vertebral body strength were obtained when

using this model and more interestingly, even when reducing the tested range to a single slice analysis. This said, it has been concluded that the beam theory method can be used as a precursor to a biomechanical assessment of selected specimens in a laboratory environment, particularly to allow superior experimental groupings in WCF conditions over those usually based on BMD or vertebral level alone.

In a framework of investigation of the biomechanical properties of cancer bone tissue the second objective was met by performing a detailed micro-indentation study. This study was the first of its kind and highlighted that the tissue level deterioration in multiple myeloma results in only a limited impact on the underlying material properties. This hence concluded that the weakening process in multiple myeloma most probably results primarily due to structural changes occurring on the meso-scale.

Any conclusions made based on the pathological nature of the infiltration are however hampered by the fact that there is a lack of diagnostic methods to identify combined pathologies. For example cancer patients tend to be older in age and are thus more likely to develop osteopenia or osteoporosis besides developing bone lesions. Current DXA/CT based testing is not suitable for the diagnosis of underlying osteoporotic changes and hence does not provide a clear cohort of the tissue donated. This study however suggests that a density image-based fracture prediction tool accounts for the structural deterioration of bone where the material model used for density-to-modulus does not need to be adjusted, due to the presence of the osteolytic lesion at least in multiple myeloma bone. This nonetheless needs to be confirmed on other neoplastic pathologies such as breast, lung, bladder or thyroid cancers which are known for increased occurrence of developed osteoblastic lesions.

6.1.2 Original contribution

This study has aimed to provide an assessment of oncological bone, particularly in order to target compression fractures caused by structural changes within the bone. Preliminary studies within this work highlighted the necessity to account for structural changes and bone distribution. For this purpose this work proposes to build on an approach similar to that previously used by Whealan et al. [2] which was shown to provide fracture predictions with a greater association with the experimental results, even in the case of samples where lytic lesions were simulated by altering the vertebral body integration. In this study this model was adopted for use in vertebroplasty and contributed to the progress of current studies by confirming that a similar

model can provide high levels of agreement with vertebral body strength in single vertebra wedge compression fracture methods. This has been demonstrated on a large number of samples which, pooled together with the retrospective analysis of historical data, exceeded two hundred samples. All of the samples used in this study were processed in the same university laboratory using the same apparatuses for the initial and post-fracture scanning as well as for conduction of the destructive testing. Samples were scanned and tested in close collaboration with Daniel Skrzypiec, particularly for multiple myeloma samples which were later used in another vertebroplasty study (results as yet unpublished). This was possible due to the use of the same scanning and fracturing protocol up to the initial destructive testing. Osteoporotic study samples (annotated as “SpineGO”) underwent experimental testing in close collaboration with Alejandro Lopez, a visiting researcher from the University of Uppsala.

The micro-indentation study produced original results in the indentation testing of oncological samples which had not been tested in literature to this point. This study was designed in collaboration with the Initial Training Network (ITN), particularly with partners from the Vienna University of Technology and the University of Bern. Samples were collected, scanned and embedded in a laboratory in Leeds whilst the indentation testing was conducted by the author of this work in a laboratory in the University of Vienna as a laboratory secondment. The results obtained from bone testing of multiple myeloma were found to be original and were later compared to results conducted on osteoporotic bone in a study which was carried out by Uwe Wolfram [184].

6.1.3 Future perspective in structural assessment of metastatic bone

Compared to any study previously published, the results presented here also show that potentially only a single vertebral slice analysis is needed in order to permit correlation with the strength of the organ. Despite reducing the amount of information gathered about whole vertebrae, it has proven to demonstrate at least the same level of accuracy and precision as alternative methods presented elsewhere. Such a discovery highlights the potential of reducing the X-ray exposure of the patient during the radiography screening to a necessary minimum. This study has deliberately employed representative slices which are easy to identify from a fast and low pre-scan exposure (scout view). In fact, such a scout view is used in clinical CTs to select a range of axial slices, and although it does so imperfectly,

contains all the necessary information to preliminarily identify the weakest slice in relation to the rest of the vertebral body, whereas the single slice scan could be targeted for example at a site with strong lytic infiltration. This assumption is based on the principle that the scout view, similarly to DXA, provides a sum of densities perpendicular to each pixel of the scanning plane. Such a technique is however purely a theoretical assumption which would need to be tested and would possibly require that two scout-views were performed to identify any heterogeneous density violations such as lytic lesions.

Proposed by findings from the preliminary study and confirmed elsewhere, such a technique would also be sensitive to over-mineralised but less stiff osteoblastic lesions that commonly occur together with lytic lesions. In particular, the analysis of historical samples has been complicated by the presence of extra-vertebral bone formations in which the contribution to the fracture load may be minimal, unlike the formation of osteophytes in osteoporosis reported in previous results which appears to significantly resist compressive load. This is supported by a previous finding in which it has been demonstrated that the extra-vertebral lesions arising from the metastatic bone formation are akin to relatively immature woven bone which provides relatively little structural support. This was however not confirmed in the main work of this thesis due to a limited availability of cancer samples with osteoblastic lesions. Nonetheless, this rather interesting discovery should be noted for future studies which aim to investigate the contribution of these lesions which are known to impair any attempt to perform density predictions in radiography screening.

Based on this validation study, this stand-alone fracture prediction tool can be used as a fast and robust benchmarking tool for the relative strength distribution of cancer pathology. To confirm the agreement obtained by calibrating the material model and to improve the statistical variability of the cancer population, more samples should be tested in destructive experiments to fully prove its potential for clinical use.

Lastly, this model is limited to a loading scheme which is however challenging to relate to a physiological situation *in-vivo*. This question is best addressed by multibody simulations where the loading conditions to which the organ is subjected can be predicted based on inverse kinematics measured non-invasively. A combination of the two approaches, by applying patient-specific loading conditions to CT-image-based predictions, could

allow the prevention of vertebral failures to take place during a routine patient screening instead of in finding them late at the ambulance services.

6.2 PVP use in treatment of vertebral compression fractures

6.2.1 Osteo-conductive cement augmentation

Calcium phosphate vertebroplasty augmentation previously showed great potential as it enables a natural recovery of the weakened bone. The results of this cadaveric study show that this particular ceramic cement almost doubled the strength of the cadaveric vertebrae, while the stiffness was almost halved when compared to the stiffness of an intact vertebral body. On the other hand the lack of correlation between injected volume and strength suggests limited possibilities to improve strength to higher limits if necessary.

Regarding the effect of employing a different volume of cement, the results reported that even smaller volumes (~2mL, 10% of the vertebral body volume) may be sufficient to stabilise the fracture, suggesting that the volume of introduced cement is not a decisive factor in terms of biomechanical improvement if the provisional restoration here presented is sufficient prior to the bone recovery. While it has been suggested that the volume of PMMA cements used should be kept as low as possible, osteo-conductive cements can direct natural bone growth. Therefore the volume can be adjusted according to the bioactive character of the cement and therefore to achieve the optimal conditions for healing of the bone.

6.2.2 Low-modulus PMMA cement augmentation

Based on the results herein presented, this work concludes that undertaking vertebroplasty using PMMA cements results in an increase of stiffness and strength in fractured vertebrae regardless of how such deterioration might have occurred. The results presented in fact show a stabilising effect in all of the tested groups. Nonetheless, the metastatic bone and osteoporotic bone reacted differently to augmentation. In metastatic bone the effect of vertebroplasty was similar, regardless of the cement used. In contrast, the effect on osteoporotic samples has demonstrated that there is a significant difference between the two cements. Although both cements were proved to restore the stiffness to its initial values, low-cement was found to restore the stiffness closer to the values obtained prior to the fracture, whereas the standard cement resulted in a marginally increased stiffness. This in fact suggests that low modulus cement demonstrates

improved properties which could potentially address the worrying issue of adjacent fractures.

Furthermore, it is believed that the difference in contribution is most likely due to a variation in morphology between the tested pathologies. This observation has been made based on the discovery that the contribution of cements' material properties to bone strength and stiffness was more apparent in high-porosity osteoporotic samples, compared to less porous bone obtained from two metastatic patients. This said, there are a number of conclusions to be made:

- i. Vertebroplasty using both PMMA cements results in an increase in bone stiffness and strength;
- ii. The effect of vertebroplasty is related to the morphology of the bone prior to its augmentation;
- iii. The effect of vertebroplasty is possibly driven by a combination of both the cement material used and the micro-mechanical properties of the bone tissue embedded within the bone.

The latter conclusion is also based on the discussion in the previous chapter in which the composite behaviour of augmented bone observed elsewhere has been emphasised. Here, based on the results obtained from the micro-indentation study, it is also possible to conclude that conducting vertebroplasty using PMMA cement would have a similar effect also on multiple myeloma bone, as its micromechanical properties are similar to osteoporotic bone.

6.2.3 Original contribution

Results from both studies have made an innovative contribution to the field of vertebroplasty. The first study encompasses the unknown relationship between the injected volume of cement and its biomechanical output when augmented into osteoporotic tissue. This work is in fact the first to present an augmentation of three different volumes in a laboratory experiment with a subsequent re-fracture experiment. These results can be addressed in future studies tailoring the material and biomechanical properties of absorbable materials. The use of fracture prediction as a benchmarking tool also contributes to the uniqueness of these two studies due to the improved Latin-square strength-based group allocation used prior to conducting the fracturing part of the experiment.

PMMA augmentation was in fact conducted in two different pathologies of which one was related to the treatment of patients with infiltration of

cancer to their spine. The study was innovative in comparison to all others published to date in conducting a study on cement which was manufactured in a relatively easy process by tailoring the existing properties of currently available cement. Although different studies were conducted in order to reinforce the biomechanical effect of low-modulus cements, this study was conducted on a comparatively larger volume of samples comparing pathologies with different morphologies.

The CaP study was conducted in collaboration with the Initial Training Network (ITN) partner BONESUPPORT AB. Nonetheless, the biomechanical experiment was conducted entirely by the author of this work in teamwork with ITN colleague Nicola Brandolini. The results presented in this work were analysed independently of any collaborating partner.

The PMMA study was conducted in collaboration with another university, while the initial fracturing, scanning, fracture prediction and preparation of samples for augmentation were conducted by the author of this work alone or in collaboration with Alejandro Lopez – a visiting researcher from the University of Uppsala. The augmentation was performed by the surgeon Vishal Borse in a joint experimental session. The results were analysed separately in shared discussions.

6.2.4 Future perspective in CaP and PMMA augmentation

In agreement with other studies, the results presented here suggest that PMMA and CaP vertebroplasty are safe in terms of improving the biomechanical properties of a vertebral bone after fracture. These results should however be interpreted with care and only in the context of a biomechanical cadaveric study conducted with the intention of answering very specific questions. Further pre-clinical and clinical validations need to be conducted prior to its general use. Based on the PMMA study presented here it has been concluded that using normal cement compared to a low-modulus cement risks an unnecessary increase in stiffness, which is believed to be a considerable factor in the increased occurrence of adjacent fractures. This conclusion however requires confirmation in dynamic testing to assess the fatigue properties of the materials used in addition to the quasi-static experiments presented in this work. Also, as this study was limited to relatively constrained loading conditions, a clearer understanding of boundary conditions and directional load changes is required to reinforce these conclusions.

Secondly, the most significant limitation of the calcium phosphate study is without any doubt the cadaveric nature of the experiment. These preliminary results however suggest that this material is safe in terms of biomechanical stiffness and strength for a short time following the procedure, although animal or clinical studies would need to be conducted in order to provide valuable information regarding bone recovery. Moreover, with potential bone recovery, the current cement could be also deployed in the burst fracture typically used in the case of younger patients. This however requires testing under conditions which would have a much higher short-term impact, possibly using a weight drop testing machine.

The results in this work also suggest that very little is known about the relationship between morphology and the resulting effect of the augmentation. The experiment presented here should hence be conducted to address a larger sample population of different bone morphologies in order to fully deploy the potential of the augmentation treatment. Alternatively or alongside this, reproducing the experiment to assess the flow of cement would volunteer more information regarding material distribution and could further respond to the elementary questions which have arisen from this work.

Finally, throughout this thesis a number of potential applications of the fracture prediction tool were shown, in particular its use in the identification of weakened vertebrae with sufficient accuracy and power of prediction. This demonstrates a strong potential for the reproduction of similarly satisfying outcomes for use in investigation of prophylactic augmentation.

References

1. Cooper, C., et al., *Incidence of clinically diagnosed vertebral fractures: a population-based study in Rochester, Minnesota, 1985-1989*. J Bone Miner Res, 1992. **7**(2): p. 221-227.
2. Whealan, K.M., et al., *Noninvasive Imaging Predicts Failure Load of the Spine with Simulated Osteolytic Defects*. Journal of Bone and Joint Surgery. American Volume, 2000. **82**(9): p. 1240-1247.
3. Furtado, N., et al., *A biomechanical investigation of vertebroplasty in osteoporotic compression fractures and in prophylactic vertebral reinforcement*. Spine, 2007. **32**: p. E480-E487.
4. Gielen, E., et al., *Osteoporosis in men*. Best Pract Res Clin Endocrinol Metab, 2011. **25**(2): p. 321-335.
5. Kanis, J.A. and O. Johnell, *Requirements for DXA for the management of osteoporosis in Europe*. Osteoporosis International, 2005. **16**: p. 229-238.
6. Coleman, R.E., *Metastatic bone disease: clinical features, pathophysiology and treatment strategies*. Cancer Treatment Reviews, 2001. **27**(3): p. 165-176.
7. Katagiri, H., et al., *Prognostic factors and a scoring system for patients with skeletal metastasis*. Journal of Bone & Joint Surgery, British Volume, 2005. **87-B**(5): p. 698-703.
8. Gralow, J. and D. Tripathy, *Managing Metastatic Bone Pain: The Role of Bisphosphonates*. Journal of Pain and Symptom Management, 2007. **33**(4): p. 462-472.
9. Coleman, R.E., *Skeletal complications of malignancy*. Cancer, 1997. **80**, Issue Supplement 8: p. 1588-1594.
10. Coleman, R.E., *Bisphosphonates: Clinical Experience*. The Oncologist, 2004. **9**(suppl 4): p. 14-27.
11. Dudeney, S., et al., *Kyphoplasty in the Treatment of Osteolytic Vertebral Compression Fractures as a Result of Multiple Myeloma*. Journal of Clinical Oncology, 2002. **20**(9): p. 2382-2387.
12. Klimo, P. and M.H. Schmidt, *Surgical management of spinal metastases*. Oncologist, 2004. **9**(2): p. 188-196.
13. Cortet, B., et al., *Percutaneous vertebroplasty in patients with osteolytic metastases or multiple myeloma*. Rev Rhum Engl Ed, 1997. **64**(3): p. 177-183.
14. Weill, A., et al., *Spinal metastases: indications for and results of percutaneous injection of acrylic surgical cement*. Radiology, 1996. **199**(1): p. 241-247.
15. Buchbinder, R., et al., *A Randomized Trial of Vertebroplasty for Painful Osteoporotic Vertebral Fractures*. New England Journal of Medicine, 2009. **361**(6): p. 557-568.
16. Kallmes, D.F., et al., *A Randomized Trial of Vertebroplasty for Osteoporotic Spinal Fractures*. New England Journal of Medicine, 2009. **361**(6): p. 569-579.
17. Klazen, C.A., et al., *Vertebroplasty versus conservative treatment in acute osteoporotic vertebral compression fractures (Vertos II): an open-label randomised trial*. Lancet, 2010. **376**(9746): p. 1085-1092.

18. Barr, J.D., et al., *Percutaneous vertebroplasty for pain relief and spinal stabilization*. Spine (Phila Pa 1976), 2000. **25**(8): p. 923-928.
19. Mundy, G.R., *Metastasis: Metastasis to bone: causes, consequences and therapeutic opportunities*. Nat Rev Cancer, 2002. **2**(8): p. 584-593.
20. Griffith, J.F. and H.K. Genant, *Bone mass and architecture determination: state of the art*. Best Practice & Research Clinical Endocrinology & Metabolism, 2008. **22**(5): p. 737-764.
21. Ferguson, S.J. and T. Steffen, *Biomechanics of the aging spine*. European Spine Journal, 2003. **12**: p. S97-S103.
22. McCalden, R.W., J.A. McGeough, and C.M. Court-Brown, *Age-Related Changes in the Compressive Strength of Cancellous Bone. The Relative Importance of Changes in Density and Trabecular Architecture*. The Journal of Bone & Surgery, 1997. **79**: p. 421-7.
23. Boger, A., et al., *Adjacent vertebral failure after vertebroplasty: a biomechanical study of low-modulus PMMA cement*. European Spine Journal, 2007. **16**: p. 2118-2125.
24. Kinzl, M., et al., *The mechanical behavior of PMMA/bone specimens extracted from augmented vertebrae: A numerical study of interface properties, PMMA shrinkage and trabecular bone damage*. Journal of Biomechanics, 2012. **45**(8): p. 1478-1484.
25. Kinzl, M., et al., *The effect of standard and low-modulus cement augmentation on the stiffness, strength, and endplate pressure distribution in vertebroplasty*. European Spine Journal, 2012. **21**: p. 920-929.
26. Wijayathunga, V.N., et al., *Development of specimen-specific finite element models of human vertebrae for the analysis of vertebroplasty*. Proceedings of the Institution of Mechanical Engineers, Part H: Journal of Engineering in Medicine, 2008. **222**(2): p. 221-228.
27. Molloy, S., J.M. Mathis, and S.M. Belkoff, *The effect of vertebral body percentage fill on mechanical behavior during percutaneous vertebroplasty*. Spine (Phila Pa 1976), 2003. **28**(14): p. 1549-1554.
28. Liebschner, M.A.K., W.S. Rosenberg, and T.M. Keaveny, *Effects of Bone Cement Volume and Distribution on Vertebral Stiffness After Vertebroplasty*. Spine, 2001. **26**(14): p. --.
29. Belkoff, S.M., et al., *The biomechanics of vertebroplasty. The effect of cement volume on mechanical behavior*. Spine (Phila Pa 1976), 2001. **26**(14): p. 1537-1541.
30. Tomita, S., et al., *Biomechanical evaluation of kyphoplasty and vertebroplasty with calcium phosphate cement in a simulated osteoporotic compression fracture*. Journal of Orthopaedic Science, 2003. **8**: p. 192-197.
31. Molloy, S., L.H. Riley, and S.M. Belkoff, *Effect of Cement Volume and Placement on Mechanical-Property Restoration Resulting from Vertebroplasty*. American Journal of Neuroradiology, 2005. **26**(2): p. 401-404.
32. Tohmeh, A.G., et al., *Biomechanical Efficacy of Unipedicular Versus Bipedicular Vertebroplasty for the Management of Osteoporotic Compression Fractures*. Spine, 1999. **24**(17): p. --.

33. Zysset, P.K., *A review of morphology–elasticity relationships in human trabecular bone: theories and experiments*. Journal of Biomechanics, 2003. **36**(10): p. 1469-1485.
34. Ohman, C., et al., *Human bone hardness seems to depend on tissue type but not on anatomical site in the long bones of an old subject*. Proceedings of the Institution of Mechanical Engineers, Part H: Journal of Engineering in Medicine, 2012. **0**: p. 1-7.
35. Dall'Ara, E., R. Schmidt, and P. Zysset, *Microindentation can discriminate between damaged and intact human bone tissue*. Bone, 2012. **50**(4): p. 925-929.
36. Wolfram, U., H.J. Wilke, and P.K. Zysset, *Transverse Isotropic Elastic Properties of Vertebral Trabecular Bone Matrix Measured Using Microindentation (Effects of Age, Gender and Vertebral Level)*. Journal of Mechanics in Medicine and Biology, 2010. **10**(01): p. 139-150.
37. Zysset, P.K., et al., *Elastic modulus and hardness of cortical and trabecular bone lamellae measured by nanoindentation in the human femur*. Journal of Biomechanics, 1999. **32**(10): p. 1005-1012.
38. Oakland, R.J., et al., *The biomechanics of vertebroplasty in multiple myeloma and metastatic bladder cancer: a preliminary cadaveric investigation*. J Neurosurg Spine, 2008. **9**(5): p. 493-501.
39. Tschirhart, C.E., S.E. Roth, and C.M. Whyne, *Biomechanical assessment of stability in the metastatic spine following percutaneous vertebroplasty: effects of cement distribution patterns and volume*. J Biomech, 2005. **38**(8): p. 1582-1590.
40. Harms, J., G. Tabasso, and R. Cinanni, *Instrumented Spinal Surgery: Principles and Technique*. 1999: Thieme.
41. Mow, V.C. and W.C. Hayes, *Basic orthopaedic biomechanics. (2nd edition)*. 1997: Lippincott-Raven Publishers.
42. White, A.A. and M.M. Panjabi, *Clinical Biomechanics of the Spine*. 1990: Lippincott Williams & Wilkins; Second edition.
43. Ebraheim, N.A., et al., *Functional anatomy of the lumbar spine*. Seminars in Pain Medicine, 2004. **2**(3): p. 131-137.
44. Winter, B. and D. Knight, *Spinal cord injury*. Anaesthesia & Intensive Care Medicine, 2005. **6**(9): p. 315-317.
45. Nachemson, A., *The lumbar spine: an orthopaedic challenge*. spine, 1976. **1**(1): p. 59-69.
46. Wilke, H., et al., *New in vivo measurements of pressures in the intervertebral disc in daily life*. Spine (Phila Pa 1976), 1999. **24**(8)(0362-2436 (Linking)): p. 755-762.
47. Gibson, L.J., *The mechanical behaviour of cancellous bone*. J Biomech, 1985. **18**(5): p. 317-328.
48. Wells-Roth, D. and M. Zonenshayn, *Vascular anatomy of the spine*. Operative Techniques in Neurosurgery, 2003. **6**(3): p. 116-121.
49. Cowin(ed), S.C. and C.R. Jacobs, *Bone mechanics handbook (second edition)*, ed. S.C. Cowin. Vol. 35. 2002: Elsevier Science.
50. Mullender, M.G., et al., *Osteocyte density changes in aging and osteoporosis*. Bone, 1996. **18**(2): p. 109-113.
51. Rho, J.Y., R.B. Ashman, and C.H. Turner, *Young's modulus of trabecular and cortical bone material: Ultrasonic and microtensile measurements*. Journal of Biomechanics, 1993. **26**(2): p. 111-119.

52. Rho, J.-Y., T.Y. Tsui, and G.M. Pharr, *Elastic properties of human cortical and trabecular lamellar bone measured by nanoindentation*. *Biomaterials*, 1997. **18**(20): p. 1325-1330.
53. Wolff, J., *Law of bone remodelling*. 2012, [S.I.]: Springer.
54. Chen, H., et al., *Regional variations of vertebral trabecular bone microstructure with age and gender*. *Osteoporosis International*, 2008. **19**: p. 1473-1483.
55. Wegrzyn, J., et al., *Role of trabecular microarchitecture and its heterogeneity parameters in the mechanical behavior of ex vivo human L3 vertebrae*. *Journal of Bone and Mineral Research*, 2010. **25**(11): p. 2324-2331--.
56. Parfitt, A., et al., *Relationships between surface, volume, and thickness of iliac trabecular bone in aging and in osteoporosis. Implications for the microanatomic and cellular mechanisms of bone loss*. *J Clin Invest*, 1983. **72**(4): p. 1396-1409--.
57. Hildebrand, T., et al., *Direct three-dimensional morphometric analysis of human cancellous bone: microstructural data from spine, femur, iliac crest, and calcaneus*. *J Bone Miner Res*, 1999. **14**(7): p. 1167-1174.
58. Lochmüller, E.-M., et al., *Does thoracic or lumbar spine bone architecture predict vertebral failure strength more accurately than density?* *Osteoporosis International*, 2008. **19**: p. 537-545.
59. Kabel, J., et al., *Connectivity and the elastic properties of cancellous bone*. *Bone*, 1999. **24**(2): p. 115-20.
60. Whitehouse, W.J., *The quantitative morphology of anisotropic trabecular bone*. *Journal of microscopy*, 1974. **101**(Pt 2)(0022-2720 (Linking)): p. 153-168.
61. Reisinger, A., D. Pahr, and P. Zysset, *Principal stiffness orientation and degree of anisotropy of human osteons based on nanoindentation in three distinct planes*. *J Mech Behav Biomed Mater*, 2011. **4**(8): p. 2113-2127--.
62. Delmas, P.D., et al., *Underdiagnosis of vertebral fractures is a worldwide problem: the IMPACT study*. *Journal of Bone and Mineral Research*, 2005. **20**(4): p. 557-563.
63. Salvo, N., et al., *The role of plain radiographs in management of bone metastases*. *J Palliat Med*, 2009. **12**(2): p. 195-198.
64. Brinckmann, P., M. Biggemann, and D. Hilweg, *Prediction of the compressive strength of human lumbar vertebrae*. *Clinical Biomechanics*, 1989. **4**(Supplement 2): p. iii-iv.
65. Crawford, R.P., C.E. Cann, and T.M. Keaveny, *Finite element models predict in vitro vertebral body compressive strength better than quantitative computed tomography*. *Bone*, 2003. **33**(4): p. 744-50--.
66. Dall'Ara, E., et al., *A nonlinear finite element model validation study based on a novel experimental technique for inducing anterior wedge-shape fractures in human vertebral bodies in vitro*. *Journal of Biomechanics*, 2010. **43**(12): p. 2374-2380.
67. Von Stechow, D., et al., *Metastatic cancer bone tissue behaves mechanically as a rigid porous foam*. *PDF*. *Transactions of the orthopaedic research society*, 2003. **28**: p. 995.
68. Nazarian, A., et al., *Bone Volume Fraction Explains the Variation in Strength and Stiffness of Cancellous Bone Affected by Metastatic*

- Cancer and Osteoporosis*. *Calcified Tissue International*, 2008. **83**: p. 368-379.
69. Hulme, P.A., S.K. Boyd, and S.J. Ferguson, *Regional variation in vertebral bone morphology and its contribution to vertebral fracture strength*. *Bone*, 2007. **41**(6): p. 946-957.
70. Bouxsein, M., *Bone quality: where do we go from here?* *Osteoporosis International*, 2003. **14**: p. 118-127.
71. Johnell, O. and J. Kanis, *An estimate of the worldwide prevalence and disability associated with osteoporotic fractures*. *Osteoporosis International*, 2006. **17**: p. 1726-1733.
72. Strom, O., et al., *Osteoporosis: burden, health care provision and opportunities in the EU*. *Archives of Osteoporosis*, 2011. **6**: p. 59-155.
73. Gehlbach, S.H., et al., *Recognition of Vertebral Fracture in a Clinical Setting*. *Osteoporosis International*, 2000. **11**: p. 577-582.
74. Kado, D.M., et al., *Vertebral fractures and mortality in older women: a prospective study*. *Study of Osteoporotic Fractures Research Group*. *Arch Intern Med*, 1999. **159**(11): p. 1215-1220.
75. Dempster, D.W., et al., *A simple method for correlative light and scanning electron microscopy of human iliac crest bone biopsies: Qualitative observations in normal and osteoporotic subjects*. *Journal of Bone and Mineral Research*, 1986. **1**(1): p. 15-21.
76. Genant, H.K., et al., *Vertebral fracture assessment using a semiquantitative technique*. *Journal of Bone and Mineral Research*, 1993. **8**(9): p. 1137-1148.
77. Greenspan, S.L., et al., *Instant Vertebral Assessment: A Noninvasive Dual X-ray Absorptiometry Technique to Avoid Misclassification and Clinical Mismanagement of Osteoporosis*. *Journal of Clinical Densitometry*, 2001. **4**(4): p. 373-380.
78. Sullivan, S., et al., *Vertebral Fractures and the Misclassification of Osteoporosis in Men With Prostate Cancer*. *Journal of Clinical Densitometry*, 2011. **14**(3): p. 348-353.
79. Gauthier, A., et al., *Burden of postmenopausal osteoporosis in Germany: estimations from a disease model*. *Archives of Osteoporosis*, 2012. **7**: p. 209-218.
80. Gauthier, A., et al., *Epidemiological burden of postmenopausal osteoporosis in the UK from 2010 to 2021: estimations from a disease model*. *Archives of Osteoporosis*, 2011. **6**: p. 179-188.
81. Cawston, H., et al., *Epidemiological burden of postmenopausal osteoporosis in France from 2010 to 2020: estimations from a disease model*. *Archives of Osteoporosis*, 2012. **7**: p. 237-246.
82. Kaufman, J.M. and S. Goemaere, *Osteoporosis in men*. *Best Pract Res Clin Endocrinol Metab*, 2008. **22**(5): p. 787-812.
83. Melton, L.J., et al., *Fracture Risk With Multiple Myeloma: A Population-Based Study*. *Journal of Bone and Mineral Research*, 2005. **20**(3): p. 487-493.
84. Roodman, G.D., *Mechanisms of Bone Metastasis*. *New England Journal of Medicine*, 2004. **350**(16): p. 1655-1664.
85. Li, S.a., et al., *Estimated number of prevalent cases of metastatic bone disease in the US adult population*. *Clinical Epidemiology*, 2012. **4**(1): p. 87-93.

86. Constans, J., et al., *Spinal metastases with neurological manifestations. Review of 600 cases.* J Neurosurg, 1983. **59**(1): p. 111-118--.
87. Galasko, C.S., *Skeletal metastases.* Clin Orthop Relat Res, 1986. **210**(210): p. 18-30.
88. Wong, D.A., V.L. Fornasier, and I. MacNab, *Spinal metastases: the obvious, the occult, and the impostors.* Spine (Phila Pa 1976), 1990. **15**(1): p. 1-4.
89. Hentschel, S.J., et al., *Percutaneous vertebroplasty and kyphoplasty performed at a cancer center: refuting proposed contraindications.* Journal of Neurosurgery: Spine, 2005. **2**(4): p. 436-440--.
90. Munshi, N.C., *Plasma Cell Disorders: An Historical Perspective.* ASH Education Program Book, 2008. **2008**(1): p. 297.
91. Raab, M.S., et al., *Multiple myeloma.* Lancet, 2009. **374**(9686): p. 324-339.
92. Sirohi, B. and R. Powles, *Multiple myeloma.* Lancet, 2004. **363**(9412): p. 875-887.
93. Kyle, R.A., et al., *Review of 1027 Patients With Newly Diagnosed Multiple Myeloma.* Mayo Clin Proc, 2003. **78**(1): p. 21-33.
94. Mahindra, A., T. Hideshima, and K.C. Anderson, *Multiple myeloma: biology of the disease.* Blood Reviews, 2010. **24**, **Supplement 1**: p. S5-S11.
95. Oakland, R.J., et al., *A preliminary cadaveric study investigating the biomechanical effectiveness of vertebroplasty in treating spinal metastases and multiple meyloma.* Journal of Bone & Joint Surgery, British Volume, 2009. **91-B**(SUPP III): p. 497.
96. Szturz, P., et al., *Regression of an osteolytic lesion in a patient with multiple myeloma treated with clodronate after a successful therapy with bortezomib-based regimen.* Klin Onkol, 2011. **24**(3): p. 216-220.
97. Takahashi, H., et al., *Classification of intramural metastases and lymph node metastases of esophageal cancer from gene expression based on boosting and projective adaptive resonance theory.* J Biosci Bioeng, 2006. **102**(1): p. 46-52.
98. Ulmar, B., et al., *The Tokuhashi score: significant predictive value for the life expectancy of patients with breast cancer with spinal metastases.* Spine (Phila Pa 1976), 2005. **30**(19): p. 2222-2226.
99. Costa, L. and P.P. Major, *Effect of bisphosphonates on pain and quality of life in patients with bone metastases.* Nat Clin Prac Oncol, 2009. **6**(3): p. 163-174.
100. Wysowski, D.K., *Reports of Esophageal Cancer with Oral Bisphosphonate Use.* New England Journal of Medicine, 2009. **360**(1): p. 89-90.
101. Salari, P. and M. Abdollahi, *Long term bisphosphonate use in osteoporotic patients; a step forward, two steps back.* J Pharm Pharm Sci, 2012. **15**(2): p. 305-317.
102. Quraishi, N.A., Z.L. Gokaslan, and S. Boriani, *The surgical management of metastatic epidural compression of the spinal cord.* J Bone Joint Surg Br, 2010. **92**(8): p. 1054-1060.
103. Holman, W.L., et al., *Infection in ventricular assist devices: prevention and treatment.* Ann Thorac Surg, 2003. **75**(90060): p. S48-57.

104. Halpin, R.J., B.R. Bendok, and J.C. Liu, *Minimally invasive treatments for spinal metastases: vertebroplasty, kyphoplasty, and radiofrequency ablation*. J Support Oncol, 2004. **2**(4): p. 339--51; discussion 352-5.
105. Ahn, H., et al., *The effect of pre-vertebroplasty tumor ablation using laser-induced thermotherapy on biomechanical stability and cement fill in the metastatic spine*. Eur Spine J, 2007. **16**(8): p. 1171-1178--.
106. Barragan-Campos, H.M., et al., *Percutaneous Vertebroplasty for Spinal Metastases: Complications*. Radiology, 2006. **238**(1): p. 354-362.
107. Cotten, A., et al., *Percutaneous vertebroplasty for osteolytic metastases and myeloma: effects of the percentage of lesion filling and the leakage of methyl methacrylate at clinical follow-up*. Radiology, 1996. **200**(2): p. 525-530.
108. Schulman, K.L. and J. Kohles, *Economic burden of metastatic bone disease in the U.S. Cancer*, 2007. **109**(11): p. 2334-2342.
109. Genant, H.K., et al., *Comparison of semiquantitative visual and quantitative morphometric assessment of prevalent and incident vertebral fractures in osteoporosis*. Journal of Bone and Mineral Research, 1996. **11**(7): p. 984-996.
110. Kiliñer, C., et al., *Load sharing within a human thoracic vertebral body: an in vitro biomechanical study*. Turk Neurosurg, 2007. **17**(3): p. 167-177.
111. Goulet, R.W., et al., *The relationship between the structural and orthogonal compressive properties of trabecular bone*. J Biomech, 1994. **27**(4): p. 375-389.
112. Mueller, T.L., et al., *Non-invasive bone competence analysis by high-resolution pQCT: an in vitro reproducibility study on structural and mechanical properties at the human radius*. Bone, 2009. **44**(2): p. 364-371.
113. Gebhard, F. and M. Schultheiss, *Orthopaedic spine surgery- an instrumentational course textbook*. 2008, Springer Stainkopff Verlag. p. 129-136.
114. Erkan, S., et al., *Biomechanical comparison of transpedicular versus extrapedicular vertebroplasty using polymethylmethacrylate*. Journal of Spinal Disorders and Techniques, 2010. **23**(3): p. 180-185.
115. Diamond, T.H., B. Champion, and W.A. Clark, *Management of acute osteoporotic vertebral fractures: a nonrandomized trial comparing percutaneous vertebroplasty with conservative therapy*. American Journal of Medicine, 2003. **114**(4): p. 257-265.
116. Kaufmann, T.J., A.T. Trout, and D.F. Kallmes, *The Effects of Cement Volume on Clinical Outcomes of Percutaneous Vertebroplasty*. American Journal of Neuroradiology, 2006. **27**(9): p. 1933-1937.
117. Reidy, D., et al., *A biomechanical analysis of intravertebral pressures during vertebroplasty of cadaveric spines with and without simulated metastases*. Spine (Phila Pa 1976), 2003. **28**(14): p. 1534-1539.
118. Nieuwenhuijse, M.J., et al., *Optimal intravertebral cement volume in percutaneous vertebroplasty for painful osteoporotic vertebral compression fractures*. Spine (Phila Pa 1976), 2012. **37**(20): p. 1747-1755.

119. Laredo, J.D. and B. Hamze, *Complications of percutaneous vertebroplasty and their prevention*. Skeletal Radiology, 2004. **33**(9): p. 493-505.
120. Dean, J.R., K.T. Ison, and P. Gishen, *The strengthening effect of percutaneous vertebroplasty*. Clin Radiol, 2000. **55**(6): p. 471-476.
121. McKiernan, F., T. Faciszewski, and R. Jensen, *Quality of life following vertebroplasty*. Journal of Bone and Joint Surgery. American Volume, 2004. **86-A**(12): p. 2600-2606.
122. Uppin, A.A., et al., *Occurrence of New Vertebral Body Fracture after Percutaneous Vertebroplasty in Patients with Osteoporosis*. Radiology, 2003. **226**(1): p. 119-124.
123. Cortet, B., et al., *Percutaneous vertebroplasty in the treatment of osteoporotic vertebral compression fractures: an open prospective study*. J Rheumatol, 1999. **26**(10): p. 2222-2228.
124. Bajammal, S.S., et al., *The use of calcium phosphate bone cement in fracture treatment. A meta-analysis of randomized trials*. J Bone Joint Surg Am, 2008. **90**(6): p. 1186-1196.
125. Nakano, M., et al., *Percutaneous transpedicular vertebroplasty with calcium phosphate cement in the treatment of osteoporotic vertebral compression and burst fractures*. Journal of Neurosurgery: Spine, 2002. **97**(3): p. 287-293.
126. Schachar, N.S., *An update on the nonoperative treatment of patients with metastatic bone disease*. Clin Orthop Relat Res, 2001. **382**(382): p. 75-81.
127. Janjan, N.A., *Radiation for bone metastases: conventional techniques and the role of systemic radiopharmaceuticals*. Cancer, 1997. **80**(8 Suppl): p. 1628-1645.
128. Fourney, D.R., et al., *Percutaneous vertebroplasty and kyphoplasty for painful vertebral body fractures in cancer patients*. J Neurosurg, 2003. **98**(1 Suppl): p. 21-30.
129. Algra, P.R., et al., *Do metastases in vertebrae begin in the body or the pedicles? Imaging study in 45 patients*. AJR Am J Roentgenol, 1992. **158**(6): p. 1275-1279.
130. Gazelle, G.S., et al., *Tumor Ablation with Radio-frequency Energy1*. Radiology, 2000. **217**(3): p. 633-646.
131. Galibert, P., et al., *[Preliminary note on the treatment of vertebral angioma by percutaneous acrylic vertebroplasty]*. Neuro-Chirurgie, 1987. **33**(2): p. 166-168.
132. Voormolen, M.H.J., et al., *Percutaneous Vertebroplasty Compared with Optimal Pain Medication Treatment: Short-Term Clinical Outcome of Patients with Subacute or Chronic Painful Osteoporotic Vertebral Compression Fractures. The VERTOS Study*. American Journal of Neuroradiology, 2007. **28**(3): p. 555-560.
133. Martin, J.B., et al., *Vertebroplasty: clinical experience and follow-up results*. Bone, 1999. **25**(2 Suppl): p. 11S--15S.
134. Wardlaw, D., et al., *Efficacy and safety of balloon kyphoplasty compared with non-surgical care for vertebral compression fracture (FREE): a randomised controlled trial*. Lancet, 2009. **373**(9668): p. 1016-1024.
135. Liu, J., et al., *Comparing pain reduction following vertebroplasty and conservative treatment for osteoporotic vertebral compression*

- fractures: a meta-analysis of randomized controlled trials.* Pain Physician, 2013. **16**(5): p. 455-464.
136. Diamond, T.H., et al., *Percutaneous vertebroplasty for acute vertebral body fracture and deformity in multiple myeloma: a short report.* Br J Haematol, 2004. **124**(4): p. 485-487.
 137. Wenger, M. and T.M. Markwalder, *Surgically controlled, transpedicular methyl methacrylate vertebroplasty with fluoroscopic guidance.* Acta Neurochir (Wien), 1999. **141**(6): p. 625-631.
 138. Lieberman, I.H., D. Togawa, and M.M. Kayanja, *Vertebroplasty and kyphoplasty: filler materials.* Spine J, 2005. **5**(6 Suppl): p. 305S--316S.
 139. Joshi, A. and A. Glazer, *Vertebroplasty: Current concepts and outlook for the future.* The Orthopaedic Journal at Harvard Medical School, 2001. **3**: p. pp 103-107.
 140. Masala, S., et al., *Is 3T-MR spectroscopy a predictable selection tool in prophylactic vertebroplasty?* Cardiovasc Intervent Radiol, 2010. **33**(6): p. 1243-1252.
 141. Farooq, N., et al., *Can Vertebroplasty Restore Normal Load-Bearing to Fractured Vertebrae?* Spine, 2005. **30**(15): p. --.
 142. Kamano, H., et al., *New vertebral compression fractures after prophylactic vertebroplasty in osteoporotic patients.* AJR Am J Roentgenol, 2011. **197**(2): p. 451-456.
 143. Keaveny, T.M., et al., *Biomechanics of trabecular bone.* Annual Review of Biomedical Engineering, 2001. **3**(1): p. 307-333.
 144. Whyne, C.M., S.S. Hu, and J.C. Lotz, *Burst fracture in the metastatically involved spine: development, validation, and parametric analysis of a three-dimensional poroelastic finite-element model.* Spine (Phila Pa 1976), 2003. **28**(7): p. 652-60.
 145. Snyder, B.D., et al., *Noninvasive Prediction of Fracture Risk in Patients with Metastatic Cancer to the Spine.* Clin Cancer Res, 2009. **15**(24): p. 7676-7683.
 146. Windhagen, H., J.A. Hipp, and W.C. Hayes, *Postfracture Instability of Vertebrae With Simulated Defects Can Be Predicted From Computed Tomography Data.* Spine, 2000. **25**(14): p. --.
 147. Windhagen, H.J., et al., *Predicting failure of thoracic vertebrae with simulated and actual metastatic defects.* Clin Orthop Relat Res, 1997. **344**(344): p. 313-9.
 148. Buckley, J.M., et al., *Quantitative computed tomography-based predictions of vertebral strength in anterior bending.* Spine (Phila Pa 1976), 2007. **32**(9): p. 1019-1027.
 149. Kopperdahl, D.L., J.L. Pearlman, and T.M. Keaveny, *Biomechanical consequences of an isolated overload on the human vertebral body.* Journal of Orthopaedic Research, 2000. **18**(5): p. 685-690.
 150. Buckley, J.M., et al., *An improved metric for quantifying the stiffnesses of intact human vertebrae.* Proc Inst Mech Eng H, 2009. **223**(5): p. 537-543.
 151. Maquer, G., J. Schwiedrzik, and P.K. Zysset, *Embedding of human vertebral bodies leads to higher ultimate load and altered damage localisation under axial compression.* Computer Methods in Biomechanics and Biomedical Engineering, 2012. **(in-print)**: p. 1-12.

152. Ebbesen, E.N., et al., *Lumbar vertebral body compressive strength evaluated by dual-energy X-ray absorptiometry, quantitative computed tomography, and ashing*. Bone, 1999. **25**(6): p. 713-724.
153. Hosseini, H.S., D.H. Pahr, and P.K. Zysset, *Modeling and experimental validation of trabecular bone damage, softening and densification under large compressive strains* Journal of the Mechanical Behavior of Biomedical Materials 2012. **15**(0): p. 93-102.
154. Sun, K. and M.A.K. Liebschner, *Biomechanics of prophylactic vertebral reinforcement*. Spine (Phila Pa 1976), 2004. **29**(13): p. 1428--35; discussion 1435.
155. Kamel, H.K., et al., *Failure to diagnose and treat osteoporosis in elderly patients hospitalized with hip fracture*. Am J Med, 2000. **109**(4): p. 326-328.
156. Kanis, J.A., et al., *FRAX and its applications to clinical practice*. Bone, 2009. **44**(5): p. 734-743.
157. Duan, Y., et al., *The fracture risk index and bone mineral density as predictors of vertebral structural failure*. Osteoporos Int, 2006. **17**(1): p. 54-60.
158. Bousson, V., et al., *Trabecular bone score (TBS): available knowledge, clinical relevance, and future prospects*. Osteoporos Int, 2012. **23**(5): p. 1489-1501.
159. Wilcox, R.K., *The biomechanical effect of vertebroplasty on the adjacent vertebral body: a finite element study*. Proc Inst Mech Eng H, 2006. **220**(4): p. 565-572.
160. Whyne, C.M., S.S. Hu, and J.C. Lotz, *Biomechanically derived guideline equations for burst fracture risk prediction in the metastatically involved spine*. J Spinal Disord Tech, 2003. **16**(2): p. 180-5.
161. Tschirhart, C.E., J.A. Finkelstein, and C.M. Whyne, *Biomechanics of vertebral level, geometry, and transcortical tumors in the metastatic spine*. J Biomech, 2007. **40**(1): p. 46-54.
162. Bland, J. and D. Altman, *Statistical methods for assessing agreement between two methods of clinical measurement*. Lancet, 1986. **1**(8476): p. 307-10--.
163. GSYS, version 2.4.0. 2011, Japan Nuclear Reaction Data Center (JCPRG) , Hokkaido University, Japan.
164. Macneil, J.A. and S.K. Boyd, *Bone strength at the distal radius can be estimated from high-resolution peripheral quantitative computed tomography and the finite element method*. Bone, 2008. **42**(6): p. 1203-1213.
165. Chevalier, Y., et al., *A patient-specific finite element methodology to predict damage accumulation in vertebral bodies under axial compression, sagittal flexion and combined loads*. Computer Methods in Biomechanics and Biomedical Engineering, 2008. **11**(5): p. 477-487.
166. Jones, A.C. and R.K. Wilcox, *Assessment of factors influencing finite element vertebral model predictions*. J Biomech Eng, 2007. **129**(6): p. 898-903.
167. Dall'Ara, E., et al., *QCT-based finite element models predict human vertebral strength in vitro significantly better than simulated DEXA*. Osteoporosis International, 2012. **23**: p. 563-572.

168. Zeinali, A., B. Hashemi, and S. Akhlaghpour, *Noninvasive prediction of vertebral body compressive strength using nonlinear finite element method and an image based technique*. Phys Med, 2010. **26**(2): p. 88-97.
169. Pahr, D.H., et al., *HR-pQCT-based homogenised finite element models provide quantitative predictions of experimental vertebral body stiffness and strength with the same accuracy as $\frac{1}{4}$ FE models*. Computer Methods in Biomechanics and Biomedical Engineering, 2012. **15**(7): p. 711-720.
170. Buckley, J.M., K. Loo, and J. Motherway, *Comparison of quantitative computed tomography-based measures in predicting vertebral compressive strength*. Bone, 2007. **40**(3): p. 767-774.
171. Imai, K., et al., *In Vivo Assessment of Lumbar Vertebral Strength in Elderly Women Using Computed Tomography-Based Nonlinear Finite Element Model*. Spine, 2008. **33**(1): p. --.
172. Chevalier, Y., D. Pahr, and P.K. Zysset, *The role of cortical shell and trabecular fabric in finite element analysis of the human vertebral body*. J Biomech Eng, 2009. **131**(11): p. 111003.
173. Hou, F.J., et al., *Human vertebral body apparent and hard tissue stiffness* Journal of Biomechanics 1998. **31**(11): p. 1009-1015.
174. Zysset, P.K., *Indentation of bone tissue: a short review*. Osteoporosis International, 2009. **20**: p. 1049-1055.
175. Hamed, E., et al., *Multi-scale modelling of elastic moduli of trabecular bone*. Journal of The Royal Society Interface, 2012.
176. Hamed, E., Y. Lee, and I. Jasiuk, *Multiscale modeling of elastic properties of cortical bone*. Acta Mechanica, 2010. **213**(1-2): p. 131-154.
177. Akkus, O., *Elastic Deformation of Mineralized Collagen Fibrils: An Equivalent Inclusion Based Composite Model*. Journal of Biomechanical Engineering, 2005. **127**(3): p. 383-390.
178. Yuan, F., et al., *A new model to simulate the elastic properties of mineralized collagen fibril*. Biomech Model Mechanobiol, 2011. **10**(2): p. 147-160.
179. Ji, B. and H. Gao, *Elastic properties of nanocomposite structure of bone* Composites Science and Technology 2006. **66**(9): p. 1212-1218.
180. Yoon, Y. and S. Cowin, *The estimated elastic constants for a single bone osteonal lamella*. Biomechanics and Modeling in Mechanobiology, 2008. **7**(1): p. 1-11.
181. Jasiuk, I. and M. Ostoja-Starzewski, *Modeling of bone at a single lamella level*. Biomechanics and Modeling in Mechanobiology, 2004. **3**(2): p. 67-74.
182. Hengsberger, S., G. Boivin, and P.K. Zysset, *Morphological and Mechanical Properties of Bone Structural Units: A Two-Case Study*. JSME International Journal Series C, 2002. **45**(4): p. 936-943.
183. Weaver, J.K., *The Microscopic Hardness of Bone*. The Journal of Bone & Joint Surgery, 1966. **48**(2): p. 273-288.
184. Wolfram, U., H.-J. Wilke, and P.K. Zysset, *Rehydration of vertebral trabecular bone: influences on its anisotropy, its stiffness and the indentation work with a view to age, gender and vertebral level*. Bone, 2010. **46**(2): p. 348-354.

185. Hoffler, C.E., et al., *Heterogeneity of bone lamellar-level elastic moduli*. Bone, 2000. **26**(6): p. 603-609.
186. Hoffler, C.E., et al., *Age, gender, and bone lamellae elastic moduli*. J Orthop Res, 2000. **18**(3): p. 432-437.
187. Dall'ara, E., et al., *Tissue properties of the human vertebral body sub-structures evaluated by means of microindentation*. J Mech Behav Biomed Mater, 2013. **25**: p. 23-32.
188. Hodgkinson, R. and J.D. Currey, *Young's modulus, density and material properties in cancellous bone over a large density range*. Journal of Materials Science: Materials in Medicine, 1992. **3**(5): p. 377-381.
189. Helgason, B., et al., *Mathematical relationships between bone density and mechanical properties: A literature review*. Clin Biomech (Bristol, Avon), 2008. **23**(2): p. 135-146.
190. Verhulp, E., et al., *Micro-finite element simulation of trabecular-bone post-yield behaviour--effects of material model, element size and type*. Comput Methods Biomech Biomed Engin, 2008. **11**(4): p. 389-395.
191. Keyak, J.H., I.Y. Lee, and H.B. Skinner, *Correlations between orthogonal mechanical properties and density of trabecular bone: use of different densitometric measures*. J Biomed Mater Res, 1994. **28**(11): p. 1329-1336.
192. Keller, T.S., *Predicting the compressive mechanical behavior of bone*. J Biomech, 1994. **27**(9): p. 1159-1168.
193. Anderson, M.J., J.H. Keyak, and H.B. Skinner, *Compressive mechanical properties of human cancellous bone after gamma irradiation*. J Bone Joint Surg Am, 1992. **74**(5): p. 747-752.
194. Dalstra, M., et al., *Mechanical and textural properties of pelvic trabecular bone*. J Biomech, 1993. **26**(4-5): p. 523-535.
195. Keaveny, T.M., et al., *Differences between the tensile and compressive strengths of bovine tibial trabecular bone depend on modulus*. J Biomech, 1994. **27**(9): p. 1137-1146.
196. Keaveny, T.M., et al., *Systematic and random errors in compression testing of trabecular bone*. J Orthop Res, 1997. **15**(1): p. 101-110.
197. Linde, F., I. Hvid, and F. Madsen, *The effect of specimen geometry on the mechanical behaviour of trabecular bone specimens*. J Biomech, 1992. **25**(4): p. 359-368.
198. Kaneko, T.S., et al., *Mechanical properties, density and quantitative CT scan data of trabecular bone with and without metastases*. J Biomech, 2004. **37**(4): p. 523-530.
199. Lotz, J.C., T.N. Gerhart, and W.C. Hayes, *Mechanical properties of metaphyseal bone in the proximal femur* Journal of Biomechanics 1991. **24**(5): p. 317-329.
200. Snyder, S.M. and E. Schneider, *Estimation of mechanical properties of cortical bone by computed tomography*. J Orthop Res, 1991. **9**(3): p. 422-431.
201. Kopperdahl, D.L. and T.M. Keaveny, *Yield strain behavior of trabecular bone* Journal of Biomechanics 1998. **31**(7): p. 601-608.
202. Morgan, E.F., H.H. Bayraktar, and T.M. Keaveny, *Trabecular bone modulus-density relationships depend on anatomic site*. J Biomech, 2003. **36**(7): p. 897-904.

203. Lotz, J.C., T.N. Gerhart, and W.C. Hayes, *Mechanical Properties of Trabecular Bone from the Proximal Femur: A Quantitative CT Study*. Journal of Computer Assisted Tomography, 1990. **14**(1): p. --.
204. Rice, J.C., S.C. Cowin, and J.A. Bowman, *On the dependence of the elasticity and strength of cancellous bone on apparent density*. Journal of Biomechanics, 1988. **21**(2): p. 155-168--.
205. Rincon-Kohli, L. and P. Zysset, *Multi-axial mechanical properties of human trabecular bone*. Biomechanics and Modeling in Mechanobiology, 2009. **8**: p. 195-208.
206. Carter, D.R. and W.C. Hayes, *The compressive behavior of bone as a two-phase porous structure*. J Bone Joint Surg Am, 1977. **59**(7): p. 954-962.
207. Guise, T.A., et al., *Basic Mechanisms Responsible for Osteolytic and Osteoblastic Bone Metastases*. Clinical Cancer Research, 2006. **12**(20): p. 6213s-6216s.
208. Matlab, version 8.0 (R2012b) 2012, The MathWorks Inc.
209. Panjabi, M.M., et al., *Thoracic human vertebrae. Quantitative three-dimensional anatomy*. Spine (Phila Pa 1976), 1991. **16**(8): p. 888-901.
210. Silva, M.J., et al., *Strength reductions of thoracic vertebrae in the presence of transcortical osseous defects: effects of defect location, pedicle disruption, and defect size*. Eur Spine J, 1993. **2**(3): p. 118-125.
211. Taneichi, H., et al., *Risk factors and probability of vertebral body collapse in metastases of the thoracic and lumbar spine*. Spine (Phila Pa 1976), 1997. **22**(3): p. 239-245.
212. Sleiman, E., *The prediction and verification of vertebrae fracture loads using surrogate models. Comparing predicted fracture loads of surrogate vertebrae models*. 2011.
213. Kopperdahl, D.L., E.F. Morgan, and T.M. Keaveny, *Quantitative computed tomography estimates of the mechanical properties of human vertebral trabecular bone*. Journal of Orthopaedic Research, 2002. **20**(4): p. 801-805--.
214. Schileo, E., et al., *An accurate estimation of bone density improves the accuracy of subject-specific finite element models*. J Biomech, 2008. **41**(11): p. 2483-2491.
215. Singer, K., et al., *Prediction of thoracic and lumbar vertebral body compressive strength: correlations with bone mineral density and vertebral region*. Bone, 1995. **17**(2): p. 167-174.
216. Mosekilde, L. and L. Mosekilde, *Sex differences in age-related changes in vertebral body size, density and biomechanical competence in normal individuals*. Bone, 1990. **11**(2): p. 67-73.
217. Faulkner, K.G., C.E. Cann, and B.H. Hasegawa, *Effect of bone distribution on vertebral strength: assessment with patient-specific nonlinear finite element analysis*. Radiology, 1991. **179**(3): p. 669-674.
218. Homminga, J., et al., *Osteoporosis changes the amount of vertebral trabecular bone at risk of fracture but not the vertebral load distribution*. Spine (Phila Pa 1976), 2001. **26**(14): p. 1555-1561.

219. McBroom, R.J., et al., *Prediction of vertebral body compressive fracture using quantitative computed tomography*. J Bone Joint Surg Am, 1985. **67**(8): p. 1206-1214.
220. Aslan, M.S., et al. *3D Vertebral Body Segmentation Using Shape Based Graph Cuts*. in *Pattern Recognition (ICPR), 2010 20th International Conference on*. 2010.
221. Hanaoka, S., et al. *Whole vertebral bone segmentation method with a statistical intensity-shape model based approach*. in *Medical Imaging 2011: Image Processing*. 2011.
222. Hanaoka, S., et al., *3-D graph cut segmentation with Riemannian metrics to avoid the shrinking problem*. Med Image Comput Comput Assist Interv, 2011. **14**(Pt 3): p. 554-561.
223. Panjabi, M.M., et al., *Biomechanical time-tolerance of fresh cadaveric human spine specimens*. Journal of Orthopaedic Research, 1985. **3**(3): p. 292-300.
224. Software, B.M.T. 2010, Instron, MA, USA.
225. Hipp, J.A., A.E. Rosenberg, and W.C. Hayes, *Mechanical properties of trabecular bone within and adjacent to osseous metastases*. J Bone Miner Res, 1992. **7**(10): p. 1165-1171.
226. Melton, r., LJ, et al., *Epidemiology of vertebral fractures in women*. Am J Epidemiol, 1989. **129**(5): p. 1000-1011.
227. Viceconti, M., et al., *Extracting clinically relevant data from finite element simulations*. Clin Biomech (Bristol, Avon), 2005. **20**(5): p. 451-454.
228. Uthgenannt, B.A., et al., *Skeletal self-repair: stress fracture healing by rapid formation and densification of woven bone*. J Bone Miner Res, 2007. **22**(10): p. 1548-56.
229. Merlotti, D., et al., *Current options for the treatment of Paget's disease of the bone*. Open Access Rheumatology: Research and Reviews, 2009: p. 107.
230. Fajardo, R.J., et al., *Specimen size and porosity can introduce error into microCT-based tissue mineral density measurements*. Bone, 2009. **44**(1): p. 176-184.
231. Meganck, J.A., et al., *Beam hardening artifacts in micro-computed tomography scanning can be reduced by X-ray beam filtration and the resulting images can be used to accurately measure BMD*. Bone, 2009. **45**(6): p. 1104-1116.
232. Hong, J., et al., *Failure of trabecular bone with simulated lytic defects can be predicted non-invasively by structural analysis*. J Orthop Res, 2004. **22**(3): p. 479-486.
233. Eastell, R., et al., *Classification of vertebral fractures*. Journal of Bone and Mineral Research, 1991. **6**(3): p. 207-215.
234. Roux, J.-P., et al., *Contribution of trabecular and cortical components to biomechanical behavior of human vertebrae: an ex vivo study*. J Bone Miner Res, 2010. **25**(2): p. 356-361.
235. (IPL), I.P.L. microCT100, Scanco medical, AG, Bazeldorf, Switzerland.
236. Ridler, T.W. and E.S. Calvard, *Picture Thresholding Using an Iterative Selection Method*. Systems, Man and Cybernetics, IEEE Transactions on, 1978. **8**(8): p. 630-632.
237. R, version 2.12.1. 2010, R Development Core Team.

238. Augat, P., et al., *Anisotropy of the elastic modulus of trabecular bone specimens from different anatomical locations*. Med Eng Phys, 1998. **20**(2): p. 124-131.
239. Cendre, E., et al., *High-resolution computed tomography for architectural characterization of human lumbar cancellous bone: relationships with histomorphometry and biomechanics*. Osteoporos Int, 1999. **10**(5): p. 353-360.
240. Bevill, G., S.K. Easley, and T.M. Keaveny, *Side-artifact errors in yield strength and elastic modulus for human trabecular bone and their dependence on bone volume fraction and anatomic site*. J Biomech, 2007. **40**(15): p. 3381-3388.
241. Bevill, G., F. Farhamand, and T.M. Keaveny, *Heterogeneity of yield strain in low-density versus high-density human trabecular bone*. J Biomech, 2009. **42**(13): p. 2165-2170.
242. Ladd, A.J., et al., *Finite-element modeling of trabecular bone: comparison with mechanical testing and determination of tissue modulus*. J Orthop Res, 1998. **16**(5): p. 622-628.
243. Follet, H., et al., *Effects of preexisting microdamage, collagen cross-links, degree of mineralization, age, and architecture on compressive mechanical properties of elderly human vertebral trabecular bone*. J Orthop Res, 2011. **29**(4): p. 481-488.
244. Ouyang, X., et al., *Morphometric texture analysis of spinal trabecular bone structure assessed using orthogonal radiographic projections*. Med Phys, 1998. **25**(10): p. 2037-2045.
245. Crawford, R.P. and T.M. Keaveny, *Relationship between axial and bending behaviors of the human thoracolumbar vertebra*. Spine (Phila Pa 1976), 2004. **29**(20): p. 2248-2255.
246. Wolfram, U., H. Wilke, and P.K. Zysset, *Rehydration of vertebral trabecular bone: influences on its anisotropy, its stiffness and the indentation work with a view to age, gender and vertebral level*. Bone, 2010. **46**: p. 348--354.
247. Mazza, G., et al., *Anisotropic Elastic Properties of Vertebral Compact Bone Measured by Microindentation*. Journal of Biomechanics, 2008. **41**: p. S75--.
248. Oliver, W.C. and G.M. Pharr, *An improved technique for determining hardness and elastic modulus using load and displacement sensing indentation experiments*. Journal of Materials Research, 1992. **7**: p. 1564-1583.
249. Yandell, B.S., *Practical Data Analysis for Designed Experiments*. 1997: Taylor & Francis.
250. Croucher, P.I. and J.F. Apperley, *BONE DISEASE IN MULTIPLE MYELOMA*. British Journal of Haematology, 1998. **103**(4): p. 902-910.
251. Komatsubara, S., et al., *Suppressed bone turnover by long-term bisphosphonate treatment accumulates microdamage but maintains intrinsic material properties in cortical bone of dog rib*. Journal of Bone and Mineral Research, 2004. **19**(6): p. 999-1005.
252. Roschger, P., et al., *Bone mineralization density distribution in health and disease*. Bone, 2008. **42**(3): p. 456-466.

253. Deramond, H., N.T. Wright, and S.M. Belkoff, *Temperature elevation caused by bone cement polymerization during vertebroplasty*. Bone, 1999. **25**(2 Suppl): p. 17S--21S.
254. Konno, S., et al., *The European Spine Society AcroMed Prize 1994. Acute thermal nerve root injury*. Eur Spine J, 1994. **3**(6): p. 299-302.
255. Wilkes, R.A., J.G. Mackinnon, and W.G. Thomas, *Neurological deterioration after cement injection into a vertebral body*. J Bone Joint Surg Br, 1994. **76**(1): p. 155.
256. Berman, A.T., et al., *Thermally induced bone necrosis in rabbits. Relation to implant failure in humans*. Clin Orthop Relat Res, 1984(186): p. 284-292.
257. Mathis, J.M., et al., *Percutaneous vertebroplasty: a developing standard of care for vertebral compression fractures*. AJNR Am J Neuroradiol, 2001. **22**(2): p. 373-381.
258. Belkoff, S.M., et al., *Biomechanical evaluation of a new bone cement for use in vertebroplasty*. Spine (Phila Pa 1976), 2000. **25**(9): p. 1061-1064.
259. Ginebra, M.P., et al., *New processing approaches in calcium phosphate cements and their applications in regenerative medicine*. Acta Biomater, 2010. **6**(8): p. 2863-2873.
260. Turner, T.M., et al., *Vertebroplasty comparing injectable calcium phosphate cement compared with polymethylmethacrylate in a unique canine vertebral body large defect model*. Spine J, 2008. **8**(3): p. 482-487.
261. Urrutia, J., et al., *Early histologic changes following polymethylmethacrylate injection (vertebroplasty) in rabbit lumbar vertebrae*. Spine (Phila Pa 1976), 2008. **33**(8): p. 877-882.
262. Oshima, M., et al., *Evaluation of biomechanical and histological features of vertebrae following vertebroplasty using hydroxyapatite blocks*. Orthopedics, 2010. **33**(2): p. 89-93.
263. Ikenaga, M., et al., *Biomechanical characterization of a biodegradable calcium phosphate hydraulic cement: a comparison with porous biphasic calcium phosphate ceramics*. J Biomed Mater Res, 1998. **40**(1): p. 139-144.
264. Knaack, D., et al., *Resorbable calcium phosphate bone substitute*. J Biomed Mater Res, 1998. **43**(4): p. 399-409.
265. Bai, B., et al., *The Use of an Injectable, Biodegradable Calcium Phosphate Bone Substitute for the Prophylactic Augmentation of Osteoporotic Vertebrae and the Management of Vertebral Compression Fractures.*, in *The Use of an Injectable, Biodegradable Calcium Phosphate Bone Substitute for the Prophylactic Augmentation of Osteoporotic Vertebrae and the Management of Vertebral Compression Fractures*. 1999, From the Musculoskeletal Research Center, Department of Orthopaedic Surgery, Hospital for Joint Diseases Orthopaedic Institute, New York, New York.: (C) 1999 Lippincott Williams & Wilkins, Inc. p. 1521--.
266. Baroud, G., et al., *Load shift of the intervertebral disc after a vertebroplasty: a finite-element study*. Eur Spine J, 2003. **12**(4): p. 421-426.

267. Lim, T.-H., et al., *Biomechanical evaluation of an injectable calcium phosphate cement for vertebroplasty*. Spine (Phila Pa 1976), 2002. **27**(12): p. 1297-1302.
268. Heini, P.F., et al., *Augmentation of mechanical properties in osteoporotic vertebral bones – a biomechanical investigation of vertebroplasty efficacy with different bone cements*. European Spine Journal, 2001. **10**(2): p. 164-171.
269. Ikeuchi, M., et al., *Mechanical augmentation of the vertebral body by calcium phosphate cement injection*. J Orthop Sci, 2001. **6**(1): p. 39-45.
270. Bailey, R.A., *Orthogonal Partitions in Designed Experiments*. 1996. **8**(1-2): p. 45-77--.
271. Grover, L.M., et al., *In vitro ageing of brushite calcium phosphate cement*. Biomaterials, 2003. **24**(23): p. 4133-4141.
272. Avizo, version 8.0. 2013, Visualization Sciences Group, SAS.
273. Claes, L., et al., *Influence of size and stability of the osteotomy gap on the success of fracture healing*. J Orthop Res, 1997. **15**(4): p. 577-584.
274. Jensen, M.E., et al., *Percutaneous polymethylmethacrylate vertebroplasty in the treatment of osteoporotic vertebral body compression fractures: technical aspects*. American Journal of Neuroradiology, 1997. **18**(10): p. 1897-904.
275. Tarsuslugil, S.M., et al., *Development of calcium phosphate cement for the augmentation of traumatically fractured porcine specimens using vertebroplasty*. J Biomech, 2013. **46**(4): p. 711-715.
276. Bohner, M. and G. Baroud, *Injectability of calcium phosphate pastes* Biomaterials 2005. **26**(13): p. 1553-1563.
277. Montufar, E.B., Y. Maazouz, and M.P. Ginebra, *Relevance of the setting reaction to the injectability of tricalcium phosphate pastes*. Acta Biomater, 2013. **9**(4): p. 6188-6198.
278. Grover, L.M., et al., *Frozen delivery of brushite calcium phosphate cements* Acta Biomaterialia 2008. **4**(6): p. 1916-1923.
279. Hernandez, L., et al., *New injectable and radiopaque antibiotic loaded acrylic bone cements*. J Biomed Mater Res B Appl Biomater, 2008. **87**(2): p. 312-320.
280. Kurtz, S.M., et al., *Static and fatigue mechanical behavior of bone cement with elevated barium sulfate content for treatment of vertebral compression fractures*. Biomaterials, 2005. **26**(17): p. 3699-3712.
281. Ananthakrishnan, D., et al., *The effect on anterior column loading due to different vertebral augmentation techniques*. Clin Biomech (Bristol, Avon), 2005. **20**(1): p. 25-31.
282. Trout, A.T., D.F. Kallmes, and T.J. Kaufmann, *New fractures after vertebroplasty: adjacent fractures occur significantly sooner*. AJNR Am J Neuroradiol, 2006. **27**(1): p. 217-223.
283. Jensen, M.E. and J.E. Dion, *Percutaneous vertebroplasty in the treatment of osteoporotic compression fractures*. Neuroimaging Clin N Am, 2000. **10**(3): p. 547-568.
284. Wilkins, C.H. and S.J. Birge, *Prevention of osteoporotic fractures in the elderly*. Am J Med, 2005. **118**(11): p. 1190-1195.

285. Harrop, J.S., et al., *Primary and Secondary Osteoporosis' Incidence of Subsequent Vertebral Compression Fractures After Kyphoplasty*. Spine, 2004. **29**(19): p. --.
286. Berlemann, U., et al., *Adjacent vertebral failure after vertebroplasty. A biomechanical investigation*. J Bone Joint Surg Br, 2002. **84**(5): p. 748-752.
287. Polikeit, A., L.P. Nolte, and S.J. Ferguson, *The effect of cement augmentation on the load transfer in an osteoporotic functional spinal unit: finite-element analysis*. Spine (Phila Pa 1976), 2003. **28**(10): p. 991-996.
288. Bostrom, M.P. and J.M. Lane, *Future directions. Augmentation of osteoporotic vertebral bodies*. Spine (Phila Pa 1976), 1997. **22**(24 Suppl): p. 38S--42S.
289. Kallmes, D.F. and M.E. Jensen, *Percutaneous vertebroplasty*. Radiology, 2003. **229**(1): p. 27-36.
290. Race, A., K.A. Mann, and A.A. Edidin, *Mechanics of bone/PMMA composite structures: an in vitro study of human vertebrae*. J Biomech, 2007. **40**(5): p. 1002-1010.
291. López, A., et al., *Compressive mechanical properties and cytocompatibility of bone-compliant, linoleic acid-modified bone cement in a bovine model*. J Mech Behav Biomed Mater, 2014. **32**: p. 245-256.
292. Fields, A.J., et al., *Influence of vertical trabeculae on the compressive strength of the human vertebra*. J Bone Miner Res, 2011. **26**(2): p. 263-269.
293. Helgason, B., et al., *Influence of cement stiffness and bone morphology on the compressive properties of bone-cement composites in simulated vertebroplasty*. J Biomed Mater Res B Appl Biomater, 2013. **101**(2): p. 364-374.
294. López, A., et al., *Low-modulus PMMA bone cement modified with castor oil*. Biomed Mater Eng, 2011. **21**(5-6): p. 323-332.
295. Stephen, W.H., *Archimedes revisited: a faster, better, cheaper method of accurately measuring the volume of small objects*. Physics Education, 2005. **40**(5): p. 468--.
296. Whealan, K.M., et al., *Noninvasive imaging predicts failure load of the spine with simulated osteolytic defects*. J Bone Joint Surg Am, 2000. **82**(9): p. 1240-51.

List of Abbreviations

aBMD		Areal BMD (radiographic BMD)	[mg/cm ²]
ANOVA	-	Analysis of variance (statistics)	
BMD	or	Bone mineral density	[mgHA/cm ³]
vBMD			
BV/TV	-	Bone volume fraction	[1] or [%]
CaP	-	Calcium phosphate	
CDHA	-	Calcium deficient hydroxyapatite	
Conn.D	-	Bone connectivity density	[mm ⁻³]
CS	-	Cross-section	
CSA	-	Cross-sectional area	[mm ²]
CT	-	Computed tomography	
DXA	-	Dual Energy X-ray Absorbtiometry	
E	-	Modulus of elasticity	[GPa]
EA	-	Axial stiffness	[N]
EI	-	Bending (Flexural) stiffness	[Nm ²]
Ei	-	Indentation modulus	[GPa]
FE	-	Finite element	
FRI	-	Fracture Risk Index	
Fz	-	Theoretical strength	[kN]
GOBJ	-	MicroCT (Scanco) VOI	
GUI	-	Graphical User Interface	
H	-	Micro-hardness	[MPa]
HA	-	Hydroxyl-apatite	
ISQ	-	MicroCT (Scanco) reconstructed data file	
LVDT	-	Linear variable differential transformers	
MBD	-	Myeloma bone disease	
mets	-	Metastases from primary cancer (in this context any other than MM cancer)	
microCT	-	Pre-clinical micro-computed tomography	
MIL	-	Bone mean intercept of length (degree of isotropy)	
minCSA	-	Minimum cross-section area	[mm ²]
MM	-	Multiple myeloma cancer	
MM.L	-	Micro-indentation sample group: samples with invasion to the vertebral bone, samples taken from proximity of the lesion	
MM.L.C	-	Micro-indentation sample group: samples with invasion to the vertebral bone, samples taken distantly from the lesion	
MM.N	-	Micro-indentation sample group: donors diagnosed with MM cancer without visible lesions	
Non-MM	-	Micro-indentation sample group: donors without diagnosed MM cancer	

OP	-	Osteoporosis	
PKP	-	Percutaneous Kyphoplasty	
PMMA	-	Poly(methyl_methacrylate)	
p-qCT	-	Pre-clinical qualitative computed tomography	
PVP	-	Percutaneous vertebroplasty	
qCT	-	Qualitative computed tomography	
R ²	-	Coefficient of determination (statistics)	
RCT	-	Randomised controlled trials	
RMS	-	Root mean square (statistics)	
RSQ	-	MicroCT (Scanco) raw data file	
SEG_CYL	-	Segmented trabecular bone binary stack within the representative VOI	
SLA	-	Stereo-lithography (SLA)	
SLS	-	Selective Laser Sintering (SLS)	
SRE	-	Skeletal related event	
Tb.N	-	Number of trabeculae	[1/mm]
Tb.Sp	-	Trabecular separation (spacing)	[mm]
Tb.Th	-	Trabecular thickness	[mm]
TBS	-	Trabecular Bone Score	
VB	-	Vertebral body	
VCF	-	Vertebral compression fractures	
VOI	-	Volume of Interest	
V _{VB}	-	Vertebral body volume	
WCF	-	Wedge compression fracture	
We	-	Elastic energy	[pJ]
WHO	-	World Health Organisation	
Wp	-	Plastic energy	[pJ]
wt%	-	% by weight	
α-TCP	-	Alpha-tri-calcium phosphate	
ε	-	Bone strain	[%]
ρ	-	Tissue density	[mg/cm ³]
ρ _{app}	-	Apparent density	[mg/cm ³]
ρ _{ash}	-	Ash density	[mg/cm ³]
ρ _{BMD}	-	Bone mineral density	[mgHA/cm ³]
ρ _{ct}	-	CT density	[HU]
ρ _{dry}	-	Apparent dry density	[mg/cm ³]
K	-	Humidity	[%]
T	-	Temperature	[°C]
3D	-	3-dimensional (volumetric)	

Appendix A: Historical data assessment

Specimen	Quantitative assessment		Experimental data		Fracture prediction Fz [kN]	
	Extra-vertebral body lesion	BMD [mgHA/cm ³]	Stiffness [kN/mm]	F(zero-slope) [kN]	Entire VB CSA	Extra-VB formations masked
Bladder mets - T6	enlarged osteoblastic lesion	115.6	2.47	1.88	2.45	2.24
Bladder mets - T7	enlarged osteoblastic lesion	95.7	2.11	1.81	2.69	2.07
Bladder mets - T8	small osteoblastic lesion	78.1	1.46	1.45	2.21	2.14
Bladder mets - T9	small osteoblastic lesion	93.5	2.13	1.91	4.03	2.70
Bladder mets - T10	enlarged osteoblastic lesion	78.3	2.04	2.08	5.47	2.17
Bladder mets - T11	enlarged osteoblastic lesion	136.1	1.16	2.00	4.87	2.19
Bladder mets - T12	no osteoblastic lesion	92.7	1.43	1.52	2.09	1.81
Bladder mets - L1	small osteoblastic lesion	94.0	2.92	2.59	2.81	2.78
Bladder mets - L2	no osteoblastic lesion	88.4	1.04	1.73	3.47	3.35
Bladder mets - L3	very small	80.5	1.87	2.71	3.03	2.99
Bladder mets - L4	No lesion but fractured	115.4	1.52	2.63	3.13	2.22
Bladder mets - L5	no osteoblastic lesion	114.5	2.73	4.20	4.86	4.71

Table 20 Historical data: Experimental, BMD and fracture prediction data of metastatic samples from a donor with bladder cancer

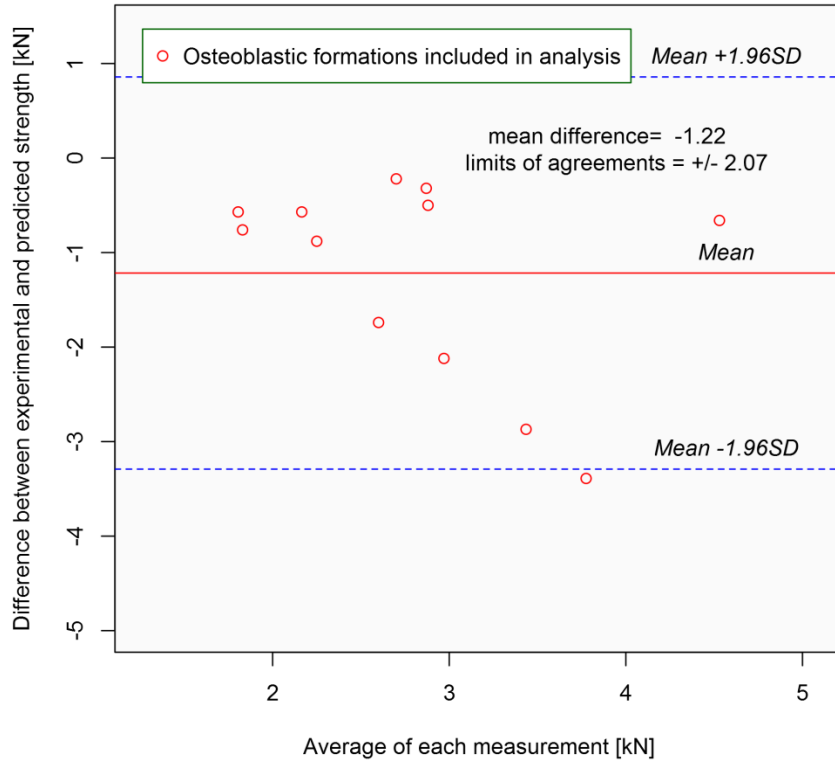


Figure 62 Initial fracture prediction assessment (without masking the CSA)

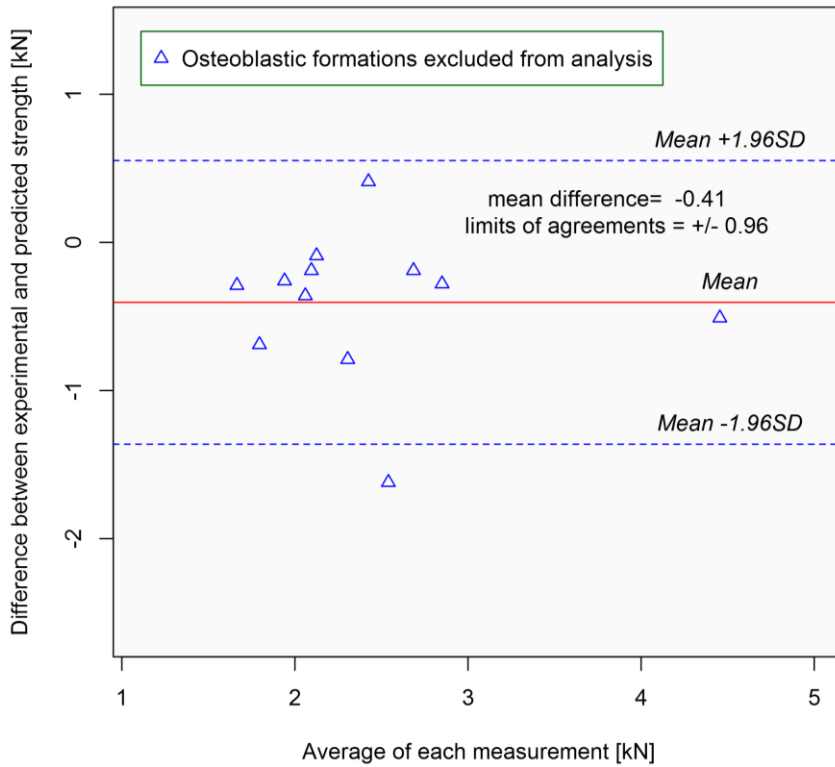


Figure 63 Additional fracture prediction assessment (masking the Osteoblastic lesions)

Appendix B: Validation of vertebral body segmentation

To validate the approach in terms of both accuracy and precision, the calculated volume was confirmed against measured volume. In this study, volumetric measurements based on the sum of all cross-sectional areas obtained from the microCT measurements were directly compared to those experimentally obtained using a buoyancy principle.

For this validation study seventeen porcine vertebral bodies of different sizes were harvested, the posterior elements were fully removed and the remaining vertebral body was separated from any soft tissue. Here the volumes were measured using the Archimedes principle [295]. In summary, the vertebral body was submerged into a solution and hence was subjected to an upwards force due to buoyancy where the force is equal to amount of water displaced. This force was then expressed as the change in weight of water before and after submerging the VB (Figure 64).

The volumetric measurements were compared in terms of the percentage difference between methods, where the buoyancy method was taken as the reference [162]. The initial comparison of these two methods (blue dataset on Figure 65) uncovered a substantial but consistent difference in microCT measurement data (average $\Delta V=9.55\%$, $RMS=9.6\%$). This was further investigated and in fact, through the application of this study, uncovered a faulty calibration of the microCT machine introduced by the manufacturer two years before this study. The manufacturer later proposed a re-calibration tool which was used to adjust all scans for the correct voxel size and were used on all scans following this final calibration.

The corrected dataset improved in terms of volumetric bias to $\Delta V=-1.59\%$ (-0.19cm^3) with precision of $RMS=2.25\%$ (0.34cm^3). The remaining difference can be explained by residual soft tissue on the VB which is not visible under microCT assessment. Hence the vertebral body image segmentation tool has proved to be sufficiently precise and accurate in estimating the boundary based on microCT images.

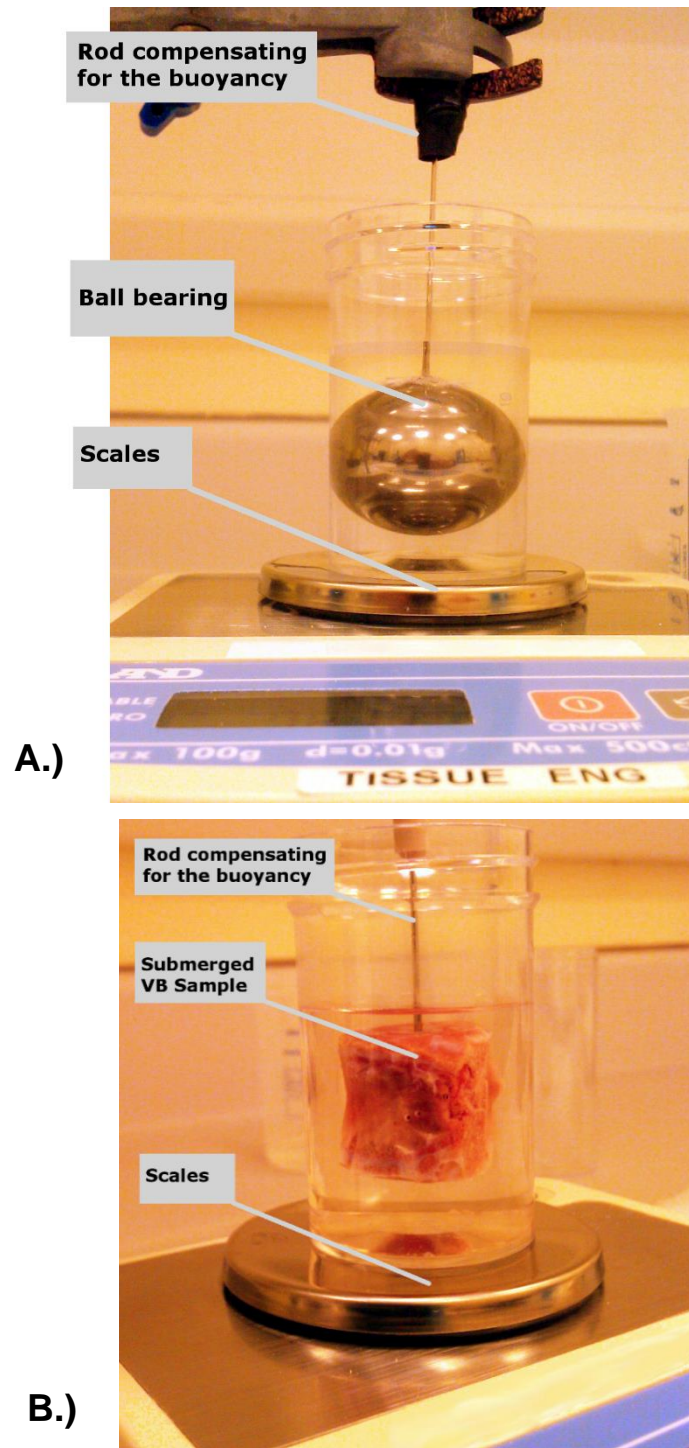


Figure 64: The buoyancy principle has been used to measure the volume of a vertebral body. First (depicted in (A)) the experimental setup and the principle have been tested on a metal ball-bearing with known volume ($\Delta V < 0.2\%$) and later used on porcine vertebral bone samples (in (B)). Compared to the traditional Archimedes principle, here the volume is not required to be measured in terms of displacement but can be calculated based on change of weight (with precision of $0.01\text{g} = 0.01\text{cm}^3$)

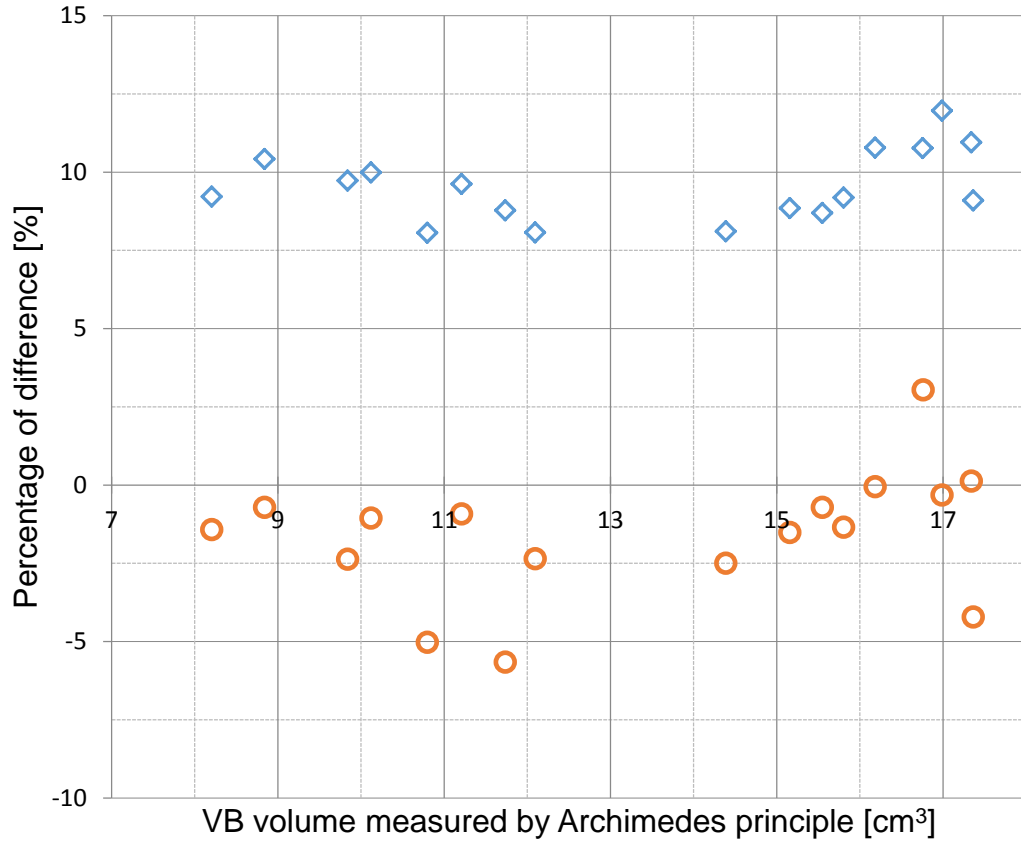


Figure 65: Validation of vertebral body image segmentation script. The numerical approach was validated by means of compared volumes obtained experimentally and using the microCT approach. Initial results (in the graph as blue diamond markers) have later highlighted a discrepancy in measurements and led to uncovering faulty calibration of the microCT by the manufacturer. Corrected data (depicted as red squares) were found to possess volumetric differences of -1.59% (-0.19cm³) (RMS 2.25% (0.34cm³))

Appendix C: Donors' medical records available for this study

	Primary (1) and secondary (2) cause of death	History of (H/O)	Drugs known to be administered within the last 6 months prior to TOD
SpineBS 1	1 Chronic Cardial Failure 2 Peripheral Vascular Disease, Liver Abscess	Arthritis, Liver disease, Brest Cancer (treated)	Information not available
SpineBS 2	1 Carcinomatosis, 1b Gastric adenocarcinoma	Information not available	Information not available
SpineBS 3	1 Bronchopneumonia, 2 Adenocarcinoma of lung and emphysema	Hypertensive and ischemic heart disease	Information not available
SpineGo 1	1 Respiratory failure 2 Dialated cardiomyopathy	Osteoporosis, mild severity CHF diag ~5yrs prior TOD Hysterectomy ~30yrs prior TOD Emphysema & COPD diag ~30yrs prior TOD Smoker (3 per day ~40yrs)	Xanax, morphine, antibiotic, Antibiotics prior to TOD
SpineGo 2	1 Debility with likely pneumonia, ESRF 2 Persistent Cdif, R hip fx from fall	Fell and Fx R femur 2mos prior TOD (plate input) Mild arthritis in knees, shoulder, hip-taking Celebrex; mild osteoporosis- Rx-actonel and vit D Melanoma removed 20yrs-neck HTN Interstitial lung disease, resting capacity 92%, Renal failure recent OU Cataract Sx 15yrs ago UTI-amplicitin, CDIF 2 weeks ago on ABX and curred 2 wks prior flu-like symptoms, ABX for UTI and CDIF-2 wks prior Social drinker(2x/week), no tabacco Blood transfusion 2 mths prior TOD - 3 units after Femur Sx, 2 units a few days after	Protonix, Oxycontin, Benicar, Actonel, Vit D, Lovonox, Fe, Multi-Vit, Miralax, Sonata, Lidoderm, Metanex, Sena
... table continued on following page...			

	Primary (1) and secondary (2) cause of death	History of (H/O)	Drugs known to be administered within the last 6 months prior to TOD
SpineGo 4	1 Aspirating pneumonia	Mild arthritis in rt shoulder dx 10 prior to TOD, mild osteo of spine dx 10 yrs prior to TOD, memory loss 1yr prior to TOD, pneumonia 3 times w/in 4yrs prior to TOD, aspiration pneumonia COD, hearing aid 4yrs prior to TOD, UTI 2009- abx use 1wk prior to TOD, Cataract sx both eyes 10-20 yrs prior to TOD Full hysterectomy 30yrs prior to TOD, left hip replacement 1994/1995, left knee sx 1996, pneumonia 3x w/in 4yrs prior to TOD	Diovanm benzonate, abx, tylenol PM, iron, Spiriva, flu shot, blood transfusion
SpineGo 5	1 Haemopericardium, 2 Ventricular perforation, 1c Myocardial	Infarction	Information not available
SpineGo 6	1 Metastatic oesophageal carcinoma	Hysterectomy 1980's, appendectomy when young, COPD, no Chemo in last 6 months	Information not available
Spine 1 mets	1 Respiratory failure, Metastatic inflammatory carcinoma 2 left inflammatory breast carcinoma, lft. Breast CA	Breast CA dx 7yrs prior to TOD, chemotherapy and radiation for tx, Mets: upper spine, R hip, liver Hysterectomy No bedsores Bilat mastectomy 10yrs ago, lap flap 6yrs ago, Thoracic sx 5yrs prior TOD, partial hysterectomy 4yrs ago, ovaries removed, chemo port placed 6yrs prior TOD	
Spine 2 mets	1 Metastatic lung cancer	Ca w mets to spine, liver, ribs, no other bone disease Cancer: dx cancer 5mos prior TOD left lung, liver, ribs, spine, melanoma dx 3yrs prior TOD CHF and irregular heartbeat, refused pacemaker Open bedsore on tailbone not sure of exact size (bedsores 3,4) Memory loss (began 10mos prior TOD) Traumas: fell walking down stairs at his home (not reported), one week prior getting out of bed fell- hospice examined after that fall no inj Smoker: 1ppd >20yrs Appendectomy 50yrs prior, hernia sx over 20yrs prior, endarterectomy neck sx bilat 10yrs prior TOD	Information not available
... table continued on following page...			

	Primary (1) and secondary (2) cause of death	History of (H/O)	Drugs known to be administered within the last 6 months prior to TOD
Spine 1 MM	1 Pulmonary Oedema 2 Renal Failure and malignant myeloma	87 yr old Female Unsure on height and weight Myeloma and nothing else significant, information from Solicitor as this lady's wishes had been expressed in her will and we did not receive a copy of the GP questionnaire. Findings at autopsy did not find anything significant or intimate that the donor had had any other surgeries or suffered any other medical conditions	Information not available
Spine 3 MM	1 Multiple myeloma	(Material Transfer Agreement not available)	Information not available
Spine 4 MM	1 Multiple myeloma	Myeloma, diagnosed: 05/2010, mets to shoulder and head Hypertension Hx of kidney stones 20y prior death Diabetes type II Hearing loss in both ears, no aids Smoker (15y) Alcohol – minimal	Morphine, Ativan, (bisphosphonates not mentioned)
Spine 5 MM	1 Cardiorespiratory failure	Multiple myeloma diagnosed 08/2009 Cirrhosis due to alcohol abuse (dx 6y prior) Cataract sx 1y prior, side unk Heavy alcohol use Smoker (15y, 1ppd)	Morphine (bisphosphonates not mentioned)
Spine 6 MM	1 Immunoglobulin G Kaapa multiple myeloma stage 3	Multiple Myeloma w/o remission, unk of Tx if any, unk dxd Hernia Sx, unk location on body, approx. 60 years prior	None specified

... table continued on following page...

	Primary (1) and secondary (2) cause of death	History of (H/O)	Drugs known to be administered within the last 6 months prior to TOD
Spine 7 MM	1 Terminal multiple myeloma	<p>Fall at his home a few times and threshold 2 months ago</p> <p>Arthritis in knees, pain in back was thought to be from arthritis, pain scale 5, self-medication (OTC Tylenol arthritis). No formal DX on arthritis</p> <p>Multiple Myeloma diagnosed 3y prior to death. Oral chemotherapy, bone strengthening infusions every month, off chemo and in remission for a year</p> <p>Quintuple bypass surgery 10y prior to death, veins in both legs stripped 10 y prior to death</p> <p>Depression 5y prior to death.</p> <p>Allergies: Seasonal, fish, NSAIDS, Cephalosporin</p> <p>6-8y prior to death last TB testing: negative</p> <p>Dialysis for the last 17y (diagnosed 17y prior to death)</p> <p>Acid reflux</p> <p>Loss of hearing in his left ear, dxd 10y prior to death</p>	<p>Simvastatin 40mg 1poqd, Omeprazole 20mg po bid, Rocatrol .25mcg 1poqd, Dexamethasone 40mg 10tabs per week, Primidone 50mg 1 pot id, Setraline HCL 50mg 1poqd, Fludrocortisone Acatate .1mg po bid, Vitamin D 50,000 UI 1 po month, Full spectrum B w/ Vit C OTC, Tylenol Artitis pain, Critical, Loperamide HCL 2mg (dosage not known)</p>

Table 21 Medical history details as acquired from GIFT banks.

Appendix D: Morphology assessment

Appendix D.1: Osteoporosis

Morph.Index	bmd [mgHA/cm ³]	BV/TV [1]	Tb.Sp [mm]	Tb.Th [mm]	Tb.N [1/mm]	Conn.D [1]
Spine 1 BS	147.7 (±22.8)	0.17 (±0.03)	1.34 (±0.16)	0.32 (±0.03)	1.41 (±0.14)	0.62 (±0.12)
Spine 2 BS	124.9 (±7.9)	0.19 (±0.02)	1.14 (±0.13)	0.3 (±0.03)	1.21 (±0.11)	0.88 (±0.09)
Spine 3 BS	69.5 (±9.2)	0.11 (±0.01)	1.74 (±0.17)	0.3 (±0.01)	1.77 (±0.16)	0.37 (±0.08)
SpineGO 1	122.9 (±11.2)	0.15 (±0.02)	1.33 (±0.15)	0.3 (±0)	1.38 (±0.14)	0.69 (±0.11)
SpineGO 2	124.3 (±11.5)	0.2 (±0.01)	0.94 (±0.04)	0.27 (±0.01)	1.01 (±0.04)	1.47 (±0.12)
SpineGO 4	194.6 (±7.9)	0.22 (±0)	1.02 (±0.09)	0.31 (±0.02)	1.09 (±0.07)	1.51 (±0.08)
SpineGO 5	137.3 (±5.7)	0.17 (±0.01)	1.16 (±0.1)	0.3 (±0)	1.23 (±0.09)	0.83 (±0.12)
SpineGO 6	111.9 (±63.6)	0.16 (±0.05)	1.48 (±0.33)	0.33 (±0.08)	1.48 (±0.32)	0.61 (±0.41)

Table 22 Morphology assessment: Osteoporosis (mean ± stdev)

Appendix D.2: Metastases

Morph.Index	bmd [mgHA/cm ³]	BV/TV [1]	Tb.Sp [mm]	Tb.Th [mm]	Tb.N [1/mm]	Conn.D [1]
Spine 1 mets	178.8 (±26.6)	0.31 (±0.02)	0.72 (±0.03)	0.3 (±0.02)	0.84 (±0.02)	2.53 (±0.2)
Spine 2 mets	125.8 (±14.5)	0.23 (±0.03)	0.89 (±0.09)	0.32 (±0.03)	0.97 (±0.09)	1.29 (±0.31)

Table 23 Morphology assessment: Metastases to spine (mean ± stdev)

Appendix D.3: Multiple myeloma

Morph.Index	BMD [mgHA/cm ³]	BV/TV [1]	Tb.Sp [mm]	Tb.Th [mm]	Tb.N [1/mm]	Conn.D [1]
Spine MM 4	111.4 (±12.5)	0.11 (±0.01)	2.56 (±0.74)	0.36 (±0.08)	2.61 (±0.71)	0.33 (±0.08)
Spine MM 5	166.8 (±24.1)	0.2 (±0.01)	1.04 (±0.06)	0.32 (±0.01)	1.13 (±0.05)	0.99 (±0.1)
Spine MM 6	107.5 (±5.2)	0.16 (±0.01)	1.18 (±0.03)	0.28 (±0.01)	1.26 (±0.03)	0.84 (±0.07)
Spine MM 7	159	0.17	1.54	0.35	1.68	0.64

Table 24 Morphology assessment: multiple myeloma (mean ± stdev)

Appendix E: Cadaveric testing: Strength/stiffness per level

Appendix E.1: Osteoporosis

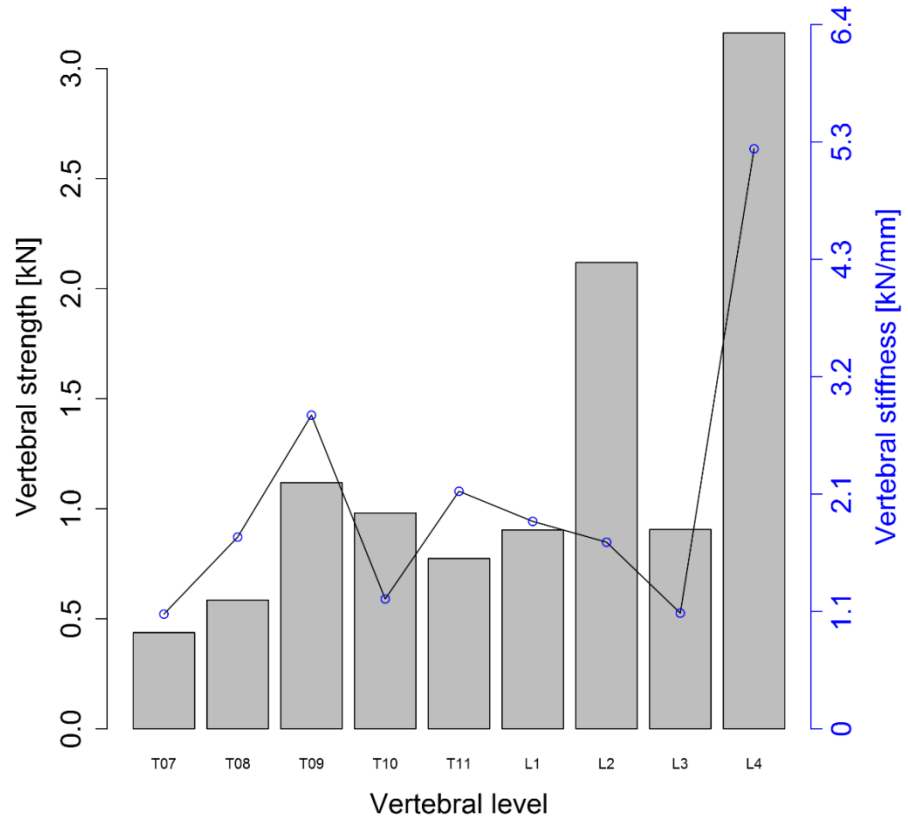


Figure 66 Strength and stiffness data for osteoporotic study for each spine and vertebral level used in the study - Spine BS 1

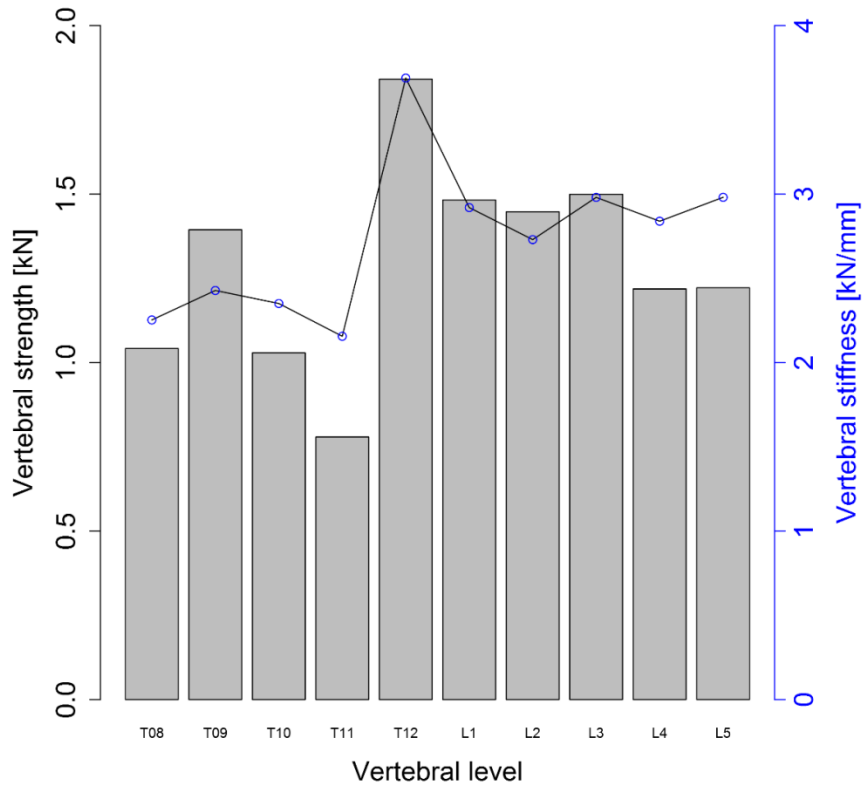


Figure 67 Strength and stiffness data for osteoporotic study for each spine and vertebral level used in the study - Spine BS 2

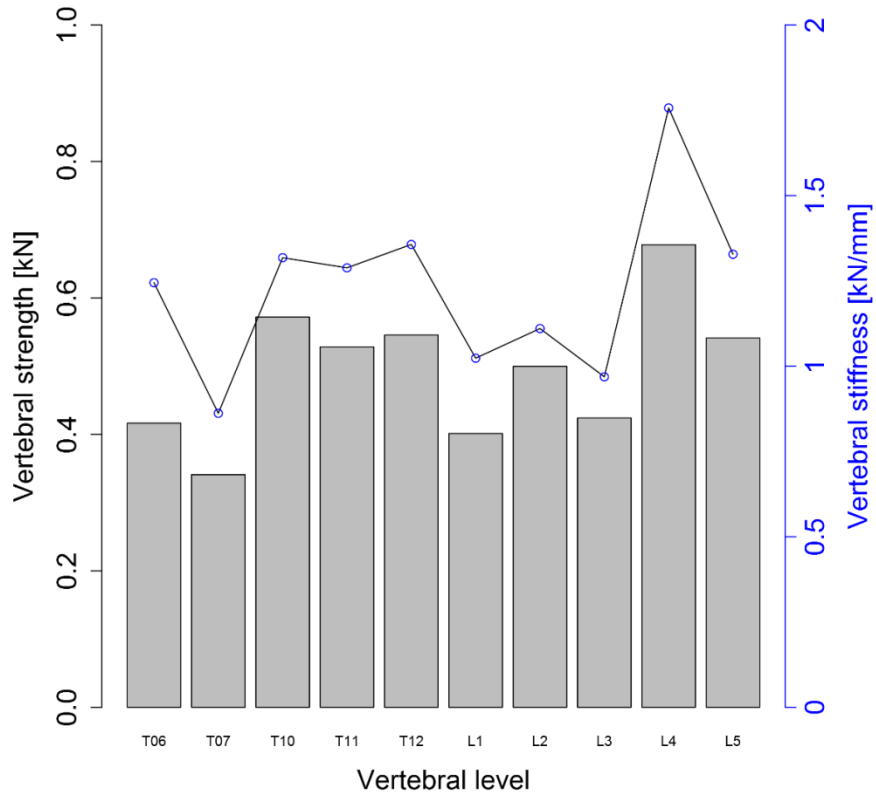


Figure 68 Strength and stiffness data for osteoporotic study for each spine and vertebral level used in the study - Spine 3 BS

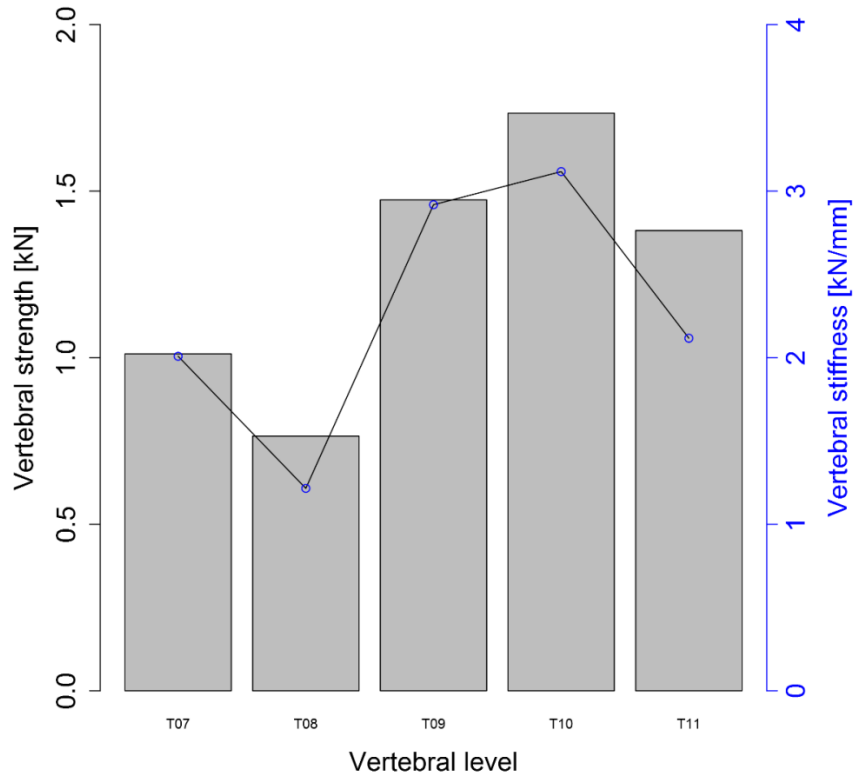


Figure 69 Strength and stiffness data for osteoporotic study for each spine and vertebral level used in the study - SpineGo 1

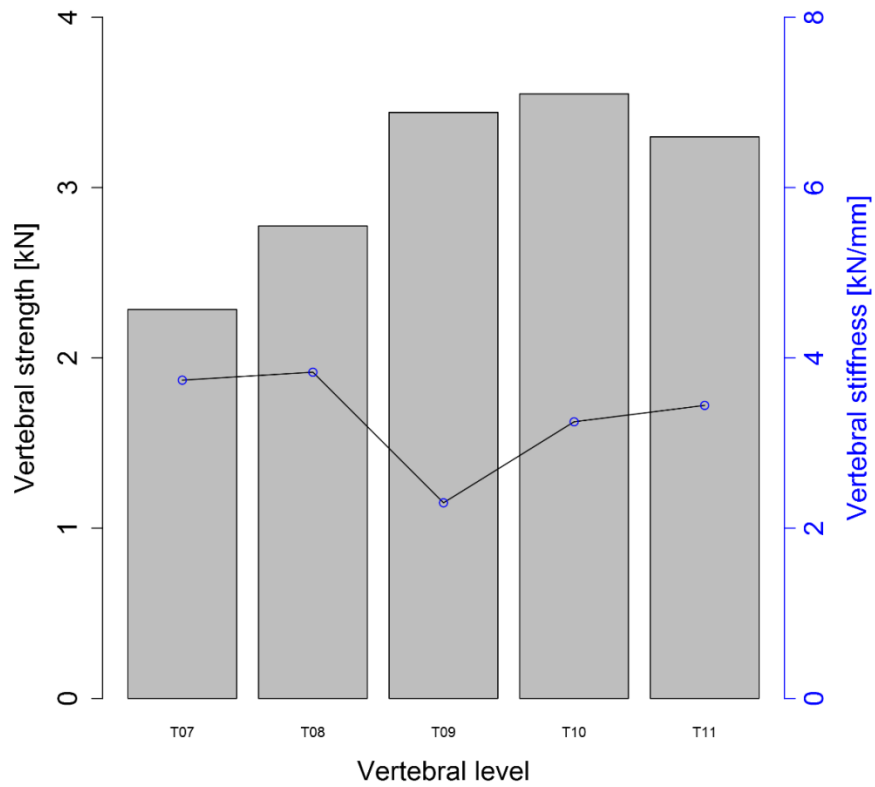


Figure 70 Strength and stiffness data for osteoporotic study for each spine and vertebral level used in the study - SpineGo 2

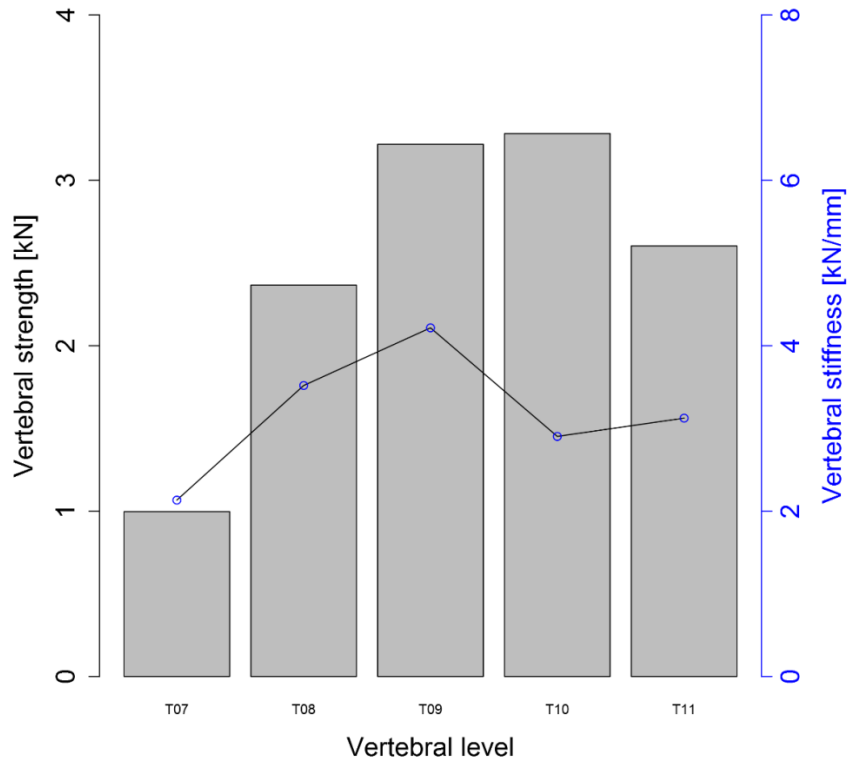


Figure 71 Strength and stiffness data for osteoporotic study for each spine and vertebral level used in the study – SpineGo 4

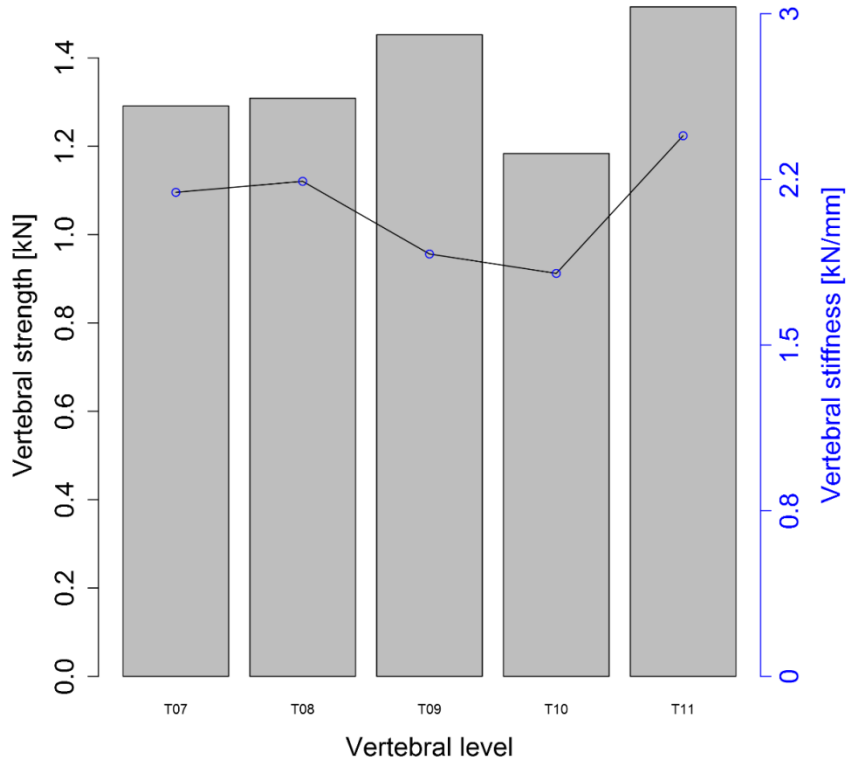


Figure 72 Strength and stiffness data for osteoporotic study for each spine and vertebral level used in the study – SpineGo 5

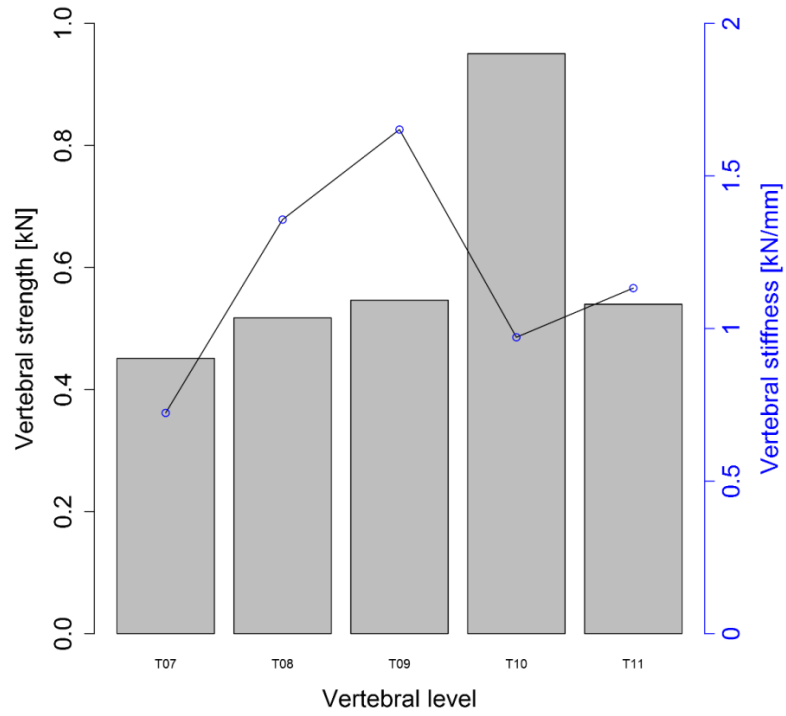


Figure 73 Strength and stiffness data for osteoporotic study for each spine and vertebral level used in the study – SpineGo 6

Appendix E.2: Multiple myeloma

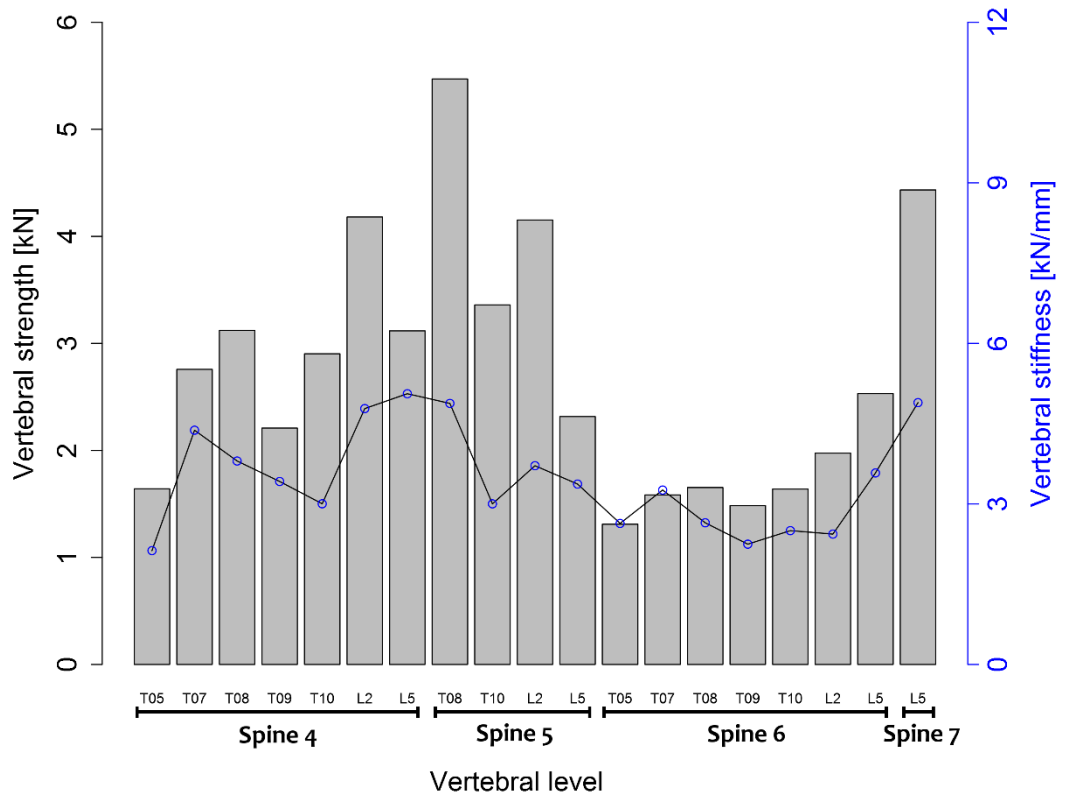


Figure 74 Multiple myeloma samples: Initial strength and stiffness for corresponding donor and spine level

Appendix E.3: Metastases

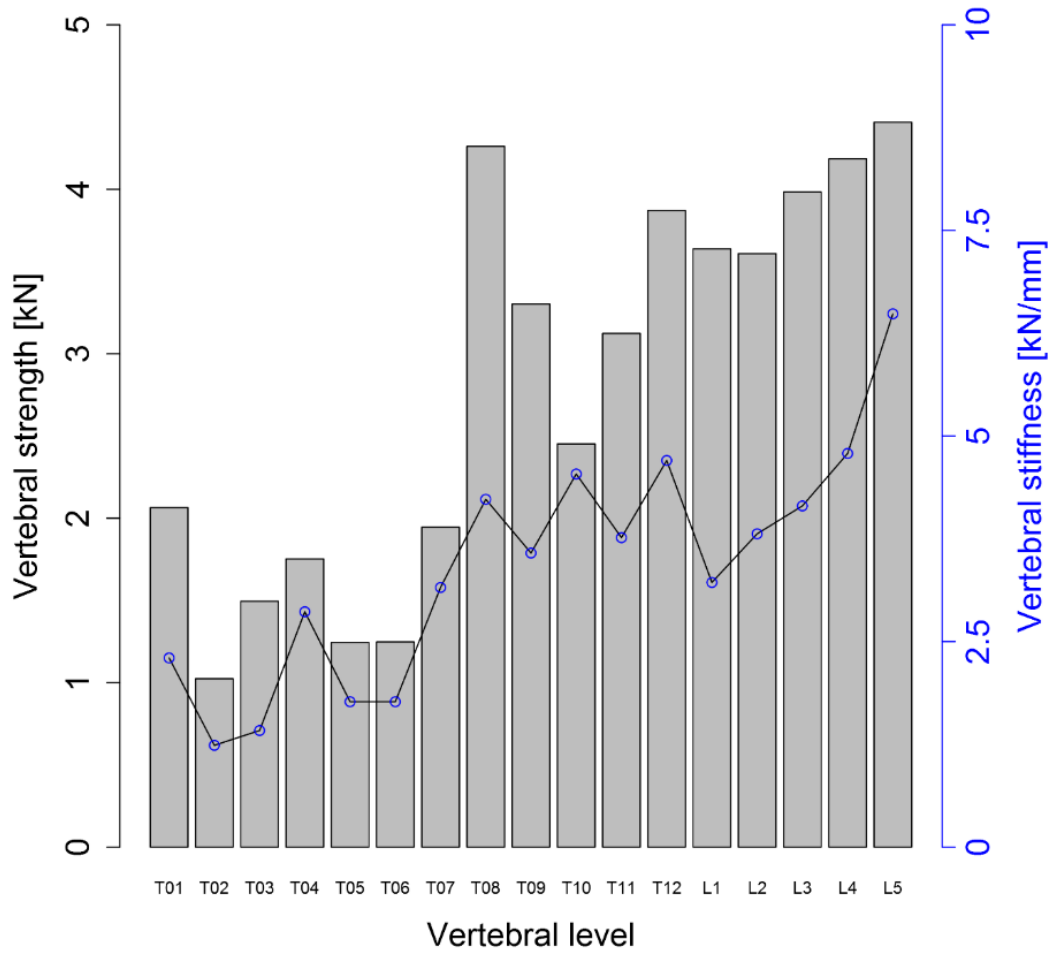


Figure 75 Spine 1 mets: Initial strength and stiffness for corresponding spinal level

Appendix F: Micro-indentation

Appendix F.1: Post-hoc statistical analysis

		Indentation modulus [GPa]							
		Axial				Transverse			
		diff	lwr	upr	p-value	diff	lwr	upr	p-value
MM.L.C-MM.L		1.2	-0.3	2.7	0.136	0.2	-0.7	1.1	0.818
MM.NL-MM.L		0.0	-1.4	1.4	0.999	0.0	-0.9	0.8	0.996
MM.NL-MM.L.C		1.2	-3.0	0.6	0.254	-0.3	-1.4	0.9	0.840
		Hardness [MPa]							
		Axial				Transverse			
		diff	lwr	upr	p-value	diff	lwr	upr	p-value
MM.L.C-MM.L		25.6	-16.6	67.8	0.313	9.6	-21.9	41.2	0.740
MM.NL-MM.L		2.3	-35.9	40.5	0.989	5.8	-24.2	35.9	0.885
MM.NL-MM.L.C		-23.3	-74.1	27.5	0.510	-3.8	-42.4	34.8	0.969
		Elastic Energy [pJ]							
		Axial				Transverse			
		diff	lwr	upr	p-value	diff	lwr	upr	p-value
MM.L.C-MM.L		412	-1078	1902	0.782	328	-1091	1747	0.841
MM.NL-MM.L		28	-1320	1376	0.999	312	-1042	1667	0.842
MM.NL-MM.L.C		-384	-2178	1410	0.862	-16	-1755	1722	0.999
		Plastic Energy [pJ]							
		Axial				Transverse			
		diff	lwr	upr	p-value	diff	lwr	upr	p-value
MM.L.C-MM.L		2871	-1566	7308	0.269	837	-1975	3650	0.752
MM.NL-MM.L		667	-3346	4683	0.914	946	-1739	3631	0.672
MM.NL-MM.L.C		-2202	-7545	3141	0.581	108	-3337	3554	0.997
		Ductility measure ($W_p/(W_e+W_p)$) [1]							
		Axial				Transverse			
		diff	lwr	upr	p-value	diff	lwr	upr	p-value
MM.L.C-MM.L		0.0	0.0	0.0	0.870	0.0	0.0	0.0	0.977
MM.NL-MM.L		0.0	0.0	0.0	0.880	0.0	0.0	0.0	0.989
MM.NL-MM.L.C		0.0	0.0	0.0	0.998	0.0	0.0	0.0	0.998

Table 25 Post-hoc statistical analysis for multiple myeloma bone material properties

Appendix F.2: Humidity and temperature adjustment

Adjustment to the same humidity (κ) and temperature (τ) was performed by using a least square fit of the indentation moduli (E_i), micro-hardness (H) and both indentation energies (W_e , W_p) to a bilinear, affine function (eq. (1.11) with confidents according to (1.12), (1.13), (1.14) and (1.15):

$$E_i, H, W_{elast}, W_{plast} = a_1\tau + a_2\kappa + a_3\tau\kappa + a_4 \quad (1.11)$$

whereas coefficients for each adjustment were:

$$E_i: [a_1, a_2, a_3, a_4] = [-1.33, -1, 0.04, 46.92] \text{ GPa} \quad (1.12)$$

$$H: [a_1, a_2, a_3, a_4] = [71.9, 38.3, -1.7, -1116.8] \text{ MPa} \quad (1.13)$$

$$W_e: [a_1, a_2, a_3, a_4] = [5141, 3069, -131, -103004] \text{ pJ} \quad (1.14)$$

$$W_p: [a_1, a_2, a_3, a_4] = [3591, 1772, -85, -16035] \text{ pJ} \quad (1.15)$$

Parameters of the fit have been provided for the purpose of this thesis by the author of the micro-indentation study comprising a non-affected population, Uwe Wolfram [36]. All four indentation variables were subsequently adjusted to the average humidity $\kappa_{ref} = 50.33\%$ and temperature $\tau_{ref} = 21.62^\circ\text{C}$.

Appendix F.3: Results – graphical form

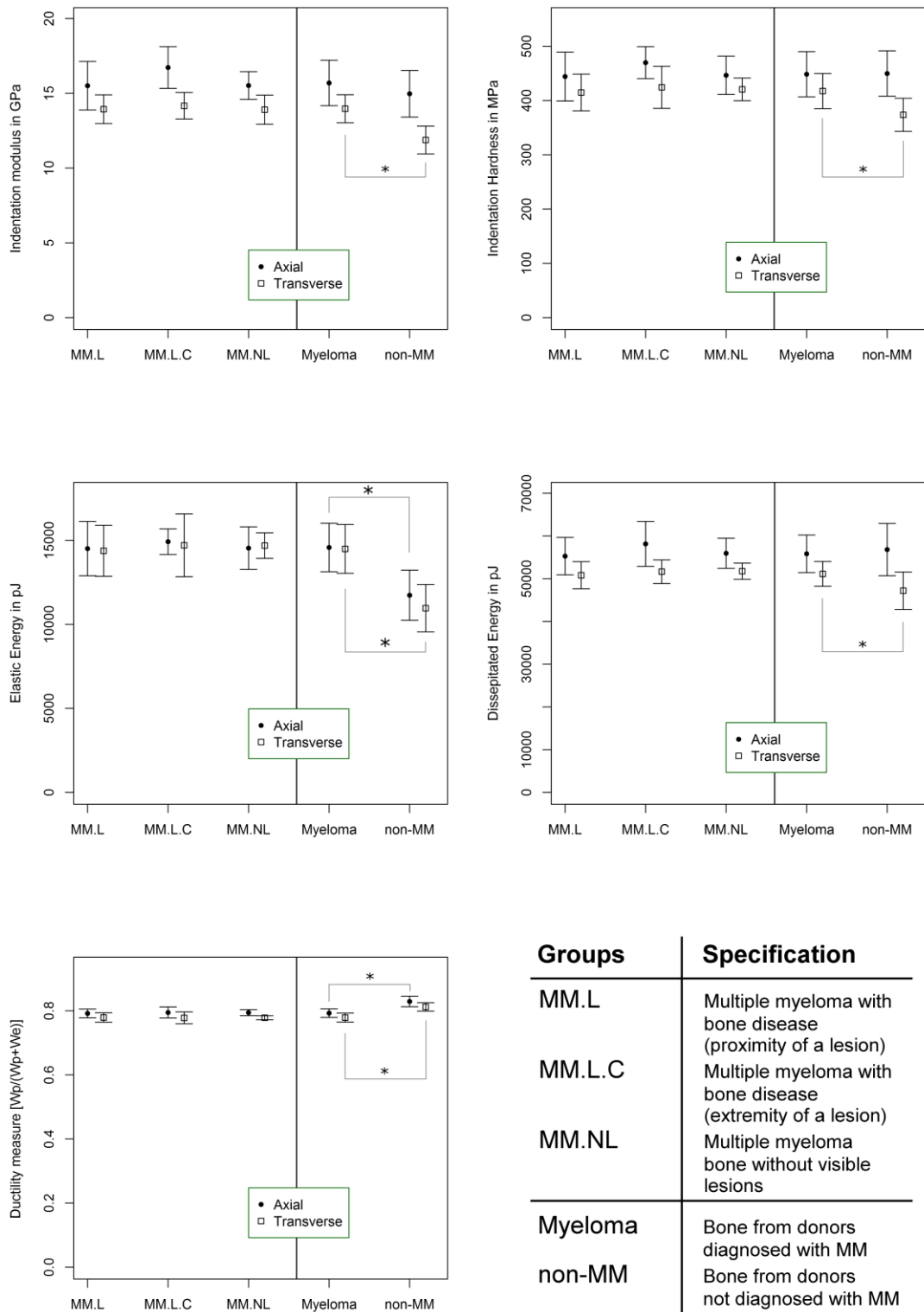


Figure 76 Graphical interpretation of means (\pm stdev) of micro-indentation properties of multiple myeloma bone

Appendix G: Bi-axial eccentric loading

Appendix G.1: Introduction to asymmetric beam theory

A number of approximations has been done in this work. In one, a single vertebra body is taken into account as a part of long thin beam (spine) and hence considered as a slandered beam in which the stress distribution is solved using Euler-Bernoulli beam theory. In another, the bone mineral component, measured by means of radiation tomography, is assumed to stand for material properties such as Young's modulus (E , [GPa]) and yield strength (ϵ , [%]).

This section focuses on approximation that the natural vertebral body loading results in bending towards merely anterior direction and that the loading axis is located closely to the mirror neutral axis. Such assumption allows neglecting the contribution of the eccentric loading with respect to the mirror (anterio-posterior) axis and allows considering point of the highest stress to be located merely anteriorly from the loading axis. This is however valid only when the ratio of eccentricity (moment M_y/M_x stress contribution) remains substantial with respect to primary bending moment (M_y). While this approach has been applied by number of other authors [145, 232, 296], this section aims to justify this approximation by providing extension of the Euler-Bernoulli model when accounting for eccentric loading with respect to both, the primary (bending) and the secondary (mirror) neutral axes. This extension will be tested on highly asymmetric vertebral body profiles with simulated metastatic infiltration (from subsection 3.1.2.4) and on a human cadaver sample with a substantial degree of metastatic VB invasion (subsection 3.3.2.3), where all reanalysed data have been compared to those predicted as a part of the main body of this thesis and to those obtained experimentally.

Appendix G.2: Theoretical consideration for asymmetric beam profile

Appendix G.2.1: Bi-axial eccentric loading in asymmetric profile: definition

The problem of eccentric loading arises when the load is offset from the modulus weighted centroid of the kern with respect to both neutral axes.

Such eccentric loading notably alters the stress distribution along the axial stress with bending introduced by a moment $F \cdot e_1$. This can be illustrated by looking at each of the stress-profiles separately. Here, the stress contribution due to compressional (normal) loading and additional moment can be super-positioned to obtain the full stress profile (depicted as uni-axial eccentric loading in Figure 77). A secondary moment M_x can result in offsetting the modulus weighted centroid in y direction introducing additional moment due to significant mirror non-symmetry along the x axis. Similarly to the situation depicted previously, a stress resulting from such moment is to be super-positioned for the full stress-distribution profile.

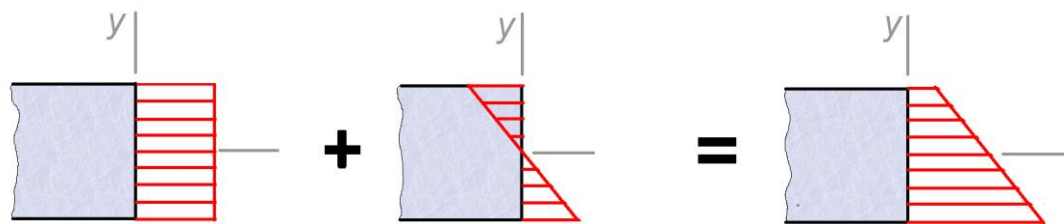


Figure 77 stress profile due to eccentric loading considered as super-positioned stress induced by (i) compression loading (left) and (ii) bending moment (right)

This said, the strain at each point resulting from such stress profile can be obtained by combining contribution of each of the components in a general form presented in eq. (1.16). Here $M_x = F \cdot e_1$, $M_y = F \cdot e_2$ are the eccentric loading moments due to load offsets e_1 and e_2 with respect to the neutral axes; and notation of each component remains dependent on whether causing compression or tension.

$$\varepsilon_{(x,y)} = \frac{F}{EA} \pm \frac{M_y \cdot x}{EI_y} \pm \frac{M_x \cdot y}{EI_x} \quad (1.16)$$

Appendix G.2.2: Moment notation

While compression stress is conventionally noted as negative, this work aims to investigate compressional fracture load and hence compressional stress will be noted as positive. Whether a moment is causing positive or negative stress has been decided on four possible cases due to eccentricity. A case where the eccentricity “ e_1 ” is positioned posteriorly to the neutral axis is highly unlikely and will not be considered. Furthermore, as the nature of the loading was purely compressional (free loading plate using a ball-joint discussed in subsection 3.2.2.4) the tension stress due to introduced eccentricity becomes nil and only positive moments should be accounted for.

Whether a moment contributes to the compressional stress or not is hence depicted in Figure 78 listed for two possible cases whether the loading axis is located on left or right from the mirror neutral axis.

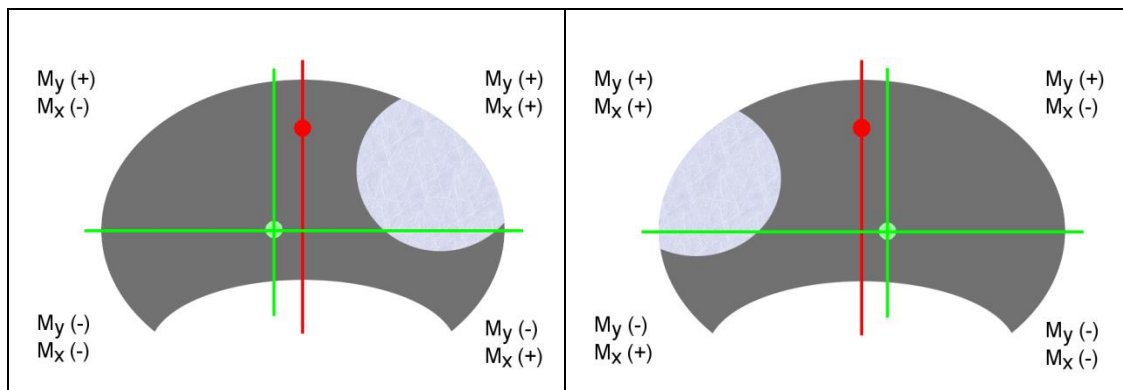


Figure 78 Moment notation with respect to modulus weighted centroid (Green) in asymmetrical vertebrae where the cross-sectional profile has been altered due to presence of a lesion (pale blue)

Appendix G.3: Application of asymmetric beam theory

In total eight “fail” images of the plastic models have been reanalysed accounting for bi-axial eccentricity. In addition a sample with the highest degree of infiltration has been included in the analysis. Here, the plastic models represented a range of samples with a considerable VB shape alteration whereas the latter cadaver sample was selected due to its high asymmetric vertebral body cross-section profile as a result of a severe metastatic infiltration.

In summary, the numerical prediction has been altered to account for:

- i. EI_y next to stand-alone EI_x ;
- ii. Parametric form of all axes used to allow fast solution of their geometrical relations;
- iii. Both eccentricity moments: M_x , M_y ;
- iv. Stress-distribution in each voxel within the vertebral body mask;
- v. Estimation of the minimal fracture load;
- vi. Visualisation of point of failure at which the threshold of 1% strain will be likely to breach.

Appendix G.4: Fracture prediction when accounting for bi-axial eccentric loading: Results

Values of the theoretical strength at which the VB fails (Table 26) were predicted in very close range to values in the main body of the thesis ($y = 0.997*x - 0.4829$ [kN], $R^2 = 0.99$). Besides, the predicted values were closely

associated with the experimental values giving satisfying $R^2 > 0.94$ for plastic models (Figure 79), where the Bland-Altman agreement testing failed to indicate notable differences between error of prediction with respect to the position of the simulated lesion (difference between predicted and tested values does not highlight any outliers with respect to the VB strength depicted in Figure 80). As for the human sample, the results (also in Table 26) indicate close agreement with previously presented prediction as well to the strength obtained experimentally.

Sample type	Lesion type	Single moment/fixed point of highest strain [kN]	Accounting for eccentric loading [kN]	Experimental fracture load [kN]
Plastic (SLA)	No lesion	14.52	14.43	12.83
	Anterior lesion	4.62	4.22	3.28
	lateral lesion	7.26	7.02	4.06
	Latero-posterior lesion	11.88	10.80	10.46
Plastic (SLS)	No lesion	19.58	19.60	17.63
	Anterior lesion	6.38	5.81	2.5
	lateral lesion	9.90	9.53	5.67
	Latero-posterior lesion	16.06	14.65	15.73
Human sample	Spine 2 mets – T8 (Severely infiltrated cadaver sample)	3.07	2.91	3.11

Table 26 Predicted and experimental values in *in-silico* assessment of vertebral strength in simulated metastatic infiltration and a real sample

As a novelty compared to the previous method used, a point of highest stress concentration has been identified. Here, in cases of high degree of asymmetry or absence of most anterior point located directly on the mid-sagittal axis this point has been identified and although not validated experimentally appears to be estimated in an understandable location. This point has been located without user intervention as a point of highest stress based on point-by-point assessment (Figure 81).

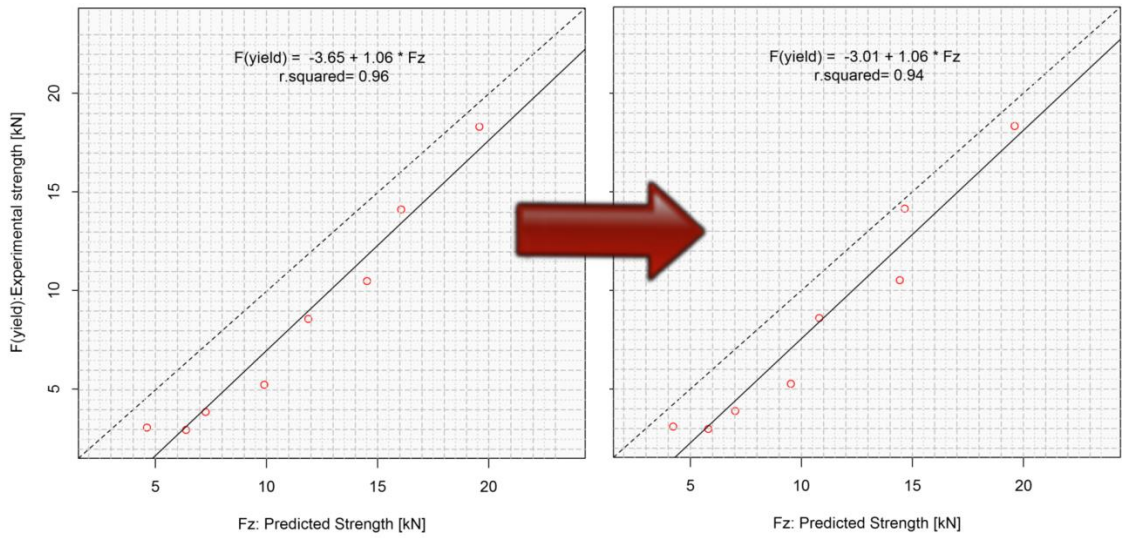


Figure 79 Predicted strength was highly associated with values experimentally obtained in both cases where only uni-axial (left) or bi-axial eccentricity (right) has been considered

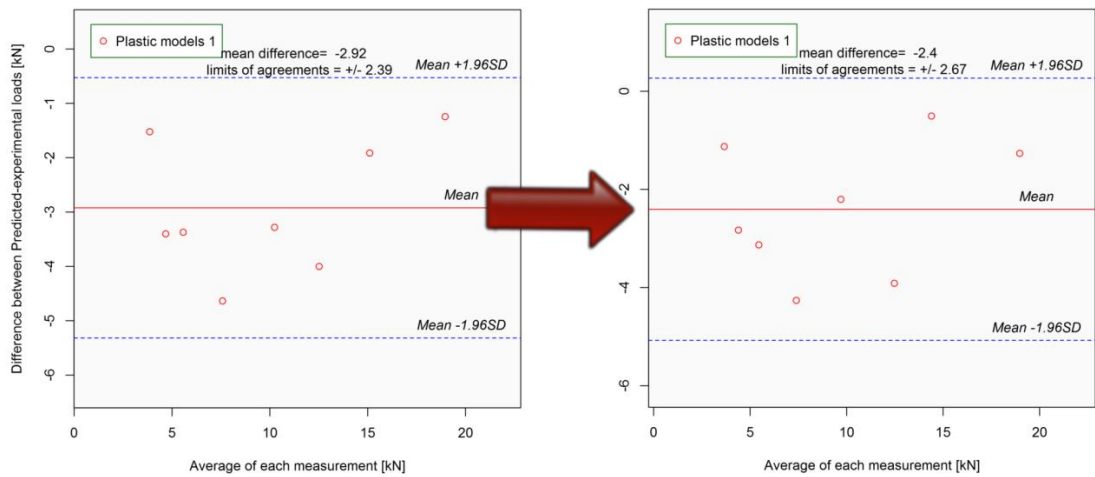


Figure 80 No notable difference in prediction error with respect to overall vertebral strength has been found between the two methods used (left: uni-axial eccentricity used in the main body of the thesis, right: extension to bi-axial eccentricity)

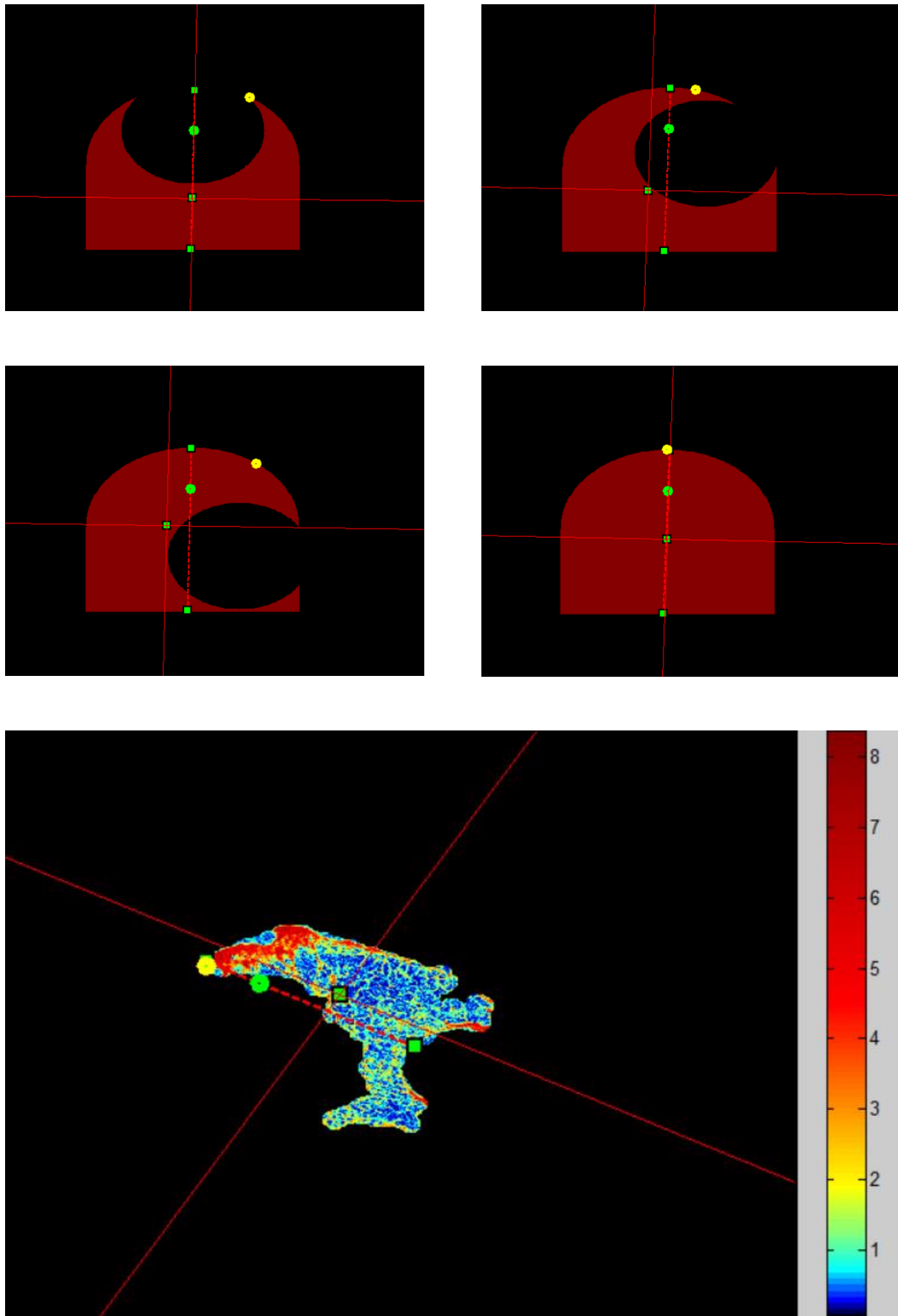


Figure 81 Accounting for spatially varying point of the highest stress allowed to identify where is the vertebra likely to fail (yellow marker). Figure depicts four tested simulated lesions along a real metastatic sample, in all illustrating position of loading axis (green round marker) located on the mid-sagittal axis (red-dashed line), neutral axes (red-solid lines) intersecting the modulus weighted centroid (square green marker)

Appendix G.5: Conclusion when comparing uni and bi- axis eccentric loading with respect to fracture prediction

Reanalysing the data while accounting for the bi-axial eccentricity provided enhanced robustness of the tool for analysing where the bone is prone to be fractured. While the approach used in the main body of the thesis fails to identify site of the highest stress, accounting for both components can point out which part of the bone is likely to fracture. On the other hand, qualitative results in terms of predicting the fracture strength did not show notable difference for the particular loading scenario. In fact, the correlation between predicted and experimental fracture load slightly decreased while remaining results in a very similar range. This was shown even on samples where asymmetry has been modelled to an exaggerated degree. In real samples, the difference between accounting for uni-axial or bi-axial eccentricity in the wedge compression fracture (WCF) was 5.3%. In all cases, these differences are at a limit generally accepted as the experimental error in biomechanical experimental studies.

The section concludes that not accounting for the secondary moment in this thesis has not hampered validity of the values predicted due to predominant contribution of the primary eccentricity moment but could be highly beneficial for qualitative assessment of stress distribution throughout the entire kernel in highly degenerated bone. Furthermore the approach here presented should be used when adapting for complex loading scenario.

Appendix H: Image processing: vertebral body boundary estimation

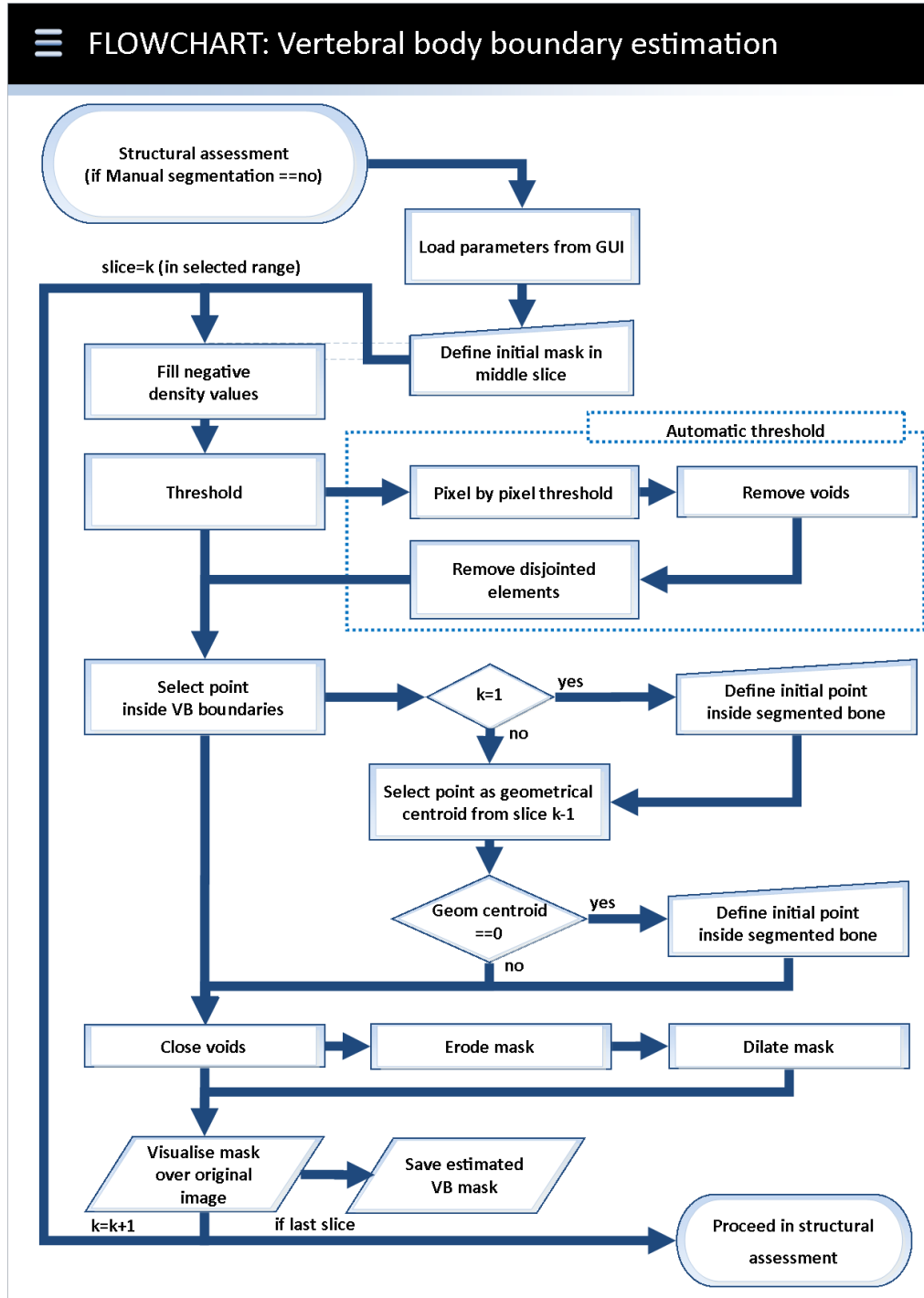


Figure 82 Boundaries of the vertebral body have been estimated using a custom-compiled script. Here, ct-images have been treated on slice-by-slice basis while storing the original image along the binary mask. Binarisation comprised of replacing any negative density values with background (marrow) density, followed by thresholding with subsequent void filling subroutine